Metal oxide and metal oxide-silica thin films deposited by low pressure plasma process : Comparative study of films obtained from Zirconium (IV) tert-Butoxide and Titanium (IV) Isopropoxide

Ines Martinko

THÈSE

En vue de l'obtention du

DOCTORAT DE L'UNIVERSITÉ DE TOULOUSE

Délivré par :

Université Toulouse 3 Paul Sabatier (UT3 Paul Sabatier)

Présentée et soutenue par :
Ines Martinko

le lundi 16 juillet 2018

Titre :

Couches minces d'oxydes métalliques et d'oxydes métalliques-siliciés déposées par procédé plasma basse pression: Étude comparative des couches réalisées à partir de Zirconium (IV) tert-Butoxide et Titanium (IV) Isopropoxide

---

École doctorale et discipline ou spécialité :
ED GEET : Ingénierie des PLASMAS

Unité de recherche :
LAboratoire PLAsma et Conversion d'Énergie (UMR 5213)

Directeur/trice(s) de Thèse :

Patrice Raynaud, Directeur de recherche, CNRS, LAPLACE

Jury :

Jean-Pascal Cambronne, Professeur d'université, UPS, LAPLACE, Toulouse	Président du jury
Laurent Thomas, Professeur d'université, UPVD, PROMES, Perpignan	Rapporteur
Stéphanie Roualdes, Maître de conférence, UM, IEM, Montpellier	Rapportrice
Rony Snyders, Professeur d'université, UMONS, ChIPS, Mons	Examinateur
Alberto Palmero, Directeur de recherche, CSIC, ICMS, Sevilla	Examinateur
Patrice Raynaud, Directeur de recherche, CNRS, LAPLACE, Toulouse	Directeur de thése

Université Fédérale
Toulouse Midi-Pyrénées

THÈSE

En vue de l'obtention du

DOCTORAT DE L'UNIVERSITÉ DE TOULOUSE

Délivré par :

Université Toulouse 3 Paul Sabatier (UT3 Paul Sabatier)

Présentée et soutenue par :
Ines Martinko

le lundi 16 juillet 2018

Titre :

Metal oxide and metal oxide-silica thin films deposited by low pressure plasma process: Comparative study of films obtained from Zirconium (IV) tert-Butoxide and Titanium (IV) Isopropoxide

---

École doctorale et discipline ou spécialité :
ED GEET : Ingénierie des PLASMAS

Unité de recherche :
LAboratoire PLAsma et Conversion d'Énergie (UMR 5213)

Directeur/trice(s) de Thèse :

Patrice Raynaud, Directeur de recherche, CNRS, LAPLACE

Jury :

Jean-Pascal Cambronne, Professeur d'université, UPS, LAPLACE, Toulouse	Président du jury
Laurent Thomas, Professeur d'université, UPVD, PROMES, Perpignan	Rapporteur
Stéphanie Roualdes, Maître de conférence, UM, IEM, Montpellier	Rapportrice
Rony Snyders, Professeur d'université, UMONS, ChIPS, Mons	Examinateur
Alberto Palmero, Directeur de recherche, CSIC, ICMS, Sevilla	Examinateur
Patrice Raynaud, Directeur de recherche, CNRS, LAPLACE, Toulouse	Directeur de thése

*Acknowledgements • Remerciements • Zahvale*

First and foremost, I would like to express my deepest appreciation to my thesis supervisor, M. Patrice Raynaud. Patrice, through all the good times and the hard times, the laughter and the tears, you have always shown your immeasurable humanity and kindness. Thank you for your guidance, advice, for all your encouragement, and for the never-ending supply of positive energy. You have always said *on va y arriver! Et on y est arrivé!* :) Thank you for providing me with the opportunity to gain such a rewarding experience, to grow as a person and to discover the world of science. I am eternally grateful to you for believing in me. Merci Patrice.

I would also like to express my gratitude to the members of the jury: *le président*, M. Jean-Pascal Cambronne, *les rapporteurs*, M. Laurent Thomas and Mme. Stéphanie Roualdes, and *les examinateurs,* M. Alberto Palmero and M. Rony Snyders, for accepting to evaluate this work, for a rewarding discussion and valuable advice. It has been an honour to defend this thesis before you all as members of the jury.

Over the course of this thesis I have encountered kind people from different laboratories, cities and countries, who have contributed to this work in various ways.

M. Alberto Palmero and M. Rafael Alvarez, I would like to express my profound gratitude to you for your timely acceptance of our collaboration proposal, for your advice and enthusiasm that have helped me to a very great extent to successfully complete this thesis.

I am grateful to M. Jérôme Cornil, M. Vincent Lemaur and M. Yoann Olivier for kindly welcoming me in Mons and introducing the world of DFT computations to me.

I would also like to thank M. Vincent Rouessac and M. Arie van der Lee, for their time and answers to all my questions about analysing techniques EP and XRR.

When I first arrived in France, LAPLACE became my home. I am grateful to all personnel of laboratory LAPLACE for making me feel welcome and for their technical, scientific and administrative support.

I would like to thank everyone in my research group MPP: Nicolas G., Kremena, Simon, Nicolas N., Richard, Hubert and Frédéric, for their kind concern, their help, and their valuable advice.

I am grateful to Cédric T., for being welcoming and kind, and for going out of his way to help in my never-ending struggle with the disobedient CNET reactor, and Benoît S. and Benoît L., for their kindness and their readiness to help.

Days in the lab would not have been such a delight without my fellow labmates. I am happy to have met you all and to have shared my laboratory days with you: Morgane, Jaco, Adriana, Joanna, Francesco, Xavier, Mathias, Clémence, Olivier, Marvin, Xi, Rémi, Rick, Raphaël, Jonathan, Amanda, Flora.. And especially, with my Lucie. Lucie, thank you for your infinite kindness, and for being there for me.

Finally, this thesis becomes a reality with the kind support, love and encouragement from my family and friends.

Kika, Doli, Andreja, Goran, Nikola my English Language Guru, Irena, thank you for all the moments we have shared and for the friendships that have grew stronger even with thousands of kilometres between us.

My *famille*, and my *belle famille*, Baka, Marko, Veruča, Jakov, Ema, Dani and David, thank you for wholeheartedly caring and for sharing the happiness with me. Ema *i* Dani, I am forever grateful to you for always calling and answering and cheering me up.

Mama, Tata, *i Seka,* I am eternally thankful for your unconditional love. *Seka*, thank you for always being there for me. *Mama i Tata*, thank you for your never-ending support that has encouraged me through all the years of my education and growing up.

I, šećer na kraju, Boni, the love of my life. You have been with me and there for me through it all, through the good and the hard times, the calm before the storms, and through the teary storms. It is impossible to find the words to describe my gratitude, my feelings for you. You have made this achievement possible. ♡

Table of Contents

List of abbreviations

a. u.	Arbitrary unit
AFM	Atomic force microscopy
ALD	Atomic layer deposition
at.%	Atomic percentage
CCP	Capacitively coupled plasma
CSD	Chemical solution deposition
CVD	Chemical vapour deposition
DBD	Dielectric barrier discharge
DC	Direct current
DFT	Density functional theory
ECR	Electron cyclotron resonance
EP	Ellipsometry porosimetry
FTIR	Fourier transform infrared spectroscopy
HMDSO	Hexamethyldisiloxane
IBICVD	Ion-beam initiated chemical vapour deposition
ICP	Inductively coupled plasma
IR	Infrared
MC	Monte Carlo
MMP-DECR	Microwave multi polar – distributed electron cyclotron resonance
MOCVD	Metalorganic chemical vapour deposition
MS	Mass spectrometry
MW	Microwave
OES	Optical emission spectroscopy
PEALD	Plasma enhanced atomic layer deposition
PECVD	Plasma enhanced chemical vapour deposition
PVD	Physical vapour deposition
RF	Radio frequency
SE	Spectroscopic ellipsometry
SEM	Scanning electron microscopy
TEOS	Tetraethyl orthosilicate
TEOT	Titanium tetra ethoxide
TTIP	Titanium tetra isopropoxide
XPS	X-ray photoelectron spectroscopy
XRD	X-ray diffraction
XRR	X-ray reflectometry
ZTB	Zironium tetra tert-butoxide

General introduction

Research presented in this manuscript has been performed at LAboratory on PLAsma and Conversion of Energy (LAPLACE, Toulouse, France) within the Materials and Plasma Processes (MPP) group. The MPP research group has developed extensive expertise in the domain of Plasma Enhanced Chemical Vapour Deposition (PECVD). The group is experienced in working with different types of plasma reactors and experimental conditions, ranging from very low pressure (~1 mTorr ≈ 0.13 Pa) to atmospheric pressure. Furthermore, low pressure PECVD of $SiO_xC_yH_z$ thin films from organosilicon precursors, Hexamethyldisiloxane (HMDSO) and Tetraethoxysilane (TEOS), has been the subject of numerous research projects [1]–[10].

In the described context, a joint laboratory, PIXCELL-Lab, was created in 2004 between ESSILOR, a renowned global company in the domain of ophthalmologic optics, and academic research laboratories LAPLACE, CIRIMAT and LAAS. The objective of this cooperative effort was to develop a pixelated optical system. Within the framework of this collaboration, Mr R. Cozzolino carried out thesis research focusing on addition of an antireflective property to the pixelated optical system [11]. The construction of desired antireflective coating was based on the combination of a layer with low refractive index, studied in the thesis of Ms I. Savin [4], and a layer with high refractive index, the subject of Mr R. Cozzolino's work. Zirconium dioxide was chosen as a high refractive index material due to its desirable properties such as: n = 1.8-2.2, high transmittance in the visible spectral range, high hardness, low thermal conductivity and strong oxidation resistance. A metalorganic precursor, Zirconium tetra tert-Butoxide (ZTB), was selected for the purpose of synthesizing zirconium oxide thin films. The study has shown the possibility of depositing a zirconium oxide thin film, with high refractive index (n = 1.96) and high optical transparency, from a metalorganic precursor. However, film barrier properties were compromised by the appearance of columnar morphology. To the best of our knowledge, columnar growth mode has not been observed in organosilicon thin films synthesized by low pressure PECVD.

The outlined results had motivated further investigation of ZTB as a precursor and $ZrO_xC_yH_z$ thin film deposition within the framework of the thesis delivered by Mr R. Verhoef [12]. The main objective was to identify molecular and atomic species created in the plasma phase. Chemical composition of the plasma phase was studied in a Radio Frequency Inductively Coupled Plasma (RF ICP) reactor located at Chemistry of Plasma Surface Interactions (ChIPS) laboratory in Mons, Belgium. In the second step, deposited thin films were analysed in order to relate their characteristics to the chemical composition of the plasma. The films were synthesized in the RF ICP reactor at ChIPS, as well as in the

Microwave Multipolar Plasma excited by Distributed Electron Cyclotron Resonance (MPP-DECR) reactor at LAPLACE.

The study has shown that changes in process parameters strongly influence plasma phase chemical composition, as well as thin film characteristics. In the two plasma modes, ICP and ECR, columnar morphology appeared when plasma gas mixture was rich in oxygen gas. It was indicated that columnar growth is not bound to the chemical composition of the films. A wide range of compositions was obtained by varying the power in 100% ZTB plasma, and by adding oxygen gas to the plasma gas mixture. Columnar growth was not observed at 100% ZTB regardless of the chemical composition of deposited thin films.

Our ambition to research the plasma phase of metalorganic PECVD process in a multi-dipolar ECR reactor was motivated by the previously performed studies. We envisioned coupling an experimental investigation by in-situ Fourier Transform Infrared Spectroscopy (FTIR) and Mass Spectrometry (MS) with Density Functional Theory (DFT) calculations. However, technical conditions, had prevented us from performing the study in the given time framework. Specifically, the required, new and sophisticated, plasma analysis system had not been operational at the time.

Accordingly, we had chosen to shift our focus to thin films grown in low pressure metalorganic plasma. Metal oxide nanocoatings are of great scientific and technological interest, in areas ranging from microelectronic industry and optical devices to biomedical applications. These thin films have been synthesized by various techniques such as sol-gel process, standard Chemical Vapour Deposition (CVD) and PECVD. These procedures frequently use metalorganic molecules as precursors.

The thesis presented here aims to serve towards the advancement of general principles that govern low pressure *metalorganic* PECVD. For this purpose, we have introduced another metalorganic precursor, Titanium tetra isopropoxide (TTIP), in addition to ZTB. The objective of this work is to explore and compare the behaviour of $ZrO_xC_yH_z$ and $TiO_xC_yH_z$ thin film growths in low pressure metalorganic plasma and final characteristics of the deposited films. Our research strategy includes a comparative examination of changes induced by variation in the oxygen gas fraction, as well as the total pressure of the plasma gas mixture.

Furthermore, particular attention was given to thin film growth mode, specifically columnar growth. It has been reported that columnar morphology disappears with a very low addition of HMDSO to TTIP/O_2 plasma gas mixture [13]. Therefore, we have explored the deposition of “composite” $ZrSi_xO_yC_zH_w$ and $TiSi_xO_yC_zH_w$ thin films from a combination of metalorganic (ZTB or TTIP, respectively) and organosilicon (HMDSO) precursors.

With respect to the objectives of this work, the thesis manuscript is organised in five chapters. In *Chapter I* we review the fundamental principles of the PECVD process and the basic plasma phase characteristics. Literature survey provides the description of general characteristics of zirconium and titanium oxide thin films, as well as research findings on low pressure PECVD from ZTB and TTIP plasmas. Further, we report on characteristics of "composite" metal-silicon-oxide thin films synthesized by PECVD and other deposition processes.

Chapter II focuses on the experimental context of this study. We review the basic principles and the characteristics of multi-dipolar ECR plasma. Further, the PECVD reactor is introduced in detail, and so are the particularities of precursor molecules: ZTB, TTIP and HMDSO. We also present different diagnostic techniques used to probe the plasma phase and to examine thin film characteristics.

Chapter III is dedicated to the study of thin film growth at different values of O_2 gas percentage of ZTB/O_2 and TTIP/O_2 plasma gas mixtures. We begin with a qualitative OES analysis of the plasma phase and continue with a comparative examination of various thin film characteristics. In collaboration with colleagues at Institute of Material Science in Sevilla (Spain), we couple the experimental results with Monte Carlo (MC) simulations to explain the differences in morphological features between thin films grown in oxygen-rich ZTB and TTIP plasmas.

In *Chapter IV* we study modifications of thin film characteristics induced by an increase in total pressure of plasma gas mixtures. Thin films have been grown in O_2-rich ZTB/O_2 and TTIP/O_2 plasmas to allow examination of the behaviour of columnar growth mode with increasing pressure.

Chapter V explores thin film growth in ZTB/HMDSO/O_2 and TTIP/HMDSO/O_2 plasmas. We analyse the physico-chemical characteristics of "composite" thin films as well as the evolution of morphological features as HMDSO gas is added to O_2-rich metalorganic plasma.

Lastly, *General conclusion and perspectives* paragraph gives a summary of research results and their interpretation. It also introduces perspective research directions based on the conclusions presented in this thesis.

Chapter I

Fundamental scientific principles and literature review

Introduction

One of the objectives of this chapter is to introduce the scientific context of the research presented in this thesis. To begin with, we review fundamental aspects of thin film formation and different deposition techniques. Second, we present the characteristics of the plasma phase and the process of generating plasma. Afterwards, the PECVD deposition technique is described in more detail.

In the second part, we review the literature on physico-chemical, morphological and structural characteristics of zirconia and titania thin films synthesized by PECVD. We also examine the characteristics of “composite” zirconia-silica and titania-silica oxide thin films deposited by PECVD and other deposition techniques.

Finally, as a conclusion, we define the objective and the strategy of our research.

I.2 Thin films: fundamental aspects

The term *thin film* denotes a layer of material typically ranging from few atomic layers to few micrometres in thickness. The fabrication of thin films dates to ancient times. More than 5000 years ago, Egyptian craftsmen recognized the exceptional malleability of gold and used a hammering process to produce golden leaves of remarkable thinness. Samples found in Luxor were measured to be only 0.3 μm thick [14]. Even though thin films have been in use for centuries, corresponding scientific research and production have widely expanded in the last century primarily due to the semiconductor industry and the demand for miniaturization of integrated circuits [15]–[17]. Nowadays, thin film technology is of high importance in numerous fields of science and industry ranging from aerospace industry to medical applications [18]–[22].

I.2.1 Thin film formation

In the following text, we focus on the first steps of thin film formation from a vapour phase as explained by the “capillarity” theory. This approach is of qualitative nature, and although quantitatively inaccurate, it provides useful predictions [14]. First stages of film formation include the nucleation process [14], [23]–[27]. Atoms and molecules impinge on the substrate where they are physisorbed due to permanent or fluctuating dipole moment that induces the Van der Waals attraction. Physisorbed species are then chemisorbed and they participate in nuclei formation (see Figure I-1).

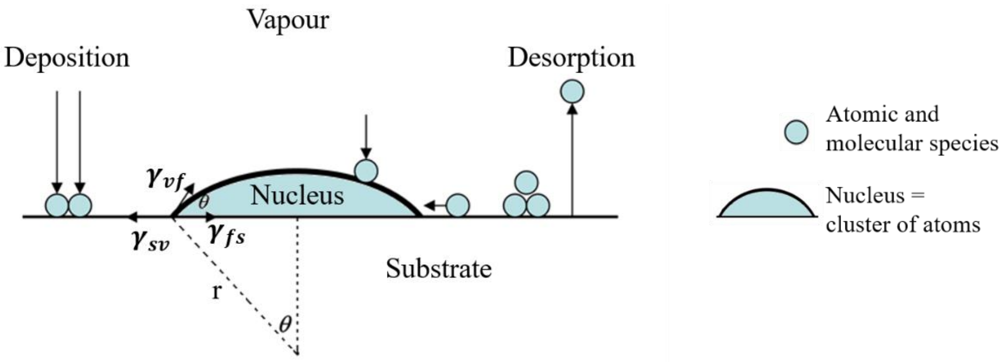

Figure I-1: Schematic representation of a nucleation process during vapour phase deposition (adapted from [14]). θ is the substrate-nucleus contact angle; γ_{sv}, γ_{fs} and γ_{vf} are the substrate-vapour, film-substrate and vapour-film interfacial tensions, respectively.

Nucleus is a cluster of atoms formed due to thermodynamic fluctuations. For thin film growth, nuclei at a critical size are needed. Formed cluster of atoms with a radius less than the critical radius $r*$ is unstable and will lose atoms. Unstable clusters have too high and thermodynamically unfavourable surface free energy. Incorporation of additional atoms/molecules induces an increase in free energy. In contrast, adding more matter to stable nuclei leads to a decrease in free energy. Figure I-2 graphically presents the free energy of a nucleus as a function of nucleus size. The free energy corresponding to critical radius $r*$ represents nucleation energy barrier.

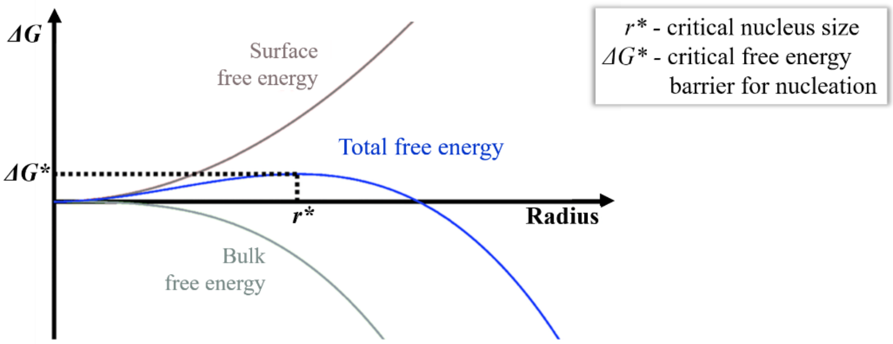

Figure I-2: Free energy change as a function of nucleus size (adapted from [28]).

The nucleation process depends on the tension between substrate-vapour γ_{sv}, film-substrate γ_{fs} and vapour-film γ_{vf} interfaces that are related by Young's equation:

$$\gamma_{sv} = \gamma_{fs} + \gamma_{vf}cos\theta \qquad \textit{Equation I-1}$$

where θ represents the contact angle between the substrate and the nucleus (see Figure I-1). Three fundamental growth modes can be distinguished based on the relations between interfacial tensions mentioned above (see Figure I-3):

1. Volmer-Weber or island growth mode appears when the interaction between the atoms/molecules is stronger than the interaction between the substrate and the atoms/molecules:

$$\gamma_{sv} < \gamma_{fs} + \gamma_{vf}$$ *Equation I-2*

2. Frank-Van der Merwe or layer-by-layer growth mode develops if atoms are more strongly bound to each other than to the substrate:

$$\gamma_{sv} \geq \gamma_{fs} + \gamma_{vf}$$ *Equation I-3*

3. Stranski-Krastanov or layer+island growth mode outsets with a layer-by-layer growth followed by island mode after few initial atomic layers.

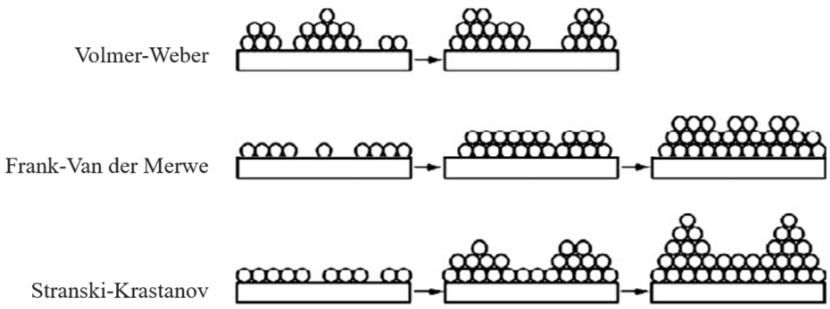

Figure I-3: Basic thin film growth modes (adapted from [14]).

I.2.2 Thin film deposition processes

Different deposition technologies have been developed with regards to the demand for variety of thin film characteristics [29]–[31]. Figure I-4 presents different techniques categorized by the precursor phase.

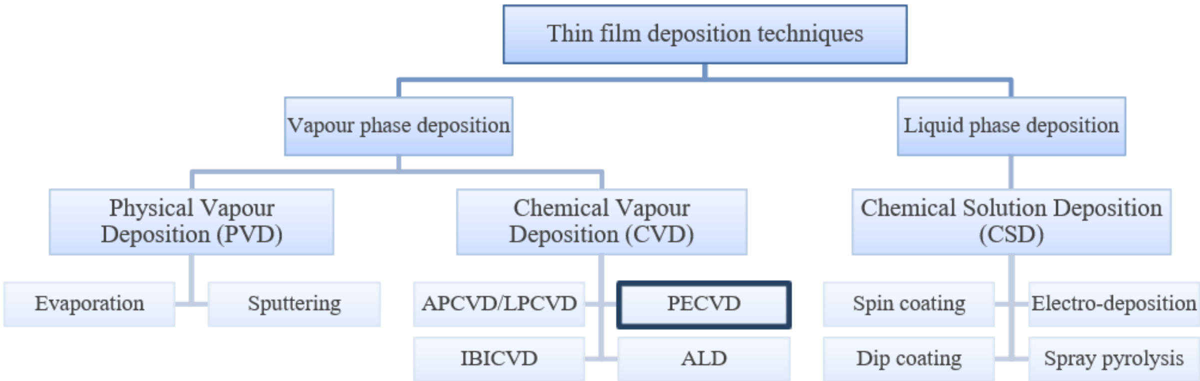

Figure I-4: Classification of thin film deposition techniques according to precursor phase (non-exhaustive list).

I.2.2.1 Chemical Solution Deposition (CSD)

CSD is a wet-chemical process and includes any deposition method of a solid thin film from a liquid chemical precursor. Precursor chemicals are dissolved or suspended in a solvent which, when deposited and heated, results in the formation of a solid thin film. The main steps in the CSD process are: (1.) choosing an appropriate precursor and solvent; (2.) preparation of the solution; (3.) wet film or pattern formation; (4.) drying of the film; (5.) removal of contamination and thermal consolidation.

I.2.2.2 Physical Vapour Deposition (PVD)

PVD is a class of processes used to deposit thin solid films from vaporized material. The main steps include: (1.) converting the solid target material into vapour by physical means; (2.) transporting the vapour from source to substrate; (3.) condensation on the substrate. Two basic PVD techniques, *evaporation* and *sputtering*, are distinguished by the method employed to vaporize the solid target material. *Thermal evaporation* uses heat to convert the source material into vapour in a high vacuum environment. Advantages of this method are high deposition rate, less substrate damage, and excellent purity. On the other hand, film composition is not easily controlled, and the step coverage is difficult to improve. *Sputtering* is a plasma-assisted technique in which the solid target material is vaporized by ionic bombardment. High energy ions are generated in the plasma phase and directed at a target. The ions sputter target atoms that are then transported to the substrate through a region of reduced pressure. Sputtering technique allows using large sized targets and subsequently achieving uniform thickness over large wafers, as well as easily controlling film thickness and alloy composition. The sputtering deposition rate can be fairly low for some materials.

I.2.2.3 Chemical Vapour Deposition (CVD)

CVD is based on the deposition of thin films on a substrate via thermally activated chemical reactions. Reactive gases are introduced into a vacuum chamber and transported to the heated substrate where a thin film is formed. Typically, CVD requires high substrate temperatures (>300°C). The process includes several mechanisms: (1.) the introduction of a reactive gas, precursor, into a reaction chamber; (2.) gas phase collisions between precursor molecules (3.) transport of the precursor to the heated substrate; (4.) adsorption of the precursor onto the substrate; (5.) diffusion, desorption and film forming reactions on the substrate. At lower temperatures the regime is limited by surface reaction rate, whereas at higher temperatures, it is limited by maximum possible rate at which reactant species arrive at the surface.

Plasma Enhanced Chemical Vapour Deposition (PECVD) process is classified as a special type of CVD, which employs an electrical discharge to decompose the precursor gas molecules. Thin films of various materials can be deposited on substrates at significantly lower temperature than in standard CVD. PECVD is used in this work, and is therefore, described in more detail in paragraph I.4 (p.19).

I.3 Plasma phase: fundamental principles

I.3.1 Definition of plasma

In the 1920s, Irving Langmuir was the first to use the term plasma to describe ionised gas appearing in a filament bulb [32]. The origin of the expression lays in the Greek word πλασμα meaning *mouldable substance*. Plasma is also known as the fourth state of matter. When heating matter in a solid state, it first converts to liquid state, then gaseous state. By using even more energy, the substance will transform from gaseous to plasma state.

Although plasma is rarely encountered in everyday life, most of the visible matter that makes the universe is in the plasma state. Stars, stellar atmospheres, interstellar and intergalactic gas are examples of plasma systems. On Earth, matter in plasma state is found in the ionosphere and magnetosphere. Lightning and Northern Lights are further examples of the plasma phase. Plasma is used in industry for material processing, in fluorescent lamps, TV sets, energy production (nuclear fusion), waste incineration, for various medical applications, and in many other areas.

Strictly defined plasma is a state of matter in which all of the atoms and molecules are ionized, i.e. all particles are electrically charged. However, slightly ionised gases (~1%) may show plasma characteristic behaviour. Almost all plasmas on Earth are actually partially ionized gases – composed of electrically charged and neutral particles. The ionization degree of the plasma, α, is defined as the proportion of ionised particles in the plasma:

$$\alpha = \frac{n_i}{n_i + n_n} \qquad \textit{Equation I-4}$$

where n_i is the number density of ionised particles and n_n is the number density of neutral particles. Plasma is said to be weakly ionised if the value of the ionisation degree α is lower than 10^{-4} [33].

Plasma phase is characterized by the presence of collective interactions between particles. Long-range Coulomb interaction appears in the plasma due to a large number of charged particles. Particles in the gas phase interact in collisions, whereas in plasma there is a sufficient number of free charged particles, thus plasma dynamics are dominated by electric and magnetic forces. The particles interact collectively, forming an electromagnetic field where each particle interacts simultaneously with all the others.

Plasma is a quasi-neutral system composed of charged and neutral particles: *electrons*, *neutral atoms* and *molecules*, *positive* and *negative ions*, *excited* and *radical* species and *photons* produced in the relaxation process of excited species. Quasi-neutrality implies that plasma is macroscopically neutral, i.e. it is composed of an equal number of positively and negatively charged particles:

$$n_e \approx n_i \qquad \textit{Equation I-5}$$

where n_e and n_i represent electron and ion density, respectively. Plasma quasi-neutrality is derived from the concept of electrostatic or Debye shielding. The interaction between individual particles in the plasma is negligible in relation to the collective interaction. The particles in the plasma "see" each other over long distances, thus the effect of electrostatic shielding arises.

I.3.2 Plasma characteristics

For classifying and comparing different kinds of plasmas (Figure I-5), we typically use two primary parameters:

- electron temperature T_e and
- electron number density n_e.

The temperature of the particles present in the plasma is usually expressed in electronvolt (eV): 1 eV corresponds to approximately 11600 K.

Plasma phase contains “lightweight” electrons and “heavy” neutral and ionized atoms and molecules. Based on the relative temperatures of these species, plasmas are classified into two categories:

- plasmas at thermodynamic equilibrium (also called thermal plasmas) → the temperature of electrons T_e, ions T_i, and neutrals T_n is equal ($T_e = T_i = T_n$),
- plasmas at non-thermodynamic equilibrium, known as cold plasmas → the temperatures of the different plasma species are not equal, yet the electrons are characterized by much higher temperatures than the heavy particles ($T_e >> T_i$, T_n).

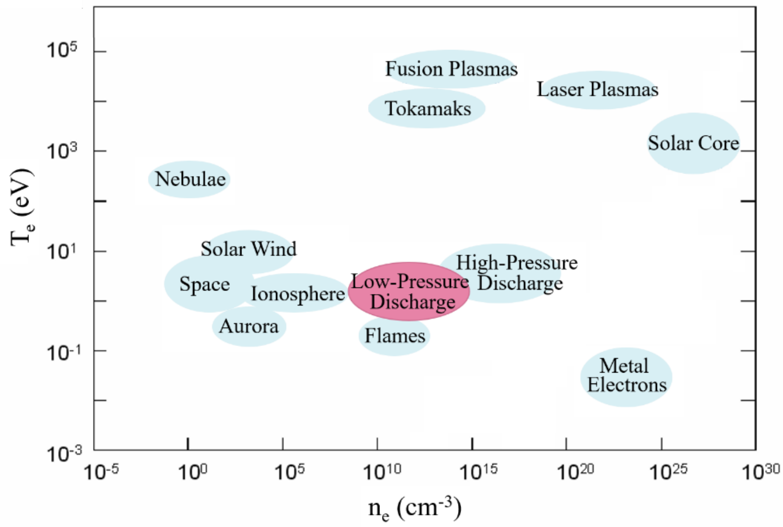

Figure I-5: Different types of plasmas classified by electron temperature and electron density (adapted from [34]).

Examples of plasmas at thermodynamic equilibrium are highly ionised plasmas with highly energetic species ($\alpha \approx 1$ and $T_e > 10^6$ K), such as fusion plasma. Partially ionised plasma ($\alpha << 1$), such as gas discharge plasmas, can be at non-thermodynamic equilibrium, as well as close to thermodynamic equilibrium depending on the pressure and discharge length. At low pressures, low collision rate due to long particle mean free path leads to inefficient energy transfer and $T_e >> T_{heavy}$. At high pressures, frequent collisions lead to efficient energy transfer and $T_e = T_{heavy}$ (e.g. lightning, plasma arc). If the discharge length is sufficiently small, we will obtain non-thermodynamic equilibrium regardless of high pressure (e.g. Dielectric Barrier Discharge - DBD). In this work, we used low pressure gas discharge plasma characterised by non-thermodynamic equilibrium.

I.3.3 Generating plasma

The ionisation of atoms is the most important process in generating and sustaining the plasma phase. For an atom to be ionised, it needs to absorb enough energy. Frequent collisions, in which new charged particles are created, sustain the plasma state. There are several ways for ionization to take place. The most notable is the direct ionization by electronic impact. An electron e^- transmits energy to an atom or molecule A during collision, so an additional electron is released, and an ion is created:

$$A + e^- \rightarrow A^+ + e^- + e^- \qquad \textit{Equation I-6}$$

This process is the most important process in low temperature plasmas where the electron energy is high enough, i.e. significantly higher than the energy of neutral atoms and ions. In addition to the direct collisional ionization, the electrons can ionize the atom gradually in several collisions. At first, the atom is excited, and in subsequent collision it is ionised:

$$A + e^{-} \rightarrow A^{*} + e^{-}$$ *Equation I-7*

$$A^{*} + e^{-} \rightarrow A^{+} + e^{-} + e^{-}$$ *Equation I-8*

where A is a neutral particle, A^{*} excited neutral particle, A^{+} ion and e^{-} an electron. An electron can be released in a collision of two neutral atoms in excited states:

$$A^{*} + A^{*} \rightarrow A^{+} + e^{-} + A$$ *Equation I-9*

The described reaction is called ionization in a collision with a heavy particle. Heavy colliding particles can be two neutrals, ion and a neutral atom or two ions.

In high-temperature plasmas, in which photon energy is high, photoionization is a significant process. The photon of energy hv is absorbed by a neutral atom A providing sufficient energy to ionize the atom:

$$A + hv \rightarrow A^{+} + e^{-}$$ *Equation I-10*

If the photon energy is greater than the ionization energy, the difference transforms to kinetic energy of the released electron.

Free electron production can also be achieved in the so-called surface ionization. Electrons, ions or photons can hit the surface of the reactor wall or the electrode and new electrons emerge from the surface.

I.3.3.1 Plasma in a laboratory

In a laboratory environment, low temperature plasmas are typically generated by applying electrical energy to the gas and accelerating the few free electrons present due to cosmic or radioactive radiation of gas atoms and molecules [35], [36]. The plasma is generated and sustained by applying electric energy usually via direct current (DC), radiofrequency (RF) or microwave (MW) power. The type of source used to generate plasma defines the range of plasma parameters such as T_e, n_e and working pressure (see Table I-1).

Table I-1: Plasma parameters corresponding to different types of plasma sources (adapted from [37]).

Type of source	Pressure (mbar)	n_e (cm^{-3})	T_e (eV)
RF capacitive	10^{-3}-10	10^{11}	1-10
hollow cathode	1	10^{12}	0.1
RF inductive	10^{-3}-10	10^{12}	1
helicon	10^{-4}-10^{-2}	10^{13}	1

Type of source	Pressure (mbar)	n_e (cm^{-3})	T_e (eV)
MW			
surfatron	1000	10^{12}	5
planar	100	10^{11}	2
closed structure	1000	10^{12}	3
ECR	**10^{-3}**	**10^{12}**	**5**
DBD	1000	10^{14}	5
DC glow	10^{-3}-100		
cathode region		10^{12}	100
negative glow		10^{11}	0.1
positive column	10^{-2}-800	10^{12}	1-10
hollow cathode			0.1

Regarding pressure units, we use millitorr (mTorr) to express pressure values in this work. Generally, various pressure units are used in scientific and industrial plasma laboratories. Therefore, we present different pressure units and their values equivalent to 1 mTorr in Table I-2.

Table I-2: Units of pressure frequently used in plasma science and industry.

Unit	Symbol	Pressure values equivalent to 1 mTorr
Torr	Torr	$1 \cdot 10^{-3}$ Torr
Pascal	Pa	≈ 0.13 Pa
Bar	bar	≈ $1.33 \cdot 10^{-6}$ bar
Millibar	mbar	≈ $1.33 \cdot 10^{-3}$ mbar
Millimetre of mercury	mmHg	≈ $1 \cdot 10^{-3}$ mmHg
Atmosphere	atm	≈ $1.32 \cdot 10^{-6}$ atm

I.4 Plasma Enhanced Chemical Vapour Deposition

Plasma Enhanced Chemical Vapour Deposition (PECVD) is a special type of the CVD process. The principle is based on the deposition of material on a desired substrate exposed to reactive particles. The reactive particles are created by applying electric field to a gas confined in a reactor chamber. The gas is then transformed to plasma. The processes in the plasma phase include ionization, excitation, and dissociation, recombination of gas atoms and molecules, as well as production of photons. The particles are ionized, excited, and dissociated in collisions with accelerated electrons as presented in Equation I-6, Equation I-7 and Equation I-8 (p.17), Equation I-11 and Equation I-12:

$$AB + e^- \rightarrow A^+ + \mathrm{B} + 2e^- \text{ (dissociative ionization)} \qquad \textit{Equation I-11}$$

$$AB + e^- \rightarrow \mathrm{A} + \mathrm{B} + e^- \text{ (electron impact dissociation)} \qquad \textit{Equation I-12}$$

where A and B are neutral particles, AB neutral molecular particle, A^* excited neutral particle, A^+ ion and e^- an electron.

Reactions in the plasma phase depend on the process parameters such as gas pressure, the electric power and the gas composition. These parameters influence the type of species created in the plasma phase. The species are transported to the substrate surface where they contribute to thin film formation and growth. The thin film formation is a result of plasma-substrate interaction involving reactive surface reactions as presented in Figure I-6. The nature, size and energy of impinging species, as well as the surface temperature, influence the various surface phenomena such as adsorption, diffusion, desorption, nucleation, and coalescence.

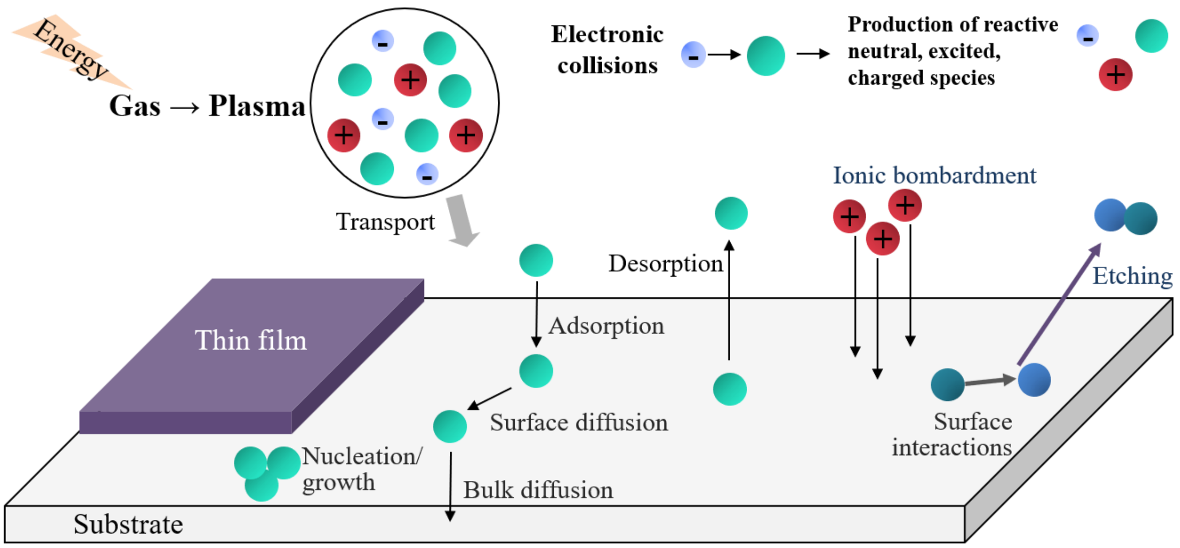

Figure I-6: Schematic presentation of plasma and surface processes in PECVD (adapted from [38]).

There is a strong dependency between external process parameters (such as pressure, electrical power, gas mixture, and surface temperature) and phenomena leading to thin film formation [29]. These parameters can be utilized to control thin film growth and obtain materials with desired properties.

I.5 Zirconium oxide and titanium oxide thin films: literature review

I.5.1 Zirconium oxide thin films deposited by PECVD

Zirconium oxide coatings are of interest to variety of areas ranging from microelectronic industry and optical devices to biomedicine and protective coatings. Their significance in both science and technology is due to desirable properties such as good thermal stability, low thermal conductivity, oxidation resistance and high hardness, biocompatibility, high dielectric constant (ε = 14–25) and wide band gap (E_g = 4.6-7.8 eV) [39]–[49]. They are widely employed as optical coatings because of their high refractive index (n = 1.8-2.2) and high transparency in visible and near infrared range [11], [50]–[53].

Zirconia thin films have been synthesized using various techniques such as sol-gel [53]–[57], PVD [51], [58]–[62], CVD [47], [63]–[67], and PECVD [12], [39], [40], [48], [49], [68]–[73] processes. In this review, we focus on the ZrO_2-like thin film synthesized by PECVD. Table I-3 summarizes the physico-chemical, morphological, and macroscopic characteristics of thin films as reported in literature.

In terms of application, the studies summarized in Table I-3 have focused on zirconia films as optical coatings with high transparency and high refractive index [11], [73], and as gate dielectric material in metal–oxide–semiconductor (MOS) transistors and storage capacitor in dynamic random access memory (DRAM) devices [48], [70]. The PECVD of the ZrO_2 thin films has mostly been performed in MW ECR and RF ICP reactors. In the deposition process, Zirconium Tetra tert-Butoxide (ZTB) is most frequently used as a precursor, while O_2 gas is employed as an oxidant. ZTB is often introduced with a carrier gas (usually argon) due to its low vapour pressure. Besides ZTB, Zirconium tetrachloride ($ZrCl_4$) has been used as precursor fairly often.

Several studies investigated the influence of gas mixture composition on thin film characteristics [12], [69], [70]. It has been reported that the carbon at.% decreases, while the refractive index and density increase with rise of O_2 gas proportion in the gas mixture. Column-like structures have been observed in O_2 rich plasmas, whereas in pure precursor plasmas films exhibit uniform morphology. The deposited films have been predominantly amorphous, sometimes with incorporated polycrystalline phases (monoclinic and tetragonal). The fraction of crystalline phase increases with oxygen addition to the gas mixture.

It has been shown that varying the process parameters influences final characteristics of the thin films. Higher substrate temperature and substrate polarization have been used to enhance the crystallization of the films as well as the refractive index [39], [48], [71], [72]. The same has been achieved by employing the post-deposition annealing process [48].

Table I-3: Characteristics of ZrO_2-like thin films obtained by PECVD: literature review.

Deposition method and growth conditions	Chemical composition and chemical bonding	Morphological and structural characteristics	Macroscopic properties (n, density)	References
MW ECR **ZTB+O_2** p_{total}: 1 mTorr P_{MW}: 800W O_2: 0-90% T_s=55°C	%O_2 ↗: ↘ C at.% ↘ C-H, ↗ Zr-O	Granular nature %O_2 ↗: uniform → columnar morphology (at ≥80% O_2)	Not reported	[12]
MW ECR **ZTB+O_2** p_{total}: 1mTorr O_2: 0-95% P_{MW}: 200-800W T_s: uncontrolled	Homogeneous in-depth composition %O_2 ↗: ↘ C at.% $ZrO_{1.5}C_{2.5}$→$ZrO_{1.4}C_{0.1}$ (bulk stoichiometry)	%O_2 ↗: Surface roughness ↗ Amorphous→amorphous+poly-crystalline (monoclinic and tetragonal) (at ≥80% O_2) Uniform→columnar morphology (at ≥80% O_2)	%O_2 ↗: density↗ (2.6→4.2g/cm^{-3}) n↗ (n_{550nm}=1.6→1.9) ↗ P_{MW} (100%ZTB): density↗ (1.8→2.7g/cm^{-3}) n↗ (n_{550nm}=1.58-1.76)	[69]
RF ICP **ZTB+O_2** O_2: 0-90% p_{total}: 4mTorr P_{RF}: 20-200W T_s: uncontrolled	P_{RF} ↗ (100%ZTB): C at.% ↗ $ZrO_3C_{2.6}$→ZrO_5C_{23} (surface stoichiometry) %O_2 ↗: ↘ C at.%	P_{RF} ↗(100%ZTB): Granular nature Uniform morphology %O_2 ↗: from uniform morphology to columnar growth (at ≥80% O_2)	Not reported	[12]
Remote RF PECVD **ZTB+O_2** T_s: 170-385°C	C at.% not detectable (<1%)	Not reported	T_s ↗→ n ↗ n: 1.70-2.04	[72]
RF ICP **ZTB+O_2** (carrier gas: Ar) p_{total}: 95-125mTorr P_{RF}: 900-1500W V_b: 0-500V T_s: 280-350 °C	Stoichiometric composition Some carbon in the films No carbide	V_b ↗: amorphous → crystalline (mainly tetragonal, small amounts of monoclinic) Columnar morphology	Not reported	[71]
MW ECR **ZTB+O_2** (carrier gas: Ar) p_{total}: 10-40mTorr O_2/Ar: 0-10 P_{MW}: 300-900W	Bonds: O-H, C-C, Zr-O, C=O, C-O, O-C-O O_2 ↗: ↘ C at.% O_2/Ar ≥ 0.2: ZrO_2 C-H ↘	O_2/Ar ↗→ roughness ↘ Amorphous+very small fraction polycrystalline (tetragonal and monoclinic)	Not reported	[70]

Deposition method and growth conditions	Chemical composition and chemical bonding	Morphological and structural characteristics	Macroscopic properties (n, density)	References
MW ECR **ZTB+O$_2$** p_{total}: 1.2mTorr P_{MW}: 500W P_{RF}(bias): 0 or 25W O_2: 83%	Not reported	Amorphous + small fraction polycrystalline (tetragonal and monoclinic) V_b↗: amorphous → crystalline	<u>V_b↗:</u> n ↗ ($n_{632.28nm}$=1.85→1.92) Anneal (700°C in N_2): n ↗ ($n_{632.28nm}$=1.92→2.04)	[48]
RF CCP **ZTB+Ar+O$_2$** (carrier gas: Ar) p_{total}: 1-4 Pa (≈7.5-30 mTorr) P_{RF}: 25-150W V_b:100-400V T_s: uncontrolled	<u>ZTB+Ar</u> C at.%: max 57% $ZrO_{6.2}C_{9.3}$ <u>ZTB+Ar+O$_2$</u> C at.%: max 27% <u>ZTB+O$_2$</u> O-H peak pronounced, C-H peak weak $ZrO_{3.8}C_{1.8}$	<u>ZTB+Ar</u> R_a=5 nm Uniform morphology <u>ZTB+Ar+O$_2$</u> Amorphous Columnar <u>ZTB+O$_2$</u> R_a=25nm Amorphous Columnar	P_{RF} ↗ → n ↗ <u>ZTB+Ar</u> n_{546nm}=1.78→1.90 transmittance: 70% <u>ZTB+Ar+O$_2$</u> n_{546nm}=1.58→1.80 <u>ZTB+O$_2$</u> max n_{546nm}=2.12 Transmittance: 85-90%	[73]
MW **ZrCl$_4$+O$_2$** (carrier gas: Ar) p_{total}:130Pa (≈975mTorr) P_{MW}:400W T_s: 300-800°C	O wt.%: 25.9% No carbon detected	Columnar with numerous intra- and intercolumnar porosities T_s=300-400°C: nanocrystalline or amorphous structures T_s=500°C, 800°C: monoclinic + indication of tetragonal/cubic	Not reported	[39]

I.5.2 Titanium oxide thin films deposited by PECVD

Titanium dioxide films have been extensively studied as a photocatalyst for various applications such as decomposing organic compounds, disinfection purposes, as well as UV-sensitive hydrophilic surfaces [74]–[78]. Due to their stability, high refractive index, and transparency over a wide spectral range, titania films are broadly used as optical coatings for dielectric interference filters, multilayer mirrors or antireflective layers [13], [79]–[81].

Various deposition processes have been used for obtaining titania thin films such as sol-gel [82]–[85], PVD [86]–[89] and CVD [90]–[93]. Table I-4 presents the characteristics of titanium oxide films grown in RF and MW PECVD as reported by different research groups. Usually, Titanium tetra isopropoxide (TTIP) or Titanium tetrachloride ($TiCl_4$) are used as precursor molecules and oxygen gas as an oxidant. Most frequently a carrier gas (Ar, O_2 or He) is used to inject the titanium precursor into the reactor.

Carbon atomic content has been detected in most films deposited by metalorganic PECVD. Decrease of carbon contamination has been observed with increase of oxygen gas proportion in the gas mixture [94] or with ionic bombardment, induced by polarisation of the substrate [95].

The films deposited in TTIP/O_2 plasma at very high O_2 gas proportion in the gas mixture exhibit mostly columnar morphology [95][96]. Li at al. have shown that the substrate polarisation induces a change in growth mode of the film, evidenced in the disappearance of column-like structures and the appearance of smooth surface and uniform morphology [97]. Films are predominantly amorphous when deposited at floating potential and uncontrolled substrate temperature, which typically remains below 150°C. At substrate temperatures higher than ~250°C, presence of anatase as crystalline phase has been detected. Increase in substrate bias voltage has also been used to increase crystallization of the films.

Regarding the optical properties, maximum values of *n* at 550nm have been found in the 1.7-2.4 range. Refractive index increases with substrate thermal heating. Post-annealing procedure can also be used to increase the refractive index and the film density [98].

Table I-4: Characteristics of TiO_2-like thin films obtained by PECVD: literature review.

Deposition method and growth conditions	Chemical composition and chemical bonding	Morphological and structural characteristics	Macroscopic properties (n, density)	References
RF CCP **TTIP+Ar** **TTIP+O_2** (carrier gas: He) T_s: uncontrolled (<35°C) V_b: from -600V to 600V	TTIP+Ar C/Ti: 4.2-5.3 TTIP+O_2 O_2 ↗: C at.% ↘ $TiO_{2.5}C_{0.8}$→ $TiO_{2.3}C_{0.6}$	Amorphous	TTIP+Ar n_{550nm}=1.58-1.84 TTIP+O_2 n_{550nm}=1.56-1.74	[94]
Remote MW **TTIP+O_2** **TTIP+O_2+Ar** p_{total}: 4mTorr P_{MW}: 400W T_s: 25-250°C	Carbon at.%: ~15% (before surface cleaning) ~4-5% (after surface cleaning)	Amorphous; at T_s>230°C presence of anatase phase TTIP+O_2 Columnar T_s=25°C narrow columns T_s=250°C columns formed by small polyhedral crystallites TTIP+O_2+Ar T_s=25°C uniform T_s=200°C globular T_s=250°C columnar	T_s ↗ → n ↗ TTIP+O_2 n_{550nm}=2.1→2.2 TTIP+O_2+Ar n_{550nm}=1.9→2.4	[96]

Deposition method and growth conditions	**Chemical composition and chemical bonding**	**Morphological and structural characteristics**	**Macroscopic properties (n, density)**	**References**
RF ICP **TTIP+ O_2** (carrier gas: O_2) P_{RF}: 300W p_{total}: 3-5 mTorr V_b: V_f, -15V T_s: uncontrolled (<100°C)	V_b: V_f → -15 V O/Ti=1.92→2.08 C at.%=10→4% O-H ↘ C-O ↗ and C=O ↗	V_f: amorphous V_b: amorphous+rutile detected All columnar with granular surface morphology	V_b: V_f → -15 V n_{633nm}=2.0→2.32 density=3.0 →3.7 g/cm^3	[95]
MW ECR **TTIP+O_2** P_{MW}: 75 W p_{total}: 1.1-1.25 mTorr T_s: 100 °C	O/Ti > 2 C at.%: ~13 %	Not reported	TTIP ↗ → n ↘ n_{500nm}=2.38→2.1 for p_{TTIP}=0.1→0.25mTorr	[81]
Remote MW **TTIP+O_2+H_2** (carrier gas: He) P_{MW}: 500W p_{total}: 0.1 Torr T_s: 100-300°C	T_s ↗ → O-H ↘ H_2/O_2 ↗ → O-H ↘, Ti-O-Ti ↘	Amorphous	T_s ↗ → n ↗ $n_{632.8nm}$=1.9→2.35 H_2/O_2 ↗ → n ↘ $n_{632.8nm}$=2.18→1.92	[99]
RF CCP **$TiCl_4$+O_2** (carrier gas: Ar) P_{RF}: 100-300W V_b: -60V	Cl at.%: 5.4-7.1% Ti at.%: 37.2-30% O at.%: 48.5-61.5% P_{RF}↗ (100→300W): O/Ti ↗ (1.3→2.05)	Amorphous Annealing(450°C)→amorphous+ anatase P_{RF}↗→ roughness ↗ (rms:4.6→11.6 nm) Surface granules forming large aggregates	P_{RF}↗ → n↗, transmittance ↗ n_{550nm}=2.09→2.39	[80]
MW ECR **$TiCl_4$+O_2** P_{MW}: 400 W p_{total}: 10 mTorr V_b: V_f, -41V T_s: uncontrolled Annealing (optional): 600°C in N_2	No Cl detected	V_f: amorphous (Vb=-41V): anatase (V_f+annealing): anatase+rutile Roughness: 1.2 nm (V_f) 6.5 nm (V_f+ annealing) 7.4 nm (-41V+ annealing)	Density: 3.2 g/cm^{-3} (V_f) 3.62 g/cm^{-3} (V_f+annealing) 3.85 g/cm^{-3} (-41V+annealing) $n_{632.8nm}$ (V_f) 2.25→ (+annealing) 2.30 (-41V) 2.3→ (+annealing) 2.48	[98]
RF CCP **TEOT+O_2** **$TiCl_4$+O_2** (carrier gas: Ar) P_{RF}: 50-300W	TEOT+O_2 C at.%=5.5-11.1% O/Ti=2.67-2.27 P_{RF}↗→↗C at.%, ↘O/Ti $TiCl_4$+O_2 Cl at.%=3.3-7.5 O/Ti=1.39-2.03 P_{RF}↗→O/Ti ↗	TEOT+O_2 Compact, smooth surface free of defects $TiCl_4$+O_2 Smooth at P_{RF}<100W Inhomogeneous, globular surface at P_{RF}=200-300W	O_2↗ → n↗ P_{RF}↗ → n ↗ TEOT+O_2: max n_{550nm}=2.25 $TiCl_4$+O_2: max n_{550nm}=2.39	[79]

Deposition method and growth conditions	Chemical composition and chemical bonding	Morphological and structural characteristics	Macroscopic properties (n, density)	References
RF ICP **TTIP+O2** P_{RF}: 400W p_{total}: 3mTorr T_s: uncontrolled, (<150°C) V_b: V_f or (-20V)-(-150V)	O/Ti≈1.9-1.95 ~25% C at.% (surface not cleaned) O-H band, Ti-O and "carbonate" band	V_b↗ → roughness ↘; from columnar to homogeneous At V_b=-50V micropores V_f : anatase V_b=-20V : anatase +rutile V_b>|-50V|: rutile	$n_{632.8nm}$=2.25-2.49 V_f to -50V: n↗ (2.33→2.49) V_b>|-50V|: n↘	[97]

I.6 Zirconia-silica and titania-silica thin films: literature review

I.6.1 Zirconia-silica thin films

"Composite" metal oxide systems are of special interest in developing materials which exhibit properties over a considerably wider range in comparison with corresponding single components. ZrO_2-SiO_2 "composite" films have been extensively studied for microelectronic use and as protective and chemical resistant coatings [100]–[107]. Zirconia-silica films have been considered a promising candidate as gate dielectric material due to higher thermal stability, wider band gap, and better interface properties compared to metal oxides [101], [102], [104], [108], [109]. It has been reported that the relative permittivity and the band gap energy can be easily controlled by the zirconium content in the "composite" films [100].

Zr-Si oxide thin films have been synthesized by different deposition methods such as sputtering [62], [110], [111], sol-gel [105], [112], conventional CVD [103], [113]–[115], and PECVD [108]. Most studies are focused on the electrical properties of the "composite" films [104], [112], [113], [116], [117]. Studies reporting on physico-chemical and structural characteristics are less abundant. Several of the latter are summarized in Table I-5.

Uniform and smooth morphological aspect of "composite" films has been reported in the reviewed literature. These films exhibit essentially amorphous structuration. Small fractions of monoclinic and cubic phases have been detected in films with low Si atomic content [62], [110].

The films are highly transparent in the visible range. ZrO_2-SiO_2 films display lower transmittance than ZrO_2 films and higher than SiO_2 [62]. Increase of Si incorporation in the films results in a decrease of the refractive index. By modifying chemical composition, refractive index can be varied over wide range (~1.4-2.1).

In MOCVD and sputtering deposition processes, an increase of substrate temperature induced a decrease of Si atomic content in the films [62], [102], [115]. Investigations of FTIR spectra have confirmed the appearance of Zr-O and Si-O bonds in the films. Formation of Zr-Si bond has not been observed. Several groups have assigned the peak at 990 cm^{-1} to Zr-O-Si bonding structure [100], [105], [108].

Table I-5: Characteristics of $ZrSiO_4$-like thin films obtained by different processes: literature review.

Deposition method and growth conditions	Chemical composition and chemical bonding	Morphological and structural characteristics	Macroscopic properties (n, density)	References
RF CCP **$Zr(OC_3H_7)(C_{11}H_{19}O_2)_3$ +TEOS+O_2** (carrier gas: Ar) p_{total}: 40-65 Pa T_s: 400 °C	Si-O, Zr-O Zr-O-Si No silicide bond Ar (Zr precursor) ↗: $ZrSi_{5.7}O_{12.9}$→$ZrSi_{0.6}O_{3.2}$	Amorphous	Not reported	[100], [108]
RF magnetron sputtering Target: ZrO_2-SiO_2 P_{RF}: 50-150W T_s: 200-500°C p_{total}=0.65 Pa	T_s ↗: decrease in Zr/Zr+Si molar ratio	Smooth microstructure Essentially amorphous Target 90%ZrO_2-10%SiO_2: display of monoclinic structure	↗ SiO_2 → n ↘ n(ZrO_2)=2.15, n(SiO_2)=1.46 Highly transparent in the visible range Transmittance: (SiO_2)>(ZrO_2-SiO_2)>(ZrO_2)	[62]
Reactive DC magnetron sputtering Targets: Zr; As-doped Si single crystal Sputter gas: O_2+Ar p_{total}: 5-7 mTorr	Not reported	≤10% SiO_2: amorphous+small amount of cubic zirconia ≥10% SiO_2: amorphous	deposition rate ↗: density ↗ (3.5→3.85 g/cm^3 for 50%ZrO_2-50%SiO_2) %SiO_2 ↗ → n ↘ 10%SiO_2: n_{600nm}=1.95 50%SiO_2: n_{600nm}=1.65	[110]
Sol-gel Trimethoxysilane Zr propoxide	Zr-O, Si-O Si-O-Zr at 990cm^{-1} Si-O-Si, Si-C, C-H O-H (absorbed water)	Uniform and smooth surface+shallow cracks or busted bubble-like microstructures	Optically transparent	[105]
MOCVD Precursor A: $Zr^{IV}(acac)_2$-$(OSiMe_3)_2$ Precursor B: $Zr^{IV}(acac)_2$-$(OSitBuMe_2)_2$ Ar/O_2 atmosphere p_{total}: 2.5 mbar T_s: 400-600°C	C at.%: A(T_s=500°C): 10% B(T_s=450°C): 2% T_s ↗: Si at.% ↗, C at.% ↘, Carbon free films at T_s>550°C $Zr_{0.95}Si_{0.05}O_2$→ $Zr_{0.75}Si_{0.25}O_2$	Not reported	n_{633nm}=1.8-1.9 Annealing in O_2 at 900°C for 10s: n ↗ (n_{633nm}=2.36)	[102], [115]

Deposition method and growth conditions	Chemical composition and chemical bonding	Morphological and structural characteristics	Macroscopic properties (n, density)	References
PVD **Sputtering** **E-beam evaporation** T_s: 25-600°C	From $Zr_2Si_{32}O_{66}$ to $Zr_{27}Si_{15}O_{58}$ (highest Zr at.% with e-beam) No evidence of Zr-Si bond formation Homogeneous in-depth composition	Amorphous Uniform morphology	Not reported	[111]

I.6.2 Titania-silica thin films

Titania-silica thin films (TiO_2/SiO_2) have been investigated as candidates for use in optical and electronic devices, such as waveguides in bio-sensing, optical fibres, and photonic crystals [118]–[122] . Objectives of these studies involved accurately controlling refractive index or dielectric constant of “composite” films. These properties have been tailored by varying film composition. By “mixing” the silica and titania material, it is expected to obtain a wide range of refractive indices: from ~1.45 (SiO_2 bulk) to ~2.55 (TiO_2 bulk) at visible and near-infrared wavelengths.

Ti-Si oxide films have been fabricated using a variety of techniques including sputtering [123]–[126], sol-gel [119], [120], [127]–[129], and different types of CVD [130]–[133] process. Table I-6 presents characteristics of Ti-Si oxide thin films synthesized by different techniques. Composition and structure of “composite” films are dependent on the deposition process parameters. In CVD processes (MOCVD, ALD, PECVD, IBICVD), TTIP and $TiCl_4$ are most frequently used as precursors for Ti deposition. Organosilicon molecules (TEOS, HMDSO), as well as silicon chloride ($SiCl_4$) compounds have been employed as precursors for Si deposition.

It has been shown that small addition of SiO_2 to TiO_2 can transform morphology from columnar to uniform in PVD and PECVD process [13], [123]. The “composite” films are mainly amorphous. When crystalline phase of TiO_2 is detected, its presence decreases with increase of Si at.% in the films [130]. Crystallisation of the films can be slightly enhanced by post-deposition annealing [122].

Refractive indices of the films, measured at λ=550nm, were found in the 1.45-2.44 range. Specifically, films obtained by PECVD exhibited n_{550nm} values from 1.45-2.39. In the reviewed literature, refractive index has decreased as the Si/Ti atomic ratio in the films increased.

Table I-6: Characteristics of titania-silica thin films obtained by different processes: literature review.

Deposition method and growth conditions	**Chemical composition and chemical bonding**	**Morphological and structural characteristics**	**Macroscopic properties (n, density)**	**References**
PEALD Cycles: **TTIP+O_2+Ar** **TEOS+O_2+Ar** T_s: 250 °C	Homogeneous in depth composition From $TiSiO_{3.2}$ to $TiSi_{0.3}O_{2.5}$	Not reported	↗ Ti at.% (19.1→26.3): n ↗ (n_{550nm}=1.93→2.21)	[134]
RF ICP **TTIP** **+O_2+HMDSO** HMDSO: 0.2-2.0% P_{RF}: 400W p_{total}: ~3mTorr T_s: uncontrolled (<150°C)	HMDSO ↗ : (V_f) $TiSi_{0.9}O_{4.0}C_{1.6}$ → $TiSi_{9.4}O_{21.1}C_{4.8}$ (V_b=-50V): $TiSi_{0.2}O_{2.7}C_{1.0}$ → $TiSi_{5.0}O_{12.3}C_{3.2}$ (surface not cleaned) Si-O-Si, Si-O-Ti, Ti-O, Si-O, O-H	(V_f) Amorphous Columnar morphology disappears at 0.2% HMDSO HMDSO ↗ → roughness ↘ (rms=1.59-0.48nm) (V_b=-50V) Uniform <0.5%HMDSO: rutile >0.5%HMDSO: amorphous	↗HMDSO → n↘ (V_f) $n_{632.8nm}$=1.95→1.50 (V_b=-50V) $n_{632.8nm}$=2.24→1.58	[13]
Aerosol Assisted CVD Mixed solution of **TEOS+TTIP** (carrier gas: N_2) T_s: 400 °C Annealed at 950°C	TiO_2/SiO_2: 0.92/0.08 → 0.81/0.19	SiO_2 content ↗ : from anatase+amorphous to amorphous	n_{550nm}=~2.44-2.38 Content of SiO_2>16 mol.%: n decreases	[130]
RF PECVD **$TiCl_4$+$SiCl_4$+** **O_2+Ar** p_{total}: 25-50 mTorr	$TiCl_4$ ↗: Si–O–Ti ↗ $Ti_{3.1}Si_{29.1}O_{66.6}C_{l1.2}$→ $Ti_{30.4}Si_{0.8}O_{68.1}C_{l0.7}$	Annealing at 400 °C: amorphous+polycrystalline (anatase and rutile)	Ti/(Si+Ti) ↗: n ↗ (n_{550nm}=1.58→2.39)	[122]
IBICVD: **$TiCl_4$+** **$(C_2H_5O)_3SiH$** O_2^+ ions (400 eV) p_{total}:~0.07-0.08 Pa	Ti-O-Si at 940 cm^{-1}	Amorphous Compact and homogeneous morphology	Si/Ti ↗: density ↘ (3.42→2.57 g/cm^3) n↘ (n_{550nm}=1.47→2.3)	[132]
MW ECR **TTIP+$Si(CH_3)_3Cl$** (carrier gas: O_2) P_{MW}: 400W p_{total}: 0.65 Pa	Ti-O-Si at 940 cm^{-1}	Amorphous Columnar at high Ti content in the films	Si/Ti ↗: density ↘ (2.30→1.93 g/cm^3) n↘ (n_{550nm}=1.45→2.1)	[132]
Reactive co-sputtering Targets of Si and Ti; O_2 atmosphere	Homogenous in-depth composition SiO_2% ↗ (5→58%)	Amorphous	SiO_2% ↗ (5→58%): n↘ (n_{600nm} = 2.39→1.77)	[123]

I.7 Research objective and strategy

In the first part of this chapter, we have revised notions prerequisite for the study presented in the following chapters: the fundamental principles of thin film formation, plasma phase characteristics and the PECVD process. In the second part, we have reviewed the reported research on zirconium oxide, titanium oxide and “composite” metal/silicon oxide thin films deposited by different processes.

Literature review on zirconium and titanium oxide films obtained by PECVD has shown that film characteristics are strongly influenced by process parameters such as substrate temperature and substrate polarisation. Columnar growth has been observed in both types of films synthesised in oxygen-rich plasma gas mixtures. The films are predominantly amorphous with, in some experiments, a low fraction of polycrystalline phase present in the films.

Lastly, we have summarised several studies that had examined “composite” zirconia-silica and titania-silica thin films. The morphological features, density and refractive index, can be controlled by the atomic ratio of silicon to metal. “Composite” films exhibit characteristics over a significantly wider range in comparison with corresponding silicon oxide and metal oxide films.

Studies reported in the literature predominantly focus on final characteristics and macroscopic properties of zirconium and titanium oxide thin films synthesized in different experimental conditions. The applicative objective of thin film science is the control of film growth and development of materials with desired properties. For successfully achieving that objective, it is necessary to understand fundamental mechanisms, which govern the deposition process.

In PECVD, process parameters influence behaviour of the plasma phase, as well as surface conditions (e.g. substrate temperature). Species created in plasma arrive at the surface where they participate in surface reactions and thin film growth. Therefore, by modifying external process parameters, we are able to control characteristics of deposited thin films (Figure I-7).

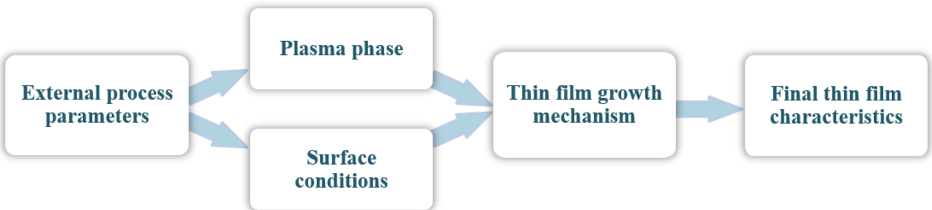

Figure I-7: Schematic presentation of relationship between different phases of PECVD process.

Metalorganic precursors are frequently employed for deposition of metal-oxide films in conventional CVD and in PECVD processes. In this work, we provide a comparative study of thin films deposited by PECVD from two different metalorganic precursors: ZTB and TTIP, with the objective of identifying behaviours characteristic of metalorganic PECVD in general.

We have chosen to study the influence of two process parameters:

- oxygen gas fraction of precursor/O_2 gas mixture, and
- total gas pressure.

At LAPLACE, influence of O_2 percentage of ZTB/O_2 gas mixture on thin film characteristics has been studied in MW multipolar plasma excited by distributed ECR [11][12]. These previous studies are used as a control for verifying our results, since we are introducing a metalorganic precursor for the first time in a differently configurated reactor at LAPLACE: a semi-industrial multi-dipolar ECR reactor. Additionally, we expanded the study to another metalorganic precursor, TTIP. To the best of our knowledge, there is a lack of systematic studies of the evolution of film properties as O_2 gas is added to TTIP/O_2 gas mixture.

The effect of total gas pressure, the second process parameter chosen in this work, is rarely studied. To the best of our knowledge, the evolution of film properties as a function of pressure in ECR plasma has not been investigated. At high O_2 fraction in the gas mixture, deposited films are almost inorganic, although the deposition rate is very low. It is possible that increasing pressure increases the deposition rate while still preserving desirable film properties such as high refractive index. This would certainly be of interest from an industrial point of view.

Additionally, we have investigated the feasibility of depositing "composite" metal/silicon oxide thin films with homogeneous composition. It has been reported that low fraction of HMDSO in TTIP/O_2 plasma compromises film columnar morphology [13]. In this work, we have examined the influence of HMDSO addition to metalorganic/O_2 gas mixture on physico-chemical and morphological film characteristics. At LAPLACE, it is the first time that the combination of two precursors, organosilicon and metalorganic, has been used in an ECR reactor.

To understand the thin film growth, it is essential to identify plasma composition. Due to technical conditions, we were unable to perform an extensive study of the plasma chemistry. Nevertheless, in this thesis, we provide hypothesis about the evolution of the plasma phase and surface mechanisms as process parameters are varied. These hypotheses have been developed on the basis of observed modifications in film characteristics coupled with previously studied ZTB plasma phase [12] and theoretical Monte Carlo simulations [135].

Chapter II

Experimental environment

Introduction

The objective of this chapter is to present the various experimental devices used for the realization and characterization of the thin films studied in this thesis. First, we introduce the ECR principle and the main characteristics of the type of plasma employed in the deposition process. Secondly, we proceed with describing different systems that compose the multi-dipolar ECR deposition reactor. Afterwards, we present the various characterization tools used to probe the plasma phase and to identify the chemical composition of the films, their physical characteristics (morphology and topography) as well as other properties. The last part of the chapter focuses on the specific precursors used in this work: metalorganic (zirconium tetra tert-butoxide – ZTB, titanium tetra isopropoxide – TTIP) and organosilicon (hexamethyldisiloxane - HMDSO) precursors are introduced.

II.1 Multi-dipolar electron cyclotron resonance plasma

II.1.1 Electron cyclotron resonance phenomenon

The deposition reactor used in this work takes advantage of the phenomenon of Electron Cyclotron Resonance (ECR) to accelerate the electrons and generate plasma [136]–[138]. ECR principle is based on the superposition of mutually perpendicular static magnetic field and an electric field of an incident electromagnetic wave.

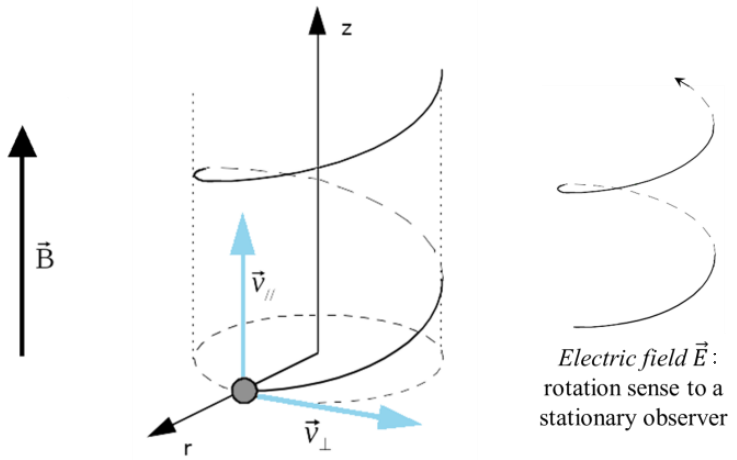

Figure II-1: Schematic representation of ECR principle: electron gyration trajectory around the lines of a static magnetic field.

Resonance is achieved when the frequency of the incident electromagnetic wave f equals the electron gyration frequency f_{ce} in the static magnetic field of strength B:

$$f_{ce} = f = \frac{1}{2\pi}\frac{e}{m_e}B$$ *Equation II-1*

where e is the electron charge and m_e electron mass. In our experimental setup, the frequency of the applied electromagnetic wave is 2.45 GHz. The Equation II-1 is satisfied in the region where the magnetic field B equals 875 Gauss. In that particular region, called the *ECR zone*, electrons "see" a continuous electric field and are thus continuously accelerated. This is the way the electrons acquire energy. They are then confined by the magnetic mirror effect and their energies allow them to collide with the precursor molecules injected into the reactor and cause the dissociation of atomic bonds. The new species, originating from the dissociation process, diffuse towards the centre and the walls of the reactor to react with surfaces and achieve (according to their nature) deposition, etching or functionalization.

Plasma generated with ECR phenomenon is characterised by:

- very low working pressure: from ~0.1 mTorr to ~10 mTorr, and
- high electron density: up to 10^{12} cm^{-3}, [136], [138], [139].

This type of plasma creation mechanism allows independently controlling the plasma generation process and the energy of the ions impinging on the treated surfaces. Certain conditions, very low ionic bombardment, enable treatment of thermo-sensitive materials such as polymers [140], [141].

II.1.2 Multi-dipolar ECR plasma source

In this work, a multi-dipolar configuration was used to generate an ECR plasma [142]–[144]. Figure II-2 shows a photograph of an elementary dipolar plasma source with identified principle elements. This type of source was developed by HEF (Hydromécanique Et Frottements) R&D Industrial Group. Each source is composed of a permanent Sm_2Co_{17} magnet with an azimuthal symmetry around its magnetization axis, a coaxial line which serves as a microwave applicator and an impedance matching system.

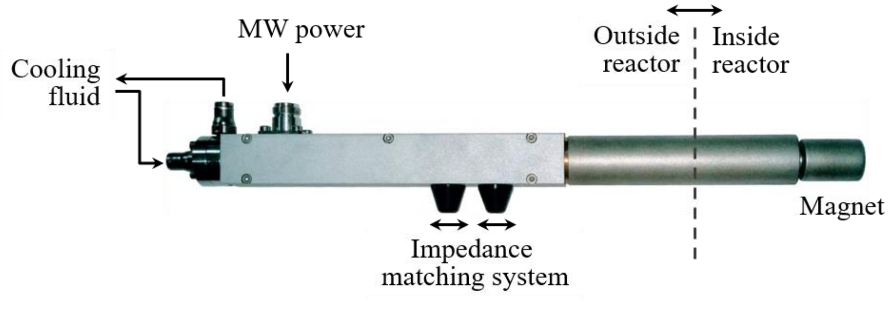

Figure II-2: Photograph of an elementary dipolar ECR plasma source.

The elementary sources can be organized in different configurations: in two- or three-dimensional networks, arrangements with alternate or identical magnetic polarities, rectangular or hexagonal networks and other. In the deposition reactor employed in our work, 12 elementary sources are organized in a 2D planar network with alternate magnetic polarities (see Figure II-3).

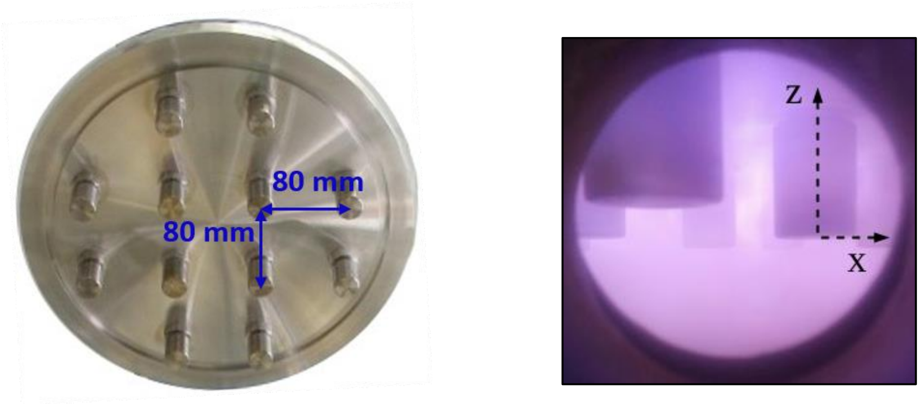

Figure II-3: Photographs of: 12 multi-dipolar magnets positioned at the top of the plasma chamber (left); magnets in argon plasma (p_{Ar}=1 mTorr, P_{MW}=800 W) (right).

Figure II-4 presents a magnetic field configuration of an individual elementary source. In multi-dipolar ECR plasmas the energetic electrons are trapped close to the multipolar magnetic field structure, i.e. the ECR zone, while the “cold” ones diffuse away from the plasma production region under the influence of density gradients and the resulting space charge electric field [145].

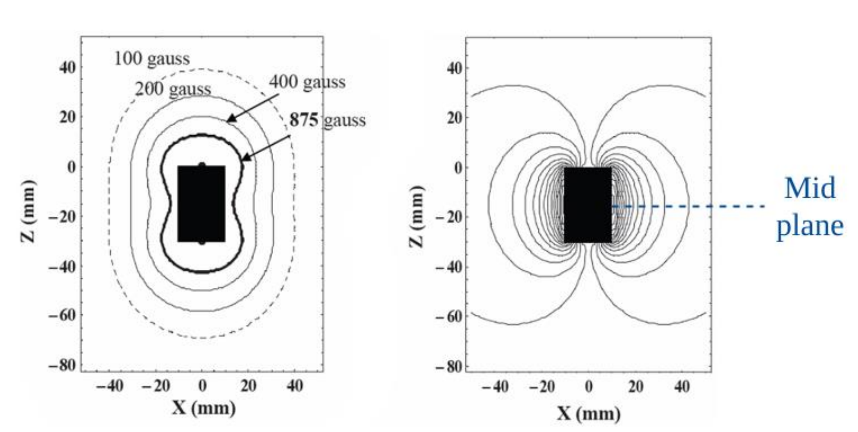

Figure II-4: Configuration of a magnetic field produced by a cylindrical magnet with axial magnetization: amplitude lines of a constant magnetic field (right); magnetic field lines (left) [146].

Bechu et al. [147] have measured the variation of electron temperature T_e and electron density N_e in H_2 plasma as a function of the radial distance from an elementary dipolar source axis (in the mid plane) (Figure II-5). When approaching the source axis, the plasma density increases up to $0.89 \cdot 10^{10}$ cm^{-3} at the closest position (40 mm from the magnet surface). At this point the relative density of cold/hot electrons equals 0.83/0.16 while at the point ~10 cm farther it increases to 0.92/0.04. The effective T_e varies from 0.7 eV to 2.8 eV when approaching the source axis.

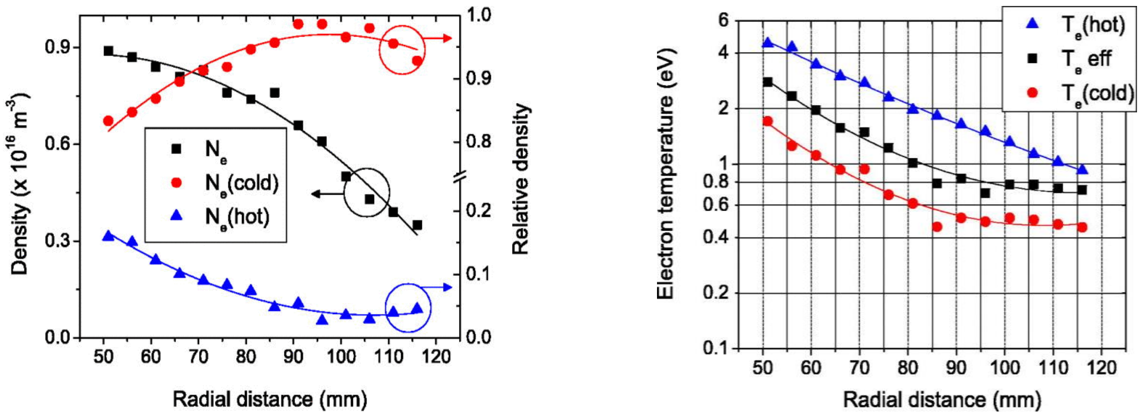

Figure II-5: Radial variations, in the mid plane, of relative density (left) and electron temperature (right) of "hot" (triangles) and "cold" (circles) electrons. Experimental conditions: H_2 plasma, p = 0.72 Pa, P_{MW} = 200 W applied to a single source [147].

Figure II-6 shows measurements of the plasma parameters characteristic to the deposition reactor used in this work. The measurements are presented as a function of distance from the centre of the plasma chamber towards the chamber wall.

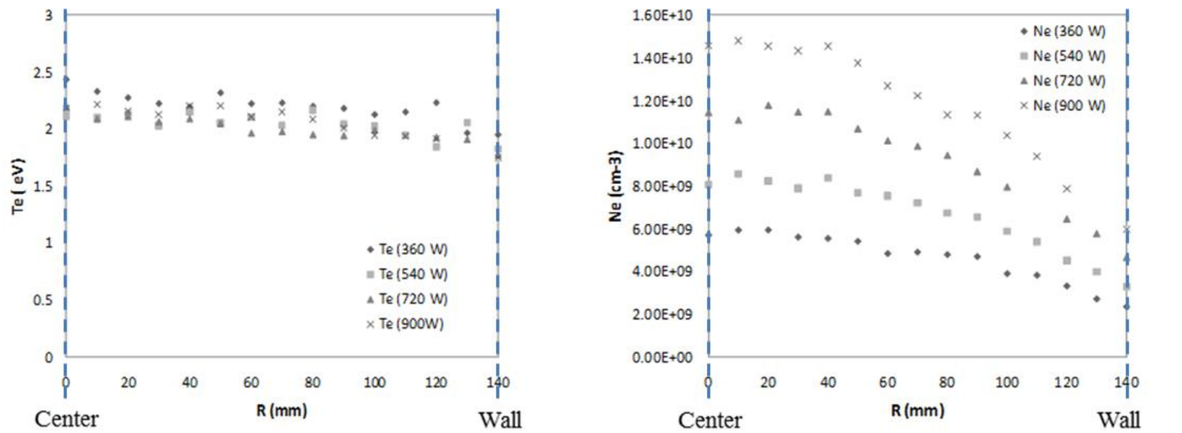

Figure II-6: Evolution of plasma parameters T_e and N_e as a function of distance from the centre of the deposition reactor Pixcell for different power values (12 elementary sources; Ar gas; p_{Ar}=3 mTorr).

Two generations of elementary sources have been used in this reactor. Measurements presented in Figure II-6 correspond to plasma created by dipolar sources of the 1st generation, whereas sources of the 2nd generation were used in this work. These two generations of sources differ only in the construction of the cooling system, thus, there should not exist a significant difference in plasma parameters between them. The measurements were performed in Ar plasma for different values of microwave power, at 3 mTorr, ~10 cm below the source. The electron temperature equals ~2-2.5 eV and it is relatively constant over the radial distance from the centre of the reactor. Electron density, as expected due to the sheath formation, decreases in the vicinity of the reactor wall and is of the order of 10^{10} cm^{-3}.

In this work, we have studied the influence of total gas pressure on thin film characteristics (Chapter IV). Therefore, it is of interest to understand how plasma parameters change with the increase in gas pressure. Bechu et al. [148] have observed the variation of plasma parameters as a function of argon gas pressure (up to 5 mTorr) in the multi-dipolar plasma reactor (Figure II-7). The elementary plasma sources (each supplied with 100 W of MW power) were positioned in two rings at the periphery of a cylindrical reactor. The parameters were measured at the centre of the reactor (45 cm diameter). Although the geometry of the reactor in question differs from ours (3D network vs 2D planar network) and the absolute values of the characteristic parameters may be different, we expect that the evolution of the plasma parameters with pressure is similar in both reactors. Up to 1 mTorr, the electron temperature T_e increases significantly, whereas it is nearly constant (~2.5 eV) at higher pressures. Plasma density increases with Ar gas pressure up to ~$5 \cdot 10^{11}$ cm^{-3}.

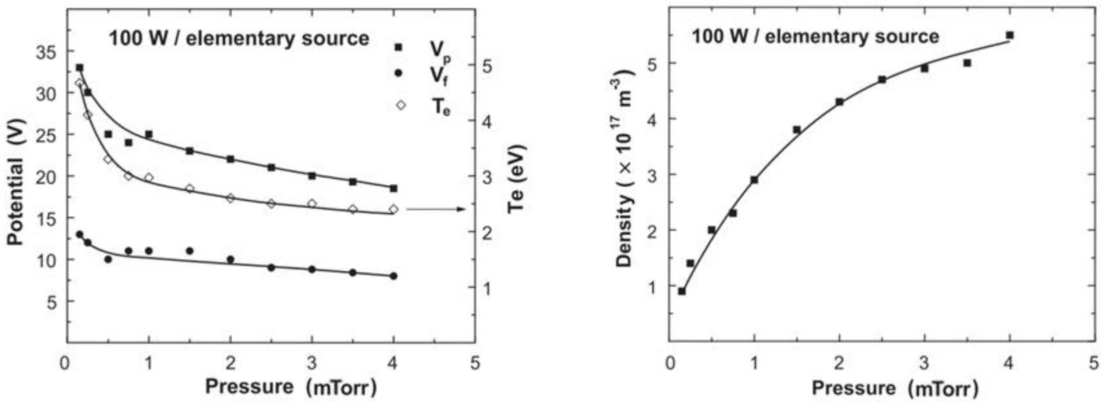

Figure II-7: Plasma potential, floating potential and T_e (a), and plasma density (b) as a function of Ar pressure (cylindrical reactor, 20 elementary plasma sources, 100 W per source) (adapted from [148]).

II.2 Plasma reactor "Pixcell"

Reactor used for thin film deposition allows generating plasma excited by the phenomenon of Electron Cyclotron Resonance (ECR). The main chamber of the reactor consists of a stainless-steel cylinder of 318 mm in inner diameter and 480 mm in height. Figure II-8 presents a 3D image of the plasma reactor setup.

Microwave signal is produced by a Metal Process generator (MAGNETRON SUPPLY 2kW) delivering a maximum power of 2000 W. Twelve elementary dipolar sources (Figure II-2, p.36) are positioned at the top of the metallic cylinder composing the enclosure. The power is equally distributed between 12 coaxial cables by a power distributor. To optimise the power transfer, it is possible to manually adjust the impedance matching system for each elementary source independently. The applied microwave power generates a temperature rise in the antennas and the reactor walls. To limit this phenomenon and to prevent overheating, a cooling fluid is circulating in the interior of the elementary plasma sources.

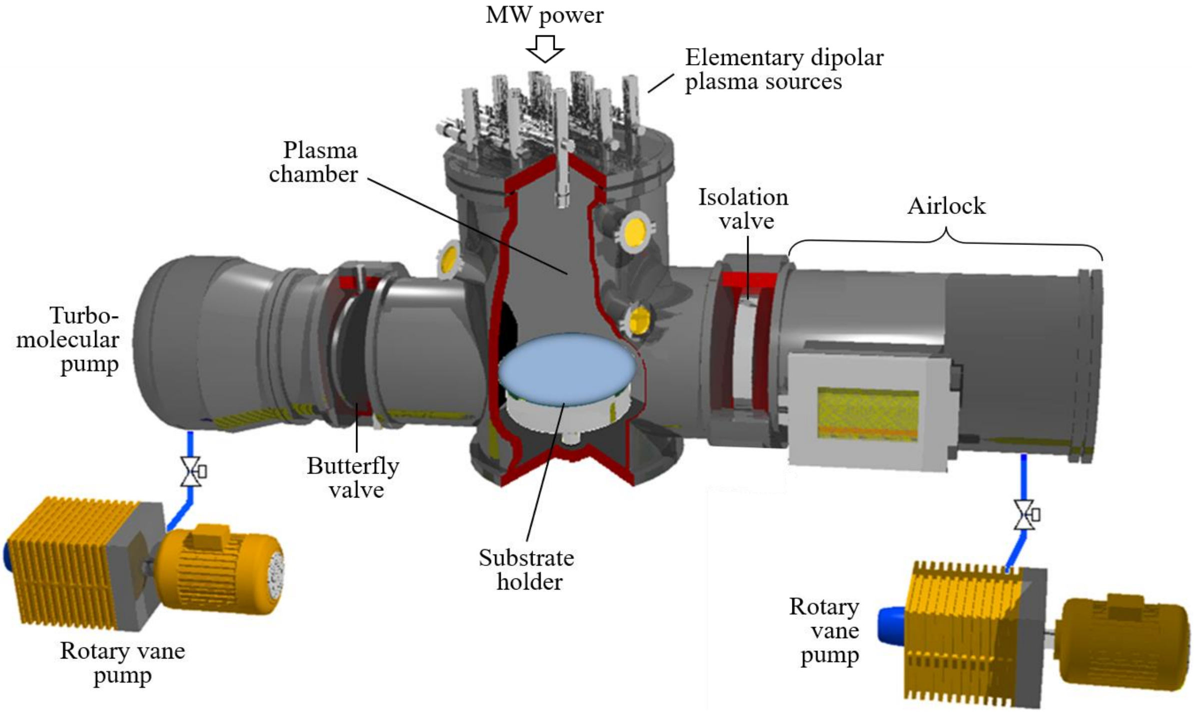

Figure II-8: 3D representation of the reactor Pixcell.

II.2.1 Airlock

Presence of an airlock resolves one of the major technological barriers. It allows the transfer of the samples under vacuum and thus renders unnecessary to equalize the reactor pressure to atmospheric pressure when loading or removing the samples. The enclosure of the reactor is therefore protected from frequent pollution. The primary vacuum ($p \approx 10^{-3}$ Torr) in the airlock is achieved by means of a two-stage rotary vane pump. The airlock is separated from the enclosure by a gate valve which can be opened when the pressure balance between the reactor and the airlock is satisfactory. The stainless-steel loading arm allows the transfer of flat samples having up to 200 mm in diameter. The airlock has been designed in such a way that it is possible to introduce 3D samples into the reactor.

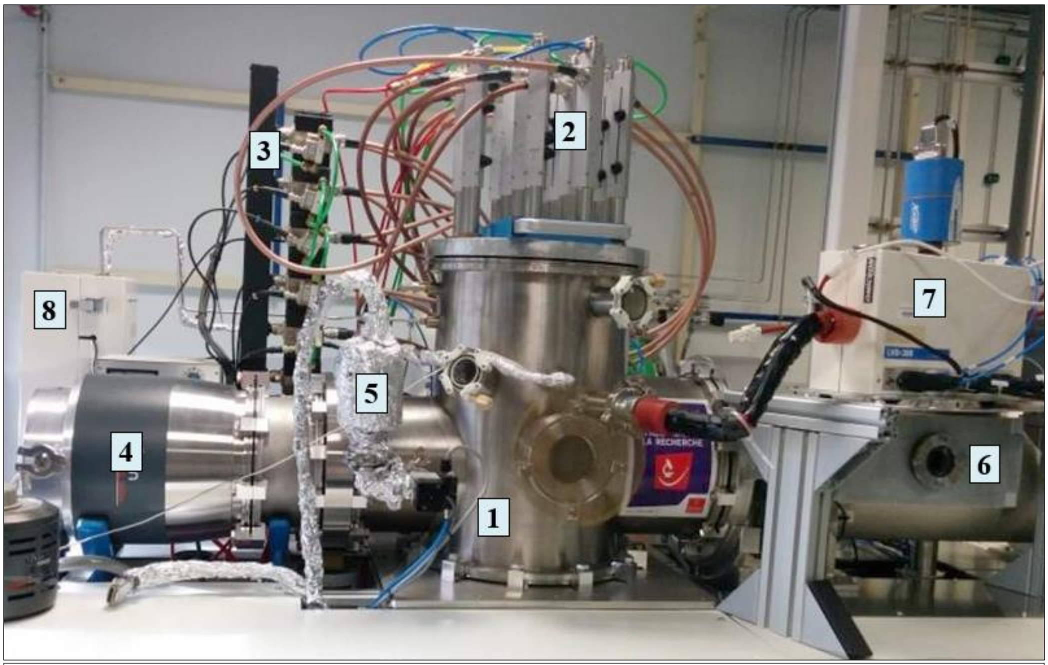

1 - Reactor chamber	6 - Airlock
2 - Elementary dipolar plasma sources	7 - Injection system of metalorganic precursors (LVD 200)
3 - MW power distributor	8 - Injection system of organosilicon precursors
4 - Turbomolecular pump	
5 - Capacitive gauge	

Figure II-9: Photograph of the reactor “Pixcell”.

II.2.2 Pumping system

Vacuum in the reactor is assured by a pumping unit consisting of a rotary vane pump, type Alcatel 20 63 SD (60 m^3/h), and a turbomolecular maglev pump type Adixen ATH 1600M (1400 l/s) with a constant rotation frequency of 650 Hz. Since the reactor operates at pressures in the ~0.1-10 mTorr range, the pumping unit is employed to achieve high vacuum level in the plasma enclosure: of the order of ~10^{-6}-10^{-7} Torr.

It is possible to control the pumping rate by varying the opening of the butterfly valve placed upstream of the turbomolecular pump. This is important in our study because it is difficult to vary the pressure of ZTB and TTIP gas over a wide pressure range due to their low vapour pressures. We defined a specific valve opening to achieve a wider range of precursor gas pressure: at 15% of valve opened we were able to control and stabilize precursor gas pressure on a much broader range, from 0.02 to ~2 mTorr.

II.2.3 Pressure measurements

Two gauges allow measuring the pressure in the deposition chamber. A dual Cold cathode/Pirani gauge, model ACC 2009 (Alcatel), measures the pressure in the range from 760 Torr to $3.8\cdot10^{-9}$ Torr:

- Pirani gauge, which works on the principle of thermal manometers, ensures the pressure measurement for pressures from 760 Torr to 10^{-3} Torr,
- cold cathode gauge, which works on the principle of ionization, measures pressures lower than 10^{-3} Torr.

Baratron MKS 627 vacuum gauge, a capacitance manometer thermostated at 45° C, is the gauge employed to control the injected gas pressure and the total working pressure during the plasma deposition process. The pressure measurement range spreads from 0.01 mTorr to 1 Torr. The gauge works on the principle of mechanical gauges with an Inconel® membrane. The advantage of this type of gauge is that the measurement is independent of the type of gas used.

II.2.4 Gas injection systems

Precursor compounds used in this work are in liquid phase at standard ambient temperature and pressure. From a practical point of view, PECVD requires injecting the precursor in gas phase into the reactor. Thus, the vapour pressure of the precursor is of utmost importance. The higher the vapour pressure, the easier it is to inject and regulate the compound. Vapour pressure of metalorganic molecules is very weak. Nevertheless, when heating the reservoir and the injection lines, it is possible to inject it at pressures sufficiently high to achieve PECVD.

II.2.4.1 ″Conventional″ gasses

For the "conventional gases", the ones in the gaseous state at the standard conditions of use, such as oxygen (O_2) and argon (Ar), the injection is achieved through two oppositely placed entry points in the top part of the enclosure. A mass flow meter is placed on each gas line in order to regulate the injected flow rates.

II.2.4.2 Metalorganic and organosilicon precursors

Precursor injection systems must be designed to control the flows injected in the reactor. These systems must be adapted to the physical and chemical properties of every precursor. The **organosilicon precursor hexamethyldisiloxane (HMDSO)** is liquid at ambient pressure and temperature and it has a fairly high vapour pressure (Figure II-10), thus it is stored in a glass flask at room temperature. The adjoining circuit is heated at 40°C by means of a rheostat fed by a heating wire to prevent condensation in the circuit and stabilize the injection. Flow control is done through a millimetre needle valve between the HMDSO containing tank and the reactor. In practice, the flow control is done by measuring pressure in the reactor (at constant pumping speed a constant pressure corresponds to a constant flow). This type of injection allows stabilizing HMDSO vapour pressure ranging from 0.01 mTorr to 10 mTorr. The HMDSO is injected into the reactor through two oppositely placed points few cm above the substrate holder (Figure II-14).

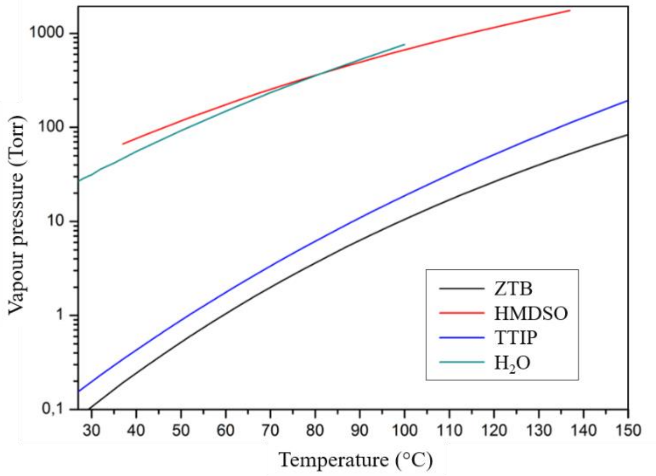

Figure II-10: Vapour pressure as a function of temperature for: H_2O, HMDSO, ZTB and TTIP [12].

Injection systems of metalorganic precursors differ from HMDSO injection system. **Zirconium tetra tert-butoxide (ZTB)** and **titanium tetra isopropoxide (TTIP)** are also liquid at atmospheric pressure and room temperature but have a much lower vapour pressure (Figure II-10). It was, therefore, necessary to design a specific injection system, based on the same principles as the injection system of HMDSO but with a few key differences. The injection line needed to be shorter in order to have the least possible loss of load, and the system needed to be heated to obtain a sufficiently high precursor vapour pressure in the deposition chamber. To inject **ZTB**, we have used a Low Vapour Delivery (LVD 200) system constructed specifically for precursors with low vapour pressure (Figure II-11). This injection system was developed in collaboration between laboratory LAPLACE and OMICRON Technologies (France). The apparatus is composed entirely of metal elements (tank, seals, and valves) to make the system as isolated as possible. LVD system can sustain temperatures up to 150°C.

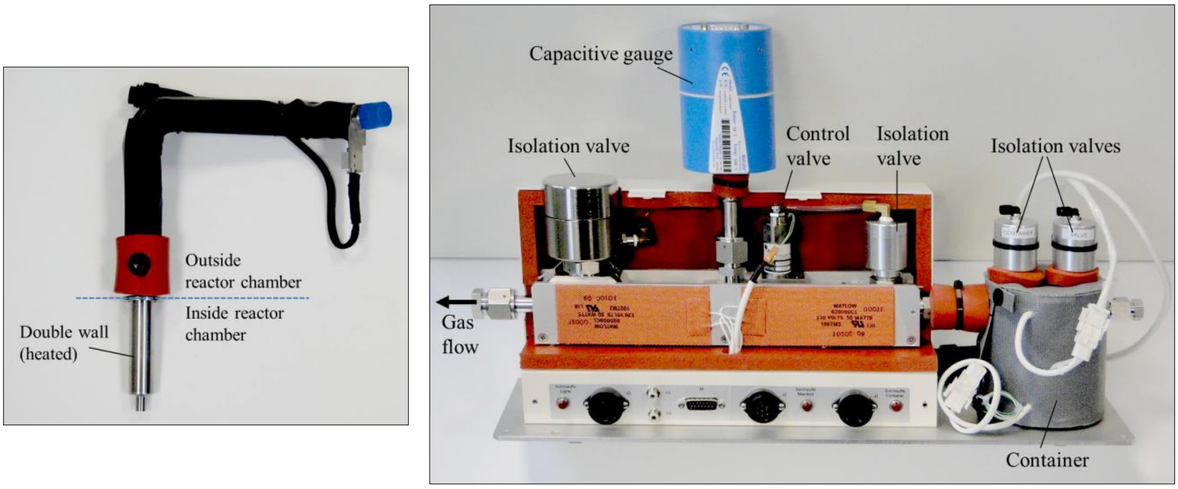

Figure II-11: Images of the LVD 200 injection system.

The working principle is based on the pressure regulation of the gas flowing through an orifice placed in such a way as to create the desired pressure drop over the line and thus allowing the control of the flow rates. Figure II-12 shows the schematic representation of the LVD system. The pressure measurement is achieved by a capacitive gauge which controls the opening of a valve (VR1) allowing the pressure regulation of the gas flowing through the orifice (OR1) and creating the desired pressure drop.

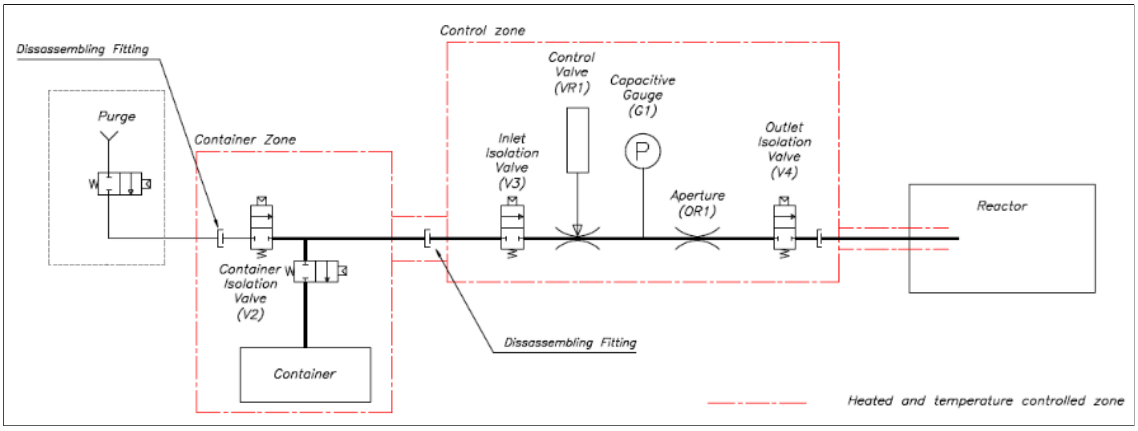

Figure II-12: Schematic representation of the LVD 200 injection system.

Thermal isolation of the setup is crucial to avoid the condensation of the precursor at possible cold points. Likewise, heating of the system is necessary to achieve stable injection and ZTB gas pressure regulation. The container temperature was set at 90 °C and the temperature of the line between 110 and 140 °C.

High performance of the LVD system is unquestionable; however, it is still a very sensitive system. During this work, at the end of the ZTB study campaign, a faulty regulating valve caused a leak that rendered the system inoperative. A chemical reaction between ZTB and air had resulted in zirconia powder creation inside the LVD system.

We have constructed another injection system by using operational parts of the LVD system (Figure II-13) to be able to proceed with our work and the study of TTIP PECVD. TTIP was stored in a metallic container heated at 90 °C and connected to the reactor by a line composed of two parts: a short metallic tube heated at 95 °C and a double walled curved tube heated at 100 °C. The flow control is done through a millimetre needle valve located between the container and the reactor. The injection is monitored by measuring the TTIP gas pressure in the reactor. This system allows stable TTIP injection in the 0.3-1.5 mTorr pressure range for the chosen pumping parameters (butterfly valve opened at 15 %).

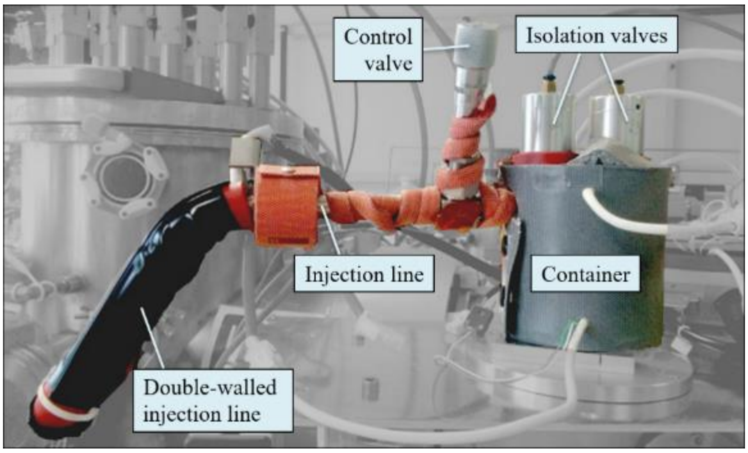

Figure II-13: Photograph of the manual precursor injection system.

II.2.5 Substrate holder

A transfer system equipped with an airlock allows transferring samples towards the substrate-holder in the plasma chamber. The substrate holder is a cylindrical stainless-steel plate whose axis coincides with that of the enclosure. The vertical position of the substrate holder can be controlled by an electrical motor. Important to note is that the position of the substrate-holder has a significant influence on the deposition rate and on the homogeneity of the deposited films. Distances between different gas injection points and the substrate holder are shown in Figure II-14. Positioning of precursor gas injection followed existing technical restrictions.

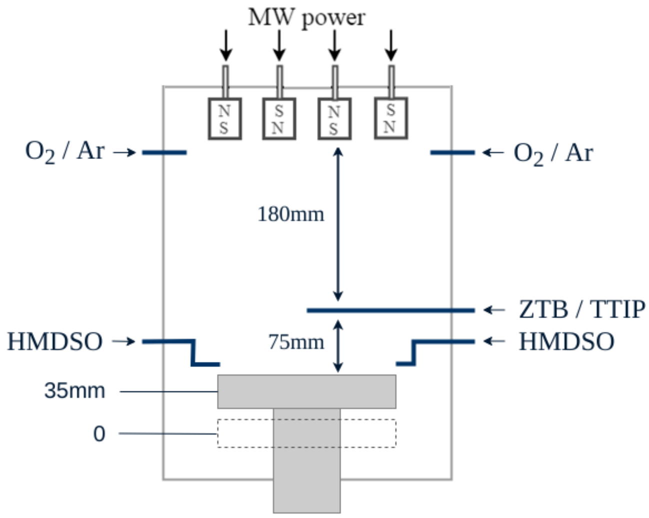

Figure II-14: Positions of gas injection points and the substrate holder during deposition process.

Substrate holder is electrically isolated from the rest of the machine. Therefore, it remains at floating potential (V_f) during the discharge. However, the holder can be connected to an RF generator operating at 13.56 MHz via an impedance matching system. The matching box, constituted of two manually adjustable capacities and a build-up coil, serves to adapt the output impedance of RF generator to the impedance of the plasma, and thus minimize the power reflected in the direction of the generator. By polarizing the substrate holder, we can control the energy of charged species impinging on the substrate and the film.

The temperature of the substrate-holder can be regulated by heating or cooling the fluid, which circulates in the interior cooling system.

II.3 Experimental protocols

Thin films were deposited on silicon (Si) substrates provided by Sil'tronix Silicon Technologies (see Table II-1 for detailed information). This type of substrate allowed analysing the deposited films with the chosen experimental techniques described in paragraph II.5. The original wafers were cleaved by a micro-cutting machine or manually, with a diamond cutter, into smaller pieces (minimal dimensions: min. length x min. width = 10 mm x 10 mm).

Table II-1: Information on the type of substrate used in this work.

Substrate	Silicon wafer
Type and doping	Intrinsic
Orientation	(100) ± 0.5°
Thickness	525 ± 25 µm
Surface	Double Side Polished
Resistivity	> 200 ohm·cm

Ahead of every deposition, the substrates were cleaned by employing the procedure presented in Figure II-15. The main objective of the cleaning procedure was to remove all organic residue from the substrate surface. Acetone is successful in removing organic pollutants and dissolving oils; however, it evaporates quickly leaving its own residue. Thus, a two-solvent method is used: after acetone rinse, substrate is rinsed with ethanol to remove acetone with its contaminants. Additionally, substrates were shortly immersed in diluted hydrofluoric acid (HF) which removes native silicon dioxide layer (typically ~20 Å thick) from the silicon substrate surface.

Substrate cleaning procedure

Rinse with acetone ($(CH_3)_2CO$)

↓

Rinse with ethanol (C_2H_5OH)

↓

Rinse with deionized (DI) water

↓

Immerse in 2% HF solution (time: 30 sec)

↓

Rinse in DI water (time: 3 min)

↓

Blow dry with dry air

Figure II-15: Steps of the silicon substrate cleaning procedure.

The deposition protocol is presented in Figure II-16. It is important to note that the subsequent order of precursor and oxygen gas injection was consistently followed:

1. *metalorganic precursor,*
2. *organosilicon precursor (if injected),*
3. *oxygen gas (if injected).*

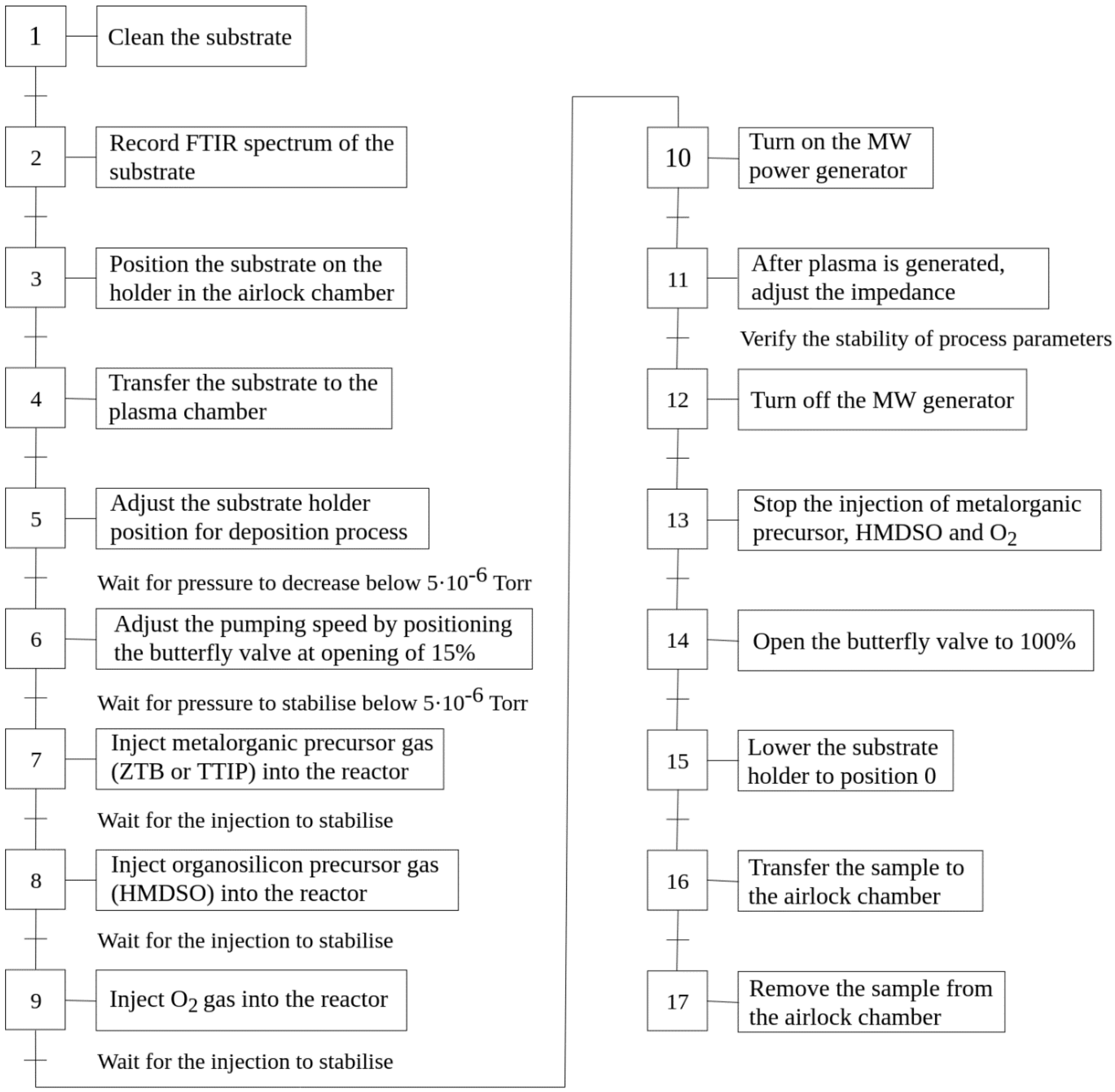

Figure II-16: Deposition protocol.

II.4 Precursor molecules

In this section we present different precursor molecules used in our study:

- two metalorganic compounds
  - Zirconium Tetra tert-Butoxide (ZTB),
  - Titanium tetra isopropoxide (TTIP), and
- an organosilicon compound
  - Hexamethyldisiloxane (HMDSO).

All precursors have been supplied by Sigma Aldrich.

II.4.1 Zirconium Tetra tert-Butoxide

Zirconium Tetra tert-Butoxide (ZTB, $ZrO_4C_{16}H_{36}$), developed by Bradley et al. [149] in the 40's, is a complex metal-organic molecule (see Figure II-17). It is a part of the family of metal alkoxides whose structural formula is:

$$[M(OR)_x]_n \qquad \textit{Equation II-2}$$

where M is the metal atom of valency x, R is an alkyl group, and n is the degree of polymerization.

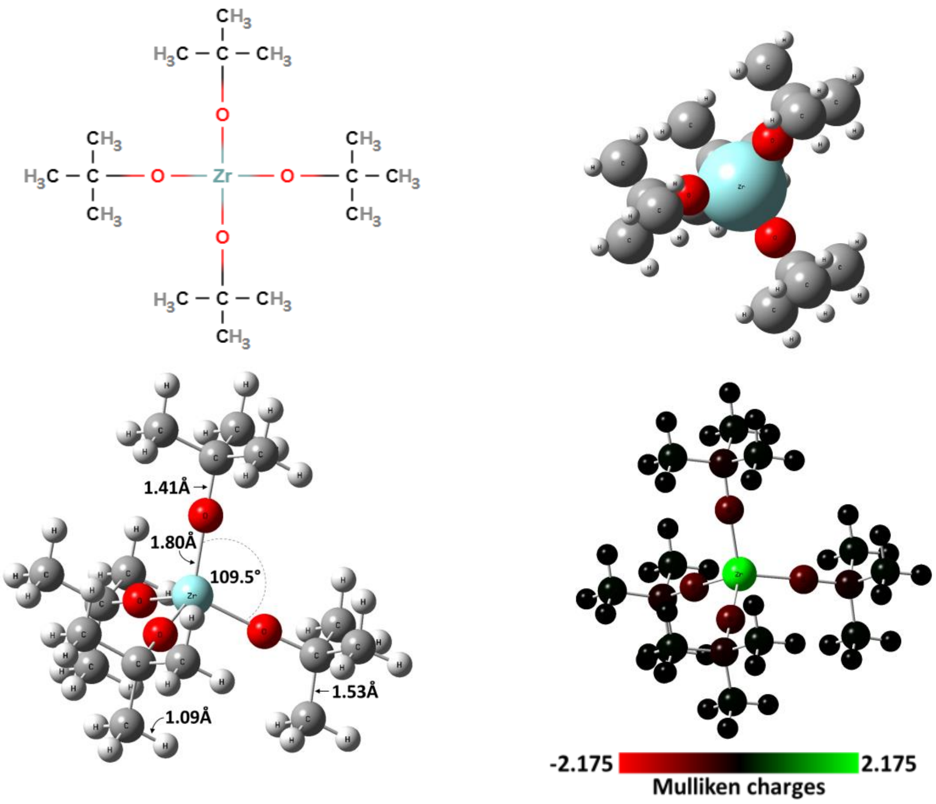

Figure II-17: Different representations of ZTB molecular structure: 2D; 3D molecule geometry optimized by DFT calculations (Gaussian 09) and visualized by GaussView 5.

From the ‘60s, ZTB has been used in the synthesis of zirconium oxide coatings. Compared to other zirconium compounds, ZTB’s strengths lie in its higher volatility, low toxicity to humans and the environment and relatively low price. Although ZTB is the most volatile molecule among zirconium compounds its vapour pressure is not nearly as high as that of organosilicon molecules (see Figure II-10). ZTB is highly sensitive to light, air and humidity.

Figure II-18 shows theoretically and experimentally obtained infrared spectra of ZTB. The theoretical spectrum, corresponding to vibrations of the ZTB molecule, has been acquired by DFT calculations. The experimental spectrum was obtained by FTIR of gas phase ZTB at very low pressure (~4mTorr) in the framework of Mr R. Verhoef's thesis [12]. The identification of the peaks present in the IR spectrum of the ZTB molecule will aid in analysis of IR spectra characteristic to thin films deposited in ZTB plasma.

We have used a combination of literature search [11], [12], [150] and visualisation of calculated frequencies in GaussView graphical interface to assign the peaks. Peak wavelength values and corresponding assignations are presented in Annex of this work. When comparing the two spectra, theoretical and experimental, differences in peak wavenumbers can be observed. These shifts are due to approximations employed in DFT calculations: anharmonic energy potential is replaced by a harmonic potential. Additionally, the scaling factor applied to the calculated wavenumbers is experimentally determined for different molecules and thus it is not specific to the ZTB molecule. Therefore, we can observe slight shifts between the experimentally and theoretically obtained IR wavenumbers even after applying the scaling factor.

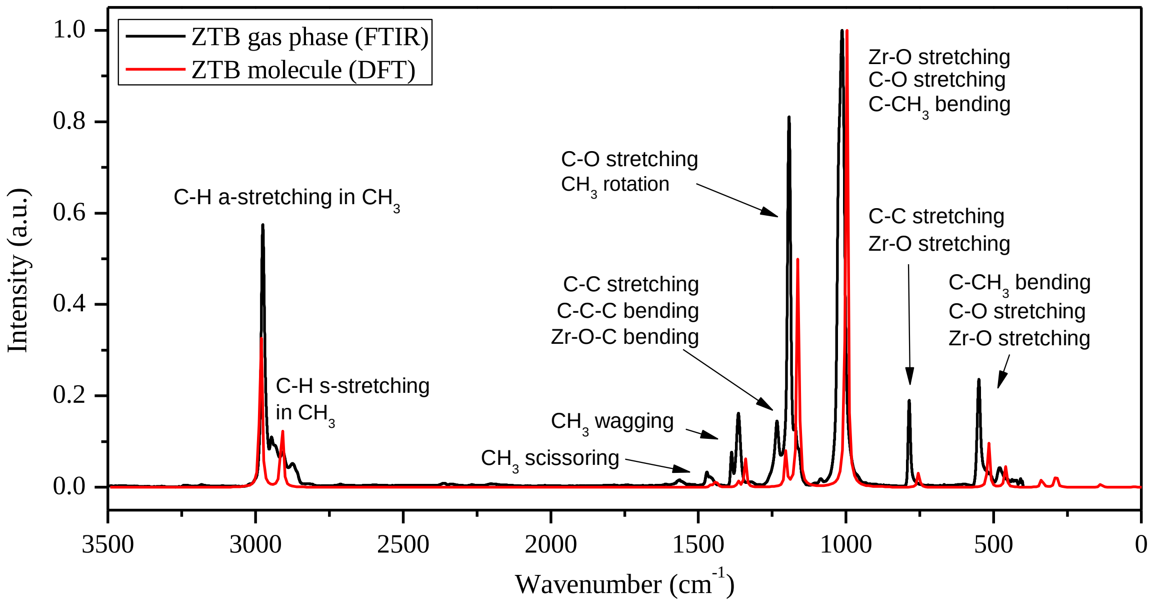

Figure II-18: Comparison of experimental [12] and calculated IR spectra of ZTB molecule.

II.4.2 Titanium Tetra Isopropoxide

Titanium tetra isopropoxide (TTIP, $TiO_4C_{12}H_{28}$) is a complex metalorganic molecule (Figure II-19) with a structure similar to ZTB's structure. Both ZTB and TTIP are composed of a central transition metal atom: zirconium ($^{40}_{91}Zr$) and titanium ($^{22}_{48}Ti$), respectively. The central atom is surrounded with four oxygen atoms that are each bonded to three hydrocarbon chains: C_4H_9 in ZTB and C_3H_7 in TTIP. TTIP's advantages are its volatility, low toxicity and low financial cost.

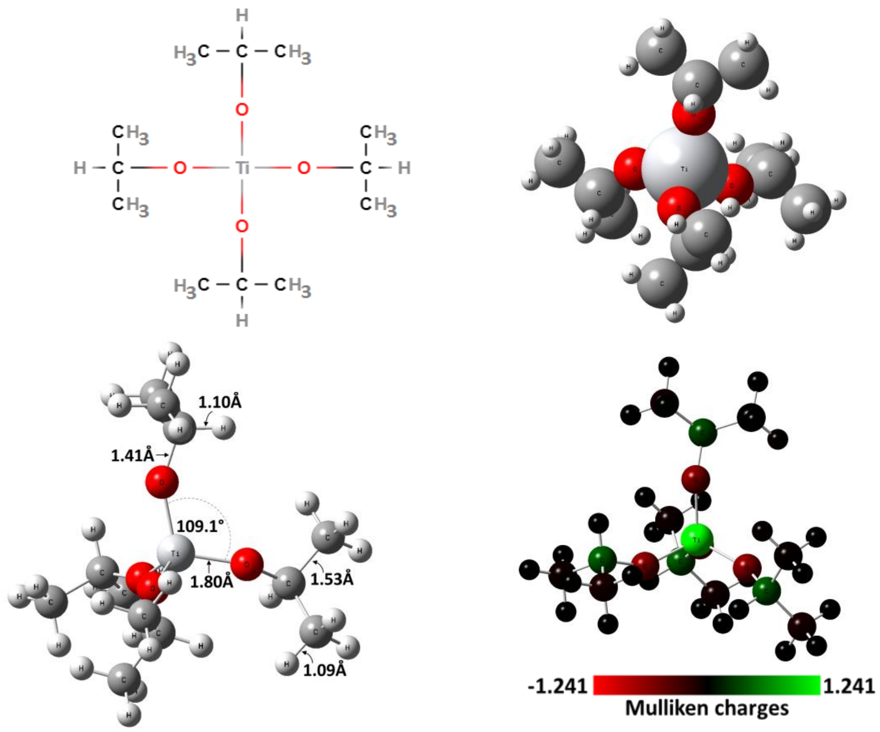

Figure II-19: Different representations of TTIP molecular structure: 2D; 3D molecule geometry optimized by DFT calculations (Gaussian 09) and visualized by GaussView 5.

An IR spectrum corresponding to TTIP molecule has been calculated by DFT and presented in Figure II-20. The peaks were assigned by visualizing calculated frequencies and reviewing the literature [151]. For peak wavelength values and corresponding assignations see Annex of this work.

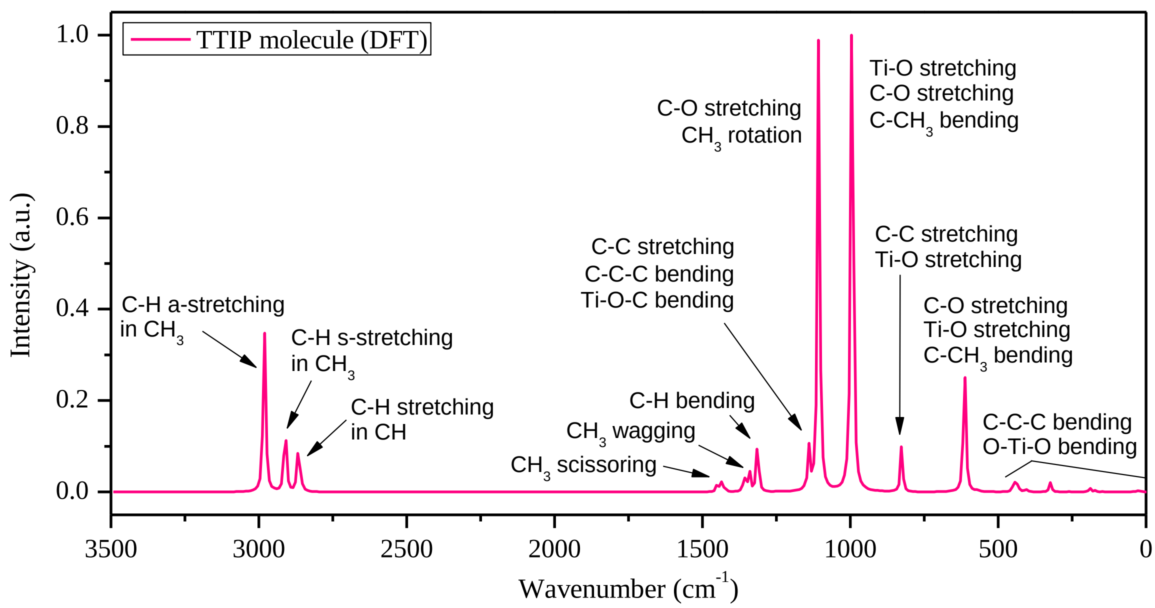

Figure II-20: IR spectrum of TTIP molecule calculated by DFT.

II.4.3 Hexamethyldisiloxane

The development of thin layers produced by PECVD from organosilicon precursors has been extensively studied for more than thirty years. Hexamethyldisiloxane (HMDSO, $OSi_2C_6H_{18}$) is the most frequently used organosilicon precursor in PECVD of $SiO_xC_yH_z$ coatings [10], [152]–[154]. Its molecular structure is presented in Figure II-21. HMDSO is liquid at ambient temperature and pressure and it is neither toxic nor explosive. Its favourable characteristics include stability, high volatility and low financial cost.

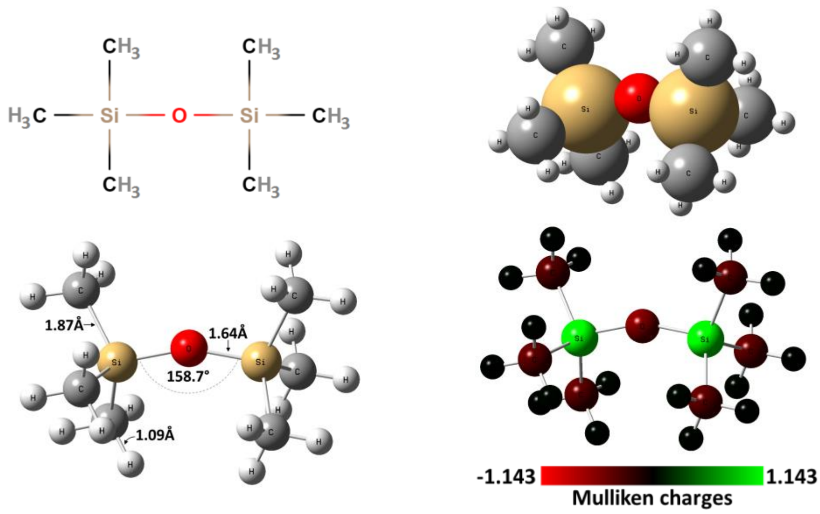

Figure II-21: Different representations of HMDSO molecular structure: 2D; 3D molecule geometry optimized by DFT calculations (Gaussian 09) and visualized by GaussView 5.

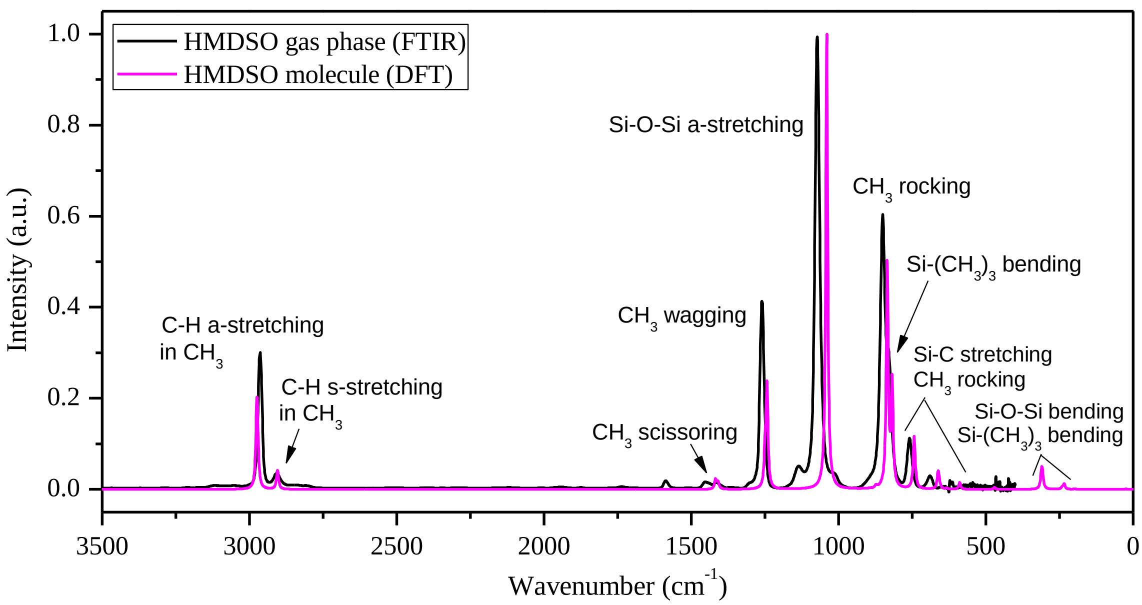

Figure II-22: Comparison of calculated and experimental [10] *IR spectra of HMDSO molecule including assignment of the peaks based on DFT and literature* [10], [155] .

In Figure II-22 IR spectrum of gas phase HMDSO measured by FTIR [10] and IR spectrum of HMDSO molecule calculated by DFT are compared. Peak wavelengths and corresponding assignations are summarised in Annex of this work.

II.5 Characterization techniques

Numerous experimental and theoretical techniques allow analysis of thin solid films and characterisation of plasma phase. Diagnostic techniques used in this study are Optical Emission Spectroscopy (OES), Mechanical Profilometry, Fourier Transform Infrared Spectrometry (FTIR), Scanning Electron Microscopy (SEM), Atomic Force Microscopy (AFM), X-ray Photoelectron Spectroscopy (XPS), Spectroscopic Ellipsometry (SE), X-ray Reflectivity (XRR), Ellipsometry Porosimetry (EP) and Density Functional theory (DFT). A succinct overview of these techniques and employed instruments with the corresponding experimental parameters is presented in the following text.

II.5.1 Optical Emission Spectroscopy (OES)

OES analysis was employed to obtain insight into the chemical composition of the plasma phase. OES is a non-invasive in-situ technique that allows identification of excited atomic and molecular species in the plasma phase by analysing the emission of electromagnetic radiation, which is a result of de-excitation of excited species.

OES of plasma is based on the analyses of light emitted from the plasma. Through collisions with electrons, plasma particles are excited to higher energy states. During relaxation to lower energy states, these particles emit electromagnetic radiation. Energy of emitted photons is equal to the difference between excited and lower energy state. Wavelength λ of the corresponding spectral line is described by the following relation:

$$E = \frac{hc}{\lambda}, \quad \text{Equation II-3}$$

where h is Planck's constant, c is the speed of light and E is the energy difference between two states, i.e. the emitted photon energy.

Every atom has precisely defined energy levels, thus each one emits characteristic radiation. Excited atoms and ions in the plasma create a unique emission spectrum. Light emitted by the discharge is a collection of spectral lines generated by different atoms in the plasma.

The emission spectra were observed and recorded by optical emission spectrometer model Acton Advanced SP2500A and the WinSpec spectroscopy software, both from Princeton Instruments. Grating of 150 grooves/mm and Step and Glue operational mode were used to record the spectra in the 200-920 nm spectral range. In Step and Glue mode, the resulting spectrum is collected as a series of incremental files. These files are then used to create a single glued data file. The software takes an exposure and, while the shutter is closed, moves the spectrometer to the next position. Final spectral resolution was equal to 0.13 nm. The optical fibre, used to transmit the signal, was positioned 15 cm below the plasma generation area (Figure II-14, p.46).

II.5.2 Mechanical profilometry

Thin film deposition rates were determined from film thickness values divided by corresponding deposition time lengths. The thickness of the deposited films has been measured by a mechanical profilometer model Alpha Step IQ from KLA Tencor located in LAPLACE Laboratory. This profilometer employs a diamond tip of 5 µm curvature radius to probe the material surface. The uncertainty of the thickness measurement of the standard sample used for calibration (thickness = 473.3 nm) is ±0.3 nm.

To measure the thickness, it is necessary to create a steep step on the samples. Two methods have been used to achieve the latter:

1. mechanical removal of deposited material by scratching with a steel cutter, and
2. use of the *lift-off* method.

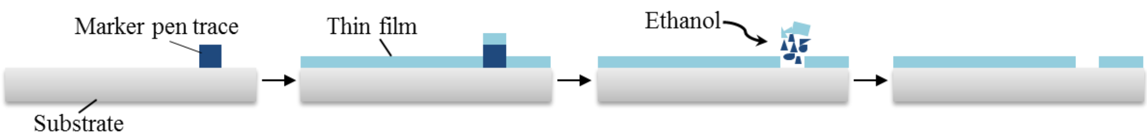

Figure II-23: Schematic presentation of the employed lift-off method.

The lift-off method includes creating a masking structure on the substrate surface by using a sacrificial material (Figure II-23). The film was deposited on a silicon wafer, which was marked by a trace of marker pen. Afterwards, ethanol (CH_3CH_2OH) was used to dissolve the marker trace and to create a clean step.

II.5.3 Fourier Transform Infrared Spectrometry (FTIR)

FTIR spectroscopy was employed to study chemical characteristics of deposited thin films. FTIR analytical technique is in common use in thin film research. It allows investigating chemical bonds present in the material. Figure II-24 shows a schematic representation of a FTIR spectrometer.

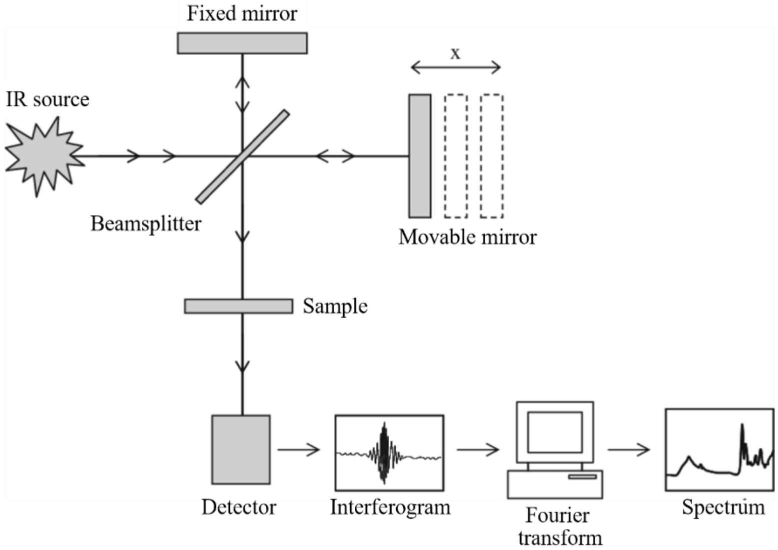

Figure II-24: Schematic representation of FTIR spectrometer (adapted from [156]*).*

When exposed to infrared radiation, molecules selectively absorb radiation of specific wavelengths causing vibrational motion. For this to occur, a vibrational mode must be IR active, i.e. it must cause a change in the dipole moment of the molecule. The frequency at which absorption occurs is an intrinsic feature of a chemical bond. Therefore, by scanning the infrared frequency range, it is possible to reconstruct the spectrum that corresponds to analysed sample, highlighting different absorption bands, and thus determining the type of bonds present.

Specific wavelength of absorbed radiation coresponds to a specific chemical bond. When applying simple harmonic oscillator approximation, frequency of bond vibration can be determined according to Hooke's law:

$$\bar{\upsilon} = \frac{1}{2\pi c}\sqrt{\frac{k}{\mu}}$$ *Equation II-4*

where $\bar{\upsilon}$ is the wavenumber of absorbed radiation, c is speed of light, k is force constant of the bond, and μ is reduced mass.

Absorbance A of a species is related to its concentration by Beer-Lambert law:

$$A = log\frac{I_0}{I} = \varepsilon Cl$$ *Equation II-5*

where I_0 is intensity of incident light, I intensity of transmitted light, ε molar absorption coefficient, C concentration of absorbing species, and l length of light path through the sample.

The measurements were performed by Bruker Vertex 70 FT-IR spectrometer with a DTGS detector located at LAPLACE. This spectrometer operates at atmospheric pressure and it is equipped with a purging system employed to remove water vapour and CO_2 from the system. The analysis has been performed in transmission mode with a resolution of 4 cm^{-1}. Every recorded spectrum is an average of 20 spectra obtained by scanning the 4000-400 cm^{-1} wavenumber range. Raw spectra have been normalised by film thickness.

II.5.4 X-ray Photoelectron Spectroscopy (XPS)

X-ray Photoelectron Spectroscopy (XPS) technique was used to study thin film chemical composition. XPS, also known as Electron Spectroscopy for Chemical Analysis (ESCA), is widely used material analysis technique based on the photoelectric effect. When a surface is irradiated with X-rays, emission of electrons from the sample is possible. X-rays excite electrons, and if their binding energy is lower than X-ray energy, they will be emitted from the atoms. Kinetic energy of emitted electron, i.e. photoelectron, (E_k) is equal to the difference between the energy of incident X-rays ($h\nu$) and the binding energy of the emitted electron (E_b):

$$E_k = h\nu - E_b.$$ *Equation II-6*

Photo-effect equation allows calculating binding energies of emitted electrons. Using this information, elements present in the material can be identified.

XPS is a surface analysis technique. Due to short inelastic mean free paths of photoelectrons, only the ones in the outer surface (depth: 10-100 Å) can escape the sample. Nevertheless, obtaining composition of a sample over its entire thickness is achievable by employing etching. An ion beam is used for etching surface layers to reveal the bulk of a sample or for only removing surface contamination.

The machine we used for obtaining atomic composition of deposited thin films is XPS Kalpha ThermoScientific located at CIRIMAT-ENSIACET in Toulouse, France. Measurement parameters are summarized below:

- X-ray: Al (Kα), E = 1486.6 eV
- Detection limit: ~0.1 at. %

- Analysis depth: 2-10 nm
- Ultra-vacuum: $p < 5.10^{-9}$ mbar
- X-ray spot: 30-400 µm
- Ar^+ gun

Example of an XPS spectrum of $ZrSi_xO_yC_wH_z$ film is shown in Figure II-25. The following peaks have been analysed to determine atomic concentration of the metal (Zr or Ti), silicon (Si), oxygen (O) and carbon (C): Zr3d, Ti2p, Si2p, O1s and C1s. Hydrogen atomic content cannot be determined by XPS technique.

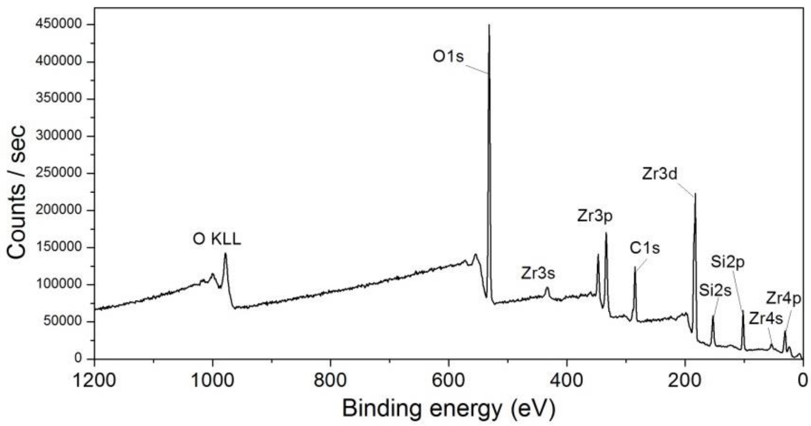

Figure II-25: Example of an XPS spectrum of $ZrSi_xO_yC_wH_z$ film.

During sample transfer and in-air storage, film surfaces have been exposed to contamination. Since XPS measurements were performed on as-deposited films after their exposure to air, the quantity of carbon and oxygen atoms detected in the films may be over-estimated.

II.5.5 Scanning Electron Microscopy (SEM)

SEM technique was used to obtain surface and cross-sectional images of deposited thin films. Unlike optical microscopy, electron microscopy uses electrons instead of light. Relatively large wavelength of visible light (400 – 700 nm) has placed a limit on image resolution in the nanometre range. In theory, an imaging source should be able to distinguish two close objects if distance between them is equal to half of the imaging energy wavelength. An electron may have significantly smaller wavelength than visible light according to de Broglie's equation:

$$\lambda = \frac{h}{p} = \frac{h}{\sqrt{2meV}} \qquad \text{Equation II-7}$$

where λ is electron de Broglie wavelength, h is Planck's constant, p electron momentum, m electron mass, e electron charge, and V potential difference. Therefore, using electrons in microscopy allows achieving considerably higher resolution.

Figure II-26 shows a schematic representation of a scanning electron microscope. SEM uses an electron beam focused to a very fine line for scanning the sample. Electrons in the beam interact with the specimen, producing various signals (secondary electrons, backscattered electrons, x-rays, etc.) that can be used to obtain information about sample topography and composition. Beam-specimen interaction results in additional electrons knocked off the specimen. These electrons are collected by a detector - an anode at a potential of a few hundred volts positive with respect to the specimen. Variation in the current that flows to the anode is used to create an image of the sample.

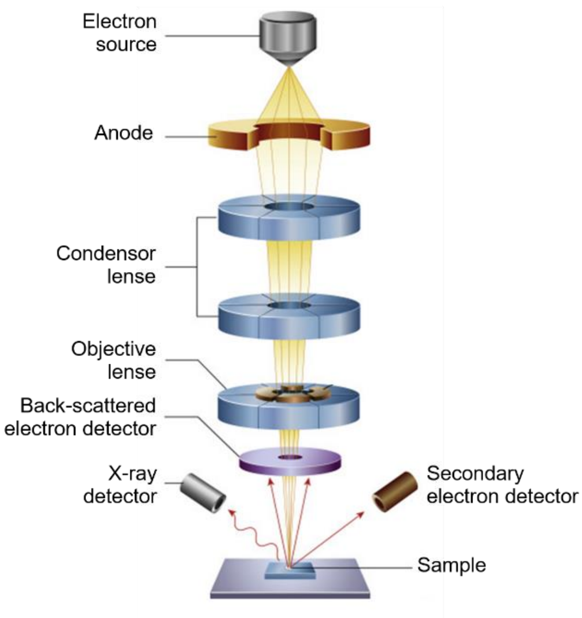

Figure II-26: Schematic representation of an SEM [157].

Electron microscope requires vacuum to operate. Without vacuum, electron beam would interact with air particles. Electrons could be absorbed by air molecules, and the latter could also contaminate the sample. Since electrons are electrically charged, SEM sample needs to be conductive enough to dissipate energy. Sample preparation includes cleaning it of any dust or debris, and if the specimen is not conductive, it is coated in a conductive material like gold or platinum through a process called sputter coating. This conductive coating enables the sample to be grounded, protecting it from being damaged by the electron beam.

Two different systems were used to record the images:

- MEB FEG JEOL JSM 6700F – EDS with an image resolution of 1 nm at 15 kV, and
- JSM-7800F Prime with a resolution of 0.8 nm in 1 kV-30 kV range.

Both machines are located at Centre de MicroCaractérisation Raimond Castaing in Toulouse, France. Prior to taking the images, all the samples have been metalized to avoid surface charging phenomenon: 1 nm thick platinum (Pt) layer was deposited on the samples by plasma sputtering.

II.5.6 Atomic Force Microscopy (AFM)

Atomic Force Microscopy (AFM) is a probe-scanning imaging technique that maps the interactions between a fine tip and atoms of a surface. Operational principle is based on approaching a cantilever, at the end of which a nanometeric tip is placed, to the surface of a sample. The cantilever is deflected as a result of the interaction forces and that deflection is measured by positioning a laser beam on the upper face of the cantilever. The laser beam reflects on a mirror to a four-quadrant photodiode that records a light signal. Schematic representation of an AFM is shown in Figure II-27.

To study the film topography, film surface was analysed by Bruker AFM model Multimode 8 (Nanoscope V software) located in LAPLACE Laboratory. The measurements were performed by using the Bruker TESPA-V2 AFM probe. The machine was operated in tapping mode to visualize the surface of the films in 3D. The resolution in the vertical direction equals 0.01 nm, whereas in the horizontal direction it corresponds to a few nanometres.

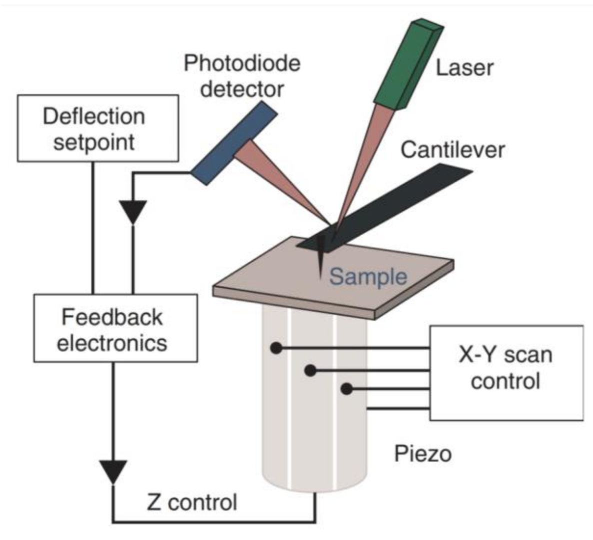

Figure II-27: Schematic representation of an AFM [158].

In the following chapter, we report on the values of two surface roughness parameters, R_a and R_{max}:

➢ Mean roughness parameter R_a is the arithmetic average of the absolute values of the roughness profile height:

$$R_a = \frac{1}{l}\int_0^1 |Z(x)|dx \qquad \textit{Equation II-8}$$

where *l* is the sampling length and *Z(x)* is the profile height at coordinate *x*.

➢ Maximum roughness depth R_{max} is the largest single roughness depth within the evaluated length.

II.5.7 X-Ray Reflectivity (XRR)

X-Ray Reflectivity technique is based on the analysis of intensity of x-ray beam reflected on a sample at grazing angles. This method allows calculating the density of deposited thin films. Figure II-28 shows an example of a reflectivity curve obtained by XRR.

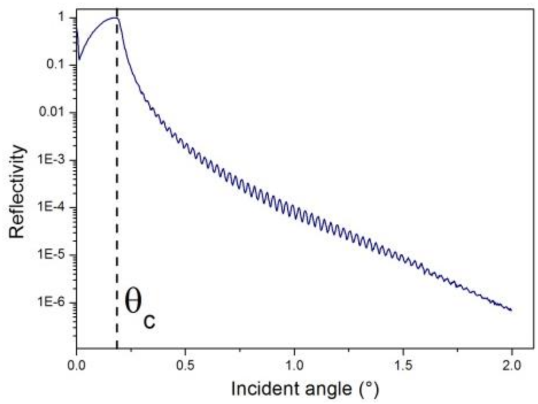

Figure II-28: Example of reflectivity as a function of incident angle measured by XRR. θ_c is the critical angle.

To extract information about a sample, X-ray reflectivity curve is analysed by fitting a simulated curve. Fitting parameters are typically density, film thickness and interfacial roughness. Thin film density is related to the critical angle; amplitude of oscillations is associated to density contrast; film thickness is related to the period of oscillations; oscillation decay rate at higher angles is connected to surface or interface roughness; and intensity decay rate at higher angles is correlated to surface roughness.

At angles inferior to critical angle θ_c, incident radiation is completely reflected. Critical angle θ_c is directly related to electron density ρ_e by the following equation:

$$\theta_c = \sqrt{\frac{\lambda^2 r_0}{\pi}\rho_e},$$ *Equation II-9*

where λ is the wavelength of the incident x-ray beam and r_0 is Bohr atomic radius. If film chemical composition is known, mass density of the film can be estimated based on the following equation:

$$n = 1 - \frac{2\pi r_0}{k_0^2}\rho_e = 1 - \frac{2\pi r_0}{k_0^2}N_A\rho_m K,$$ *Equation II-10*

where n is the refractive index, ρ_e is electron density, ρ_m is mass density, N_A is the Avogadro number, K is the coefficient related to film chemical composition, r_0 is Bohr atomic radius, and k_0 is equal to λ/2π with λ representing the x-ray wavelength.

In our work, we have used stoichiometry determined by XPS measurements. The XRR analysis was performed with an XRD machine model D5000 from Siemens at European Institute of Membranes in Montpellier, France.

II.5.8 Spectroscopic Ellipsometry (SE)

Spectroscopic ellipsometry is a non-invasive diagnostic technique employed for determining optical characteristics of a material, as well as other properties such as crystallinity, roughness or doping concentration. Ellipsometry investigates interaction of polarized light with a material by measuring a change in the polarization of light as it is reflected from a surface. It is an indirect method for determining material properties, i.e. theoretical modelling is necessary to obtain the properties from experimentally obtained physical quantities. Theoretical models use mathematical relations called dispersion formulae that help in evaluation of optical and other material properties by a ″fitting″ procedure.

Figure II-29 shows a schematic representation of the principle of spectroscopic ellipsometry. Ellipsometry measures phase difference Δ and amplitude ratio Ψ between reflected and polarized light. More precisely, it determines cos(Δ) and tan(Ψ) using a mathematical treatment of reflected beam intensity. This allows obtaining complex reflection coefficient ρ:

$$\rho = \tan(\Psi)\, e^{i\Delta} = \mathrm{f(n,k)},$$ *Equation II-11*

where n is the refractive index and k is the damping constant which describes a change in the amplitude of the electromagnetic wave propagating through a medium. For transparent materials, due to high penetration depths of light, k values are very close to zero and N ≈ n.

However, for many other materials, *n* and *k* are not constant parameters, yet they depend on the incident light wavelength: an effect known as dispersion.

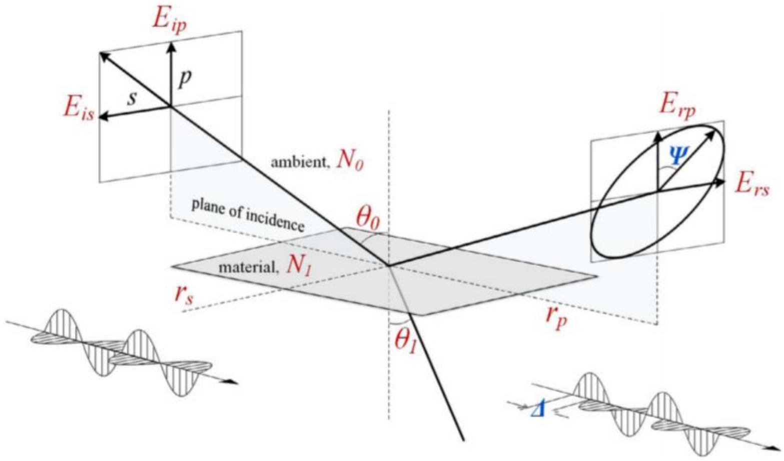

Figure II-29: Schematic representation of spectroscopic ellipsometry principle [159].

When investigating a thin layer deposited on a substrate, calculations using the measurements of tan(ψ) and cos(Δ) are not straightforward. Indeed, the reflection coefficient for a film-covered surface involves the film thickness d. Since an unknown variable is added to the system more than one solution becomes possible. This new relation can be written as follows:

$$\rho = \mathrm{f}(N_0, N_1, N_2, \lambda, \mathrm{d}, \theta_0), \qquad \textit{Equation II-12}$$

where N_0, N_1 and N_2 are refraction indices of the environment, film and substrate, respectively. λ is the incident light wavelength, θ_0 angle of incidence and *d* is film thickness. Usually, N_0, λ and θ_0 are known, while it is possible to obtain N_2, N_1 and *d*.

In our study, spectroscopic ellipsometer Semilab GES5E was used to analyse refractive indices of deposited thin films. *Cauchy absorbent* dispersion model was employed for determination of the refractive indices. The model is based on the following empirical formulae:

$$n(\lambda) = A + \frac{10^4 \cdot B}{\lambda^2} + \frac{10^9 \cdot C}{\lambda^4} \qquad \textit{Equation II-13}$$

$$k(\lambda) = 10^{-5} \cdot D + \frac{10^4 \cdot E}{\lambda^2} + \frac{10^9 \cdot F}{\lambda^4} \qquad \textit{Equation II-14}$$

where n(λ) and k(λ) are refractive index and extinction coefficient at wavelength λ, and *A, B, C, D, E, F* are fitting parameters. In this work, we report film refractive indices corresponding to the wavelength value of 632.8 nm.

II.5.9 Ellipsometry Porosimetry (EP)

Ellispometry Porosimetry is a technique developed by coupling Spectroscopic Ellipsometry with adsorption phenomenon. EP examines changes of optical properties and material thickness during adsorption and desorption of a volatile species, i.e. a vapour probe. Figure II-30 shows an example of the adsorption/desorption isotherms as function of the ratio of vapour probe partial pressure and saturated vapour pressure.

Evolution of refractive index and film thickness is used to calculate the quantity of the adsorbed probe molecules present in the films, i.e. the open porosity fraction, on the basis of Lorentz-Lorentz equations presented in the scheme below (adapted from [160]):

Vacuum

p=0

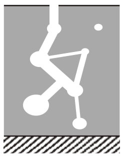

$$\frac{n^2-1}{n^2+1} = \frac{V_S}{V_0}\frac{{n_S}^2-1}{{n_S}^2+1}$$ *Equation II-15*

Saturation

p/p_0=1

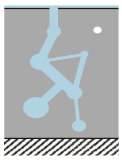

$$\frac{n^2-1}{n^2+1} = \frac{V_S}{V_0}\frac{{n_S}^2-1}{{n_S}^2+1} + \frac{V_L}{V_0}\frac{{n_L}^2-1}{{n_L}^2+1}$$ *Equation II-16*

- *n refractive index of the whole layer; n_s refractive index of the skeleton; n_l refractive index of the liquid*
  - *V_0 volume of the layer; V_S skeleton volume; V_L volume of the open pores filled with liquid L*

EP allows obtaining different material properties such as porosity, pore size distribution, hydrophobicity or diffusion coefficient.

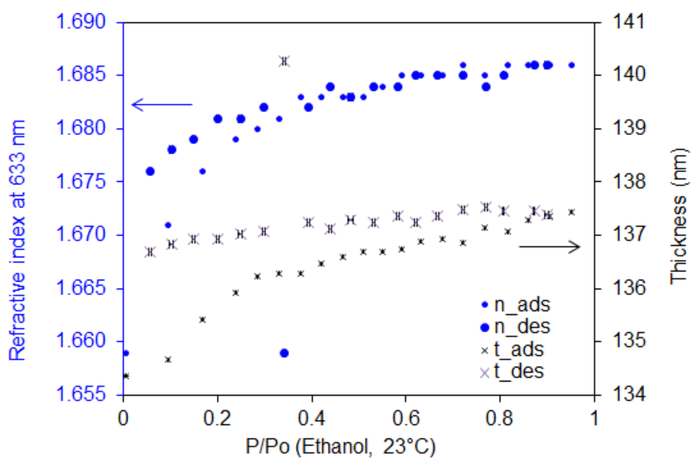

Figure II-30: Example of film refractive index and thickness evolution measured by EP during ethanol adsorption cycle.

Table II-2 presents a classification of nanoporosity by pore diameter. EP technique allows analysing microporosity and mesoporosity of a material in the range of 10 nm to several µm.

The proportion of open nanoporosity in the deposited films was examined by ellipsometric porosimetry. The experimental setup employed to examine nanoporosity of thin films deposited in our study, allows detecting pores in 2-50 nm diameter range [161].

Table II-2: Nanoporosity classified by pore diameter according to IUPAC [162].

<table>
<tr><th colspan="2">Micropores</th><th>Mesopores</th><th>Macropores</th></tr>
<tr><td colspan="2"><2 nm</td><td rowspan="2">2-50 nm</td><td rowspan="2">>50 nm</td></tr>
<tr><td>Ultra
<0.7 nm</td><td>Super
>0.7 nm</td></tr>
</table>

A system composed of a Semilab GES5E ellipsometer and a vacuum chamber (Figure II-31) was used to observe changes in the refractive index during adsorption and desorption of volatile species. Vacuum chamber serves to control vapour pressure of the probe solvent.

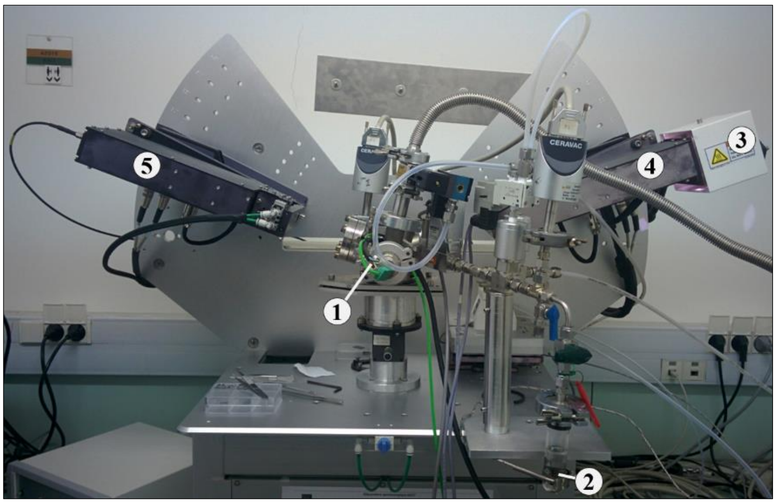

Figure II-31: Ellipsometry porosimetry setup at European Institute of Membranes in Montpellier, France. Main parts of the setup: 1 - vacuum chamber, 2 - ethanol, 3 - light source, 4 - polarizer, 5 - analyser.

Considering that the probe solvent will physisorb at the pore walls and it should condensate at room temperature, there are several requirements the probe must fulfil:

- sufficiently high vapour pressure for convenient analysis (min. several Torr),
- preferentially non-polar or weakly polar molecule; otherwise, the refractive index of condensed solvent could be different close to the pore walls than in the liquid phase,
- any chemical reaction must be avoided; pure physisorption of the probe molecule has occurred on the probe walls if the refractive index of the film comes back to its original value after a full adsorption/desorption cycle.

Some of the frequently used probe molecules are:

- ethanol, CH_3CH_2OH (kinetic diameter at 293K = 0.43 nm; dipole moment = 1.69 Debye; vapour pressure at 293K = ~59 Torr),
- water, H_2O (kinetic diameter at 293K = 0.27 nm; dipole moment = 1.85 Debye; vapour pressure at 293K = ~24 Torr),
- toluene, C_7H_8, aromatic (kinetic diameter at 293K = ~0.60 nm; dipole moment = 0.37 Debye; vapour pressure at 293K = ~28 Torr).

Regarding the requirements the probe must conform to, and the characteristics of frequently used probes listed above, ethanol was chosen as the vapour probe in this work.

Ellipsometry porosimetry measurements and the corresponding analysis were performed at European Institute of Membranes in Montpellier, France.

II.5.10 Density Functional Theory (DFT)

Synthetic vibrational spectra corresponding to precursor molecules used in this work were built by DFT theoretical calculations. DFT is a quantum computational method [163], [164], that was employed for optimization of precursor molecule geometries and calculations of their vibrational spectra (at 298K).

The goal of most quantum chemical approaches is the - approximate - solution of the Schrödinger equation. Unfortunately, it is impossible to solve the Schrödinger equation for a many-body system. Evidently, we must involve some approximations. The basic idea behind DFT is the first Hohenberg-Kohn theorem which states that all the fundamental properties of a system can be obtained from electron probability density. Electron probability density is always a function of only three space coordinates. DFT calculations can be applied to systems ranging from atomic nuclei and atoms to classical and quantum fluids. It allows calculating a great variety of molecular properties such as vibrational frequencies and ionization energies.

All calculations were performed using the Gaussian09 package [165]. GaussView 5 graphical interface was used for building the molecular structures, i.e. generating input files, as well as for visualising calculated vibrational frequencies. Regarding the computational details, the B3LYP hybrid exchange-correlation functional with the 6-311++g (3df, 3pd) basis set was used. A scaling factor of 0.9613, adapted for the functional and the basis set used in our calculations, was applied to calculated wavenumbers [166]. The servers employed to run the calculations as well as the licenced Gaussian09 package were provided by the Laboratory for Chemistry of Novel Materials at University of Mons (Belgium) in the framework of collaboration with LAPLACE laboratory.

Chapter III

Thin film growth in ZTB/O_2 and TTIP/O_2 plasmas: influence of plasma gas mixture O_2 fraction

Introduction

The objective of this chapter is to study the modifications of the thin film growth process as a function of the variations in the plasma gas mixture. Two types of thin film materials, $ZrO_xC_yH_z$ and $TiO_xC_yH_z$, have been synthesised in low pressure ZTB/O_2 and TTIP/O_2 plasmas, respectively. The films have been deposited at various values of metalorganic precursor-to-oxygen gas ratio at constant total gas mixture pressure. The corresponding process parameters are summarised in Table III-1.

Table III-1: Growth conditions of thin films deposition in ZTB/O_2 and TTIP/O_2 plasmas.

Total gas pressure	1 mTorr					
MW power	800W					
Substrate	Si (100)					
Substrate potential	Floating					
$T_{substrate}$	Uncontrolled					
Gas mixture composition	100% ZTB	75% ZTB 25% O_2	50% ZTB 50% O_2	35% ZTB 65% O_2	20% ZTB 80% O_2	5% ZTB 95% O_2
	100% TTIP	70% TTIP 30% O_2	50% TTIP 50% O_2	35% TTIP 65% O_2	20% TTIP 80% O_2	5% TTIP 95% O_2
Deposition time	< 10 min at 0-80% O_2, 30-40 min at 95% O_2					

The chapter is divided into five parts. Generally, each part begins with a predominately descriptive presentation of experimental results corresponding to films deposited in ZTB/O_2 and TTIP/O_2 plasma. This is followed by a comparison between two types of films and an interpretation of the obtained results.

First, an OES qualitative analysis of the plasma phase is presented. Afterwards, the focus shifts to characteristics of the solid phase and we review thin film growth rates. Then, film physico-chemical properties are studied by means of FTIR and XPS. Furthermore, evolution of morphological features of the film, investigated by SEM and AFM, is analysed. Experimentally observed results are coupled with findings obtained from MC simulations performed by colleagues at Institute of Material Science in Sevilla, Spain. Finally, we examine macroscopic physical properties of the film (refractive index, density and nanoporosity fraction) in a succinct manner.

III.1 OES analysis of ZTB/O_2 and TTIP/O_2 plasma phase

In a PECVD process, the formation of a thin film is the result of plasma-surface interactions. The species existing in the plasma play one of the crucial roles in the mechanism of thin film growth. Thus, to understand the growth mechanism and to control the final thin film characteristics, it is necessary to have an insight into the plasma chemistry. To achieve that, optical emission spectroscopy has been employed. The position of optical fibre in regard to the reactor allows probing the diffused part of the plasma in the centre of the plasma chamber, relatively far from the ECR zone (Chapter II, p.36).

This study is of qualitative nature: it serves to provide information on the type of excited species present in the plasma phase and the evolution of the plasma composition with regards to variations in the gas mixture ratio. In this analysis, we are not performing actinometry or presenting a detailed spectroscopic examination.

Normalization of measured data was necessary to allow the comparison of different spectra and the examination of the evolution of certain spectral lines. Therefore, argon gas was added to the gas mixture and all the emission spectra intensities were divided by the intensity of a spectral line at 750 nm which originates from an excited argon atom [167]. The first step of the experimental protocol included stabilizing the pressure of the precursor/O_2 gas mixture at 1 mTorr. Afterwards, the lowest possible quantity of argon gas allowed by the technical conditions was injected into the reactor: ~5 % relative to the total gas pressure.

To verify that the argon gas presence does not significantly alter the composition of the plasma, optical emission spectra of the pure precursor plasma and the precursor/Ar plasma have been compared. Figure III-1 shows a region of the spectra in which all appearing lines correspond to species originating from precursor and O_2 molecules; Ar lines were not observed in this part of the spectra. The comparison confirmed that the addition of a small quantity of argon gas into the metalorganic/O_2 gas mixture does not appear to noticeably influence the OES spectra of the plasma phase.

The spectra have been measured in the 250-900 nm wavelength range. In the following text, the main spectral lines are identified in both ZTB and TTIP plasmas and the corresponding species are assigned. Additionally, we have studied the evolution of normalised intensities of the spectral lines corresponding to subsequent excited species: H, CH, O, CO, CO^+, CO_2^+.

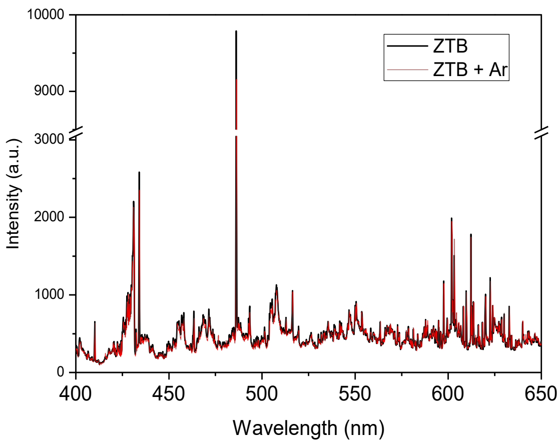

Figure III-1: Comparison of 400-650 nm region of OES spectra corresponding to precursor and precursor/Ar plasma (precursor: ZTB or TTIP, $p_{precursor}$ = 1 mTorr, p_{Ar} = 0.05 mTorr, P_{MW} = 800 W).

Different research groups have established that the evolution of intensity of the atomic oxygen spectral line normalised by the Ar line intensity, I(O)/I(Ar), is representative of the evolution of oxygen atom density in HMDSO/O_2 and TEOS/O_2 plasmas [168], [169]. Relying on the findings of aforementioned studies, here we consider the evolution of the spectral line intensity ratio I(X)/I(Ar), where X is H, CH, O, CO, CO^+ or CO_2^+, as an indication of the evolution of the plasma composition.

III.1.1 Identification of OES spectra

Figure III-2 shows emission spectra corresponding to ZTB/O_2/Ar and TTIP/O_2/Ar plasmas obtained at O_2/precursor = 1 (total pressure p(precursor+O_2+Ar) = 1.05 mTorr, P_{MW} = 800W). The peaks, listed in Table III-2, have been assigned with the help of literature [11], [170], [171]. The same spectral lines appear in emission spectra of both ZTB and TTIP plasmas. The only observable difference is found in the intensity of the peaks.

Apart from the peaks corresponding to excited Ar atoms, other assigned atomic and molecular species may originate from the precursor and O_2 molecule dissociation in collisions with accelerated electrons and/or from reactions occurring at the plasma-surface (substrate, reactor walls) interface. Chemical reactions between neutral precursor fragments in the plasma phase are disregarded due to relatively low operating pressure of 1 mTorr and low energy of the neutral particles.

Peaks assigned to excited H, O and Ar atoms are dominant in emission spectra of studied plasmas. We have assigned certain peaks to excited CO, CO^+, CO_2^+, OH, CH, C_2, H_2 species. The presence of CO_2, OH and H_2 in the plasma phase may be taken as a sign of plasma-surface reactions. CO, CH and C_2 could originate from surface reactions, as well from the precursor fragmentation due to existence of C-O, C-C, C-H bonds in both ZTB and TTIP molecules.

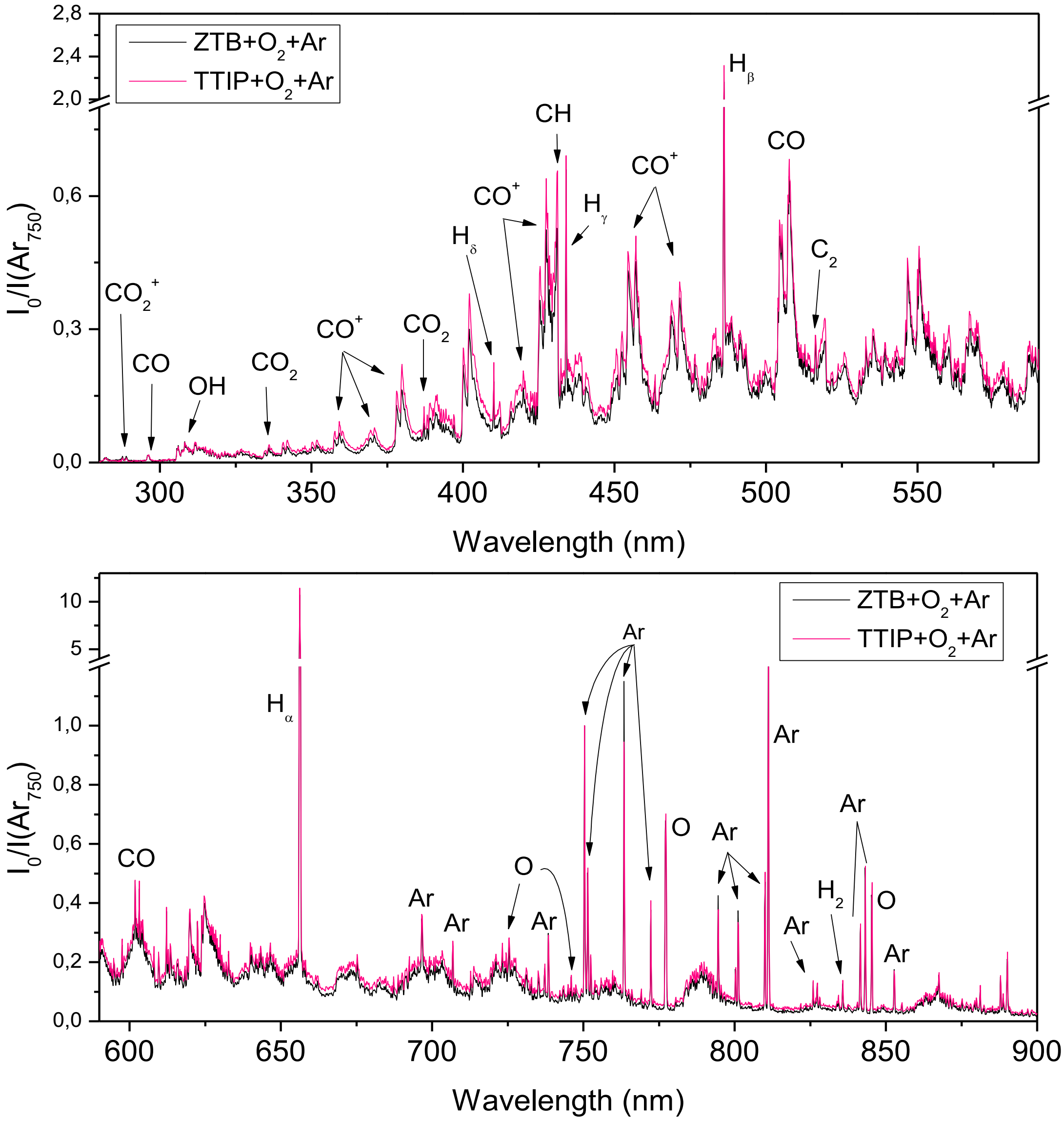

Figure III-2: Optical emission spectra of ZTB/O_2/Ar and TTIP/O_2/Ar plasma normalised by Ar spectral line intensity at 750 nm ($p_{precursor}$ = 0.50 mTorr, $p_{oxygen\ gas}$ = 0.50 mTorr, $p_{Ar\ gas}$ = 0.05 mTorr, P_{MW} = 800 W).

Table III-2: List of assigned emission spectral lines observed in ZTB/O_2/Ar and TTIP/O_2/Ar plasmas (p_{total} = 1.05 mtorr, P_{MW} = 800W, 4.8% Ar) [11], [96], [170], [171].

Radiative species	System	Wavelength (nm)
H	Balmer lines (H_α, H_β, H_γ, H_δ)	656.6, 486.9, 435.1, 411.3
H_2	-	835.7
CH	4300 Å system	431.2
CO	5B System 3rd Positive System Triplet Bands	266-383 283-370 401-647

Radiative species	System	Wavelength (nm)
	Ångström System Asundi Bands	411-663 574-860
CO^+	Comet Tail Badlet-Johnson	308-641 331-424
CO_2^+	-	287.6, 288.9
OH	3064 Å system	308.2
C_2	Swan system	516.4
O	-	725.4, 746.1, 777.4, 845.0
Ar	-	696.6, 706.8, 737.2, 738.4, 750.39, 763.4, 772.3, 794.6, 800.3, 801.1, 810.1, 811.2, 825.9

Central part of precursor molecules consists of a metal atom surrounded by four oxygen atoms. Metal atoms and metal oxide species might be present in the plasma phase due to dissociation of the precursor molecule. Table III-3 presents the wavelengths of peaks assigned to Zr, ZrO, Ti and TiO species in low temperature plasmas reported by different authors [39], [96], [172], [173]. In the investigation of the spectra observed in our study, we were not able to distinguish the emission lines corresponding to Zr and ZrO in ZTB plasmas nor the ones matching Ti and TiO in TTIP plasmas. This may be explained by low concentration of these species relative to other emissive particles in the plasma. Accordingly, corresponding emission intensities might be too low to be detected in our experimental conditions.

Table III-3: Peaks assigned to Zr and Ti species in OES spectra of low temperature plasmas: literature review.

Radiative species	Wavelength (nm)	References
Zr	350.9, 352.0	[172]
Zr^+	339.2, 343.8, 349.6	[172]
ZrO	463.7, 464.0, 622.9, 626.1, 629.3, 634.5, 637.8, 647.4, 650.8	[39], [172]
Ti	388.3, 390.5, 402.5, 429.8, 451.8, 452.3, 453.3, 517.4, 519.3, 521.0, 843.6	[96], [173]
TiO	705.5, 708.8, 712.6, 715.9	[96]
Ti^+	323.5, 323.7, 323.9, 338.4, 338.8, 375.9, 376.1, 368.5	[173]

III.1.2 Evolution of OES spectra as a function of gas mixture composition

ZTB

Figure III-3(a) presents the evolution of normalised intensities of several spectral lines as a function of O_2 gas proportion in the gas mixture. The lines of interest, corresponding to excited O, H and CH species, were observed at 777.4, 656.6 and 431.2 nm, respectively. In general, the emission of atomic O increases with addition of O_2 to the gas mixture, while emissions corresponding to H and CH decrease. In the evolution of the emission intensity of these species, two regimes can be distinguished. At low O_2 concentration in the gas mixture we observe rather slow changes. After 80% of O_2 had been added to the gas mixture, we can observe a steep increase in O emission and a drastic decrease in emissions of H and CH. This point is also a changing point for emissions at 296.7, 425.4 and 288.9 nm corresponding to CO, CO^+ and CO_2^+ (Figure III-3(b)). Emission intensities of these species achieve a maximum at ≥80 % of O_2 in the gas mixture and then decrease as the proportion of O_2 gas approaches 95%.

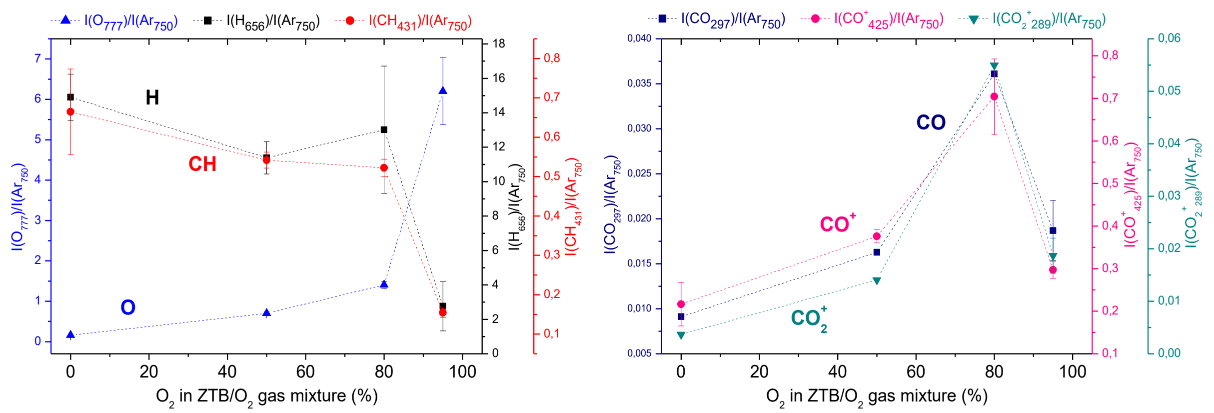

(a) (b)

Figure III-3: Evolution of spectral line intensity ratios as a function of O_2 gas percentage of ZTB/O_2 gas mixture (p_{ZTB+O2} = 1 mTorr, $p_{Ar\ gas}$ = 0.05 mTorr, P_{MW} = 800 W): (a) I(O)/I(Ar), I(H)/I(Ar), I(CH)/I(Ar), (b) I(CO)/I(Ar), I(CO^+)/I(Ar), I(CO_2^+)/I(Ar).

TTIP

Figure III-4(a) shows the spectral line emission intensity associated with H, CH and O as a function of O_2 proportion in the TTIP/O_2 gas mixture. Emission intensity of excited O atoms generally increases with increase in O_2 gas percentage added to the gas mixture, while H and CH emissions decrease. For highly oxidised gas mixture of TTIP/O_2, steep changes are observed. Figure III-4(b) presents the evolution of carbon-oxide species: CO, CO^+ and CO_2^+. With increase in O_2 gas fraction in TTIP/O_2 gas mixture, emission intensities of these excited carbon-oxide species increase to achieve maximum values at 90% of O_2 gas added to the gas mixture. With further addition of O_2 gas, the emission intensities decrease.

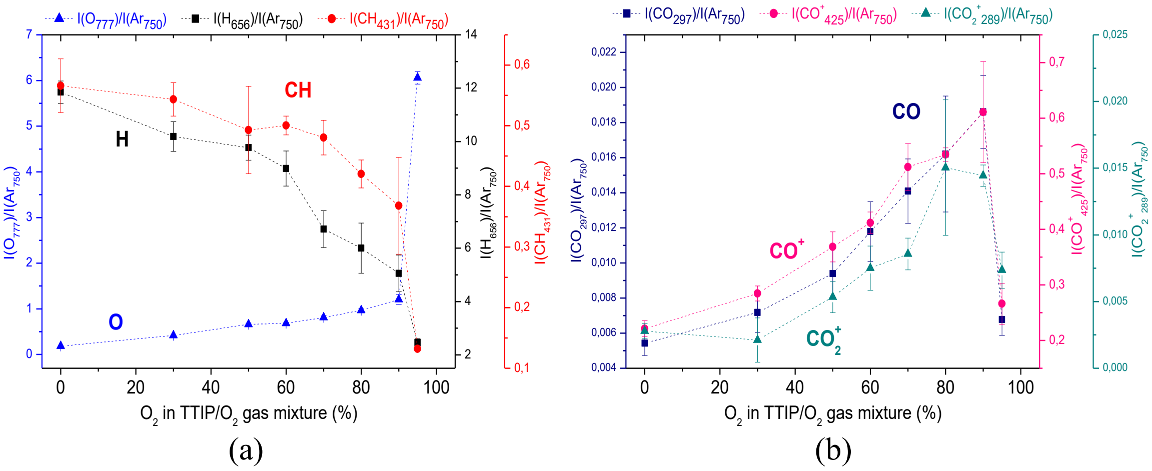

Figure III-4: Evolution of spectral line intensity ratios as a function of O_2 gas percentage of TTIP/O_2 gas mixture ($p_{TTIP+O2}$ = 1 mTorr, $p_{Ar\ gas}$ = 0.05 mTorr, P_{MW} = 800 W): (a) I(O)/I(Ar), I(H)/I(Ar), I(CH)/I(Ar), (b) I(CO)/I(Ar), I(CO^+)/I(Ar), I(CO_2^+)/I(Ar).

Figure III-5 shows the evolution of the emission intensity of excited oxygen atoms in ZTB/O_2 and TTIP/O_2 plasmas. As the O_2 gas fraction in the gas mixture increases and approaches 100%, the normalised emission intensity of oxygen atoms also increases. Granier et al. have observed similar behaviour of oxygen atom density in TTIP/O_2 ICP plasma [174].

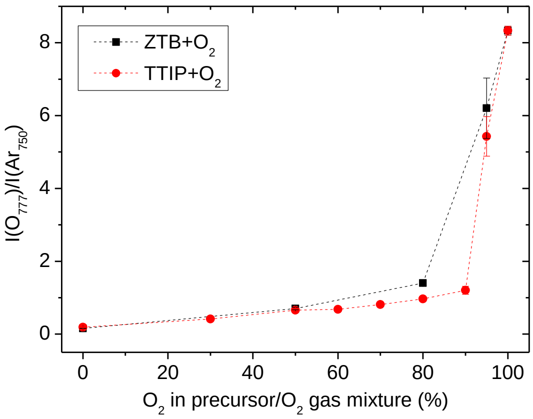

Figure III-5: Evolution of spectral line intensity ratio I(O)/I(Ar) as a function of O_2 fraction in precursor/O_2 gas mixture (precursors: ZTB or TTIP, p_{total} = 1 mtorr, P_{MW} = 800W).

Contrarily, a higher O atom density and spectral line intensity ratio I(O)/I(Ar) have been observed in O_2-rich organosilicon/O_2 plasma compared to 100% O_2 plasma [3], [174]. This has been attributed to higher probability of O atom recombination at reactor walls in 100% O_2 plasma. As low percentage of organosilicon precursor is found in the gas mixture, new reactive species are created and introduced into competition with oxygen atoms to occupy the surface recombination sites. The difference in evolution between metalorganic and organosilicon plasma might lie in different surface recombination mechanisms at play [174].

III.1.3 OES analysis: discussion

Optical emission spectra of low pressure ZTB/O_2 and TTIP/O_2 plasmas are composed of identical spectral bands. These spectra mainly consist of peaks corresponding to excited O, H, OH, CH, CO, CO^+, CO_2^+. The intensities of the peaks change as the gas mixture ratio of metalorganic precursor and O_2 gas varies. Spectral lines corresponding to excited Zr and ZrO or Ti and TiO were not recognised. In a qualitative sense, the spectra are very similar to optical emission signatures of low pressure HMDSO/O_2 and TEOS/O_2 plasmas [1], [3], [175].

The species identified in the plasmas originate from the precursor fragmentation process as well as from the surface etching reactions. The etching of carbon atoms achieved by oxygen species has been confirmed by the increase in the intensities of the peaks assigned to CO and CO_2 with O_2 gas addition. Besides atomic oxygen which plays a crucial role in removing carbon from the deposits, hydrogen is also expected to participate in the etching of the film by forming volatile species such as C_2H_2.

Regarding the C_xO_y type of species, a specific maximum in the emission intensity is observed in both ZTB and TTIP plasmas as O_2 is added to the gas mixture. Similar evolution has been observed in TEOS and HMDSO plasmas [3]. After the initial increase up to a maximal value, a decrease of intensity is noticed in O_2-rich plasma (~95% of O_2) which may be explained by extreme dilution of the metalorganic precursor in the gas mixture. The high quantity of oxygen atoms is outweighed by the deficiency of carbon atoms.

Optical emissions attributed to H and CH in ZTB/O_2 and TTIP/O_2 plasma decrease with addition of O_2 gas to the gas mixture (Figure III-3(a), p.74; Figure III-4(a), p.75). The same tendency has been observed in multipolar ECR plasma of ZTB/O_2, TEOS/O_2 and HMDSO/O_2 [1], [3], [11]. This evolution can be explained by the dilution of the precursor, i.e. the main source of carbon and hydrogen atoms, as O_2 gas fraction in the gas mixture is increased. At the same time, part of H atoms is lost at the reactor walls and substrate surface in the recombination reactions with O to form OH and H_2O, as already evidenced in the literature [168]. Similar behaviour of the C_xH_y type of species has been observed by Mr R. Verhoef in his thesis work with in situ FTIR and MS of low pressure ICP ZTB/O_2 plasma [12]. The study has shown a decrease in the FTIR absorption peaks corresponding to CH_4 and C_2H_2, while MS measurements confirmed a rapid decline in the signal attributed to species such as C_2H, C_2H_2 and C_5H_7. It has been proposed that the fragments arrive at the surface and react with atomic O rather than with atomic H and form species of type $HOCH_3$ instead of C_xH_y.

III.2 Deposition rate

Thin films were deposited in ZTB/O_2 and TTIP/O_2 plasmas at different gas mixture ratios of O_2 gas and precursor gas. Total gas pressure was constant at 1 mTorr, microwave power was set at 800 W, with substrate at floating potential. Figure III-6 shows the deposition rate values obtained from thickness profilometer measurements corresponding to films deposited in (a) ZTB/O_2 and (b) TTIP/O_2 plasma.

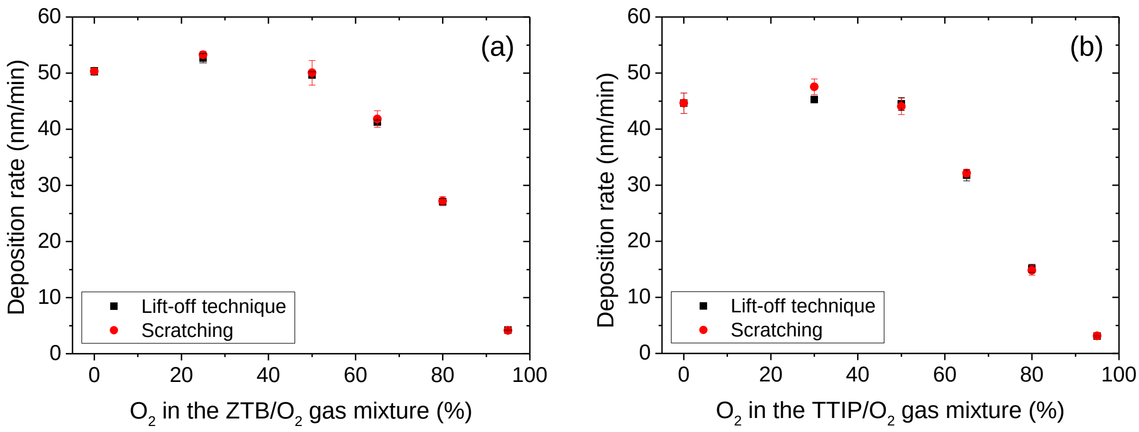

Figure III-6: Deposition rate of thin films deposited at different gas mixture ratios in (a) ZTB/O_2 and (b) TTIP/O_2 plasma (p_{total} = 1 mTorr, P_{MW} = 800 W, $V_{substrate}$= floating). Error bars correspond to standard deviation.

Growth rate is affected by several factors including the following two that have been deemed predominant:

- material etching achieved by atomic oxygen (as confirmed by OES: detection of peaks corresponding to excited OH and CO_2^+), as well as by atomic hydrogen,
- precursor dilution: quantity of precursor monomer injected into the reactor decreases as O_2 proportion in the gas mixture increases, thus less material is available for deposition.

It is remarkable that the deposition rate of both $ZrO_xC_yH_z$ and $TiO_xC_yH_z$ films evolved in the same manner (Figure III-7). Two regimes can be distinguished: an approximately constant deposition rate at low proportions of O_2 in the gas mixture (0-50%), and a consistent decrease of the deposition rate as O_2 content is further increased. During the PECVD process in question, the deposition and etching of the material are in competition. At first, deposition is favoured despite the constant dilution of the precursor. Then, as O_2 proportion surpasses 50%, the combined effect of etching and dilution prevail, and the deposition rate decreases.

Relatively small, but constant difference was observed when comparing of absolute values of growth rates between films deposited in ZTB plasma and TTIP plasma. Higher growth rates for ZTB plasmas might be partially explained by the difference in the quantity of material available for deposition, i.e. a higher number of carbon and hydrogen atoms present in a ZTB molecule (16 C and 36 H) compared to a TTIP molecule (12 C and 28 H).

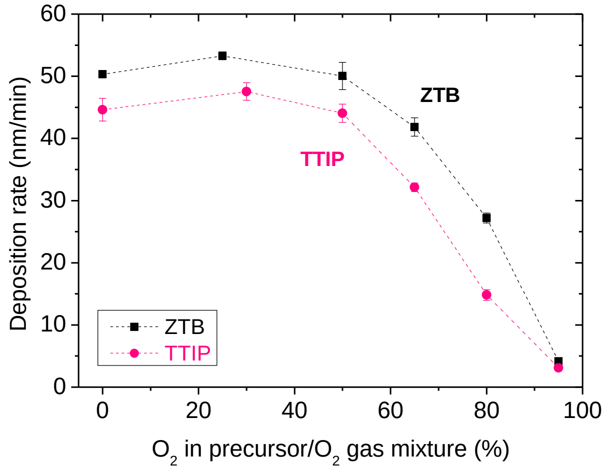

Figure III-7: Deposition rate of thin films deposited at different gas mixture ratios in ZTB/O_2 and TTIP/O_2 plasma (p_{total} = 1 mTorr, P_{MW} = 800 W, $V_{substrate}$ = floating). Error bars correspond to standard deviation.

III.3 Thin film chemical composition and bonding

III.3.1 Chemical composition

Thin films deposited at different metalorganic precursor/O_2 gas mixtures have been analysed by XPS to investigate their chemical composition. The XPS measurements were performed on as-deposited films after their exposure to air, without executing surface cleaning by argon ion etching, thus the quantity of carbon and oxygen atoms detected in the films may be over-estimated. Another detail to keep in mind is that XPS analysis does not deliver absolute values but provides relative chemical composition expressed in atomic percentages.

ZTB

Figure III-8 shows carbon, oxygen and zirconium atomic fraction in thin film as a function of O_2 gas proportion in the ZTB/O_2 gas mixture. In general, atomic percentage of carbon decreased, while that of zirconium and oxygen increased. At first, atomic composition changed slowly and evolved more abruptly after 80% of O_2 was added to the gas mixture. If we disregard hydrogen atomic content in the films, the stoichiometry, derived from XPS measurements, changed from $ZrO_{2.9}C_{4.8}$ in pure ZTB plasma to $ZrO_{1.9}C_{0.8}$ in highly oxidised plasma (95% of O_2 in the gas mixture).

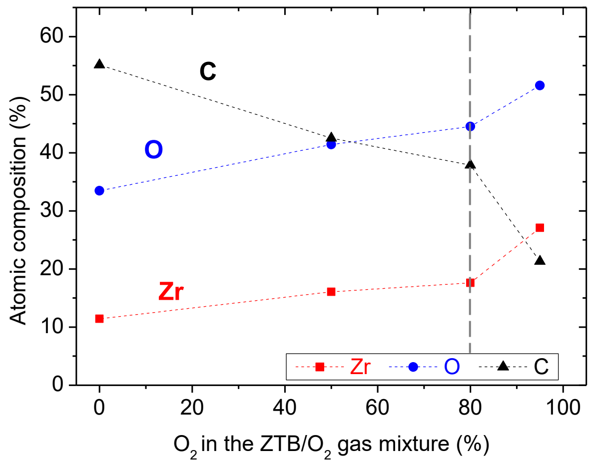

Figure III-8: Atomic composition of thin films deposited in ZTB/O_2 plasma (p_{total} = 1 mTorr, P_{MW} = 800 W, $V_{substrate}$ = floating) as a function of O_2 proportion in the gas mixture.

TTIP

XPS analysis of thin films deposited in TTIP/O_2 plasma at different gas mixture ratios yields the atomic composition in carbon, oxygen and titanium shown in Figure III-9.

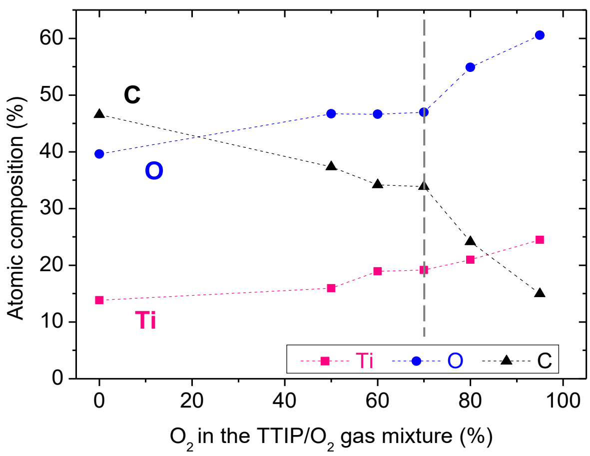

Figure III-9: Atomic composition of thin films deposited in TTIP/O_2 plasma (p_{total} = 1 mTorr, P_{MW} = 800 W, $V_{substrate}$ = floating) as a function of O_2 proportion in the gas mixture.

Generally, the films become deficient in carbon atoms as O_2 gas is added to the gas mixture. The number of C atoms per one Zr atom decreases from 3.4 to 0.6 as proportion of O_2 gas in the gas mixture increases from 0% to 95%. Atomic composition in oxygen and titanium increases as gas mixture becomes highly oxidised. A particular point in the evolution of the chemical composition can be identified at 70% O_2/30% TTIP, when the atomic composition starts changing at a higher rate than before it.

III.3.1.1 Evolution of thin film chemical composition: ZTB vs TTIP

Chemical composition of thin films evolves with changes in the precursor/O_2 gas mixture: from highly organic thin films in pure precursor plasma to almost inorganic coatings in predominately O_2 plasma. Figure III-10 shows the evolution of carbon and oxygen atomic content relative to the metal atom. The change in film composition is primarily attributed to decrease in carbon available for deposition due to precursor dilution and the etching of hydrocarbon species by atomic oxygen. The presence of volatile carbon-oxide species has been confirmed by OES (Chapter III.1.1, p.71). Data obtained by XPS analysis is summarised in Table III-4.

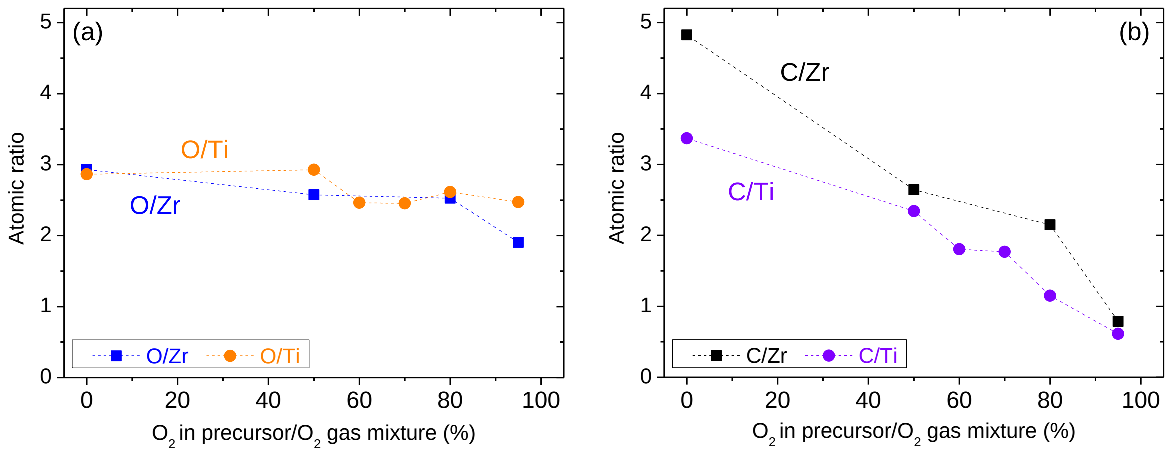

Figure III-10: Evolution of (a) O/Zr and O/Ti, (b) C/Zr and C/Ti atomic ratios in thin films deposited at different gas mixtures in ZTB/O_2 and TTIP/O_2 plasma (p_{total} = 1 mTorr, P_{MW} = 800 W, $V_{substrate}$ = floating).

Table III-4: Chemical composition and atomic ratios corresponding to films deposited in ZTB/O_2 and TTIP/O_2 plasma (p_{total} = 1 mTorr, P_{MW} = 800 W, $V_{substrate}$ = floating). Hydrogen atomic concentration is disregarded.

O_2 in plasma gas mixture (%)	**Atomic composition (%)**			**Atomic ratio**	
	O	**C**	**M***	**O/M***	**C/M***
			ZTB / O_2 plasma		
0	33.5	55.1	11.4	2.9	4.8
50	41.4	42.5	16.1	2.6	2.6
80	44.5	37.9	17.6	2.5	2.1
95	51.6	21.3	27.1	1.9	0.8
			TTIP / O_2 plasma		
0	39.6	46.6	13.8	2.9	3.4
50	46.7	37.4	15.9	2.9	2.3
80	54.9	24.1	21.0	2.6	1.1
95	60.5	15.0	24.5	2.5	0.6

M corresponds to Zr and Ti for ZTB and TTIP related data, respectively.

We observed a difference in the chemical composition of precursor molecules (Table III-5) and thin films deposited in pure precursor plasmas. Carbon atomic percentage equals 76.2% in ZTB and 70.6% in TTIP molecule, whereas concentration of carbon in thin films deposited in pure ZTB and TTIP plasmas equals 55.1% and 46.6%, respectively. The difference can be primarily explained by the formation of volatile C_xH_y species. Volatile species such as CH_4 and C_2H_2 have been detected in 100% ZTB plasma by in situ FTIR spectroscopy [12].

Table III-5: Chemical composition and atomic ratios corresponding to ZTB and TTIP molecules. Hydrogen atomic concentration is disregarded.

Molecule	Atomic composition (%)			Atomic ratio	
	O	C	M*	O/M*	C/M*
ZTB	19.0	76.2	4.8	4	16
TTIP	23.5	70.6	5.9	4	12

**M corresponds to Zr and Ti for ZTB and TTIP related data, respectively.*

In the evolution of the film composition, we can observe a particular point at which the rate of change noticeably increases (Figure III-8, Figure III-9, p.79-79). This occurs at a higher O_2 proportion in the gas mixture for films deposited in ZTB/O_2 plasma (at ≥80% of O_2) compared to films formed in TTIP/O_2 plasma (at ≥70 and <80% O_2). An increase of the rate of change has been observed in films deposited in TEOS/O_2 plasmas as well [1], [3]. Figure III-11 shows chemical composition of films synthesised in ZTB and TEOS plasmas in the same MMP-ECR reactor.

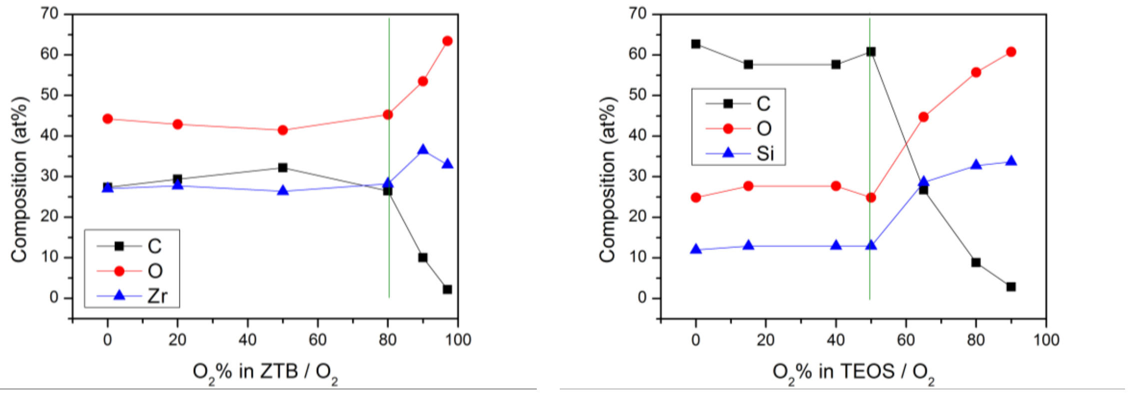

Figure III-11: Atomic composition of thin films deposited in ZTB/O_2 and TEOS/O_2 MMP-ECR plasma ($p_{total} \approx 1$ mTorr, $V_{substrate}$ = floating) (adapted from [11] and [3], respectively).

For TEOS, the change occurs at 50% O_2 in the gas mixture. TEOS molecule has a similar structure as ZTB and TTIP, however, it also has a lower number of carbon and hydrogen atoms:

$$\begin{aligned} ZTB &\rightarrow \quad ZrO_4C_{16}H_{36} \\ TTIP &\rightarrow \quad TiO_4C_{12}H_{28} \\ TEOS &\rightarrow \quad SiO_4C_8H_{20} \end{aligned}$$

The number of C atoms per O atoms present in the gas mixture might play a role in triggering a (faster) decrease of carbon at.% in the films.

III.3.2 Thin film chemical bonding

The following subchapter focuses on infrared spectra of thin films deposited in ZTB/O_2 and TTIP/O_2 plasmas at constant pressure of 1 mTorr, MW power of 800 W and at floating potential. FTIR spectroscopy is employed to study changes in chemical bonding in thin films as a function of the proportion of O_2 gas in the precursor/O_2 gas mixture. First, tentative assignation of the peaks appearing in FTIR spectra is presented. The IR bands appearing in the spectra are complex and may result from numerous overlapping peaks. Thus, we list several bonds and the corresponding chemical environments which may contribute to the IR bands in question. Secondly, we focus on the IR spectrum evolution as the precursor/O_2 gas mixture changes.

III.3.2.1 Identification of FTIR spectra

ZTB

Figure III-13 shows an FTIR spectrum corresponding to a thin film deposited in 50% ZTB/50% O_2 plasma (see Annex of this work for detailed image of the spectrum). Peaks appearing in the spectrum were assigned to C-H, O-H, C-O, C=O, C-C, C=C and Zr-O bond vibrations in various structural environments. Four wide and complex bands were observed in 4000-400 cm^{-1} IR range.

3750-2750 cm^{-1} region

Wide band in 3750-2750 cm^{-1} region was formed by overlapping peaks corresponding to stretching vibrations of **O-H** and **C-H** bonds. The part of the band originating from O-H bond vibrations was assigned to two different structural environments:

- peaks identified at 3688, 3670, 3649 cm^{-1} were assigned to O-H bond stretching in a bridged configuration [176]–[178] schematically presented in Figure III-12;

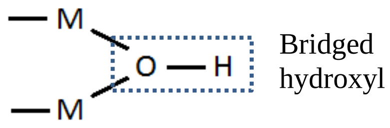

Figure III-12: Structural presentation of a bridged hydroxyl (M - metal atom).

- in the region between 3600 and 2750 cm^{-1}, the band was created by overlapping of peaks originating from O-H bond vibration in H-bonded and non-H bonded absorbed H_2O [177]; additionally.

Peaks observed at 2966, 2931, 2911, 2872, 2838 cm^{-1} were assigned to C-H bond asymmetric and symmetric stretching vibrations in CH_3, CH_2 and CH environments. These peaks have been largely evidenced in literature on metalorganic and organosilicon thin films [3], [10], [12], [69], [179], [180].

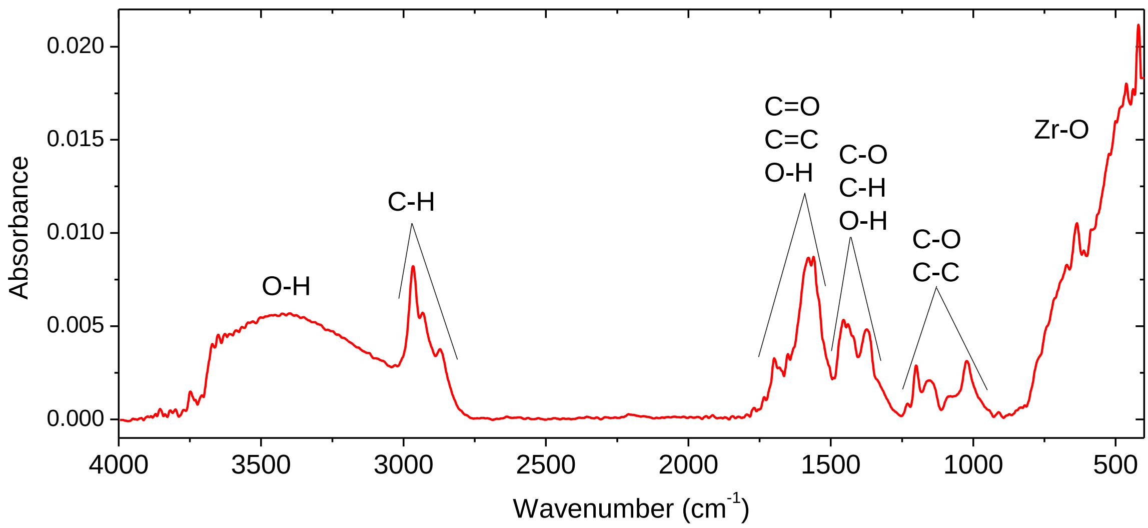

Figure III-13: FTIR spectrum of thin film deposited in 50% ZTB/50% O_2 plasma (p_{total} = 1 mTorr, P_{MW} = 800 W, $V_{substrate}$ = floating).

1800-1250 cm^{-1} region

In 1800-1250 cm^{-1} range, numerous peaks overlap and create a wide band that is challenging to analyse. We have divided the band into four wide peaks centred at 1699, 1577, 1436, 1374 cm^{-1} and a shoulder at 1315 cm^{-1}. The peak at 1699 cm^{-1} has been assigned to **C=O** bond stretching in an environment similar in structure to an ester, ketone, aldehyde or carbonate [12], [70], [181]. The examples of these chemical structures are presented in Figure III-14 and Figure III-15. Large peak centred at 1577 cm^{-1} is primarily assigned to **C=O** stretching in carbonate-like and formate-like structures (Figure III-14) reported in studies on carbon CO, CO_2 and H_2 adsorption on zirconia polymorphs [182]–[185]. The **O-H** bending vibration in absorbed H_2O may also contribute to this peak as well as **C=C** stretching in an environment similar to aromatic hydrocarbons and/or alkenes (Figure III-16) [181].

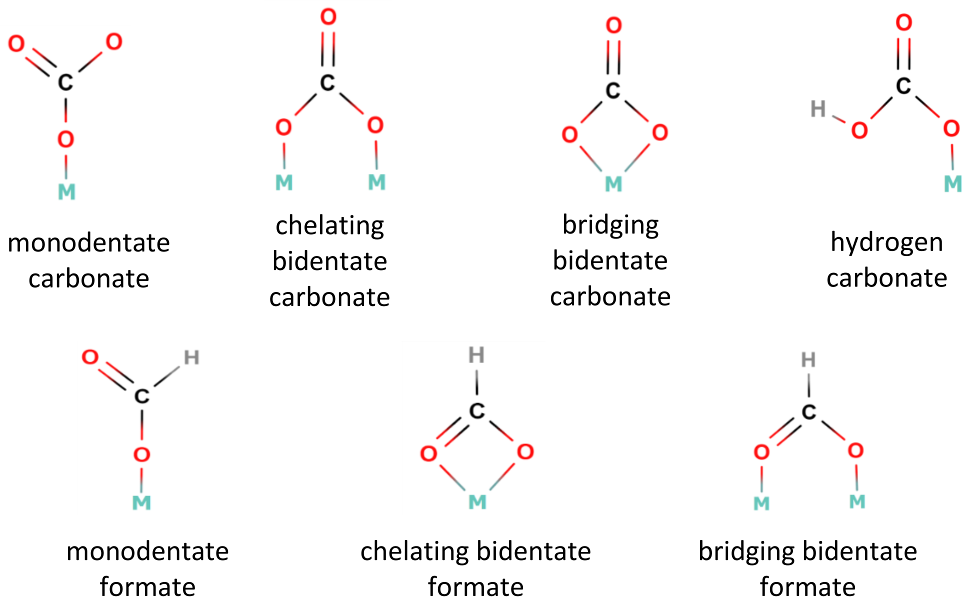

Figure III-14: Different carbonate and formate structures bonded to metal atoms (M – metal atom)(adapted from [182], [186]*).*

Peaks centred at 1436, 1374 and a shoulder at 1315 cm^{-1} have been assigned to **C-O** vibration in carbonate- and formate-like environments [ref]. Peaks corresponding to **C-H** bending in structures similar to alkanes/aldehydes/ketones/formates and **O-H** bending vibration might be observed in this IR region [50], [70], [73], [182], [183]. In FTIR spectra of liquid ZTB [11], [150], as well as in ZTB molecule synthetic spectra calculated by DFT (Chapter II.4.1, p.49), peaks appearing in 1471-1359 cm^{-1} range have been assigned to C-H bending vibrations, thus it is reasonable to expect that C-H bending vibration also contributes to peaks in this IR region of examined thin film FTIR spectra.

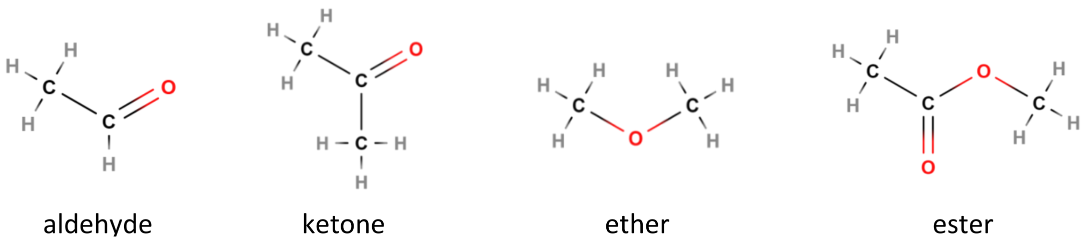

Figure III-15: Structural formula examples of an aldehyde, a ketone, an ether and an ester compound.

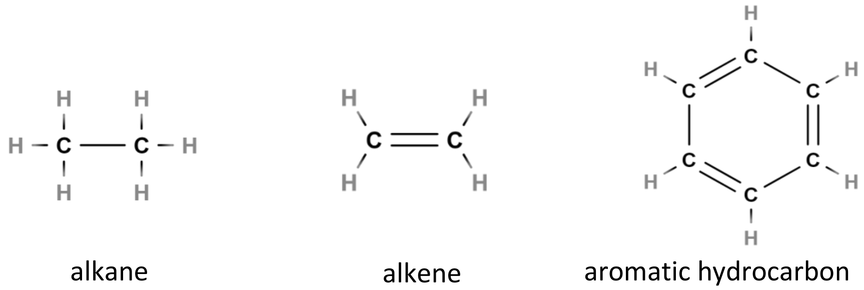

Figure III-16: Examples of hydrocarbon compounds structural formulas: an alkane, an alkene and an aromatic.

1250-900 cm^{-1} region

Four peaks centred at 1230, 1200, 1152 and 1024 cm^{-1} appear in the 1250-900 cm^{-1} region. In the synthetic IR spectrum of a ZTB molecule, peak at 1204 cm^{-1} corresponds principally to C-C stretching and C-C-C bending, peak at 1164 cm^{-1} corresponds to C-O stretching and C-C-C bending, and peak at 996 cm^{-1} corresponds to C-O and Zr-O stretching (Chapter II.4.1, p.49). In the FTIR spectrum of liquid ZTB, peaks at ~1230 and ~1188 cm^{-1} have been assigned to C-C stretching, while the peak at ~1000 cm^{-1} has been assigned to C-O stretching [11], [150]. Analogously, we assigned the peaks observed in the 1250-900 cm^{-1} IR region of thin film FTIR spectra to **C-O** and **C-C** vibrations in Zr-alkoxides (Figure III-17) and in environments similar to ethers, esters and alcohols. C-O bond stretching in carbonate structures bonded to Zr atoms may also contribute to peaks at 1152 and 1024 cm^{-1} [187].

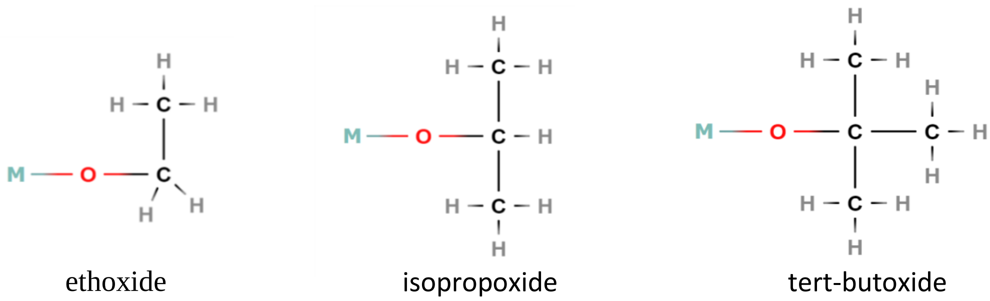

Figure III-17: Different alkoxy groups bonded to a metal atom: an ethoxide, an isopropoxide and a tert-butoxide (M – metal atom).

900-400 cm^{-1} region

In the 900-400 cm^{-1} region of IR radiation, several peaks overlap and form a wide band that corresponds mainly to **Zr-O** bond vibrations. The broadness of this band may be attributed to the amorphous nature of the films and the presence of polycrystalline phases [188]. In the FTIR studies performed on thin films deposited by different methods (PECVD, CSD), peaks corresponding to monoclinic [70], [112], [189], [190] and tetragonal [70], [112],

[190] crystalline structures have been identified (Table III-6, p.88). It is possible that in the films obtained in our study, small fractions of monoclinic and tetragonal are present in the predominately amorphous phase. Additionally, several authors have reported the presence of peaks at 480, 608, 650 and 825 cm^{-1} and assigned them to C=O vibration in O-C=O structure [73], [191].

TTIP

FTIR spectrum of thin film deposited in 50% TTIP/50% O_2 plasma is presented in Figure III-18 (see Annex of this work for enlarged image of the spectrum). The peaks in the spectrum have been assigned to vibrations of C-H, O-H, C-O, C=O, C-C, C=C and Ti-O bonds. In the following analysis, the spectrum is divided into four regions.

3750-2750 cm^{-1} region

In this IR region various peaks overlap, corresponding to O-H and C-H bond stretching vibrations. The wide band, centred at 3330 cm^{-1}, is characteristic of O-H bond vibrations in H-bonded and non H-bonded H_2O [177], [178]. Peaks appearing at 3689, 3675 and 3655 cm^{-1} were assigned to bridged OH [177], [178], [192]. Peaks identified at 2969, 2932, 2909, 2870, 2843 cm^{-1} originate from the stretching vibrations of C-H bond in $CH_{x=1,2,3}$ [181].

1800-1250 cm^{-1} region

In the 1800-1250 cm^{-1} region, a complex band appears. This band was divided into five peaks centred at 1676, 1558, 1450, 1372 and 1330 cm^{-1}. 1676 cm^{-1} peak was attributed to **C=O** bond stretching in an environment like carbonate, ester, ketone and aldehyde and to **C=C** bond stretching in alkene-like structures. Large peak at 1558 cm^{-1} is principally the result of C=O stretching in carbonate and formate structures bonded to Ti atoms [179], [193], O-H bending in absorbed H_2O and **C=C** stretching in environments similar to aromatic hydrocarbons and alkenes [181]. The wide band that includes 1450, 1372 and 1330 cm^{-1} peaks, was assigned to vibrations of C-O bond in carbonate and formate structures bonded to Ti atoms [179], [193], [194]. C-H bonds might as well contribute to this band. In this same region, peaks in the IR spectra of liquid TTIP and DFT spectra of a TTIP molecule have been assigned to C-H bond vibrations (Chapter II.4.2, p.50).

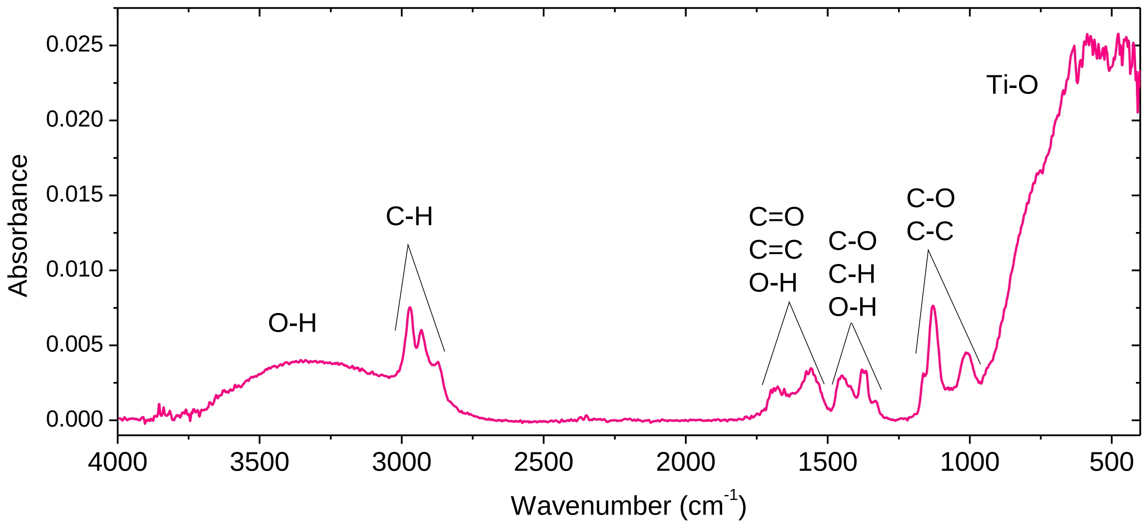

Figure III-18: FTIR spectrum of thin film deposited in 50% TTIP/50% O_2 plasma (p_{total} = 1 mTorr, P_{MW} = 800 W, $V_{substrate}$ = floating).

1250-960 cm^{-1} region

In the 1250-960 cm^{-1} range, three peaks have been identified: 1163, 1130, 1011 cm^{-1}. Peaks corresponding to C-O vibration in an environment such as ethers, alcohols, esters and carbonates have been observed in this IR region [181]. On the other hand, three distinctive peaks have been observed in this IR region in the spectra of liquid TTIP [151]: 1161, 1115, 988 cm-1, and synthetic spectra of TTIP molecule: 1141, 1108, 996 cm-1 (Chapter II.4.2, p.50). These peaks have been assigned to vibrations of C-O, C-C and C-H and Ti-O bonds. In several studies of thin film FTIR spectra, peaks detected in this range have been assigned to Ti-O-C vibration in alkoxy groups. Based on the above-mentioned literature findings and the calculated IR spectra of TTIP molecule, the peaks appearing in this region were primarily attributed to **C-O** bond stretching in titanium alkoxides and **C-C** bond vibration in alkane-like environment.

960-400 cm^{-1} region

The band spreading over 960-400 cm^{-1} was primarily assigned to Ti-O bond vibration. The broadness of Ti-O peak may be a sign of the amorphous film nature and of the Ti-O bonds in environment rich in carbon atoms and/or hydroxyl groups [188]. Nevertheless, crystalline phases may also contribute to this large band. Peaks corresponding to anatase and rutile phase have been identified in various studies of thin films deposited by CVD, PECVD, sol-gel and spray pyrolysis (see peak positions and corresponding references in Table III-6).

Table III-6: FTIR peaks assigned to Zr-O and Ti-O crystalline phases: literature review.

Assignation		**Peak position (cm^{-1})**	**References**
Zr-O	monoclinic	407, 409, 440, 490, 507, 574, 583, 629, 772	[70], [112], [189], [190]
	tetragonal	432, 436, 466, 467, 584	[70], [112], [190]
Ti-O	anatase	435, 436, 440, 450, 640, 643, 748	[13], [76], [194]–[196]
	rutile	420, 423, 460, 496, 498, 500, 535, 608, 610, 678, 799	[13], [194]–[199]

III.3.2.2 Thin film FTIR spectra: ZTB vs TTIP

Figure III-19 shows a graphical comparison of FTIR spectra corresponding to thin films deposited in 50% ZTB/ 50% O_2 and 50% TTIP/50% O_2 plasmas.

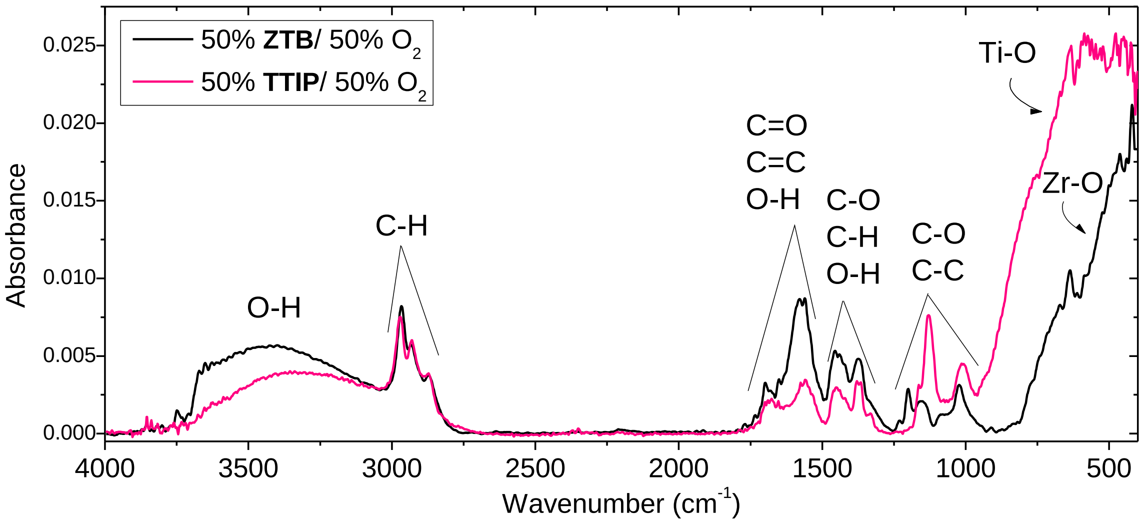

Figure III-19: FTIR spectra of thin films deposited in ZTB/O_2 and TTIP/O_2 plasmas (p_{total} = 1 mTorr, P_{MW} = 800 W, $V_{substrate}$ = floating). Absorbance: normalised by thin film thickness.

Four distinct bands were formed in both spectra. The band attributed to O-H and C-H bond vibrations extends over the same IR range (3750-2750 cm^{-1}) in both thin films deposited in ZTB and TTIP plasma. Position and form of the peaks corresponding to C-H stretching are almost identical. In the 960-400 cm^{-1} part of the spectra, peaks attributed to Zr-O and Ti-O bonds appeared. Peak positions and corresponding assignations are reported in Table III-7.

A complex band in 1750-1250 cm^{-1} region is displayed in more detail in Figure III-20. The band spreads over the same IR range in both spectra of $ZrO_xC_yH_z$ and $TiO_xC_yH_z$ films. This band was attributed mainly to C=O and C-O bonds in carbonate structures bonded to metal atoms: Zr or Ti. At first, we may notice small differences in peak forms and differences in peak height relative to other peaks in the same spectrum. Nevertheless, all four relatively wide peaks and one shoulder can be observed in spectra of both types of films.

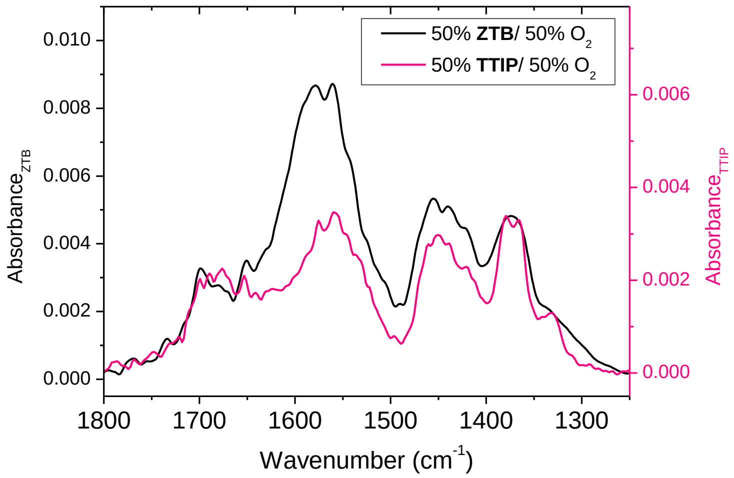

Figure III-20: Comparison of FTIR 1800-1250 cm^{-1} spectral region corresponding to thin films deposited in ZTB/O_2 and TTIP/O_2 plasmas (p_{total} = 1 mTorr, P_{MW} = 800 W, $V_{substrate}$ = floating). Absorbance: normalised by thin film thickness.

Table III-7: Identification of IR absorption peaks corresponding to thin films deposited in ZTB/O_2 and TTIP/O_2 plasma (p_{total} = 1 mTorr, P_{MW} = 800 W, $V_{substrate}$ = floating).

ZTB / O_2		**TTIP / O_2**	
Peak position (cm^{-1})	**Assignation**	**Peak position (cm^{-1})**	**Assignation**
3750-2750	O-H stretching in absorbed H_2O	3750-2750	O-H stretching in absorbed H_2O
3688, 3670, 3649	O-H stretching in Zr-OH	3689, 3675, 3655	O-H stretching in Ti-OH
2966, 2931, 2911, 2872, 2838	C-H stretching in CH_x	2969, 2932, 2909, 2870, 2843	C-H stretching in CH_x
1699	C=O stretching C=C stretching	1676	C=O stretching C=C stretching
1577	C=O stretching C=C stretching O-H bending	1558	C=O stretching C=C stretching O-H bending
1436, 1374, 1315	C-O stretching O-H bending C-H bending	1450, 1372, 1330	C-O stretching O-H bending C-H bending
1230, 1200, 1152	C-C and C-O in $ZrOC(C_xH_y)$	1163, 1130	C-C and C-O $TiOC(C_xH_y)$
1024	C-O in $ZrOC(C_xH_y)$	1011	C-O in $ZrOC(C_xH_y)$
900-400	Zr-O	960-400	Ti-O

A noticeable difference between the spectra in question was found in the 1250-900 cm^{-1} IR region, as it can be seen in Figure III-21(a). Four peaks are observed in $TiO_xC_yH_z$ films, while five peaks appear in $ZrO_xC_yH_z$ films. These peaks were assigned to C-O and C-C bond vibrations in metal alkoxide structures. The peaks at 1230 cm^{-1} and 1200 cm^{-1} in $ZrO_xC_yH_z$ look similar in form and relative intensities to 1163 cm^{-1} and 1130 cm^{-1} peaks in $TiO_xC_yH_z$.

However, they are shifted to higher wavenumbers by ~70 cm^{-1}. To further confirm the analogous assignations (C-O and C-C in $MOC(C_xH_y)$), we have looked into the FTIR signatures of liquid ZTB and TTIP [11], [151] and the theoretically built vibrational spectra (Chapter II.4, p.48). The observed shift appears in both synthetic spectra, and (Figure III-21(b)) in the spectra of liquid ZTB and TTIP as reported in Table III-8.

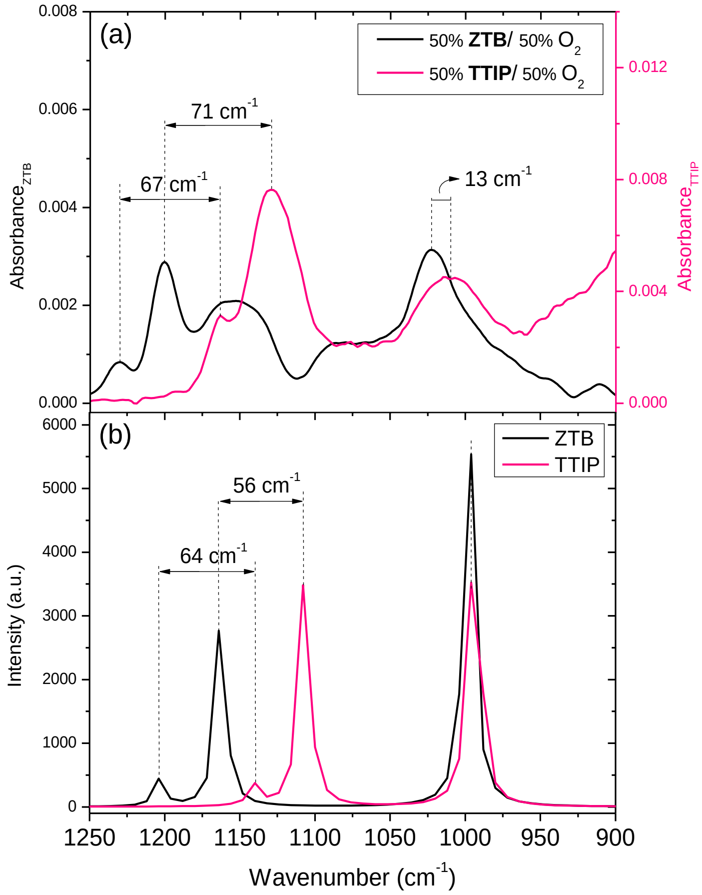

Figure III-21: Comparison of 1250-900 cm^{-1} spectral region corresponding to: (a) thin films deposited in ZTB/O_2 and $TTIP/O_2$ plasmas (p_{total} = 1 mTorr, P_{MW} = 800 W, $V_{substrate}$ = floating; absorbance: normalised by film thickness); (b) ZTB and TTIP molecules synthetic IR spectra obtained by DFT calculations.

Table III-8: Absorption peaks observed in the 1250-900 cm^{-1} region in FTIR spectra of liquid ZTB and TTIP [11], [151].

Wavenumber: $\tilde{\nu}$ (cm^{-1})		**$\Delta\tilde{\nu}$ (cm^{-1})**
ZTB_{liquid}	**$TTIP_{liquid}$**	
1229	1161	**68**
1188	1115	**73**
1000	988	**12**

III.3.2.3 Evolution of thin film FTIR spectra as a function of gas mixture composition: ZTB vs TTIP

In the following text, we focus on evolution of thin film FTIR spectra with addition of O_2 to the precursor/O_2 gas mixture (see Figure III-22). To be able to compare the IR spectra of different films, the spectra were normalised by thin film thickness.

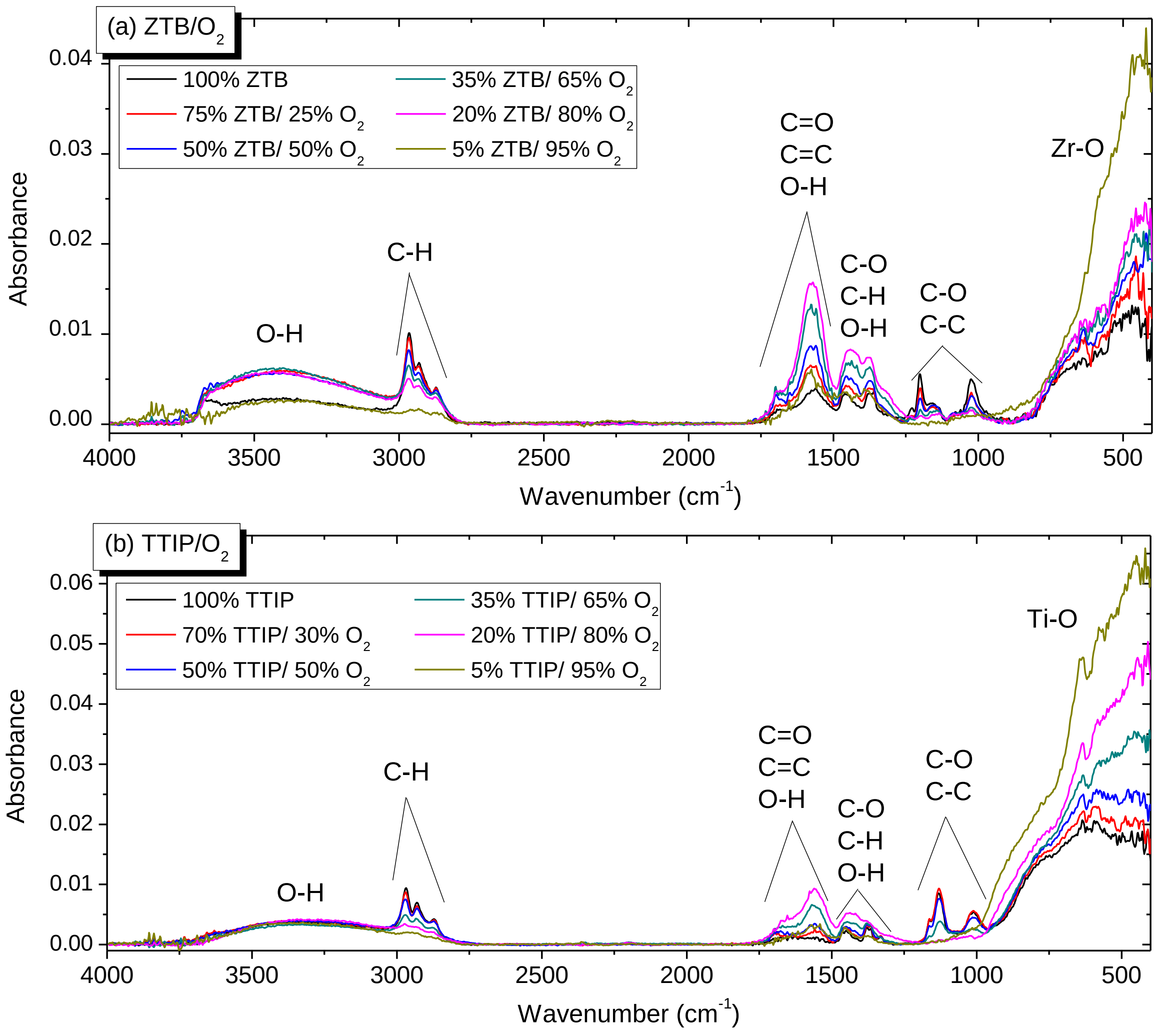

Figure III-22: FTIR spectra of thin films deposited at different O_2 proportion in ZTB/O_2 and TTIP/O_2 plasmas (p_{total} = 1 mTorr, P_{MW} = 800 W, $V_{substrate}$= floating). Absorbance: normalised by thin film thickness.

As it can be observed in the previously introduced identification of FTIR spectra, IR bands present in thin films deposited in ZTB/O_2 plasma were also present in films deposited in TTIP/O_2 plasma. Evolution of chemical bonding is analysed simultaneously for films deposited in ZTB and in TTIP plasmas. Furthermore, the FTIR spectra (4000-400 cm^{-1}) are divided into four zones to facilitate a more detailed analysis.

4000-2750 cm⁻¹ region

Figure III-23 shows the evolution of FTIR spectra in 4000-2750 cm^{-1} range. Top image corresponds to films deposited in ZTB/O_2 plasma, whereas the bottom image represents the spectra of films deposited in $TTIP/O_2$ plasma.

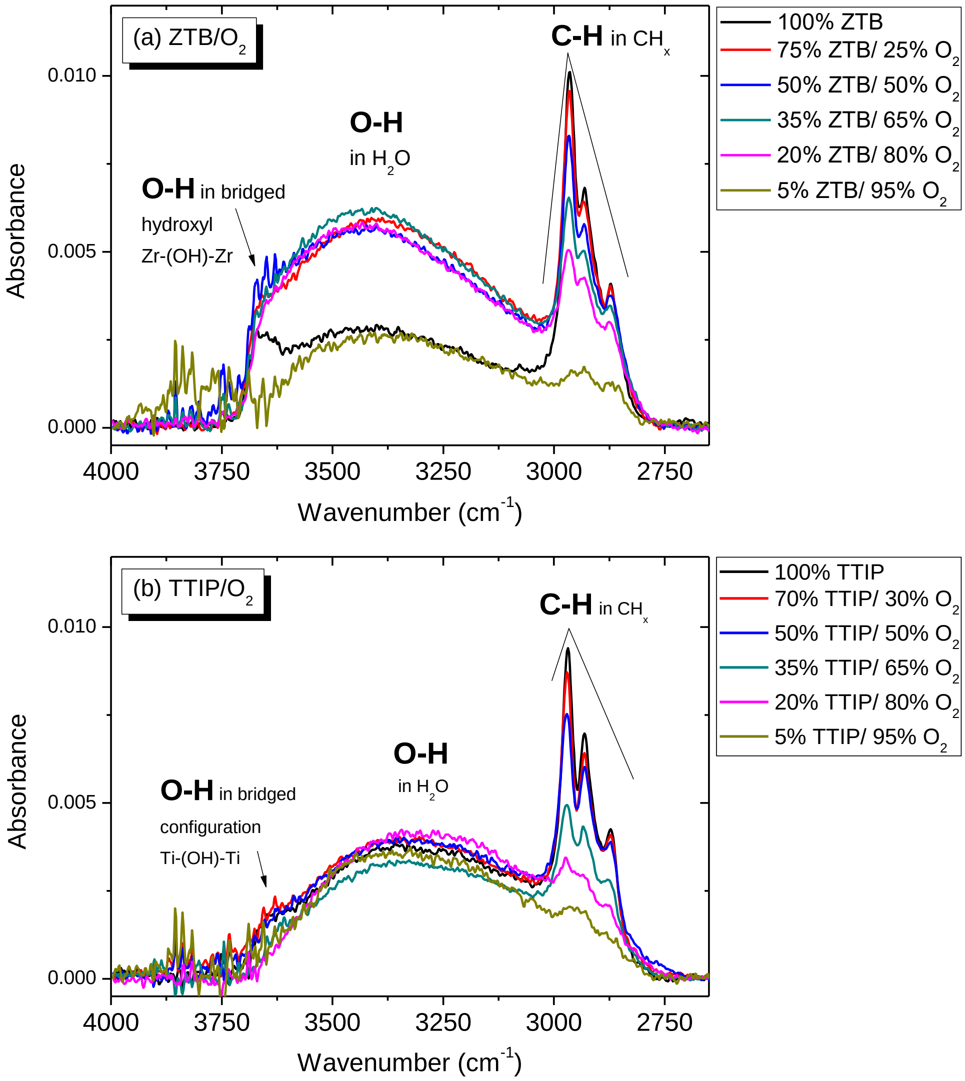

Figure III-23: FTIR spectra (3750-2750 cm^{-1}) of thin films deposited at different proportion of O_2 gas in a) ZTB/O_2 and b) $TTIP/O_2$ gas mixture (p_{total} = 1 mTorr, P_{MW} = 800 W, $V_{substrate}$= floating). Absorbance: normalised by thin film thickness.

An O-H stretching band appears in both $ZrO_xC_yH_z$ and $TiO_xC_yH_z$ films deposited in O_2-poor as well as in O_2-rich gas mixtures. Since this band appears even in films deposited in 100% precursor plasmas deficient in oxygen atoms, we suspect that principal contribution comes from O-H stretching in H_2O absorbed by films after their exposure to air. In some spectra distinct sharp peaks appear in 3900-3650 cm^{-1} region: those peaks originate from O-H stretching in H_2O vapour present in the FTIR measurement chamber.

C-H stretching band evolves in the same direction in both films deposited in ZTB and in TTIP plasmas. C-H stretching band is indicative of the amount of hydrocarbon incorporated in the films. As gas mixtures become rich in oxygen and deficient in precursor gas, the number of hydrocarbons in the films decreases. This observation is in accordance with XPS measurements that show a decrease in carbon atomic percentage (Table III-4, p.72), as well as with OES analysis that indicates a decrease in CH and H species concentration in the plasma phase (Chapter III, p.74). However, even at high O_2 proportion (95%), the band representing C-H bonding, although weak, is still present.

1800-1250 cm^{-1} region

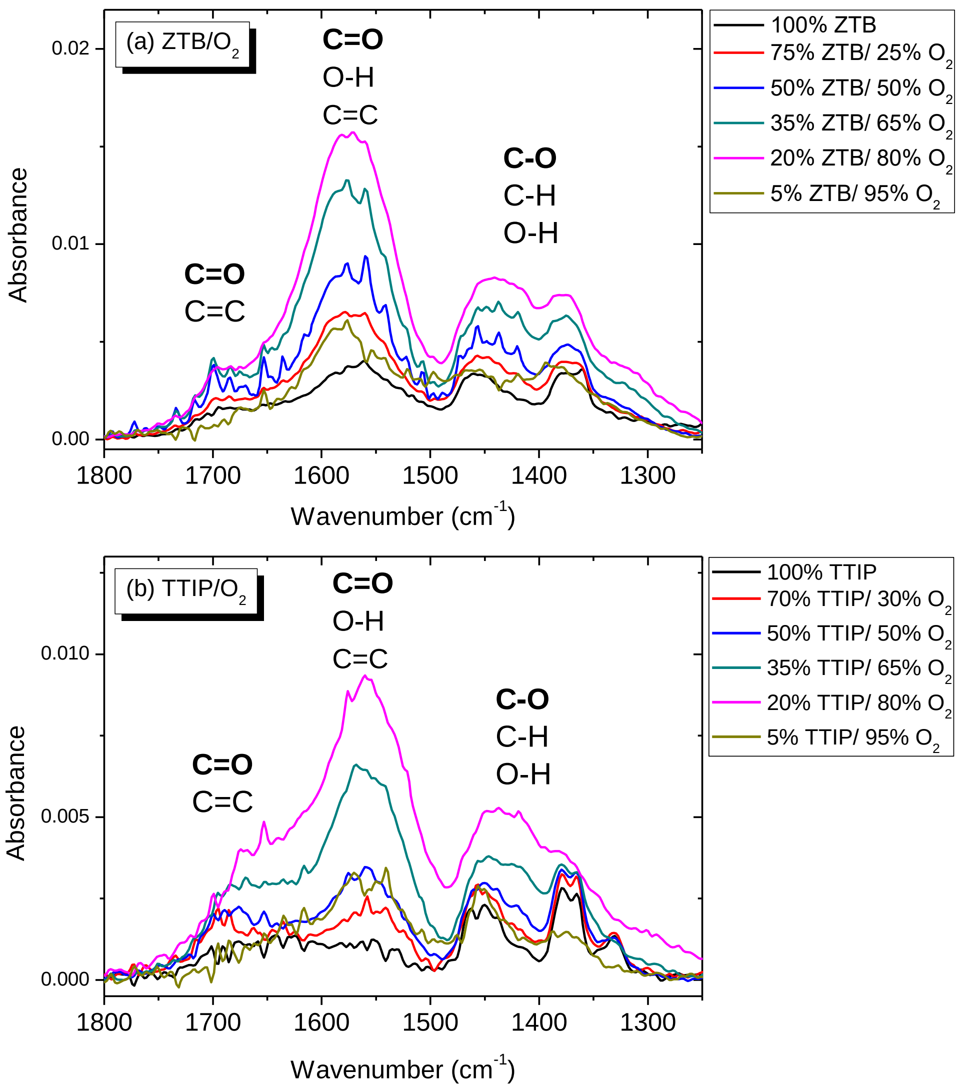

Figure III-24:FTIR spectra (1800-1250 cm^{-1}) of thin films deposited at different proportion of O_2 gas in a) ZTB/O_2 and b) TTIP/O_2 gas mixture (p_{total} = 1 mTorr, P_{MW} = 800 W, $V_{substrate}$= floating). Absorbance: normalised by thin film thickness.

A remarkable similarity is observed in the evolution of the 1800-1250 cm^{-1} band between films deposited in ZTB and in TTIP plasmas. The spectra are visible in Figure III-24 and the evolution of the band surface area with O_2 is presented in Figure III-25.

As O_2 gas proportion is increased in the precursor/O_2 gas mixture, the band absorbance increases to reach a maximum at ~80% of O_2. With further addition of O_2 to the gas mixture, from 80 to 95%, the absorbance decreases sharply. This behaviour implies that the major contribution to this band comes from C=O and C-O bonds in structural environments rich in oxygen atoms such as carbonates.

Carbonate "core" is composed of three oxygen atoms and one carbon atom: CO_3^{2-}. Evidently, oxygen atoms are needed to construct carbonate structures, therefore, with an increasing O_2 gas proportion in the gas mixture, the concentration of C-O and C=O bonds increases in the oxygen-atom rich environment in the films. At the same time, precursor, a source of carbon atoms, is diluted as O_2 is added to the gas mixture. The effect of dilution is far more prominent when O_2 proportion in the gas mixture increases from 80 to 95% than it is during the increase from 0 to 80%: O_2-to-precursor molecule ratio increases from 4 to 19, compared to an increase from 0 to 4, respectively. Thus, after achieving the maximum (at ~80% O_2), plasma becomes deficient in carbon atoms as we approach 95% of O_2 in the gas mixture, due to precursor dilution and the decreasing concentration of C=O and C-O bonds in the films. Noteworthy is the analogous behaviour of CO and CO_2 concentration in the plasma phase as indicated by OES analysis (Chapter III, p.74). Besides C=O and C-O bonds, C=C, O-H and C-H bonds may contribute to the band in this region as well.

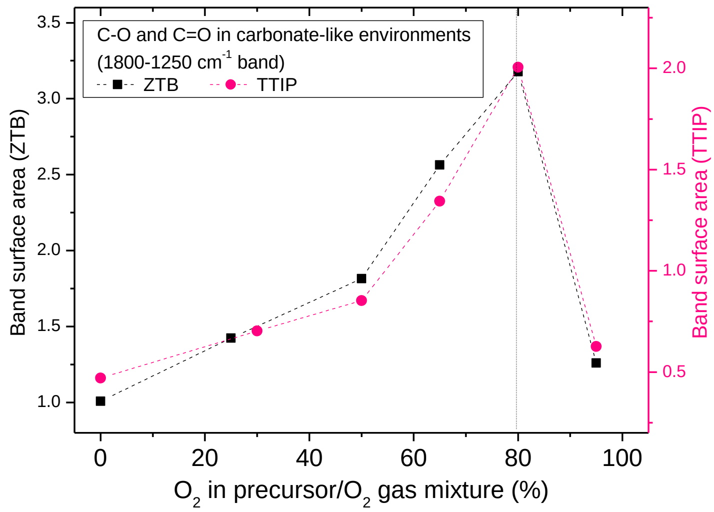

Figure III-25: Change in surface area of peaks observed in FTIR spectra of thin films deposited in ZTB/O_2 and TTIP/O_2 plasmas: 1800-1250 cm^{-1} band (primarily C-O and C=C in carbonate-like environment).

1250-960 cm^{-1} region

Figure III-26 shows FTIR spectra of (a) zirconium oxide and (b) titanium oxide films in 1250-950 cm^{-1} range. Peaks present in this range have been assigned to C-O and C-vibrations in metal alkoxide groups (M-O-C(C_xH_y), M: Zr or Ti atom). With oxygen gas addition, the peaks decrease in absorbance and become undetectable in O2-rich conditions (at 80% O_2 in TTIP and at 95% O_2 in ZTB). The evolution of the band surface area is plotted in Figure III-27.

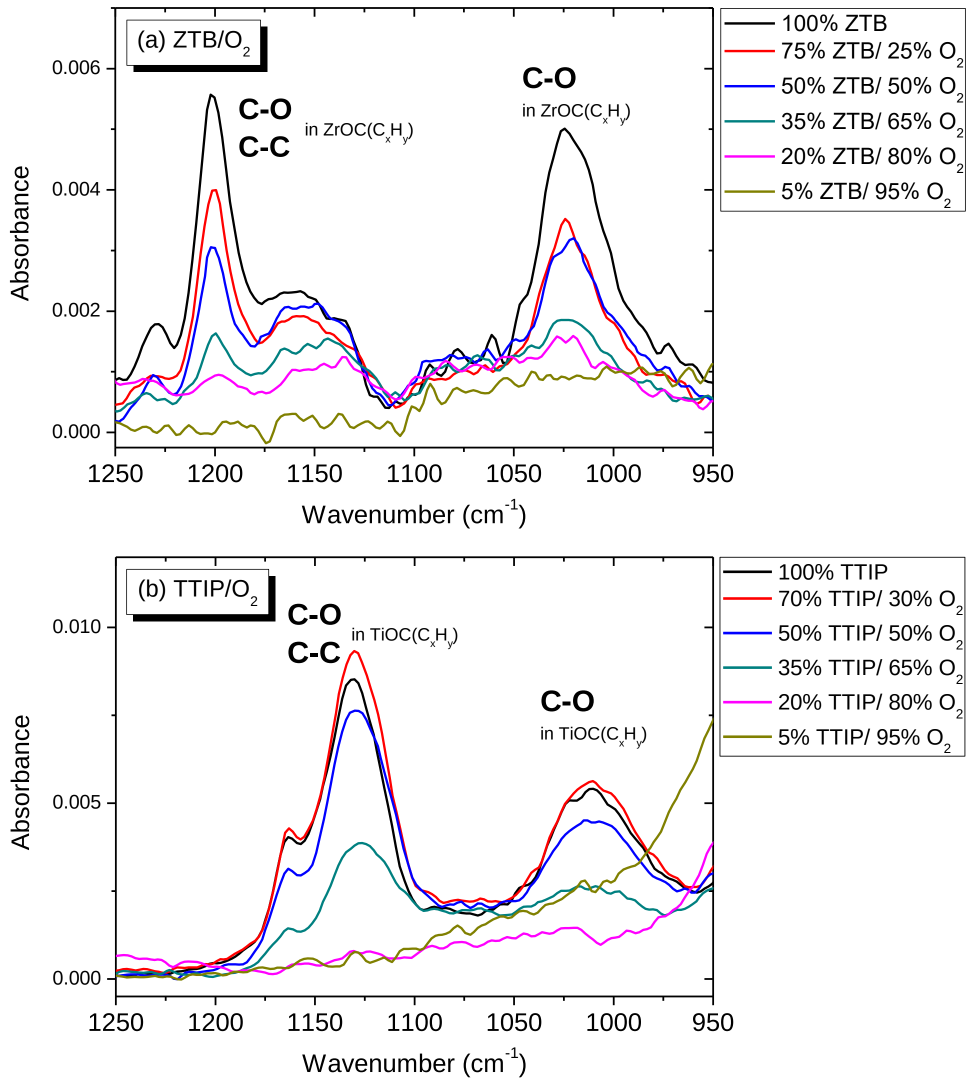

Figure III-26: FTIR spectra (1250-950 cm^{-1}) of thin films deposited at different proportion of O_2 gas in ZTB/O_2 and TTIP/O_2 gas mixture (p_{total} = 1 mTorr, P_{MW} = 800 W, $V_{substrate}$= floating). Absorbance: normalised by thin film thickness.

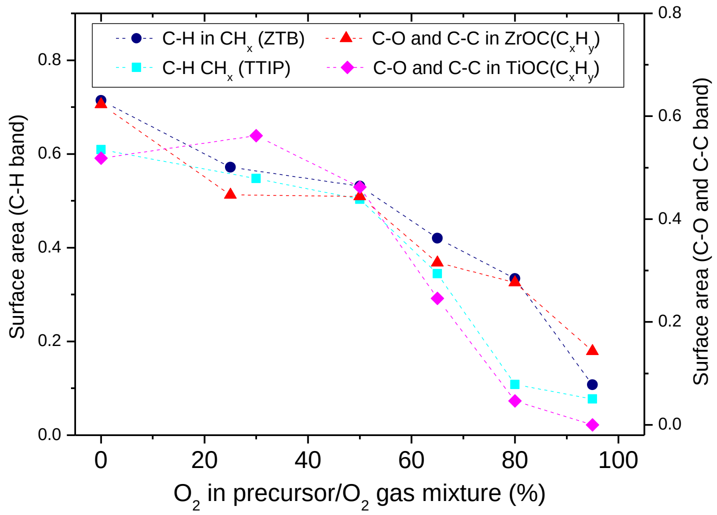

Figure III-27: Change in surface area of FTIR peaks corresponding to films deposited in ZTB/O$_2$ and TTIP/O$_2$ plasmas: 3050-2800 cm^{-1} band (C-H in CH$_x$); 1250-950 cm^{-1} band (C-O and C-C in metal alkoxide groups).

960-400 cm^{-1} region

The band observed in 960-400 cm^{-1} range in FTIR spectra of films deposited in ZTB and in TTIP plasmas results from vibrations of Zr-O and Ti-O bonds, respectively. With addition of O_2 gas to the gas mixture, the absorbance of this band increases. This indicates an increase in the concentration of Zr-O and Ti-O bonds in the films. FTIR observations agree with XPS measurements: carbon atomic % decreases and atomic % of Zr and O increase with addition of O_2 to plasma gas mixture.

III.3.3 Evolution of film chemical composition and chemical bonding: summary

The chemical composition and bonding of thin films deposited in ZTB and TTIP plasmas were studied as a function of O_2 gas proportion in the gas mixture. Both types of films exhibited similar behaviour. Overall, the carbon atomic percentage decreased, while that of oxygen and metal atoms (Zr or Ti) increased. Changes in these atomic fractions are mutually dependent, thus the observed evolution might result from the actual increase in deposition of the metal atoms and oxygen or the decrease in the deposition of carbon atoms. The former is improbable since a decrease in the growth rate was detected. Furthermore, the etching of carbon atoms was indicated by the OES study (e.g. presence of CO_2, CO in the plasma). These findings, coupled together, imply that the decrease in incorporation of carbon atoms into the film governs the change of the film chemical composition.

The changes in the film chemical composition agree with the changes observed in chemical bonding. The peaks corresponding to M-O bonds (M: Zr or Ti) increased in intensity with O_2 gas addition to the gas mixture. The decrease in carbon atomic fraction was evidenced in the decrease of C-H and C-C bonding. These bonds were replaced by C-O bonds organised in carbonate-like structures (carbonate "core": one C atom per 3 O atoms). When the gas mixture became very rich in oxygen gas (>80% O_2), the fraction of C-O bonds decreased due to the extreme dilution of the precursor, i.e. the deficiency of available carbon atoms.

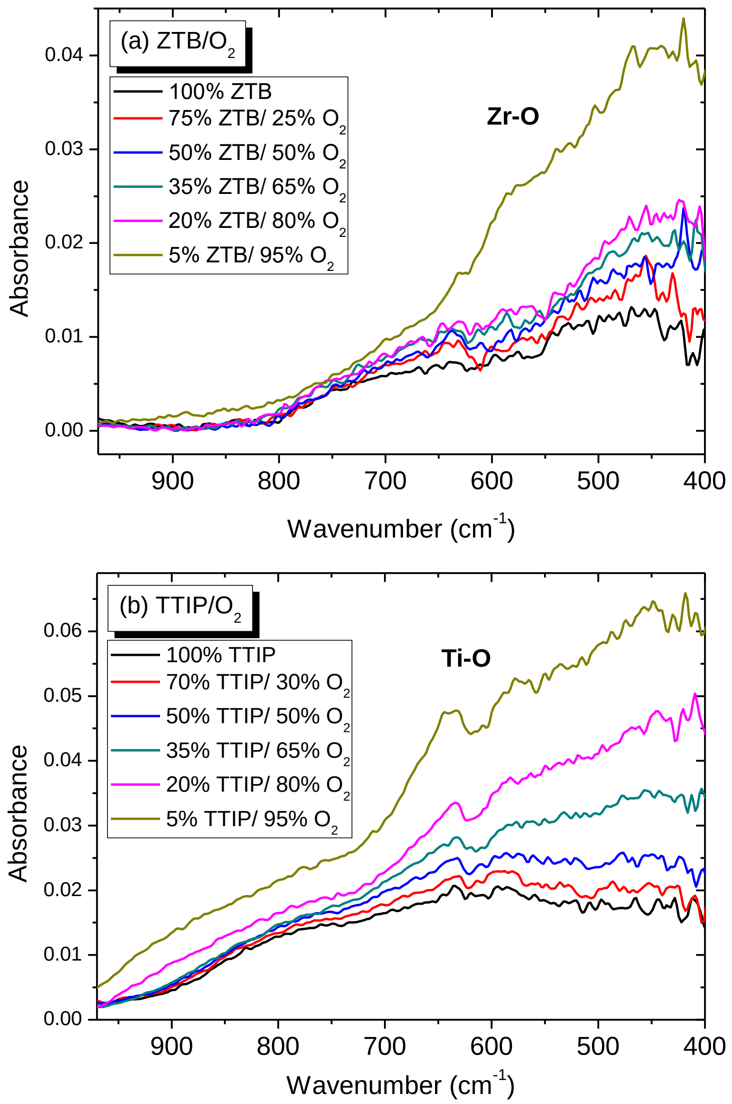

Figure III-28: FTIR spectra (950-400 cm^{-1}) of thin films deposited at different proportion of O_2 gas in a) ZTB/O_2 and b) TTIP/O_2 gas mixture (p_{total} = 1 mTorr, P_{MW} = 800 W, $V_{substrate}$= floating). Absorbance: normalised by thin film thickness.

III.4 Thin film morphology

The following text presents morphological and topographical features of films synthesised at different gas compositions. First, structural characteristics of films deposited in ZTB/O_2 and in TTIP/O_2 plasmas are exposed in a descriptive manner. This is followed by a comparative discussion of the morphological evolution of both types of films. All the examined films were in the 110-190 nm thickness range. SEM imaging has been used to study the surface and the cross-section morphology (direction: perpendicular to the substrate), while AFM has been employed to examine the film topography.

III.4.1 Evolution of morphological and topographical characteristics

ZTB

AFM images of thin films deposited at 0%, 50% and 95% of O_2 are shown in Figure III-29. This topographical study confirmed the increase of thin film surface roughness with O_2 proportion in the gas mixture (Table III-9). The roughness parameter R_a increased from 0.27 nm at 0% O_2, over 0.38 nm at 50% O_2 to 4.90 nm at 95% O_2. A more drastic difference was observed in the change of R_{max}: from 2.5 to 38 nm as O_2 increased from 0 to 95%, respectively. High surface roughness at 95% of O_2 was consistent with thin film columnar morphology observed by SEM.

Figure III-30 shows cross-sectional SEM micrographs of thin films deposited at different proportions of O_2 gas in ZTB/O_2 gas mixture. Thin films deposited at 0-80% of O_2 exhibited relatively uniform morphology over all the thickness without defined and organised features. We observed fine, randomly oriented, granular-like forms with diameters of a few nanometres throughout the film cross-sections. SEM images of films deposited at 50% and 80% of O_2 showed voids between the films and corresponding substrates. The films had possibly detached from the substrates during the cleavage procedure. This step was a part of sample preparation process for SEM imaging. Another cause of the detachment could have been film stress. To comment any further on the latter possibility, specific mechanical measurements of film extrinsic and intrinsic stresses would be necessary, and these were outside the scope of our research project. At 95% of O_2, columnar morphology had developed. The closely stacked columns, 10-40 nm in width, had grown perpendicular to the substrate surface. It appeared that the columns had grown directly from the interface with the substrate and that their width increased with height. As in previous conditions, the film consisted of small granular-like nano-formations that were, in this case, organised in columnar morphology.

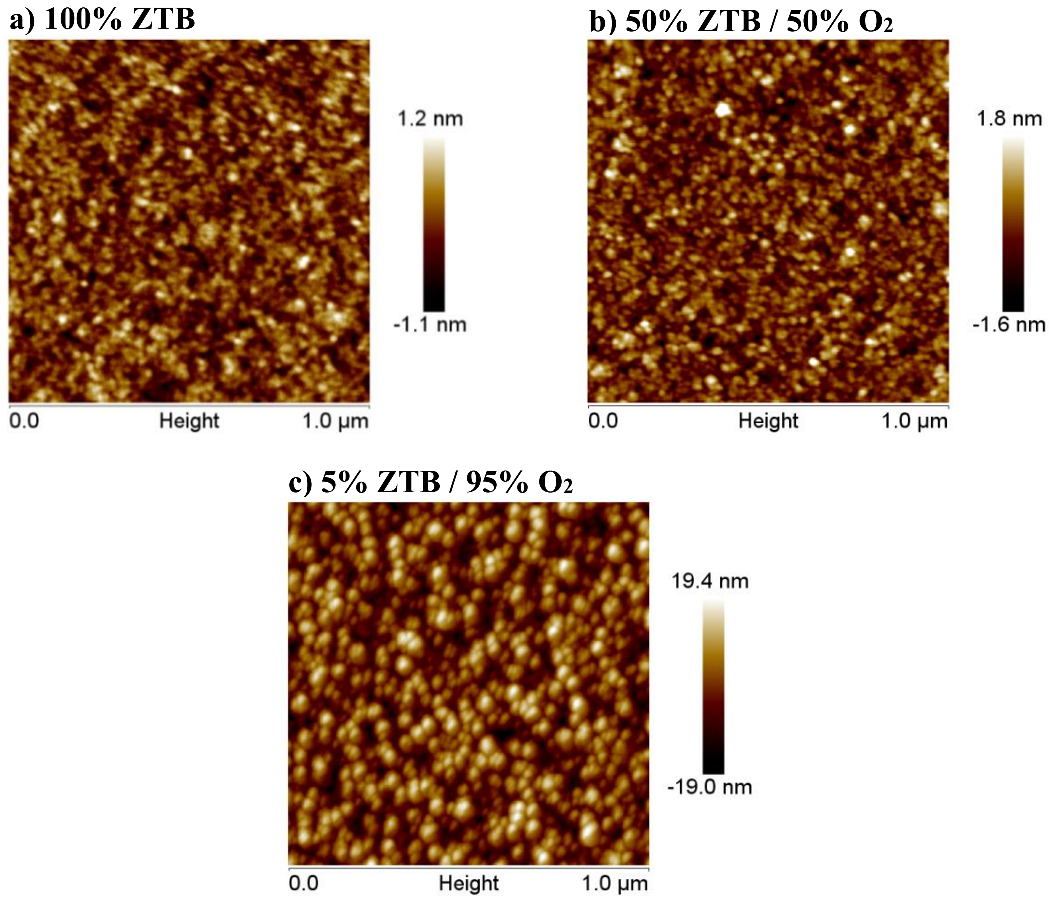

Figure III-29: AFM surface images of thin films grown in ZTB/O_2 plasma (p_{total} = 1 mTorr, P_{MW} = 800 W, $V_{substrate}$= floating): (a) 100% ZTB, (b) 50% ZTB/50% O_2, (c) 5% ZTB/95% O_2. Surface area measured: 1µm^2.

SEM imaging was employed to investigate film surface morphology, as can be seen in Figure III-31. Thin films deposited at 0-65% of O_2 do not exhibited particular surface structuration. The surfaces were formed by very fine, densely packed, grains. At 80% of O_2, it was possible to notice contours of what seemed to be an onset of columnar shapes observed from above, although it was hard to differentiate any defined features. At 95% of O_2, closely stacked and irregularly shaped structures form the surface. These structures correspond to columnar tops. Each top consisted of fine nanometric grains observed in other films as well. Most tops had diameters in the 20-40 nm range, which agreed with columnar widths observed in cross-sectional micrographs.

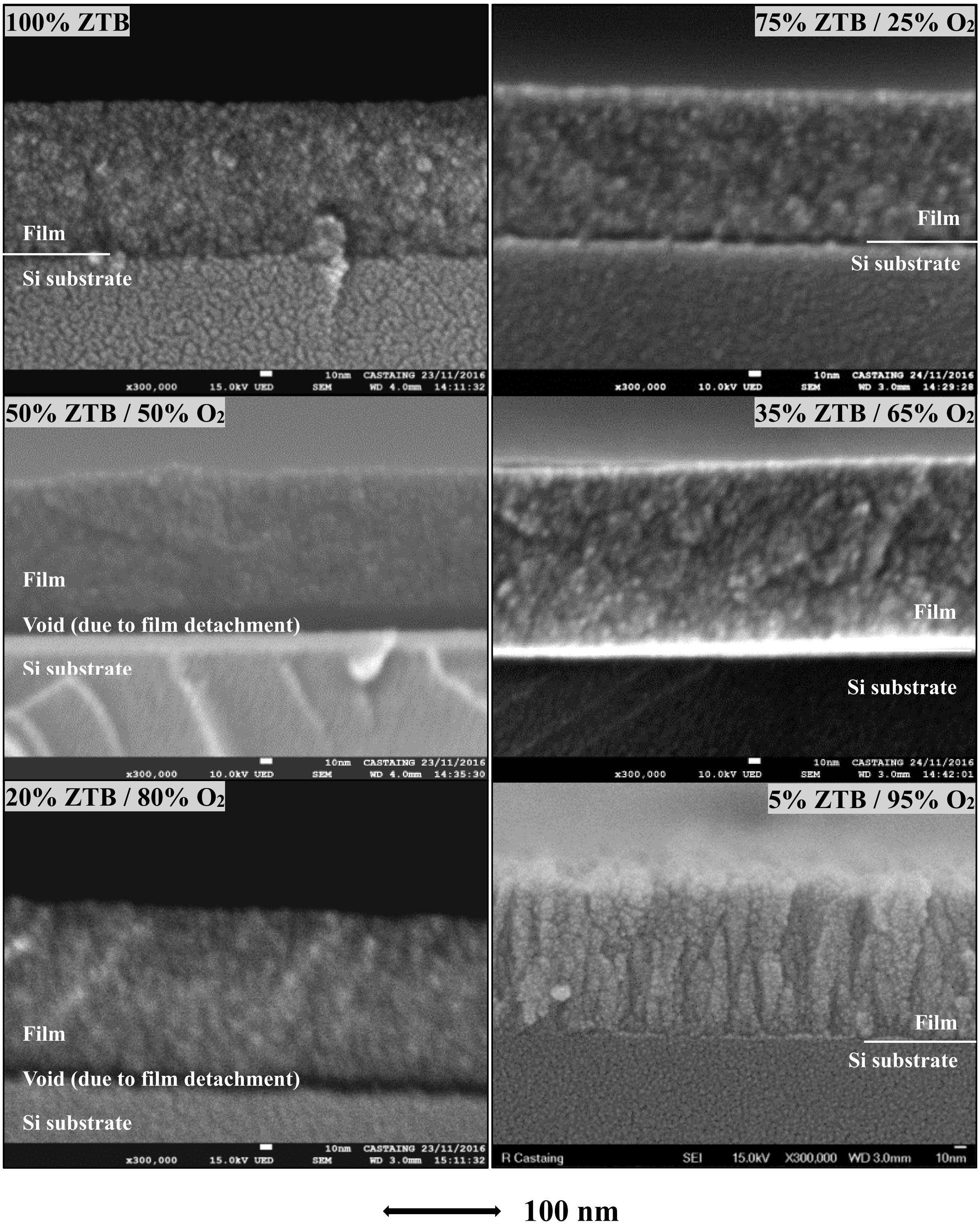

Figure III-30: SEM cross-sectional images of thin films deposited at different gas compositions in ZTB/O_2 plasma (p_{total} = 1 mTorr, P_{MW} = 800 W, $V_{substrate}$= floating). Thin film thickness: 140-170 nm.

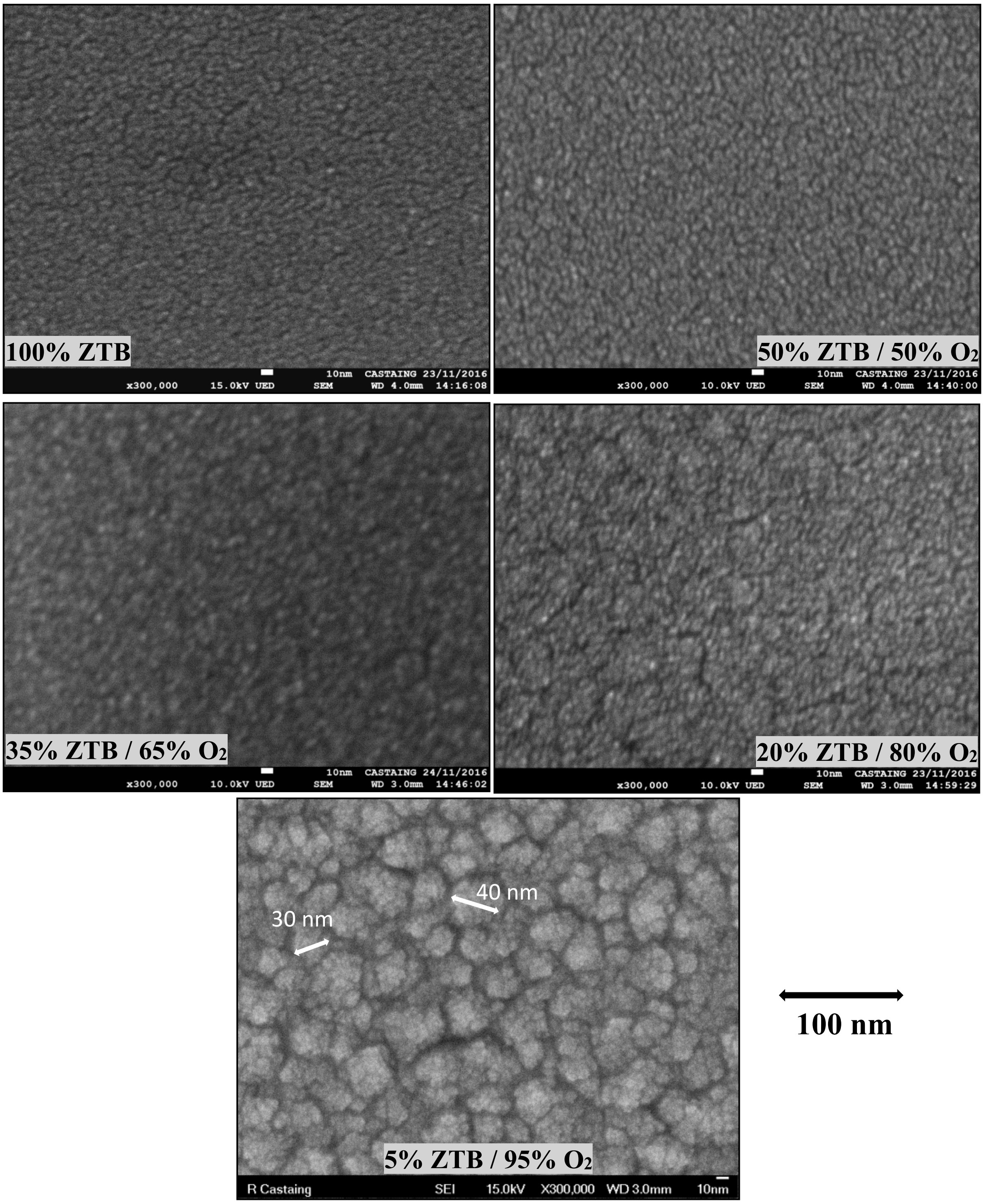

Figure III-31: SEM surface images of thin films deposited at different gas compositions in ZTB/O_2 plasma (p_{total} = 1 mTorr, P_{MW} = 800 W, $V_{substrate}$= floating). Thin film thickness: 140-170 nm.

TTIP

AFM images of thin films deposited in TTIP plasma at different fractions of O_2 gas in the gas mixture are shown in Figure III-32. and determined roughness values presented in Table III-9 reveal the increase in surface roughness as O_2 gas proportion in gas mixture increased.

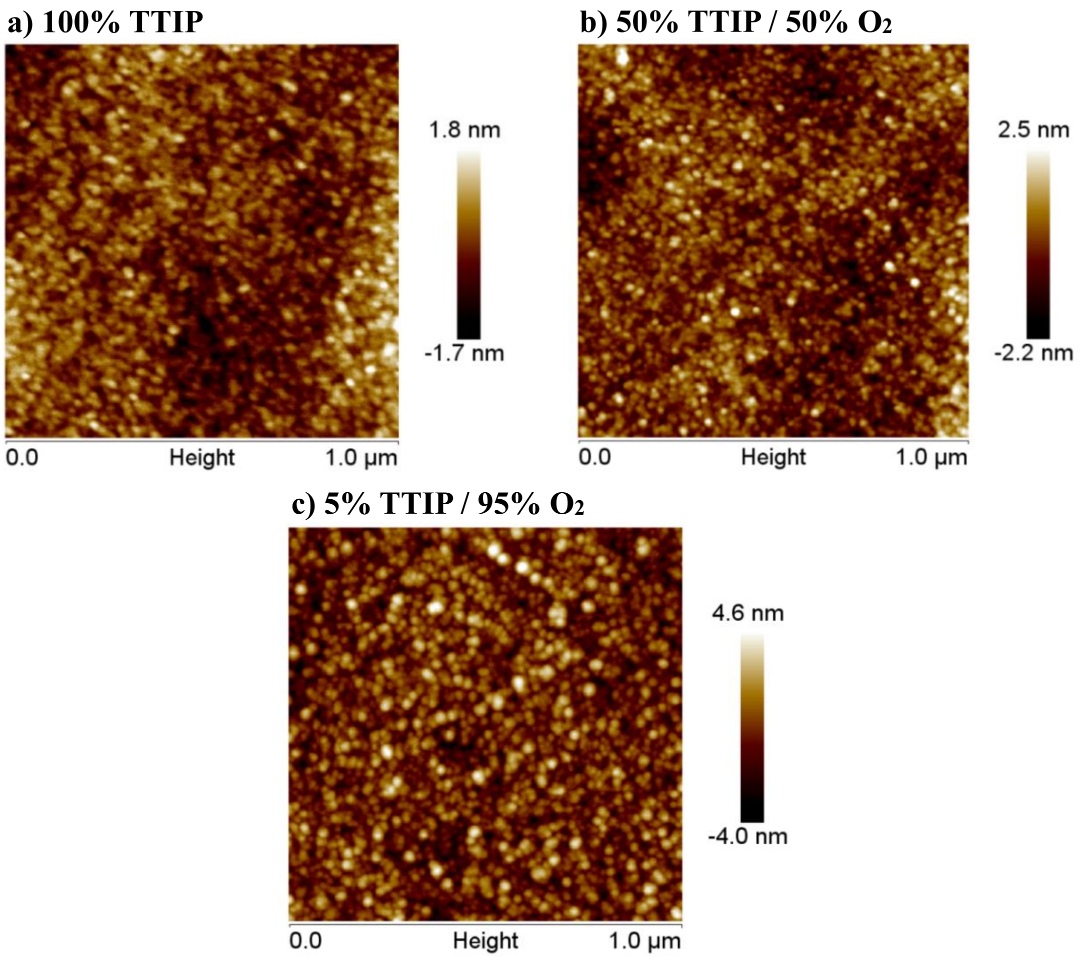

Figure III-32: AFM surface images of thin films grown in TTIP/O_2 plasma (p_{total} = 1 mTorr, P_{MW} = 800 W, $V_{substrate}$= floating): (a) 100% TTIP, (b) 50% TTIP/50% O_2, (c) 5% TTIP/95% O_2. Surface area measured: 1µm^2

Roughness parameter R_a equalled 0.39 nm, 0.53 nm and 0.98 nm at 0%, 50% and 95% of O_2, respectively. As O_2 proportion in the films increased from 0 to 95%, R_{max} increased from 3.86 to 9.07 nm. Surface morphology, observed by SEM, agreed with AFM analysis.

Table III-9: AFM surface roughness measurements corresponding to thin films grown in ZTB/O_2 and TTIP/O_2 plasma (p_{total} = 1 mTorr, P_{MW} = 800 W, $V_{substrate}$= floating). Surface area measured: 1µm^2.

O_2 in the gas mixture	ZTB / O_2		TTIP / O_2	
	R_a (nm)	R_{max} (nm)	R_a (nm)	R_{max} (nm)
0 %	0.27	2.5	0.39	3.86
50 %	0.38	4.6	0.53	5.42
95 %	4.90	38	0.98	9.07

SEM images of thin film cross sections are presented in Figure III-33. These cross-sectional images provided insight into the film bulk and allowed investigating morphology of thin films deposited at different gas compositions in TTIP/O_2 plasma. Thin films obtained at 0-65% of O_2 displayed uniform morphology with no distinguishable structures. All the films exhibited fine granular nature. At 80% of O_2, the morphology changed, and two different layers were observed: a thin, dense bottom layer with no apparent structuration and a columnar, upper layer. Relatively wide columns (20-40 nm in width) started to grow perpendicular to the substrate after thin film thickness reached 20-30 nm. With further increase in O_2 gas, at 95%, columns had grown from the interface with the substrate. These narrow columns, with widths of 10-20 nm, were densely stacked.

Figure III-34 shows SEM surface images of thin films deposited at different gas compositions. At 0-65% of O_2 in the gas mixture, no defined features were observable. The film surfaces exhibited fine granular nature that was already evidenced in the film bulk by cross-sectional SEM images. The surfaces seemed compact without any developed cracking. Increase in the O_2 proportion to 80% led to the appearance of columnar growth. In these conditions, the surface was composed of mounds with diameters in 10-40 nm range. These formations consisted of fine granular-like structures. At 95% of O_2, most surface mounds decreased in size, to diameters of 10-15 nm.

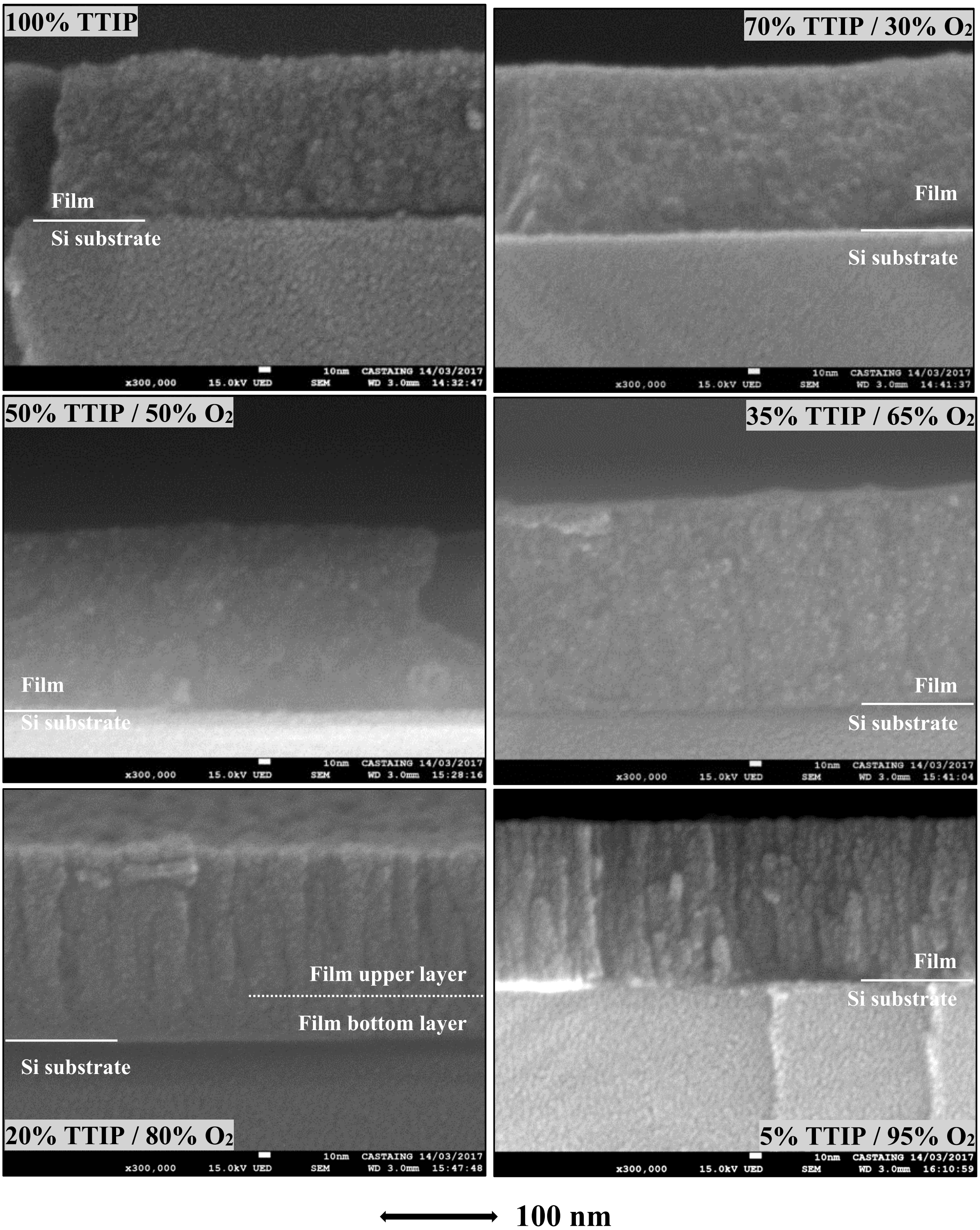

Figure III-33: SEM cross-sectional images of thin films deposited at different gas mixture ratios in TTIP/O_2 plasma (p_{total} = 1 mTorr, P_{MW} = 800 W, $V_{substrate}$= floating). Thin film thickness: 120-170 nm.

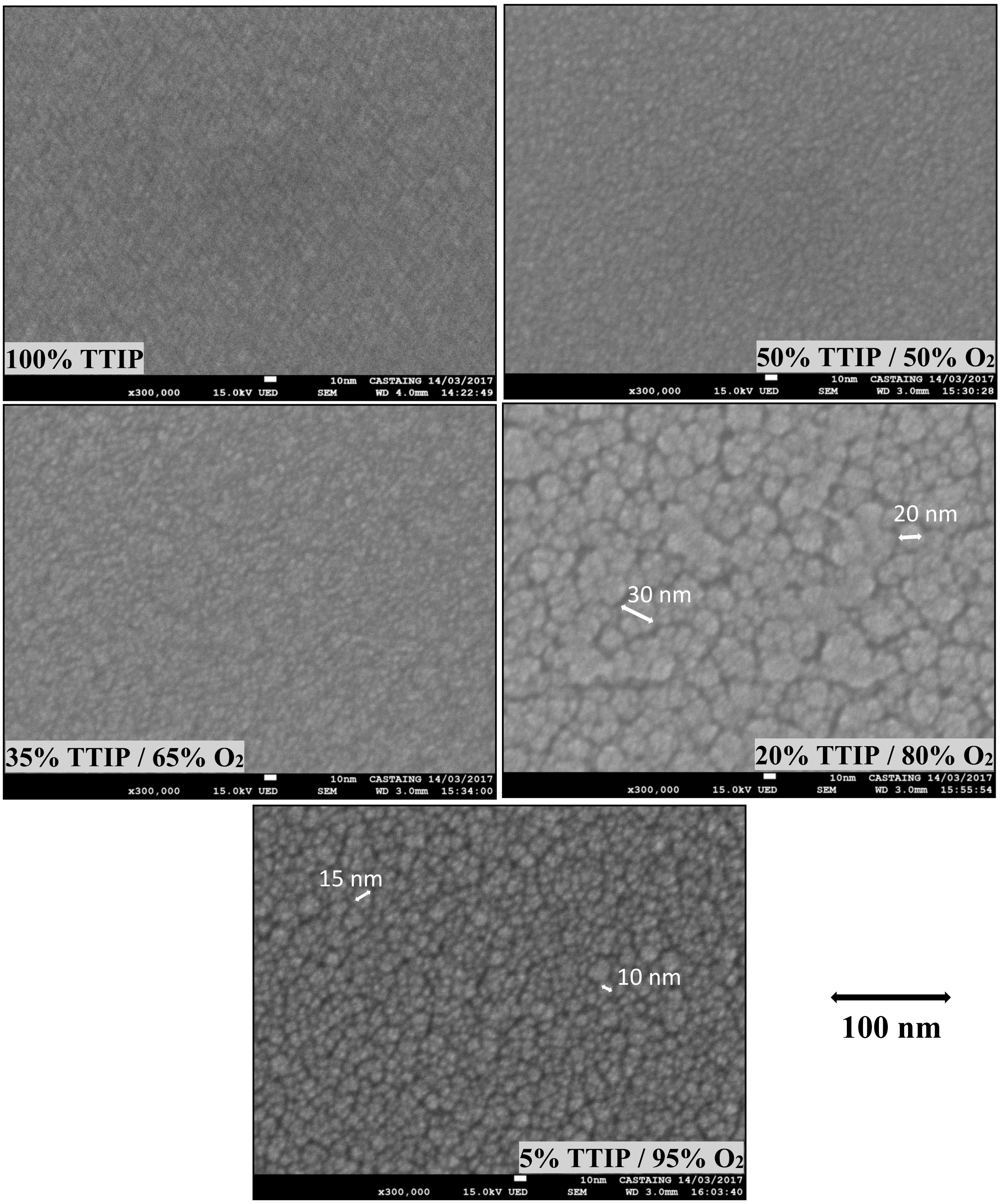

Figure III-34: SEM surface images of thin films deposited at different gas compositions in TTIP/O_2 plasma (p_{total} = 1 mTorr, P_{MW} = 800 W, $V_{substrate}$= floating). Thin film thickness: 120-170 nm.

III.4.2 From low to high oxygen gas fraction in plasma gas mixture: growth mode evolution

The preceding paragraph provides insight into morphology of the thin films deposited in ZTB and TTIP plasmas. As oxygen gas was added to the plasma gas mixture, the thin film growth mode drastically changed. In both types of plasmas, the film microstructure evolved from homogeneous to columnar. At O_2-poor conditions, there were no apparent morphological features formed in the films, whereas at O_2-rich conditions, the film morphology was organised in columnar structures.

The columnar growth has already been observed in zirconia and titania thin films deposited by PECVD [71], [73], [95], [96]. Besides experimentally observed columns, columnar thin film morphologies have been investigated by theoretical simulations [135], [200], [201]. Among the theoretical studies, a Monte Carlo (MC) model, developed by a group at the Institute of Material Science in Sevilla (Spain) [135], agrees fairly well with our experimental conditions. In the MC model, the species are assumed to have low energy and to follow an isotropic flow distribution. The thermal diffusion, desorption and re-emission processes have been neglected. In our deposition process, the substrate was at floating potential, thus the incoming species were expected to have low energy; the substrate temperature was relatively low (<100°C), so thermal diffusion could be disregarded. Due to very low working pressure, the species flow should have been predominately isotropic.

The MC model of interest focuses on a physical aspect of the problem and disregards the chemical interactions [135]. Each particle in the model represents a Ti species that follows an isotropic momentum distribution function towards the substrate. After arriving at the substrate surface, the particle is deposited and instantly transformed into a TiO_2 block. The MC simulation showed that, in the imposed conditions, the development of the columnar structures could be explained by a geometrical shadowing phenomenon. Due to the isotropic flow distribution of incoming species, the surface shadowing mechanism governs the thin film growth process resulting in films with columnar morphology [202].

In the metalorganic PECVD process, the chemical composition of plasma is fairly complex. Different precursor fragments, containing a metal atom and many or few organic parts, arrive at the surface of the substrate/film to be physisorbed. At the same time, oxygen species impinge at the surface and possibly react with the fragment enabling chemisorption of the metal atom as well as desorption of the organic part of the fragment. This several-step operation, named “the sticking mechanism”, is schematically presented in Figure III-35. In triggering the development of columnar morphology, the very complex surface processes should play a crucial role along with the geometrical shadowing [200], [202], [203].

As the plasma gas mixture evolves from O_2-poor to O_2-rich, the chemistry of the plasma phase changes and influences the physics and chemistry of surface processes. In the following text, we attempt to explain the difference between "the sticking mechanisms" of the two different conditions in a very simplified manner. A physisorbed precursor fragment containing the metal atom is relatively mobile due to low van der Waals bonding energy. This fragment will be able to move until it encounters an oxygen species. Thus, depending on the impingement rate of oxygen species, it is possible for the fragment to move more or less. If it moves more, the shadowing effect will be diminished, and the resulting film will be compact with no defined features as in the case of O_2-poor conditions. If the fragment has no time to diffuse, due to high arrival rate of oxygen species, the shadowing process will lead to columnar growth.

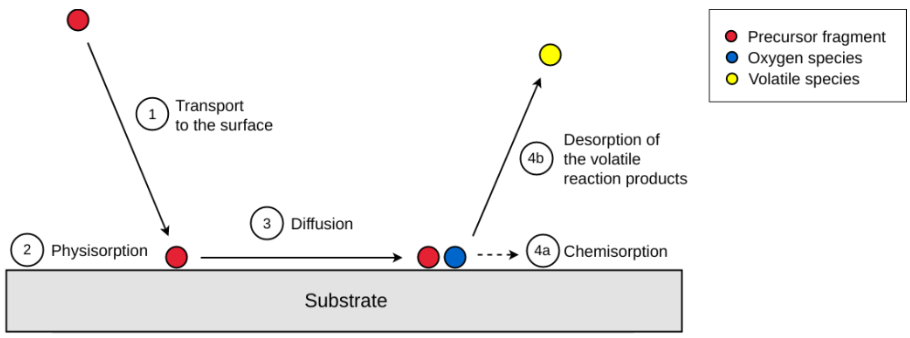

Figure III-35: Simplified schematic representation of the "sticking mechanism".

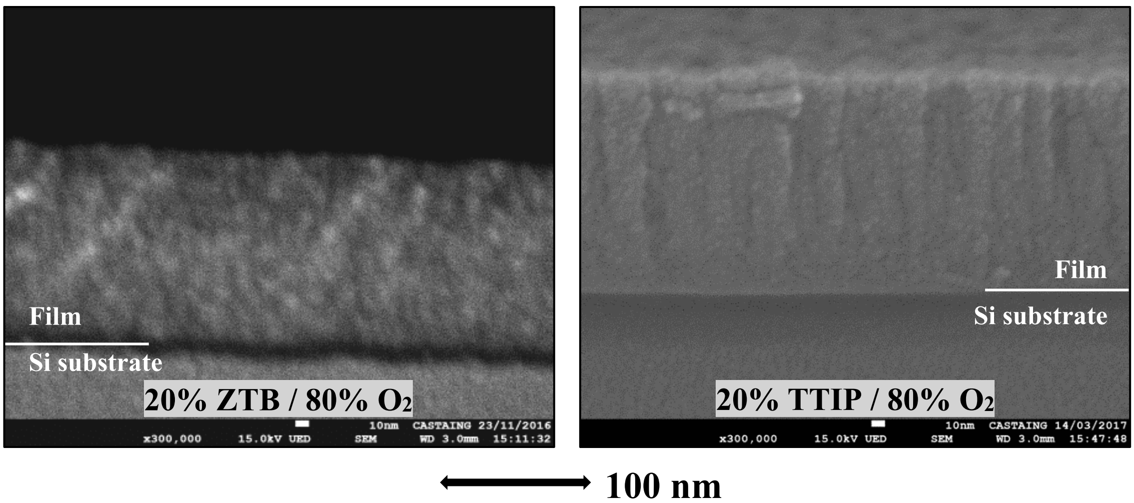

Figure III-36: SEM cross-sectional images of thin films deposited in 20% ZTB/80% O_2 and 20% TTIP/80% O_2 plasmas (p_{total} = 1 mTorr, P_{MW} = 800 W, $V_{substrate}$= floating).

Figure III-36 shows the SEM cross-sectional images of films deposited at 80% of O_2 gas in the gas mixture. In titania-like films, the columnar morphology appears at a lower proportion of O_2 when compared to the films deposited in ZTB plasma. This result was assumed to be due to the difference in the size of the organic part of the precursor molecules. Since there are fewer carbon atoms in TTIP than in ZTB, oxygen species are more effective and the "sticking mechanism" leading to columnar growth is activated at lower amounts of O_2 gas in the gas mixture. This difference was also evidenced in the XPS investigation: at 80% O_2/20% precursor, there is 24.1 at.% of carbon in titania-like films and 37.9 at.% of carbon in zirconia-like films.

III.4.3 Growth mechanisms in low pressure O_2-rich ZTB and TTIP plasmas

A striking difference was observed in the column widths between films obtained in ZTB and TTIP plasmas at 95% O_2/5% precursor (Figure III-37). At the same height, the columns formed in titania-like film are thinner (10-20 nm) in comparison with film grown in ZTB plasma (20-40 nm). The AFM analysis showed a significant difference in surface roughness between the films: the roughness parameter R_a equalled 0.98 nm and 4.90 nm for films deposited in O_2-rich TTIP and ZTB plasma, respectively.

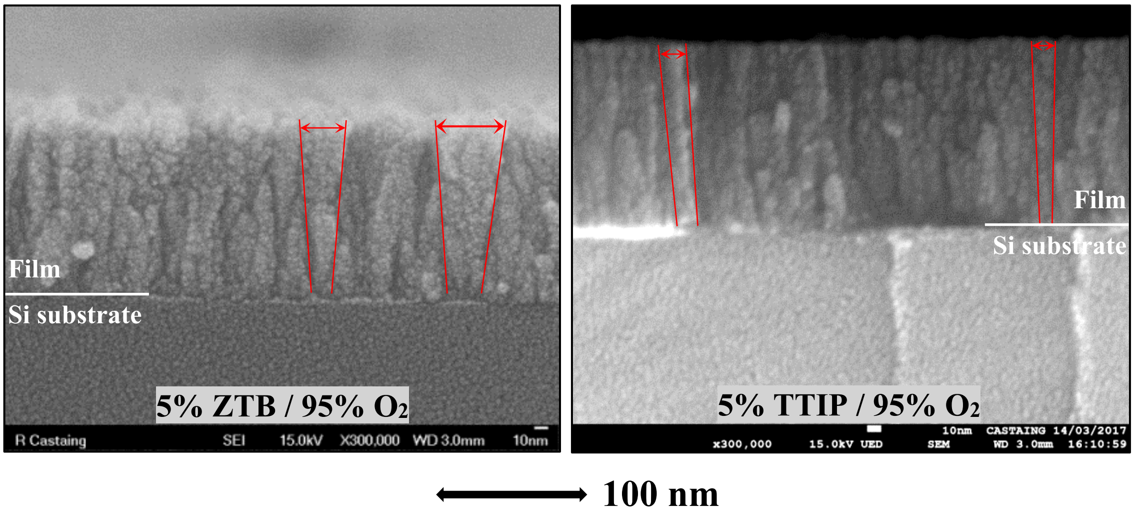

Figure III-37: SEM cross-sectional images of thin films deposited in oxygen-rich ZTB and TTIP plasmas (p_{total} = 1 mTorr, P_{MW} = 800 W, $V_{substrate}$= floating).

The complexity of a PECVD process renders it difficult to easily pinpoint specific phenomena that could cause variation in column size between the two plasmas. Any developed hypotheses would remain highly speculative if based solely on the available experimental results. Therefore, we searched for a computationally affordable model that could further corroborate potential explanations. A collaboration was established with Dr. A. Palmero and Dr. R. Alvarez at Institute of Material Science in Sevilla, Spain, who have extensively studied thin film microstructure by Monte Carlo (MC) simulations as well as experimental plasma deposition processes [58], [135], [204]–[207].

III.4.3.1 Monte Carlo simulation of thin film growth

Figure III-38 shows the schematic presentation of thin film growth process in the MC simulation. MC models employed to simulate ZrO_2 and TiO_2 thin film growth consider that the depositing particles are metal species, Zr or Ti. Each particle arrives at the surface from an initial random point. Depositing particles follow the direction defined by a polar angle of incidence θ $[0, \pi/2)$ and an azimuthal angle φ $[0, 2\pi)$. Particle direction is randomly calculated by defining an incident angle distribution function per unit time and unit surface.

After being deposited, the metal particle Zr or Ti is immediately transformed into a metal dioxide block of ZrO_2 or TiO_2, respectively. Each particle occupies a cubic volume Δ^3, where Δ equals 0.33 nm, the average distance between Zr or Ti atoms in ZrO_2 or TiO_2, respectively.

Typical simulated deposition rate is ~10 atoms/nm^{2}s, i.e. every 0.1 second 1 atom is deposited on 1 nm^2.

All of the models included the following constraints which were in agreement with the experimental conditions (as explained in paragraph III.4.2, p.106):

- no thermal mobility, desorption or re-emission,
- low energy of the incoming species.

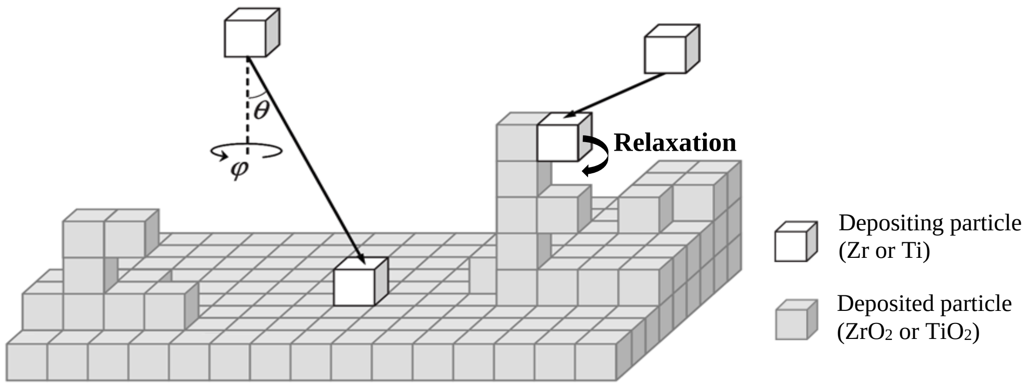

Figure III-38: Schematic presentation of thin film growth simulated by MC (adapted from [135]).

Strong correlation has been found between directionality of impinging particles and the size of formed columnar structures [135], [208]. Isotropic momentum distribution of impinging particles should lead to rough surfaces and lateral column growth, whereas a more directional flux leads to lower surface roughness and thinner columns. Accordingly, cause of the difference between morphologies formed in ZTB and TTIP plasma could lie in the particle flux distribution. TTIP fragment population might have a narrower momentum distribution: partially isotropic particle flux with preferential perpendicular direction. This hypothesis, based on different particle flux distribution was first modelled by MC.

MC model of **ZrO_2** growth imposed the following conditions:

- **isotropic flux,**
- **no surface relaxation** (particle deposited at the point of first contact with the surface),
- incoming species of low energy,
- no thermal mobility, desorption or re-emission.

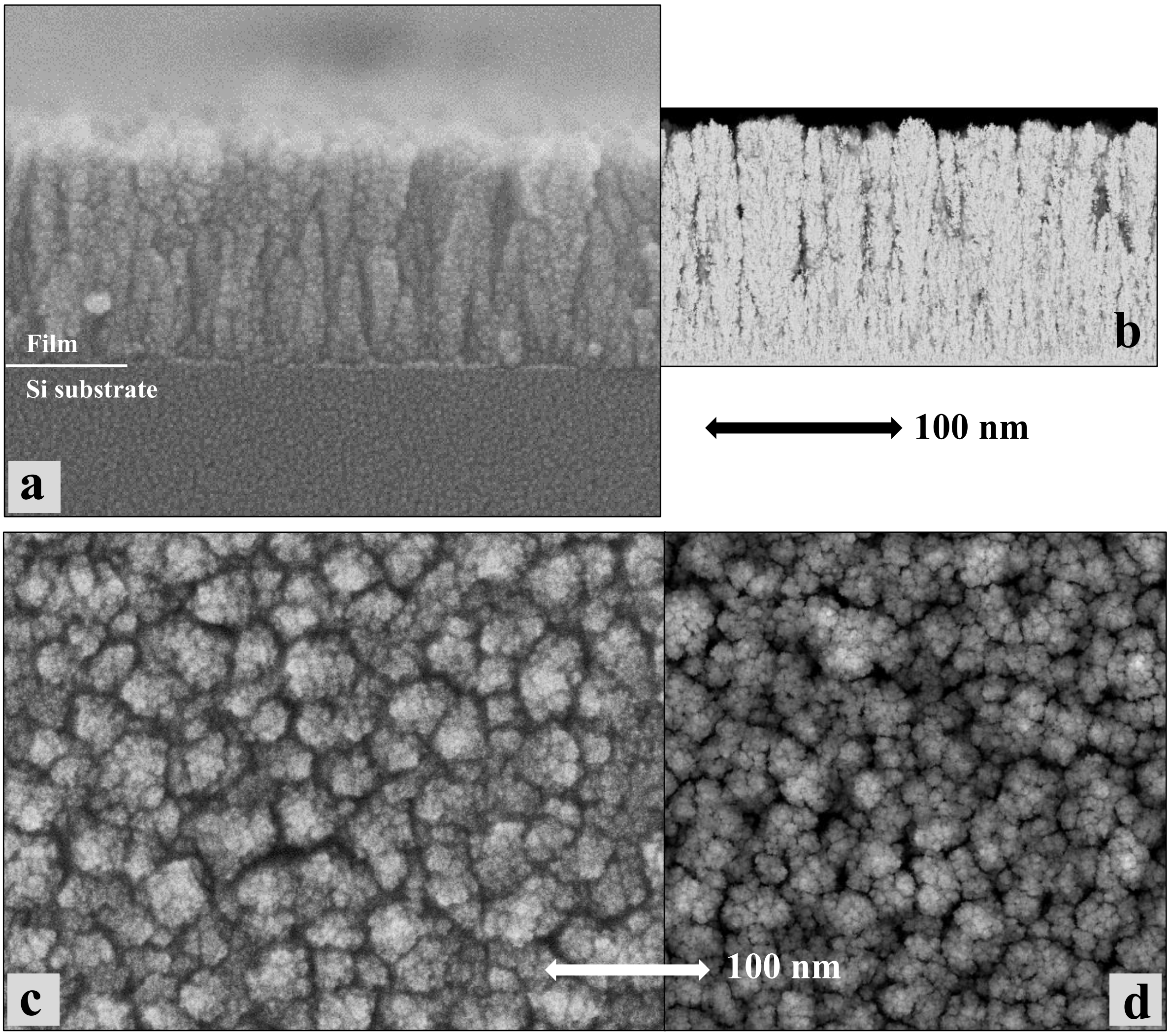

Figure III-39: Cross-sectional and surface images of thin films obtained by (a, c) PECVD from ZTB/O_2, (b, d) MC simulation of ZrO_2. PECVD process parameters: 5% ZTB/ 95% O_2, p_{total} = 1 mTorr, P_{MW} = 800 W, $V_{substrate}$= floating. MC model parameters: isotropic flux, no relaxation at the surface.

Morphology of the simulated ZrO_2 film corresponded remarkably to morphology of the film obtained by PECVD. Cross-sectional and surface images of films obtained by PECVD and MC are presented in Figure III-39. We can observe a striking similarity between the modelled film and the film deposited by PECVD, both in the cross section and surface images.

In the simulation of TiO_2 growth, particle flux was partially isotropic with preferential perpendicular direction towards the substrate. This was the only differing parameter between the simulation of ZrO_2 and TiO_2. Conditions of **TiO_2** simulated growth were:

- **perpendicular flux direction favoured**,
- **no surface relaxation** (particle deposited at the point of first contact with the surface),
- incoming species of low energy,
- no thermal mobility, desorption or re-emission.

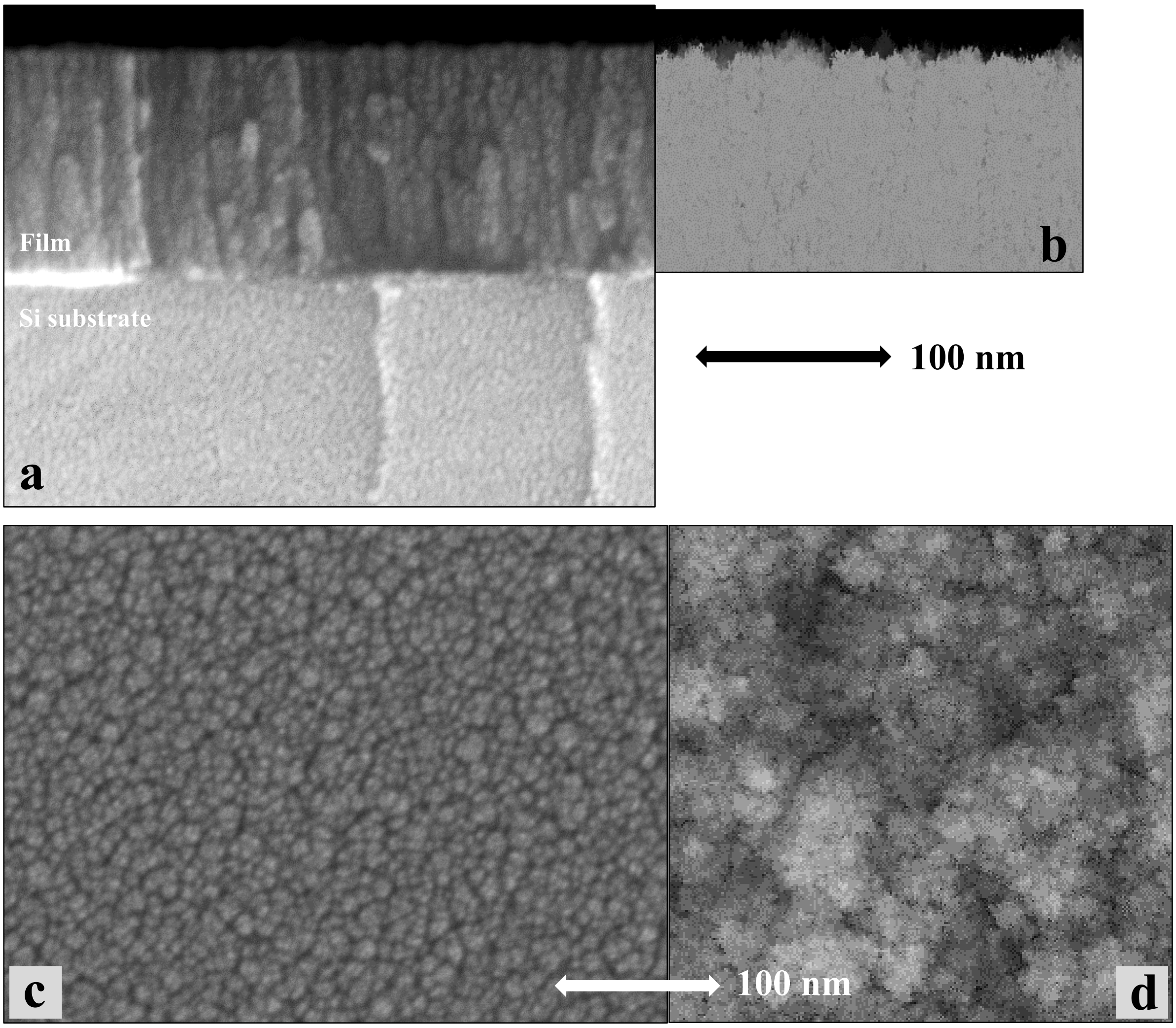

Figure III-40: Cross-sectional and surface images of thin films obtained by (a, c) PECVD from TTIP/O_2, (b, d) MC simulation of TiO_2. PECVD process parameters: 5% TTIP/ 95% O_2, p_{total} = 1 mTorr, P_{MW} = 800 W, $V_{substrate}$= floating. MC model parameters: perpendicular flux direction favoured, no relaxation at the surface.

Resulting morphology of simulated TiO_2 film disagrees completely with the morphology observed in PECVD as it can be seen in Figure III-40. Columnar structures are distinctly visible in the SEM cross-sectional image of the PECVD film, whereas in the image of simulated film we cannot distinguish any defined structures. This simulation indicates that partially isotropic particle flux with preferential perpendicular direction is not the defining parameter that leads to the growth of thinner columnar structures.

It is possible that surface conditions and reactions are significantly different between ZTB and TTIP plasmas. Precursor molecules have different physico-chemical characteristics. These two molecules are composed by different central atoms and different number of carbon and hydrogen atoms, ZTB: $ZrO_4C_{16}H_{36}$ vs TTIP: $TiO_4C_{12}H_{28}$. Central metal atoms, ${}^{40}_{91.2}Zr$ vs ${}^{22}_{47.9}Ti$, exhibit different characteristics (e.g. electronegativity χ_{Zr}=1.33 vs χ_{Ti}=1.54). In PECVD, precursor fragment containing a metal atom arrives at the substrate surface where it can be physisorbed. Depending on the complex surface processes such as electromagnetic interactions between adsorbed particles and the substrate, physisorbed fragment might diffuse to a near, energetically more favourable position. This process might have a strong influence on film morphology. To alleviate any confusion with thermally induced mobility of chemisorbed species, we address the mobility of physisorbed particles as *relaxation*.

We examined this hypothesis by an MC model which included the difference in surface relaxation between ZrO_2 and TiO_2 growth. The differing parameter, introduced in the simulation of TiO_2 film, was the possibility of relaxation. After landing on the surface, Ti species could migrate a few ångström to a near, more energetically stable position where it was then deposited. On the other hand, in the simulation of ZrO_2 film (p.110), Zr species were deposited at the point of first contact with the film surface.

Parameters set in the second MC model of **TiO_2** growth were:

- **possible surface relaxation,**
- **isotropic flux,**
- incoming species of low energy,
- no thermal mobility, desorption or re-emission.

Simulation resulted in a remarkable similarity between the simulated film and the film obtained by PECVD. The comparison of the results can be seen in cross-sectional and surface images in Figure III-41. The microstructures of modelled films strikingly match the microstructures of films grown in TTIP/O_2 plasma.

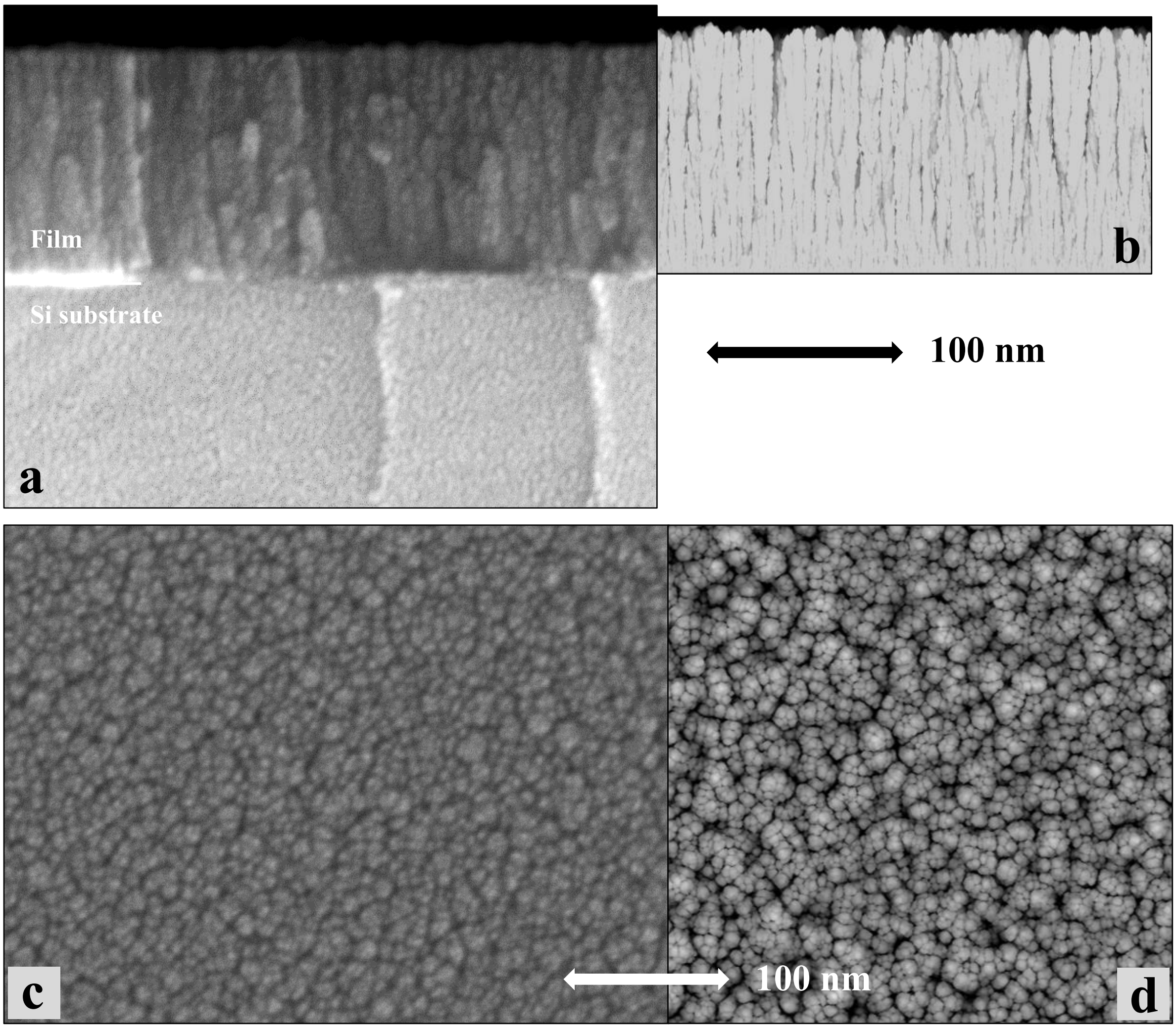

Figure III-41: Cross-sectional and surface images of thin films obtained by (a, c) PECVD from TTIP/O_2, (b, d) MC simulation of TiO_2. PECVD process parameters: 5% TTIP/ 95% O_2, p_{total} = 1 mTorr, P_{MW} = 800 W, $V_{substrate}$= floating. MC model parameters: possible surface relaxation, isotropic flux.

Based on the findings of the MC theoretical study, it is likely that the Ti species, physisorbed at the film surface, in 5% TTIP/95% O_2 PECVD might have a higher probability of diffusion to a near, energetically more stable, position in comparison with species created in 5% ZTB/95% O_2 plasma. Probability of relaxation depends on physico-chemical characteristics of the incoming particles, the film surface and their mutual interaction. The extreme complexity of the phenomena in question makes it difficult to completely reveal the plasma / surface processes. Nevertheless, combining the experimental and theoretical methods has significantly improved our insight into the O_2-rich metalorganic PECVD.

III.5 Characterization of macroscopic physical properties

Thin films synthesised at 100% precursor and 5% precursor/95% O_2 plasmas have been probed by spectroscopic ellipsometry (SE), ellipsometric porosimetry (EP) and X-ray reflectometry (XRR) to obtain values of thin film refractive index, nanoporosity profile and density, respectively.

EP analysis (Figure III-42) provided the values of nanosized pore proportion in the films. By the EP measurements in question, only open porosity could be "seen" with pore diameters in 0.47-50 nm range.

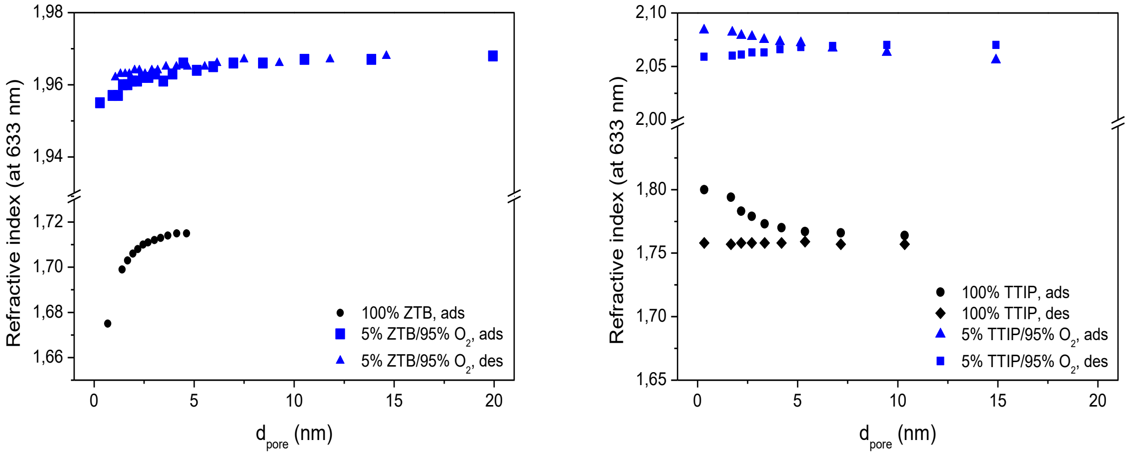

Figure III-42: Refractive index as a function of pore diameter measured by EP during ethanol adsorption and desorption on thin films deposited in ZTB/O$_2$ and TTIP/O$_2$ plasmas (p_{total} = 1 mTorr, P_{MW} = 800 W, $V_{substrate}$= floating).

Figure III-43 shows the data obtained by means of XRR. In the calculation of the density values, the chemical composition observed by XPS investigation was taken into account (Table III-4, p.73).

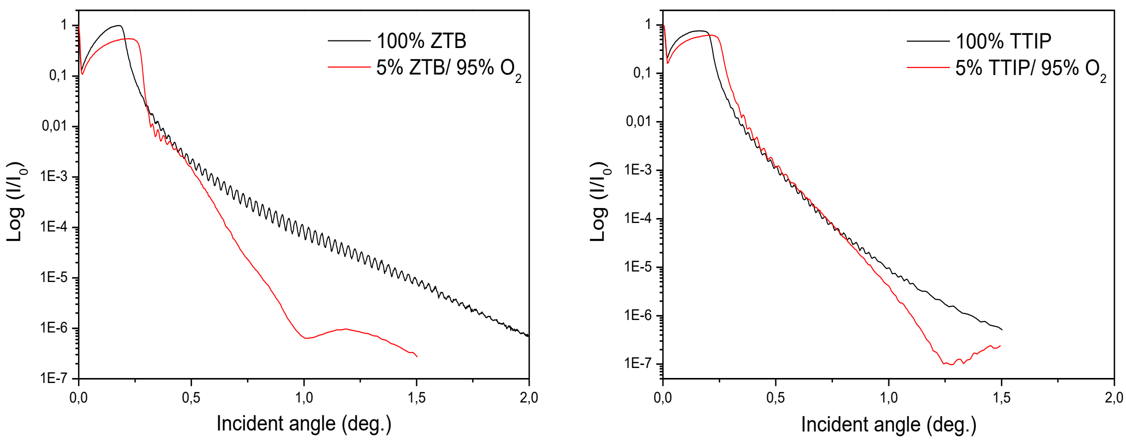

Figure III-43: XRR measurements of reflectivity as a function of an incident angle for thin films deposited in ZTB/O$_2$ and TTIP/O$_2$ plasmas (p_{total} = 1 mTorr, P_{MW} = 800 W, $V_{substrate}$= floating).

Table III-10 contains the values of the refractive index, density and nanoporosity corresponding to thin films deposited in ZTB/O_2 and $TTIP/O_2$ plasmas. The refractive index increased from 1.59 to 1.84 as gas mixture changed from 100% ZTB to 5% ZTB/95% O_2. The density of the zirconia-like films also increased from 2.09 to 3.58 g/cm^3. This behaviour was expected since thin films evolved from being highly organic to being almost inorganic as O_2 gas was added to the gas mixture (Table III-4, p.73). Likewise, refractive index of films deposited in TTIP plasmas increased: from 1.73 to 2.10. The density, starting at 2.18 g/cm^3 at 100% TTIP, reached 2.94 g/cm^3 in O_2-rich conditions.

Table III-10: Refractive index, density and nanoporosity of the thin films deposited in ZTB/O_2 and $TTIP/O_2$ plasma (p_{total} = 1 mTorr, P_{MW} = 800 W, $V_{substrate}$= floating).

Plasma gas mixture	Refractive index (at λ = 633 nm)	Density (g/cm^3)	Nanoporosity (%) (d_{pore} = 0.5-50.0 nm)
100% ZTB	1.59	2.1	7.5
5% ZTB/ 95% O_2	1.84	3.6	1.9
100% TTIP	1.73	2.2	0
5% TTIP/ 95% O_2	2.10	2.9	0

Values of the optical properties of metal oxide materials depend on the crystalline phase and the preparation method. Refractive index of ZrO_2 and TiO_2 material in the visible/infrared wavelength range equals ≥2.0 and ≥2.4, respectively [209]–[212]. The density of zirconia is found in ~5.3-6.2 g/cm^3 range and the density of titania has been measured in the 3.8-4.2 g/cm^3 range. These values are higher than the refractive indices and density values corresponding to the films obtained in our study at O_2-rich conditions. This could be explained by the presence of carbon atoms and porosity in the films. The relatively high carbon content measured at the film surface, 21.3 at.% in zirconia-like film and 15 at.% in titania-like film, implies a non-negligible fraction of carbon atoms in the thin film bulk. The nanoporosity proportion decreased to 1.9 % at 5% ZTB/95% O_2, while in titania-like films it has not been observed. Still, the total porosity content, including closed pores and the pores larger than the ones that would be observed by EP, may be important.

III.6 Conclusion

In this chapter, we have studied the influence of oxygen gas percentage of metalorganic/O_2 plasma gas mixture on the thin film growth process and the final film characteristics. In general, the characteristics of the films corresponding to ZTB and to TTIP plasmas evolve in the same manner.

It has been shown that the films evolve from highly organic to almost inorganic in nature. Carbon atoms are less deposited due to precursor dilution and etching achieved by the increasing number of oxygen atoms. Precursor dilution and thin film etching induce a decrease of the deposition rate in plasma gas mixture with over 50% of O_2 gas.

The changes in the film chemical composition are also evidenced in the chemical bonding. As the O_2 gas is added to the gas mixture, the hydrocarbon rich environments such as $MOC(C_xH_y)$ are replaced by carbonate-like structures rich in oxygen atoms (M: metal atom). The fraction of C-O and C=O bonds that form structures such as $M(CO_3)$ achieves a maximal value at ~80% of O_2. With further addition of O_2, a decrease is observed due to carbon deficient conditions. Analogous behaviour of the number of CO and CO_2 species in the plasma phase has been indicated by OES analysis.

The growth mode drastically changes as the plasma gas mixture becomes rich in oxygen gas: from uniform in all directions to columnar. The columnar structures observed in titania-like films are significantly thinner in comparison with zirconia-like films. By coupling the experimentally obtained results and Monte Carlo simulations, the difference in column width has been explained by the higher surface relaxation possibility of physisorbed Ti species in TTIP plasma relative to Zr species in ZTB plasma.

Regarding the macroscopic properties, it has been shown that the film refractive index and density increase at oxygen-rich gas mixture conditions and that the open nanosized pore content in the films is generally very low.

Chapter IV

Thin film growth in ZTB/O_2 and TTIP/O_2 plasmas: influence of plasma gas mixture total pressure

Introduction

This chapter explores the modifications of thin film characteristics induced by an increase in total gas pressure. The composition of the plasma gas mixture was maintained constant at 5% metalorganic precursor and 95% oxygen gas. The O_2-rich gas mixture was chosen since films deposited in these conditions exhibit a particular (columnar) morphology. Additionally, the deposited films are almost-inorganic metal oxides which are of interest in various scientific and industrial areas. The deposition parameters are summarized in Table IV-1.

Table IV-1: Thin film growth conditions at different total gas pressure values in ZTB/O_2 and TTIP/O_2 plasma.

Total gas pressure	1-10 mTorr
Gas mixture composition	5% metalorganic precursor / 95% O_2
MW power	800W
Substrate	Si (100)
Substrate potential	Floating
$T_{substrate}$	Uncontrolled
Deposition time	30-40 min at 1 mTorr, < 15 min at 2-10 mTorr

Each paragraph of this chapter starts with a presentation of experimentally obtained results that is followed by a discussion and comparison between $ZrO_xC_yH_z$ and $TiO_xC_yH_z$ films. To begin with, the evolution of the deposition rate is introduced. Afterwards, we examine the chemical composition and chemical bonding of the film by XPS and FTIR, and the modifications of thin film morphology based on SEM imaging. Lastly, the macroscopic physical properties of the thin film are reviewed.

The total gas pressure has achieved relatively high values (up to 10 mTorr). Due to the particularities of precursor injection systems and the gas introduction protocol (Chapter II.3, p.46), it is necessary to discuss the influence of experimental conditions on the injection of TTIP gas. The injection of ZTB was controlled by a semi-automatic system that readjusted the injection to maintain a constant value during the introduction of oxygen gas and the deposition process. In contrast, the manual injection system used for TTIP was unable to readjust the injection. Consequently, it is possible that the TTIP flow rate was compromised by subsequent introduction of O_2 gas leading to a decrease of the initially set partial pressure value. Therefore, when reviewing and comparing results corresponding to ZTB and to TTIP plasmas, it is important to keep in mind that the partial pressure of TTIP might in fact be different than the noted value.

IV.1 Deposition rate

The growth rates of thin films deposited at different pressures of ZTB/O_2 and TTIP/O_2 gas mixtures are graphically presented in Figure IV-1. The gas mixtures were composed of 5% precursor and 95% O_2 gas. The deposition rate of both types of films evolved in a similar manner: with increase in pressure from 1 to 10 mTorr, the deposition rate increased from <5 nm/min to ~50 and ~60 nm/min in TTIP/O_2 and ZTB/O_2 plasma, respectively.

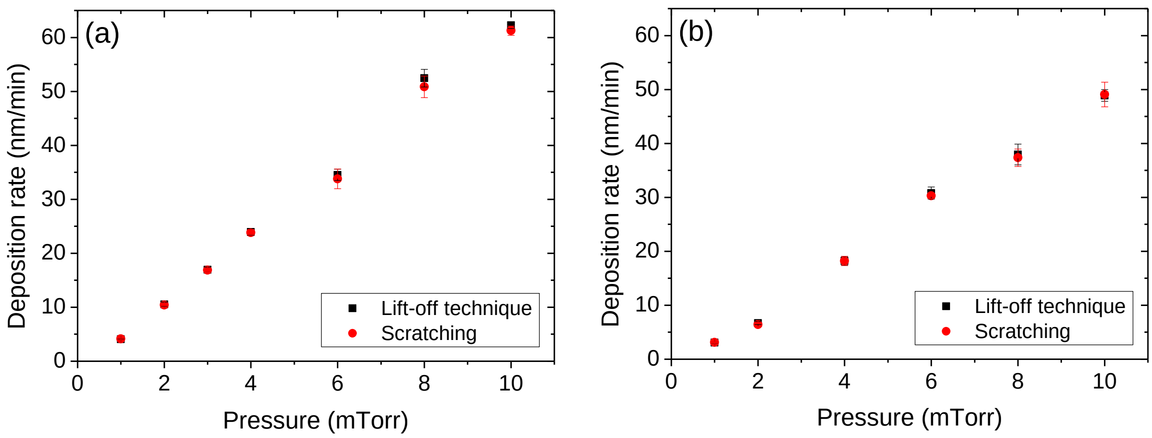

Figure IV-1: Deposition rate of thin films grown at various total gas pressures in (a) ZTB/O_2 and (b) TTIP/O_2 plasma (5% precursor/95% O_2, P_{MW} = 800 W, $V_{substrate}$ = floating). Error bars correspond to standard deviation.

Numerous phenomena, such as changes in the chemical nature of fragments arriving at the substrate or in the effectiveness of etching achieved by oxygen species, might have effect on the growth rate. It is most likely that the change in the amount of matter available for deposition has the predominant role. The precursor/O_2 gas ratio and the reactor pumping speed were constant. Therefore, to increase the pressure, precursor and oxygen gas were added to the plasma gas mixture.

IV.2 Thin film chemical composition and bonding

IV.2.1 Chemical composition

In this part, we focus on the modification of surface and bulk chemical properties induced by the increase of total gas pressure. The XPS technique was employed to probe the thin chemical composition of the film surface. The analysis depth ranges from 2 nm to 10 nm. The data obtained by XPS investigation is summarized in Table IV-2.

Table IV-2: XPS chemical composition and atomic ratios corresponding to films deposited in ZTB/O_2 and TTIP/O_2 plasmas at different gas pressure values (5% precursor/95% O_2, P_{MW} = 800 W, $V_{substrate}$ = floating).

Total gas pressure (mTorr)	Atomic composition (%)			Atomic ratio	
	M*	O	C	O/M*	C/M*
		ZTB / O_2 plasma			
1	27.1	51.6	21.3	1.9	0.8
2	25.1	51.2	23.7	2.0	0.9
4	21.8	50.4	27.8	2.3	1.3
8	19.5	46.9	33.6	2.4	1.7
10	20.4	50.2	29.4	2.5	1.4
		TTIP / O_2 plasma			
1	24.5	60.5	15.0	2.5	0.6
2	21.8	55.5	22.7	2.5	1.0
4	21.6	54.8	23.6	2.5	1.1
8	20.0	53.6	26.4	2.7	1.3
10	18.9	51.6	29.5	2.7	1.6

**M corresponds to Zr and Ti for ZTB and TTIP related data, respectively.*

ZTB

XPS examination of the coatings grown in ZTB/O_2 plasma revealed how the chemical composition of the film evolved with the increase of total gas pressure (Figure IV-2). Starting from 1 mTorr up to 8 mTorr, atomic fraction of carbon increased, and that of zirconium and oxygen modestly decreased. As pressure increased further, to 10 mTorr, carbon at.% seemed to slightly decrease and oxygen at.% increased.

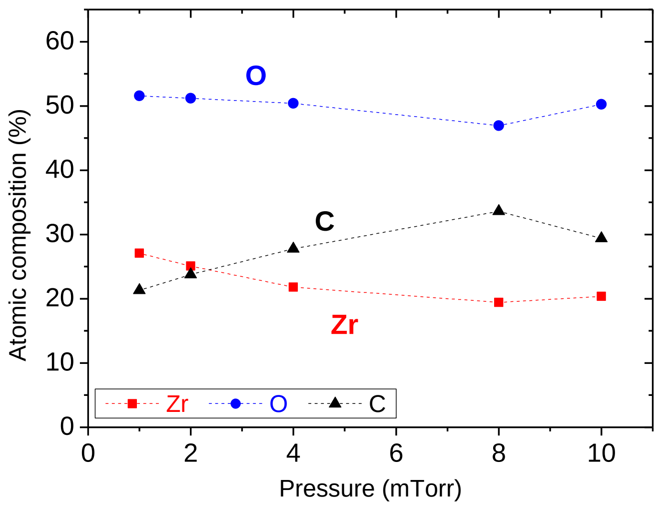

Figure IV-2: Atomic composition of thin films deposited in ZTB/O_2 plasma as a function of total gas pressure (5% precursor/95% O_2, P_{MW} = 800 W, $V_{substrate}$ = floating).

XPS data, presented in Table IV-2 and graphically in Figure IV-9, have shown that relative to zirconium atoms, the number of carbon and oxygen atoms increased with pressure. The film stoichiometry, excluding hydrogen atomic content, evolved from $ZrO_{1.9}C_{0.8}$ at 1 mTorr to $ZrO_{2.5}C_{1.4}$ at 10 mTorr.

TTIP

Figure IV-3 graphically presents the chemical composition of the thin film, obtained by XPS, as a function of TTIP/O_2 gas mixture pressure. A decrease was observed in both oxygen and zirconium atomic fractions, while the percentage of carbon atoms forming the films increased. At 1 mTorr, the films consisted of 24.5 Zr at.%, 60.5 O at.% and 15.0 C at.% (Table IV-2). The composition changed to 18.9 Zr at.%, 51.6 O at.% and 29.5 C at.% at 10 mTorr. The film stoichiometry, disregarding hydrogen presence, changed from $TiO_{2.5}C_{0.6}$ to $TiO_{2.7}C_{1.6}$ as the total gas pressure increased from 1 to 10 mTorr. Figure IV-9 graphically presents the change in stoichiometry, i.e. the number of carbon and oxygen atoms relative to zirconium atoms.

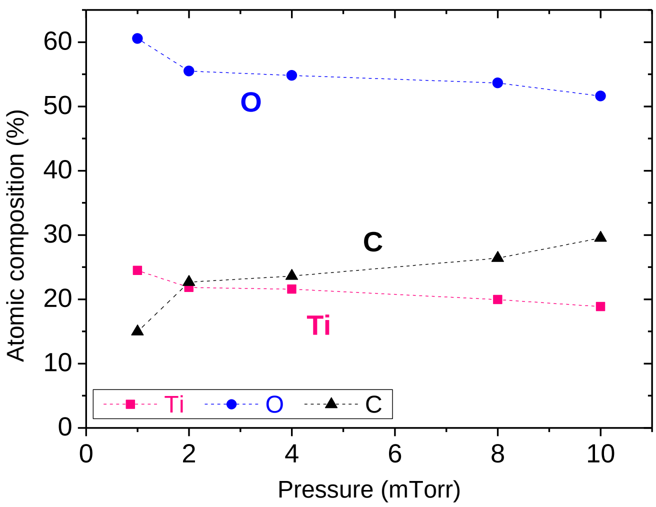

Figure IV-3: Atomic composition of thin films deposited in TTIP/O_2 plasma as a function of total gas pressure (5% precursor/95% O_2, P_{MW} = 800 W, $V_{substrate}$ = floating).

IV.2.2 Comparative analysis of thin film chemical bonding as a function of pressure: ZTB vs TTIP

Detailed identification of FTIR spectra corresponding to films deposited in ZTB/O_2 and TTIP/O_2 plasmas is presented in Chapter III (p.82). In this chapter, we focus on the changes in chemical bonding under the influence of total gas pressure. Figure IV-4 shows the 4000-400 cm^{-1} spectral range of FTIR signatures originating from thin films deposited at various pressures of precursor/O_2 gas mixture. To simplify the analysis, the spectra have been divided into three spectral regions that correspond to three distinct IR bands observed by FTIR.

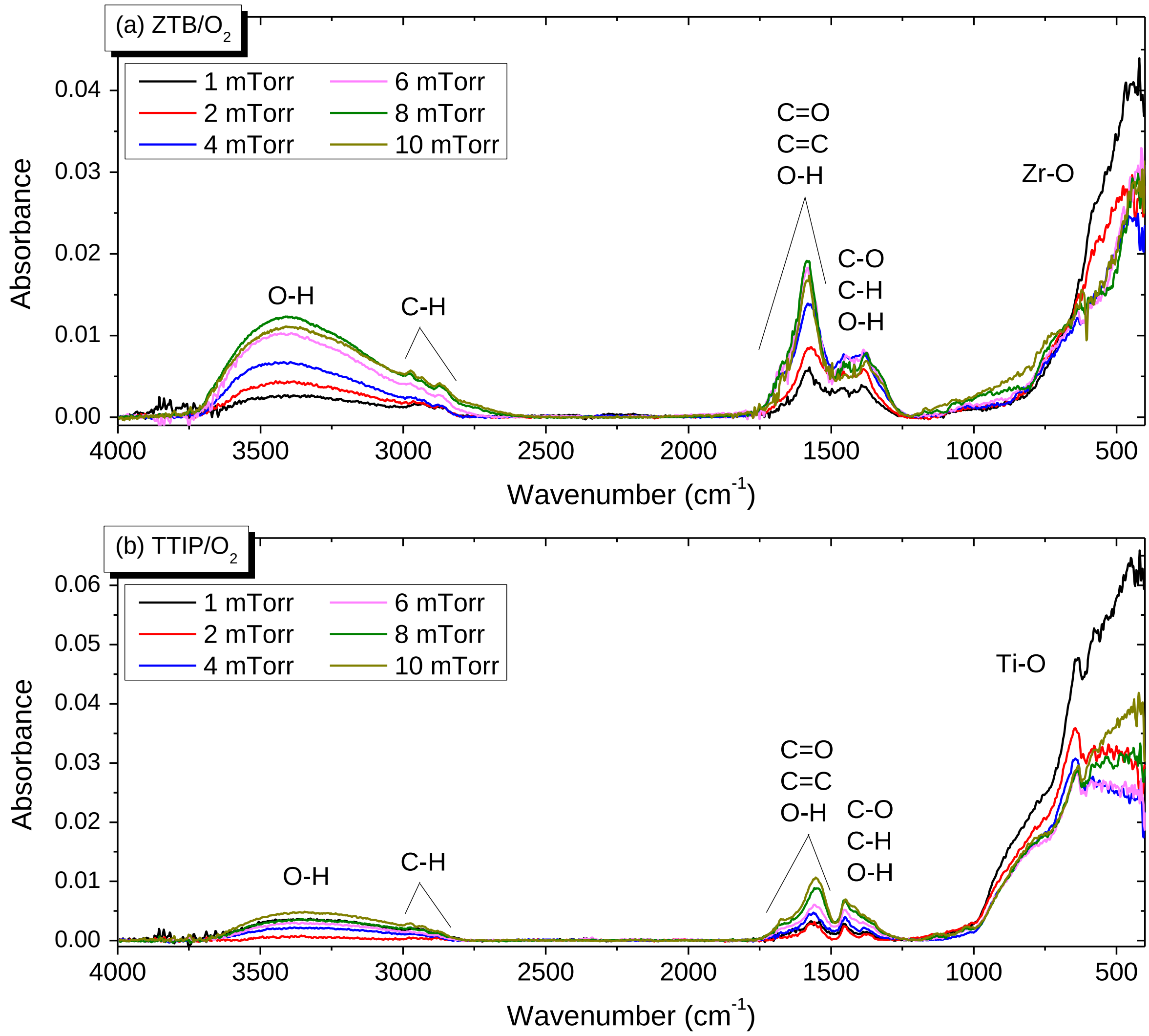

Figure IV-4: FTIR spectra of thin films deposited at different total gas pressures in ZTB/O_2 and TTIP/O_2 plasma (5% precursor/95% O_2, P_{MW} = 800 W, $V_{substrate}$ = floating). Absorbance: normalised by film thickness.

4000-2650 cm^{-1} region

Figure IV-5 shows the spectral band formed by peaks assigned to O-H and C-H bonds in the films deposited at different pressures of ZTB/O_2 and TTIP/O_2 gas mixtures. The major part of the band originates from vibrations of O-H bonds in absorbed H_2O. Since the films were exposed to air before FTIR analysis, it is reasonable to expect the absorption of water from the environment. Different films were synthesized and analysed on different days, so the environmental conditions (such as air temperature and humidity level) were different, all of which could have influenced the degree of absorbed water and the H_2O amount present in the FTIR sample chamber.

In both zirconia-like and titania-like films, it was possible to distinguish peaks corresponding to C-H bonds (in the 2970-2830 cm^{-1} range); however, changes in their intensities were minor as pressure increased. These peaks became slightly more pronounced at highest pressures (8-10 mTorr), which implies an increase of C-H bond concentration in both types of films.

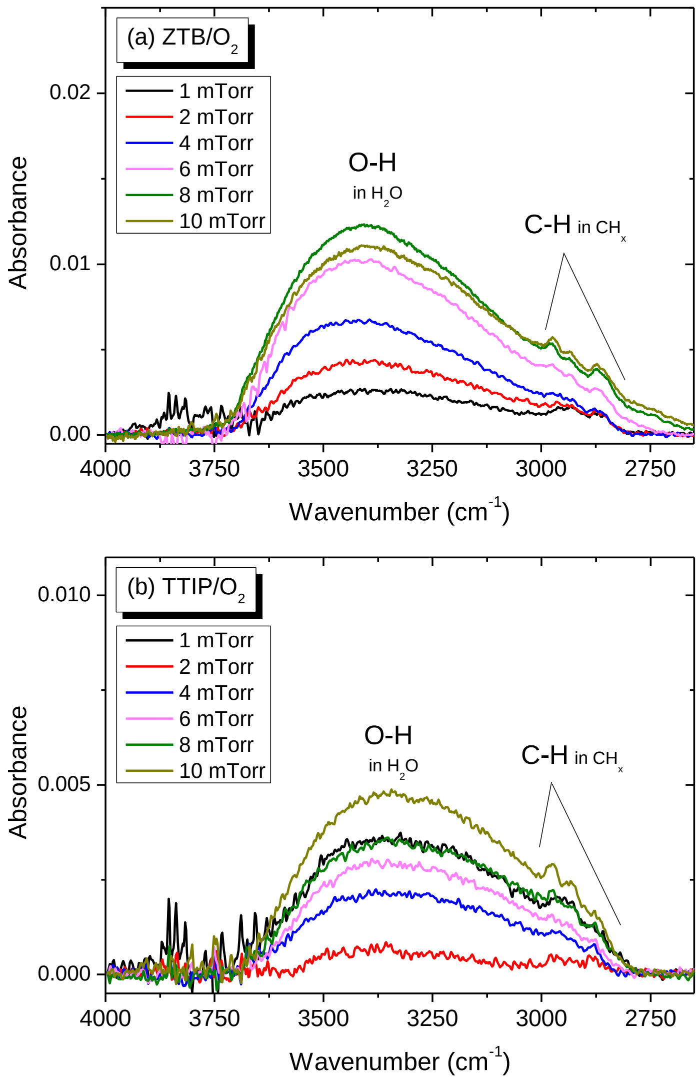

Figure IV-5: FTIR spectra (4000-2650 cm^{-1}) of thin films deposited at different total gas pressures in a) ZTB/O_2 and b) TTIP/O_2 gas mixture (5% precursor/95% O_2, P_{MW} = 800 W, $V_{substrate}$ = floating). Absorbance: normalised by film thickness.

1800-1250 cm^{-1} region

The complex 1800-1250 cm^{-1} band (Figure IV-6), appearing in zirconia- and titania-like films, was primarily assigned to C-O and C=O bonds in carbonate-like environments (Figure III-14, p.84). Contributions from C=C, C-H and O-H bonds should also be expected in this region.

In general, the band absorbance increased with pressure in both types of films as it can be seen in Figure IV-7. In films grown in ZTB plasma, the band absorbance increased up to a pressure of 4 mTorr. Afterwards, the change slowed down, to finally slightly decrease at a pressure of 10 mTorr. In titania-like films, the absorbance of the band continues to increase even at highest pressures.

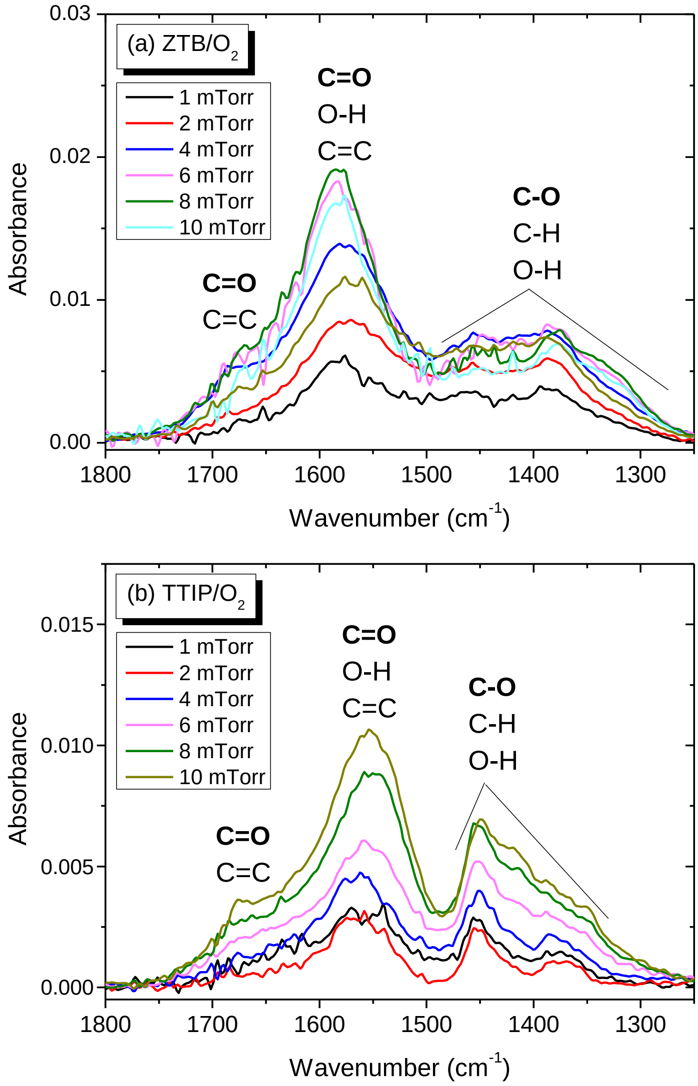

Figure IV-6: FTIR spectra (1800-1250 cm^{-1}) of thin films deposited at different total gas pressures in a) ZTB/O_2 and b) TTIP/O2 gas mixture (5% precursor/95% O_2, P_{MW} = 800 W, $V_{substrate}$ = floating). Absorbance: normalised by film thickness.

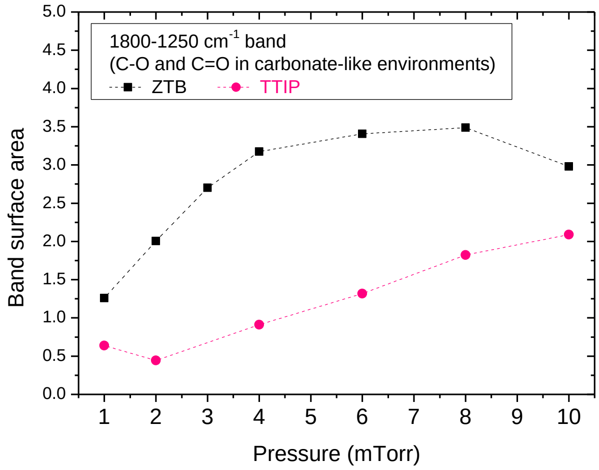

Figure IV-7: Evolution of surface area of 1800-1250 cm^{-1} band observed in FTIR spectra of thin films deposited in ZTB/O_2 and TTIP/O_2 plasmas.

1250-400 cm^{-1} region

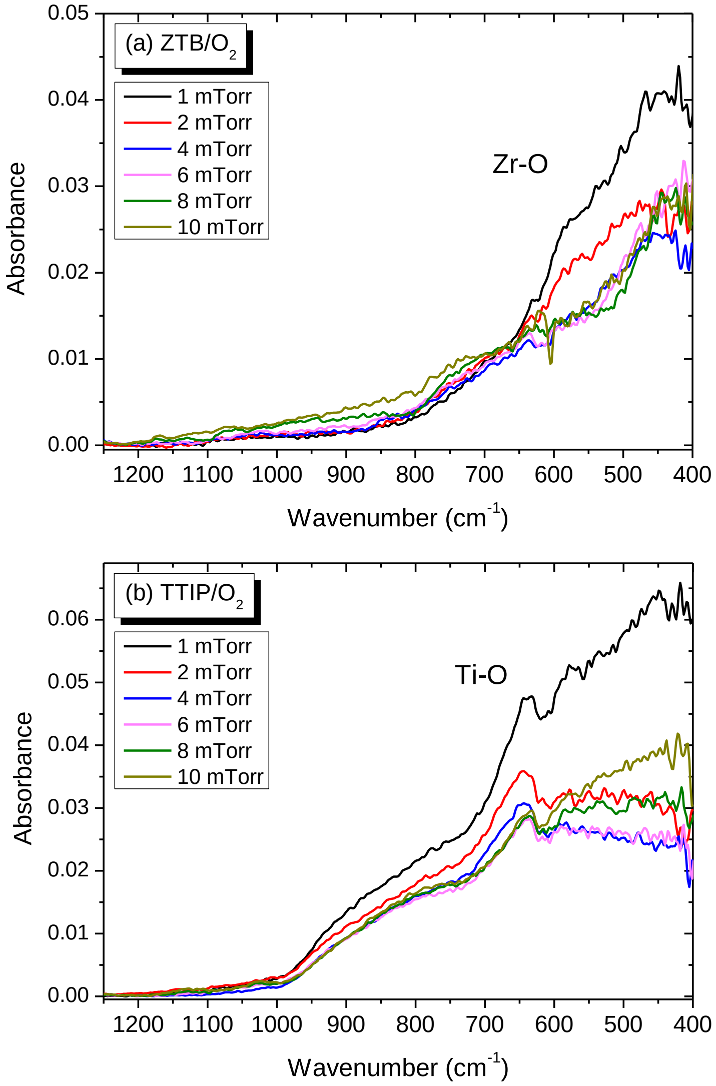

Figure IV-8: FTIR spectra (1250-400 cm^{-1}) of films deposited at different total gas pressures in a) ZTB/O_2 and b) TTIP/O_2 plasma (5% precursor/95% O_2, P_{MW} = 800 W, $V_{substrate}$ = floating). Absorbance: normalised by film thickness.

The IR band, partially spreading over the 1250-400 cm^{-1} range, has been assigned to Zr-O and Ti-O bonds in zirconia-like and titania-like films, respectively (Chapter III.3.2.1, p.82). Highest intensity corresponded to films deposited at 1 mTorr. A decrease in intensity occurred when pressure increased to 2 mTorr. Afterwards, at higher pressures, intensity of the band remained relatively stable. This behaviour was characteristic to films deposited in ZTB/O_2 as well as in TTIP/O_2 plasma.

IV.2.3 Thin film chemical composition and bonding: summary

The influence of variations in total gas pressure on chemical composition and chemical bonding of the thin film has been examined. The stoichiometric ratios corresponding to films deposited in ZTB and TTIP plasmas evolved in a similar manner as can be seen in Figure IV-9. Relative to the metal atom (Zr or Ti), films became richer in carbon and oxygen atoms. Since the growth rate increased with pressure, it is improbable that the deposition of metal atoms increased. Therefore, this development, measured by XPS, is mainly due to enhanced incorporation of carbon and oxygen atoms into the films as pressure increased.

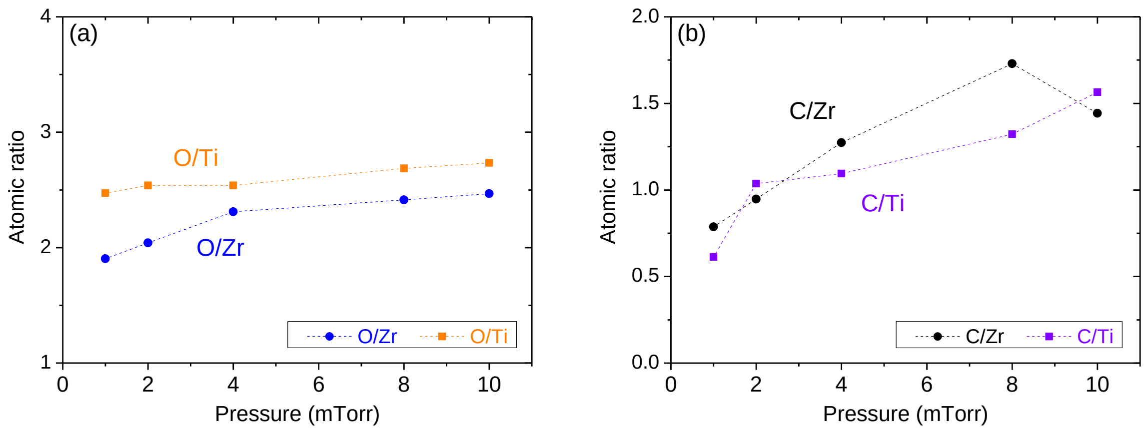

Figure IV-9: Evolution of (a) O/Zr and O/Ti, (b) C/Zr and C/Ti atomic ratios in thin films deposited at different total gas pressures in ZTB/O_2 and TTIP/O_2 plasma (5% precursor/95% O_2, P_{MW} = 800 W, $V_{substrate}$ = floating).

Regarding the chemical bonding of the thin film, similar behaviour was observed in zirconia- and titania-like films. Changes in chemical composition are manifested in the evolution of chemical bonding. Although the deposition of carbon atoms increased, a modest increase of peaks corresponding to stretching vibration of a C-H bond was observed at highest pressures. Due to a high amount of oxygen gas present in the gas mixture, the carbon had formed single and double bonds with oxygen atoms. This is evidenced by the increase of intensity of the band corresponding primarily to C-O and C=O bonds in carbonate like structures.

The reason for the change in the chemical composition and chemical bonding of the film might lie in the evolution of the chemical composition of plasma leading to different surface mechanisms. With increasing pressure, more particles were injected into the reactor and the MW power transferred to the gas remained constant, implying that the amount of power per particle decreased. The electron temperature decreases with the increase in pressure as reported in literature on multi-dipolar ECR plasma (Figure II-7, p.39) [147]. Energetic electrons are needed to drive the fragmentation process of the precursor molecules. If the electron temperature decreases, the effectiveness of precursor dissociation process should be altered.

Another phenomenon, neglected at very low pressures, might play a significant role: chemical reactions taking place in the plasma phase. The mean free path of the particles in the plasma decreases with pressure since the two are inversely correlated. As an example, an expression for the mean free path λ_{nn} of a neutral molecule between two consecutive neutral-neutral collisions is given as:

$$\lambda_{nn} = \frac{k_B T_n}{p \sigma_{nn}} \qquad \textit{Equation IV-1}$$

where p is the gas pressure, k_B the Boltzmann constant, T_n the gas temperature, and σ_{nn} the effective collisional cross section. Accordingly, collisions become more probable at higher pressures, and the probability of chemical reactions occurring in the plasma phase increases.

The described changes in the plasma processes may lead to a change in chemical composition of the plasma phase, i.e. nature and size of the fragments arriving to the substrate surface. It is possible that the fragments in question become larger and more organic as the pressure increases. Furthermore, due to the reactions of recombination taking place in the plasma phase, and the decrease of the power per particle ratio, the fraction of highly reactive oxygen atoms might decrease leading to less effective etching of carbon atoms from the film surface. Thus, the deposition mechanism is affected, and more carbon and oxygen atoms are incorporated into the films.

IV.3 Thin film morphology

IV.3.1 Evolution of morphological characteristics

ZTB

Figure IV-10 presents the SEM cross-sectional images corresponding to thin films deposited at various ZTB/O_2 gas mixture pressures. In the films obtained at 1 and 2 mTorr, nanometric granular forms are organised in densely stacked columnar structures. In both films, the columns grow in a direction perpendicular to the substrate surface, and their widths seem to increase with height. The examination of SEM images does not indicate a significant difference in the morphological features of these films.

Morphological examination of the film obtained at 4 mTorr reveals columnar growth. Some of the columns appear to be damaged, and the broken pieces can be observed in the SEM cross-sectional image. The breakage has most probably occurred during the cleavage step of the sample preparation process for SEM imaging. The columns are not closely stacked together, yet intercolumnar voids are observable.

At 6 mTorr, two microstructural organizations seem to exist. In the bottom layer of the film, no apparent and defined features are observable, yet the film seems far from compact. In the upper layer, irregular columnar structures were formed. The morphology of the film looks as a transitional step between columnar and homogeneous morphology.

In the cross-sectional images of the films deposited at 8 and 10 mTorr, a void between the substrate and the film is present. This void was most likely formed due to detachment of the film in the course of sample cleavage procedure. At 8 mTorr, a very different morphology develops: no defined features can be recognized. The film consists of fine granular formations and does not seem dense. The film grown at 10 mTorr seems homogeneous, in the sense that no apparent microstructural forms can be observed. The film appears more compact than the film obtained at 8 mTorr; still, it possesses a fine granular nature.

The micrographs presented in Figure IV-11 show the top view of zirconia-like thin films synthesized at different gas mixture pressures. The surface of the thin film deposited at 1 mTorr consists of densely packed mounds. The diameter range corresponding to the mounds correlates well with the widths of the columnar structures at maximum height.

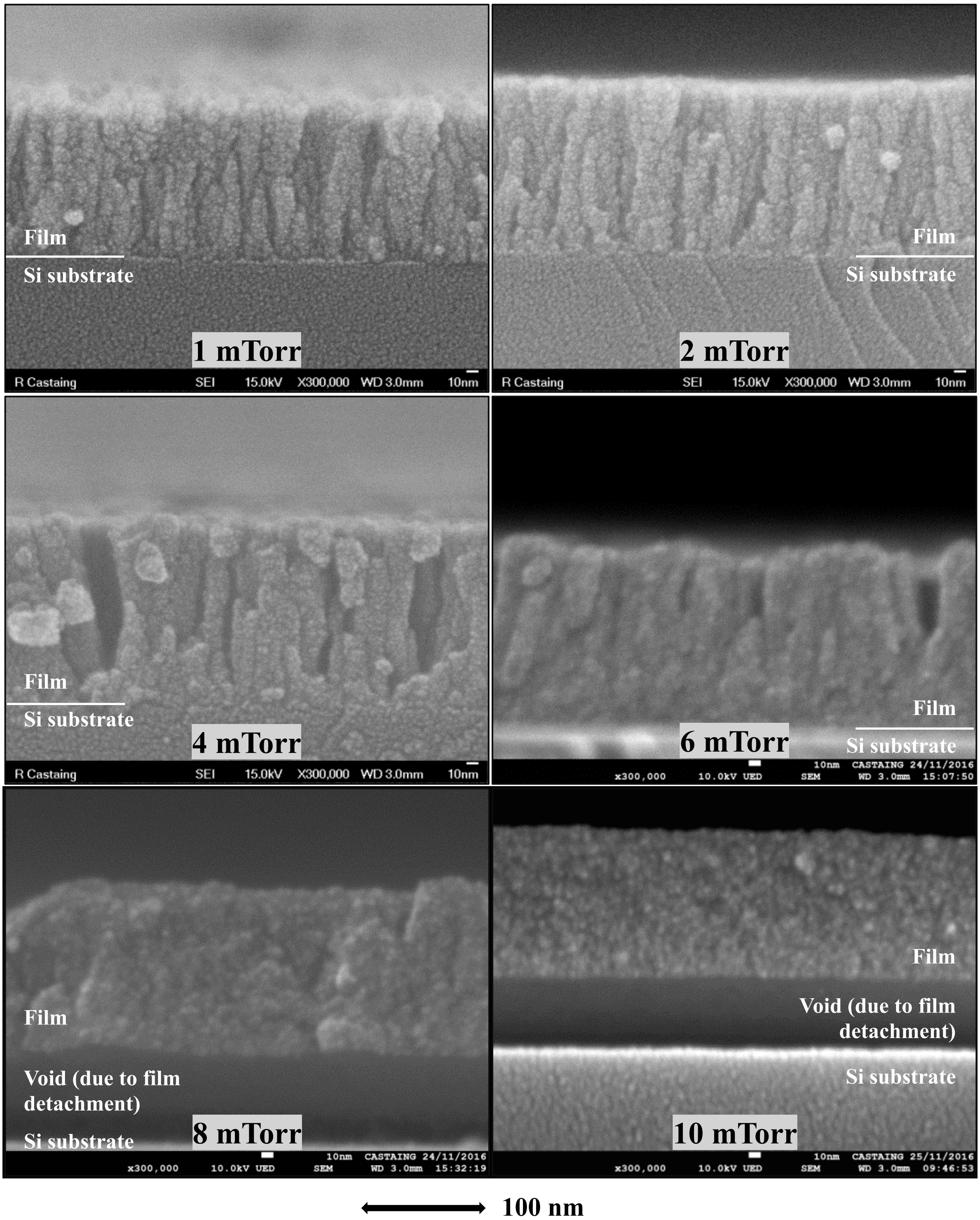

Figure IV-10: SEM cross-sectional images of thin films deposited at different total gas pressures in 5% ZTB/95% O_2 plasma (P_{MW} = 800 W, $V_{substrate}$ = floating).

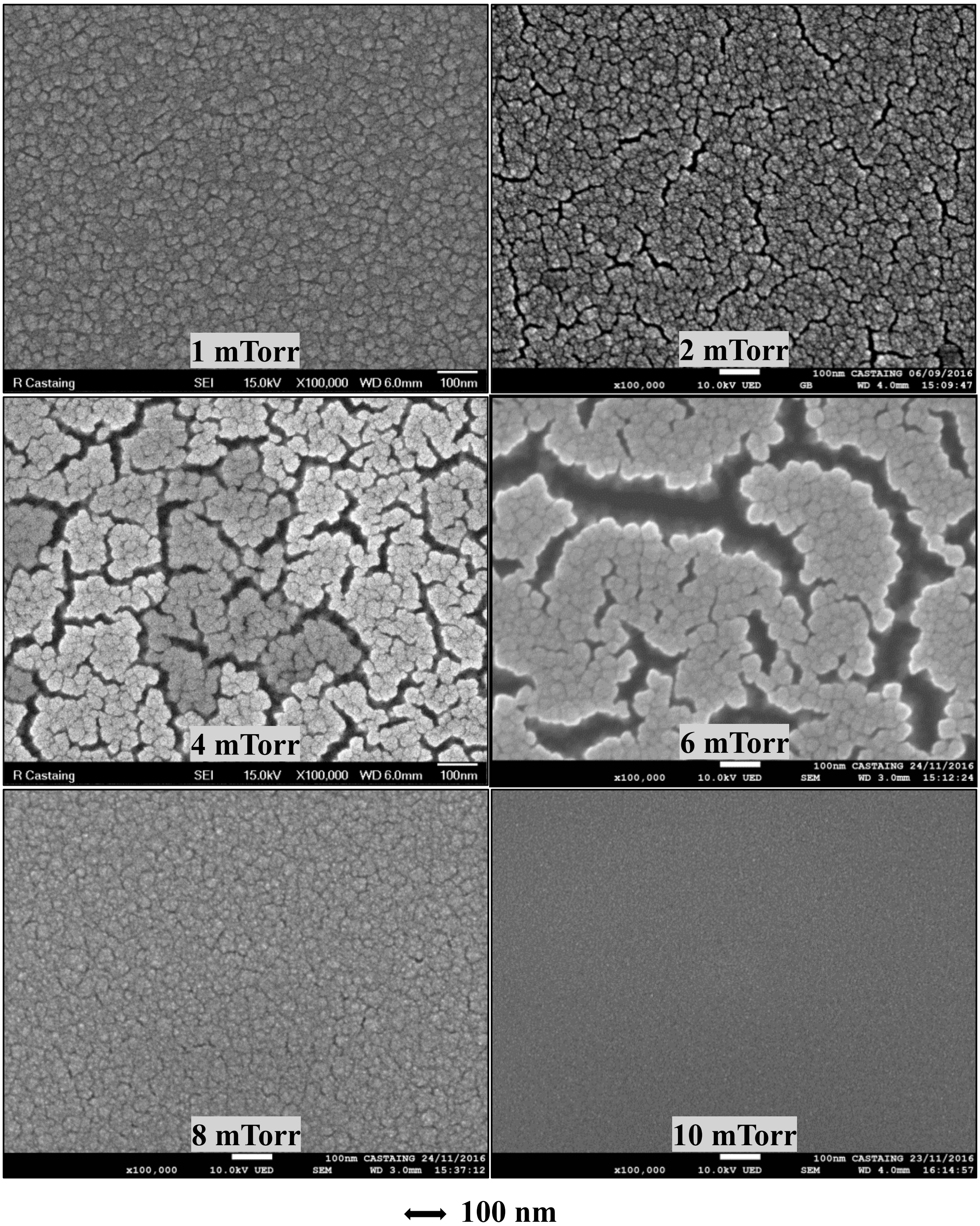

Figure IV-11: SEM surface images of thin films deposited at different total gas pressures in 5% ZTB/95% O_2 plasma (P_{MW} = 800 W, $V_{substrate}$ = floating).

The surface of the thin film deposited at 2 mTorr looks similar to the one of the film obtained at 1 mTorr. The surface is formed by irregularly shaped mounds. All the mounds are not closely stacked together, yet some relatively narrow “cracking” of the surface can be observed.

At 4 mTorr, the film surface is composed of larger “cracks” formed between groups of closely packed mounds. The edges of the mounds are fairly easy to differentiate. The voids observed between the groups of mounds have widths in 15-30 nm range.

The surface of the film grown at 6 mTorr exhibits a combination of larger formations of grouped mounds and wide “cracks”. The mounds are easily distinguishable. The voids observed on the surface have widths in 50-100 nm range. In the image, the edges of the mounds seem to be “glowing”. The bright white contour indicates that surface charging phenomenon occurred during SEM imaging. The film surface, in this case, is magnified 100 000 times. Figure IV-12 shows the micrographs obtained after zooming out at this location on the film surface. The third image represents a magnification of 5000 times: the bright spots correspond to the area that was magnified up to 100 000 times. In those areas, enhanced “cracking” is observed relative to the surrounding film surface which implies an influence of surface charging on the width of the voids present on the film surface. Thus, the surface voids may, in reality, be narrower than observed by SEM imaging.

In the film obtained at 8 mTorr, surface morphology changes drastically. The surface seems much more densely packed and no evident “cracking” forms are observable. The surface exhibits granular topography consisting of not very well-defined shapes.

At 10 mTorr, the film surface evolves even more towards a completely smooth surface on a nanometric level. The SEM image provides an indication of a compact and uniform film surface.

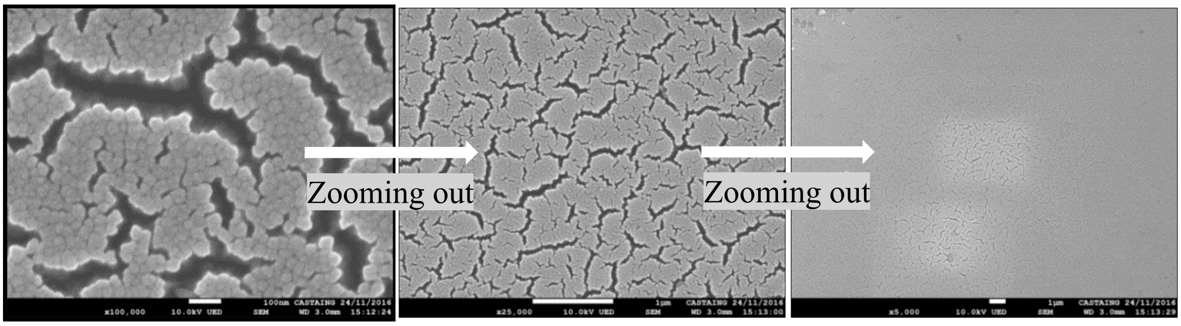

Figure IV-12: SEM images of the same location on thin film surface obtained at different levels of magnification: influence of surface charging. Thin film obtained at 6 mTorr in 5% ZTB/95% O_2 plasma (P_{MW} = 800 W, $V_{substrate}$ = floating).

TTIP

Figure IV-13 shows SEM cross-sectional images corresponding to thin films deposited in TTIP/O_2 plasma at gas mixture pressures from 1 to 10 mTorr. The film synthesized at 1 mTorr exhibits columnar morphology. The columns grow perpendicularly to the surface and appear to be closely stacked together.

With the pressure increased to 2 mTorr, column-like structures seem larger in width relative to the columns observed at 1 mTorr. The width of the columns increases with height, which is difficult to detect at 1 mTorr. The SEM micrograph gives an indication of the presence of narrow voids spreading perpendicularly to the substrate between the columnar structures.

SEM images of the films deposited at 4, 6, 8 and 10 mTorr show similar morphological features. All the films seem to consist of fine grains organized in columnar structures. Broken columns, observed in the images, are most likely a result of the sample cleavage procedure. The irregular columnar structures grow perpendicularly to the substrate and widen with height. Intercolumnar voids, directed from the substrate to the film surface, become more prominent as pressure increases.

Figure IV-14 presents SEM surface images of thin films deposited at different TTIP/O_2 gas mixture pressures. The film obtained at 1 mTorr has a dense, granular surface topography. The diameter range (10-20 nm) corresponding to the surface mounds correlates well with the column widths at maximal height observed in SEM cross-sectional images.

At 2 mTorr, the surface mounds (diameters in 25-45 nm range) become larger in comparison to the ones seen at 1 mTorr. This development is in accordance with the increase in column widths observed at maximum height.

In thin films deposited at 4-10 mTorr, the surface mounds are of similar sizes as the ones seen at 2 mTorr. The film surfaces do not appear densely packed, yet “cracking” formations are observed. These irregularly shaped voids are more pronounced at higher pressures and attain a maximal width of about 20 nm. The surface topography is in agreement with the morphology of the film bulk seen in SEM cross-sectional images.

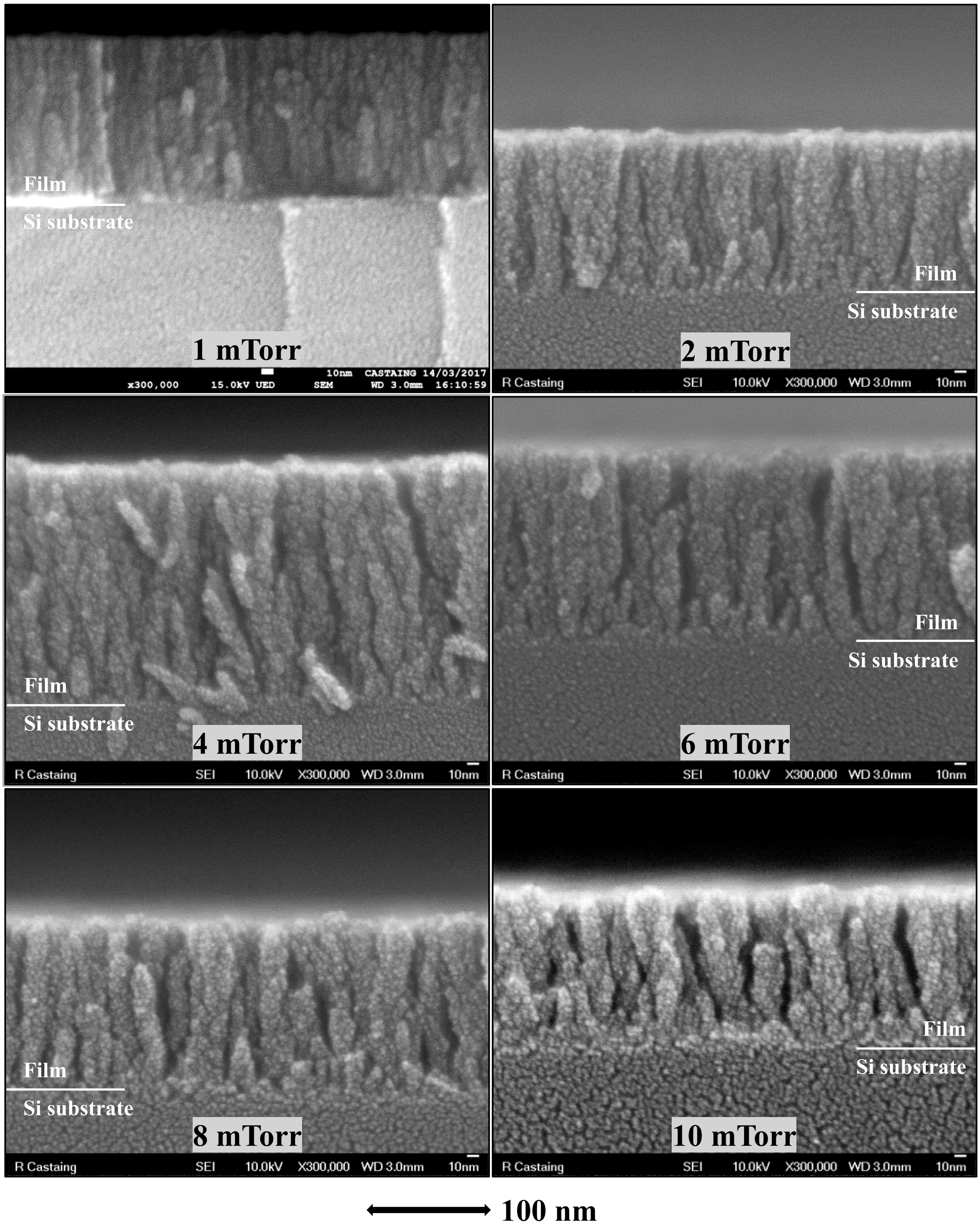

Figure IV-13: SEM cross-sectional images of thin films deposited at different total gas pressures in 5% TTIP/95% O_2 plasma (P_{MW} = 800 W, $V_{substrate}$ = floating).

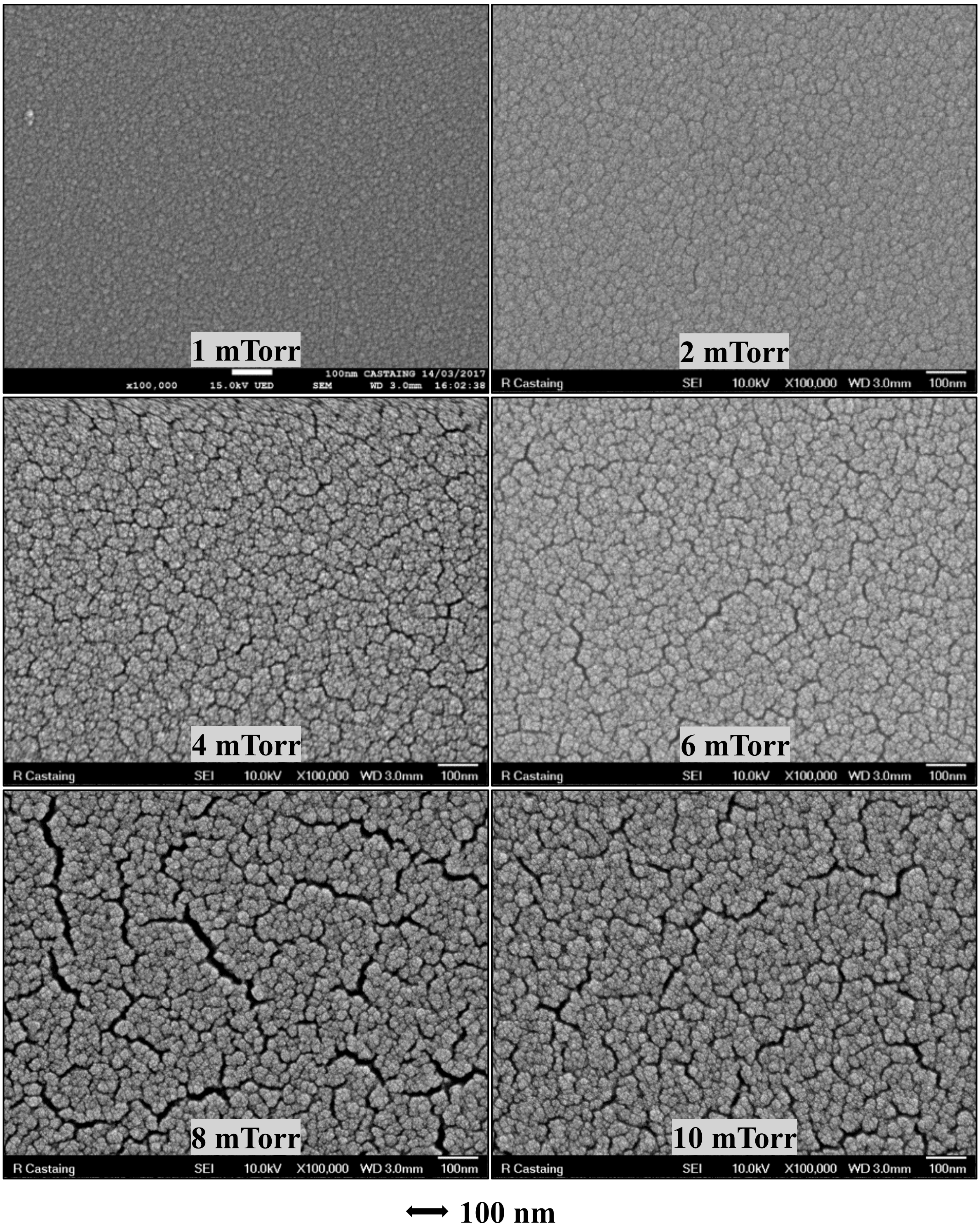

Figure IV-14: SEM surface images of thin films deposited at different total gas pressures in 5% TTIP/95% O_2 plasma (P_{MW} = 800 W, $V_{substrate}$ = floating).

IV.3.2 Morphological changes as a function of pressure: discussion

The previous text introduced observations corresponding to the changes in morphological features of the film bulk and film surface as the pressure of O_2-rich gas mixture increased.

Unlike the similar changes observed in the morphology of the thin film under the influence of oxygen fraction in the precursor/O_2 gas mixture, the increase in total gas pressure results in fairly different microstructural evolution between zirconia-like and titania-like films.

The morphology of films obtained in ZTB/O_2 plasma evolves from columnar to compact, and uniformly in all directions. Thin films exhibit columnar morphology at 1-2 mTorr. At 4 mTorr, the morphology changes significantly: large intercolumnar voids are observed. At 6 mTorr, the bottom film layer is characterized by ill-defined features, while the top layer exhibits irregular columnar structuration. With increase to 8 mTorr, a drastic change leads to no apparent structuration, and at 10 mTorr the film appears to be uniform with a smooth surface on a nanometric scale.

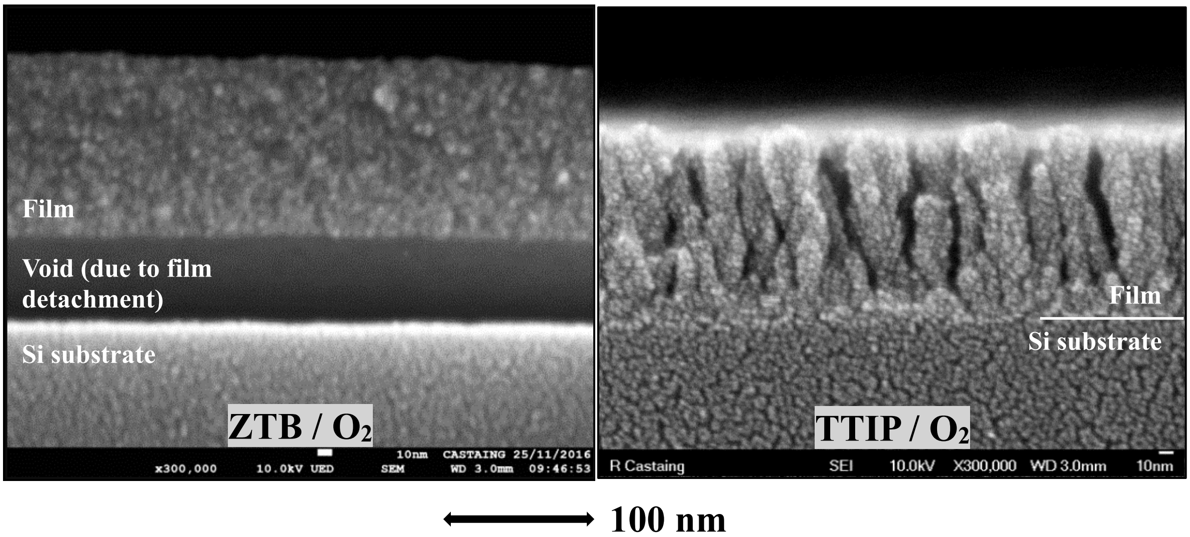

Figure IV-15: SEM cross-sectional images of thin films deposited at 10 mTorr in ZTB/O_2 and TTIP/O_2 plasmas (5% precursor/95% O_2, P_{MW} = 800 W, $V_{substrate}$ = floating).

On the other hand, the evolution of morphological features corresponding to thin films deposited in TTIP/O_2 plasma is much more subtle compared to zirconia-like films. The columnar structures are present in all analysed films. As the pressure increases, the columns and the intercolumnar voids, observed in the cross-sectional and surface SEM images, become wider. Explaining the evolution of film morphology with increasing pressure is a very difficult and complex task due to numerous and complex phenomena occurring in the plasma phase and on the substrate and thin film surface. The increase in pressure entails a decrease in the electron temperature, and the increase in probability of collisions and chemical reactions between species present in the plasma. Pressure increase might also have a significant influence on the gas flow regime, which could affect the particle momentum distribution. The increased deposition rate is also present in this interplay of changing parameters.

The distinction in morphological evolution between zirconia- and titania-like films might be a result of a number of characteristics such as the different precursor molecule or metal atom size and mass, chemical nature of the fragments formed in the plasma phase or surface relaxing mechanisms. The deposition procedures between ZTB and TTIP PECVD differed in the injection systems used for introducing the precursor into the reactor. Semi-automatic system was used for injection of ZTB, whereas a completely manual system was employed to inject TTIP. The dissimilarity in the injection system might lead to the variations of the precursor gas circulation in the reactor. Different flow pathways could induce different levels of precursor fragmentation and influence the collisions that occur in the plasma phase at higher pressures. This might result in a different nature of fragments arriving to the substrate, as well as different momentum distribution of the impinging species between ZTB and TTIP plasma.

IV.4 Characterization of macroscopic physical properties

This paragraph presents the analysis of the macroscopic physical properties of thin films deposited in 5% ZTB/95% O_2 and 5% TTIP/95% O_2 plasmas at gas mixture pressures in 1-8 mTorr range. The particularities and constraints of the EP and XRR techniques employed are commented in Chapter II.5, p.53)

Figure IV-16 shows the evolution of the refractive index, density and nanoporosity fraction of films deposited in ZTB/O_2 plasma. The refractive index (*n*) decreased immediately as pressure increased from 1 to 2 mTorr. With further pressure increase to 4 mTorr, the value of *n* decreased, while from 4 to 8 mTorr it seemed to remain relatively stable. The film density was reduced sharply from 3.6 g/cm^3 at 1 mTorr to 3.0 g/cm^3 at 4 mTorr, then continued a modest decrease to 2.8 g/cm^3 at 8 mTorr. In agreement with the overall density decrease, the fraction of nanometric open pores in the films increased from 2% to 16%.

Evolution of the refractive index and nanoporosity concentration in the films deposited in TTIP/O_2 plasma is graphically presented in Figure IV-17. Due to technical issues, the titania-like film samples were difficult to analyse by XRR and the obtained density values are not reliable enough to be included in the results presented here. Regarding refractive index values, a high rate of decline was observed: from 2.10 to 1.74 at 1 mTorr and 4 mTorr, respectively.

From 4 to 8 mTorr, *n* increased slightly to 1.79. The nanoporosity fraction of films was undetectable at 1 and 2 mTorr. However, it reached a value of 10% at 8 mTorr.

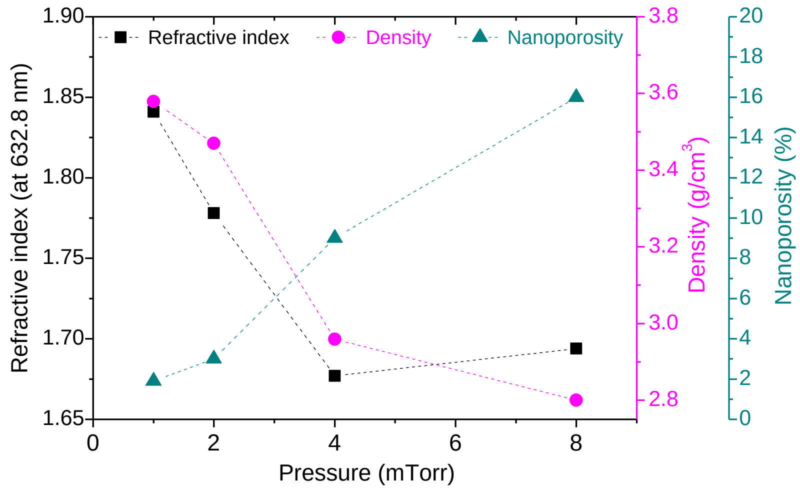

Figure IV-16: Refractive index, density and nanoporosity fraction of thin films deposited in ZTB/O_2 plasma as a function of total gas pressure (5% ZTB/95% O_2, P_{MW} = 800 W, $V_{substrate}$ = floating).

The refractive index of both kinds of films decreased with pressure in a similar manner. It has been shown that the increase of carbon fraction in the metalorganic films leads to lowered refractive index [11], [213]. XPS study has established that the C/M and O/M atomic ratios (M: metal atom) characteristic to the films increased with pressure (Table IV-2, p.121). Additionally, the XRR analysis of zirconia-like films demonstrated that the film density was reduced which implies that the void concentration increases and consequently the refractive index decreases. The change in nanoporosity fraction agrees with evolution of *n* and density values.

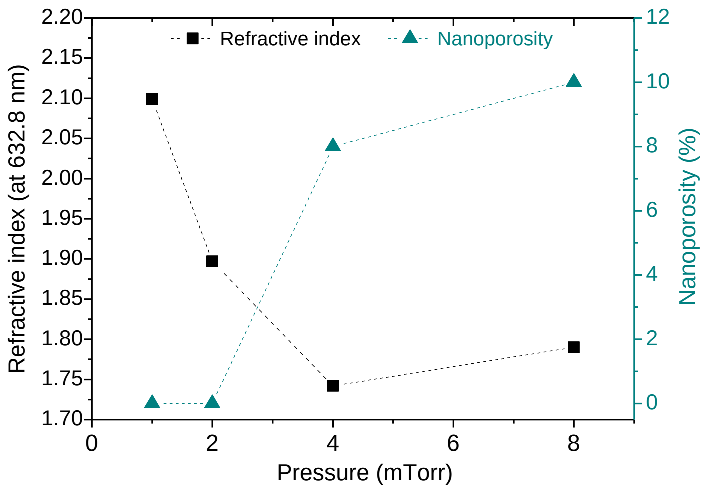

Figure IV-17: Refractive index and nanoporosity fraction of thin films deposited in TTIP/O_2 plasma as a function of total gas pressure (5% TTIP/95% O_2, P_{MW} = 800 W, $V_{substrate}$ = floating).

IV.5 Summary

In Chapter IV, we have studied the modifications of thin film characteristics that were induced by the increase in total pressure of oxygen-rich metalorganic plasma gas mixture (5% precursor/95% O_2). It has been shown that the deposition rate continuously increases with pressure. In general, films become richer in carbon and oxygen atomic content relative to the metal atom. Furthermore, an increase in concentration of C-O and C=O bonds forming the carbonate-like environment in the films has been detected.

A striking difference has been observed in the evolution of the growth mode between ZTB and TTIP plasma. It has been shown that the columnar structures disappear at 8 mTorr in films deposited in ZTB plasma. In contrast, films grown in TTIP plasma exhibit columnar growth over the whole measured pressure range. Regarding macroscopic characteristics, the refractive index decreases with pressure. The overall density (measured only for $ZrO_xC_yH_z$ films) decreases as well. On the other hand, the open nanoporosity content in the films increases with total gas pressure, although it is remaining relatively low (10-16% at 8 mTorr).

Chapter V

Thin film growth in metalorganic/organosilicon/O_2 plasma

Introduction

Chapter V explores PECVD synthesis of “composite” $ZrSi_xO_yC_zH_w$ and $TiSi_xO_yC_zH_w$ thin films. Film characteristics are examined as a function of HMDSO gas addition to a plasma gas mixture of metalorganic precursor and O_2. Deposition parameters are presented in Table V-1. High quantity of oxygen gas was chosen since columnar morphology develops in O_2-rich metalorganic PECVD, as presented in Chapter III. It was of interest to examine the behaviour of columnar growth as HMDSO is introduced to the gas mixture. In other studies, it has been reported that columnar structures disappear with addition of an organosilicon precursor to metalorganic/O_2 plasma gas mixture [13].

This chapter is divided into four parts. First, the deposition rate is presented. Second, chemical composition and FTIR spectra are analysed. Afterwards, we examine the morphological features of the films and we conclude with a comparison of refractive index and nanoporosity between the deposited thin films.

Table V-1: Thin film deposition parameters in ZTB/HMDSO/O_2 and TTIP/HMDSO/O_2 plasmas.

Total gas pressure	2.00-2.50 mTorr		
MW power	800W		
Substrate	Si (100)		
Substrate potential	Floating		
$T_{substrate}$	Uncontrolled; <100°C		
Deposition time	< 15 min		
ZTB / TTIP partial pressure	0.10 mTorr		
O_2 partial pressure	1.90 mTorr		
HMDSO partial pressure	0.10 mTorr	0.30 mTorr	0.50 mTorr
HMDSO fraction in the gas mixture	4.8%	13.0%	20.0%

It is important to note the difference in gas injection process of ZTB and TTIP. Due to reasons discussed in the introduction of Chapter IV (p.117), fraction of TTIP gas in the plasma gas mixture might, in fact, be different than the indicated values.

V.1 Deposition rate

Figure V-1 shows the evolution of the deposition rate with the addition of HMDSO into the plasma gas mixture. The growth rate increases as the organosilicon precursor is added to ZTB/O_2 and $TTIP/O_2$ gas mixtures. The observed evolution was attributed to an increase of the quantity of matter in the plasma gas mixture. Since the amount of metalorganic precursor and oxygen gas injected into the reactor was constant, and HMDSO was added to the mixture, the amount of matter available for deposition increased.

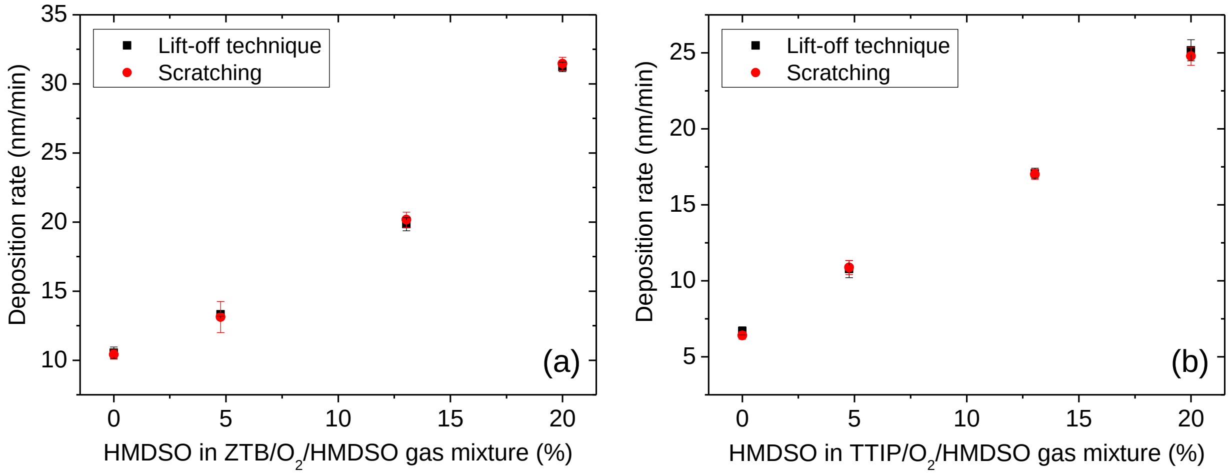

Figure V-1: Deposition rate of thin films grown in (a) $ZTB/HMDSO/O_2$ and (b) $TTIP/HMDSO/O_2$ plasma (p_{total}= 2.0-2.5 mTorr, P_{MW} = 800 W, $V_{substrate}$= floating). Error bars correspond to standard deviation.

In our experimental configuration, the growth rate of a thin film in 5% HMDSO/95% O_2 at 2 mTorr is relatively low: ~3.7 nm/min. A comparison with deposition rates in metalorganic/O_2 and metalorganic/HMDSO/O_2 plasmas is reported in Table V-2.

Table V-2: Growth rates of thin films obtained in different gas mixtures at identical precursor partial pressures ($p_{HMDSO\ or\ ZTB\ or\ TTIP}$ = 0.10 mTorr, p_{O2} = 1.90 mTorr, p_{total}=2.0-2.1 mTorr, P_{MW} = 800 W, $V_{substrate}$ = floating).

Plasma gas mixture	Deposition rate (nm/min)
5% HMDSO / 95% O_2	3.7 ± 0.1
5% ZTB / 95% O_2	10.5 ± 0.4
5% TTIP / 95% O_2	6.7 ± 0.3
4.76% ZTB / 4.76% HMDSO / 90.48% O_2	13.3 ± 0.1
4.76% TTIP / 4.76% HMDSO / 90.48% O_2	10.8 ± 0.6

V.2 Thin film chemical composition and bonding

V.2.1 Chemical composition

XPS technique was used to investigate atomic composition of thin film as HMDSO was introduced into the metalorganic/O_2 gas mixture. To verify the film homogeneity in terms of chemical composition, in-depth profiles were obtained by employing Ar ion etching during XPS measurements. The profiles corresponding to films synthesized in ZTB/HMDSO/O_2 and TTIP/HMDSO/O_2 plasmas are shown in Figure V-2.

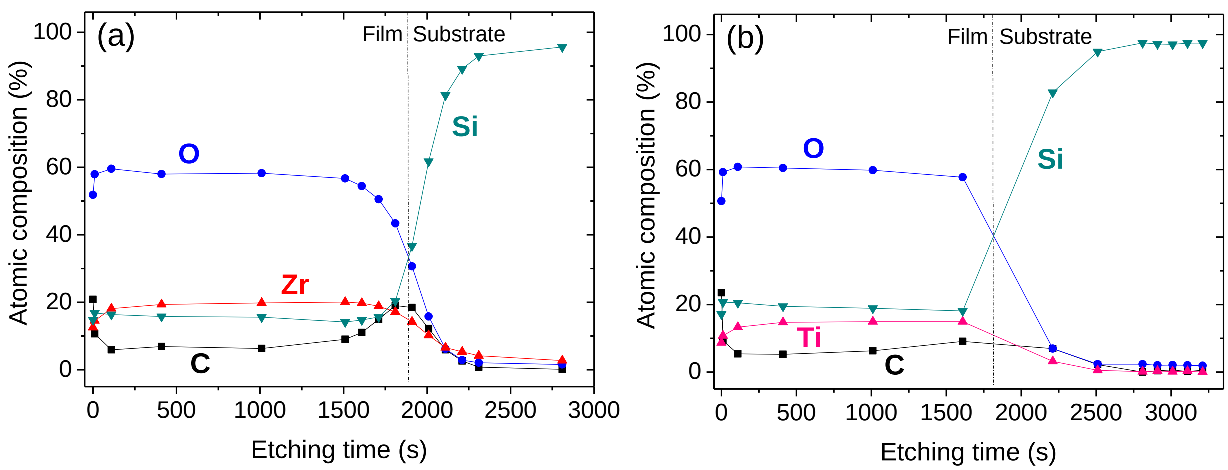

Figure V-2: XPS in-depth chemical composition profile of thin films deposited in (a) 4% ZTB/13% HMDSO/83% O_2 and (b) 4% TTIP/13% HMDSO/83% O_2 plasma (p_{total} = 2.3 mTorr, P_{MW} = 800 W, $V_{substrate}$ = floating).

In-depth analysis confirmed that the atomic content was homogeneously distributed throughout the film bulk. Differences were observed in the film substrate interface and at the film surface. The profile of the film deposited in ZTB/HMDSO/O_2 indicates an increase of the carbon atomic percentage at the film-substrate interface. The increase is not visible for the film deposited in TTIP/HMDSO/O_2, yet at this moment it is not possible to discard its presence since more measurement points are needed in the film-interface region. This phenomenon has been observed in films deposited in O_2-rich ZTB/O_2 plasmas by Mr R. Cozzolino, in the framework of his thesis at LAPLACE laboratory [11]. Carbon interface origin has been attributed to the physisorption of precursor molecules during the gas injection stabilisation step. Hydrocarbons originating from reactor walls, coated in previous deposition processes, have been identified as an additional contamination source. These hydrocarbon species are etched and contribute to film growth in the initial moments after the plasma generation step. To avoid this contamination, it is necessary to protect the substrate during gas flow stabilisation and initial "transitional" regime.

A difference in composition was observed for the first few measurement points that correspond to the film surface. A comparison between the bulks and the surfaces is presented in Table V-3.

Table V-3: Comparison of surface and bulk chemical composition analysed by XPS (p_{total} = 2.3 mTorr, P_{MW} = 800 W, $V_{substrate}$= floating).

	4% **ZTB** / 13% **HMDSO** / 83% **O_2**		4% **TTIP** / 13% **HMDSO** / 83% **O_2**	
	Stoichiometry	Carbon at. %	Stoichiometry	Carbon at. %
Surface	$ZrSi_{1.2}O_{4.1}C_{1.7}$	20.8%	$TiSi_{2.0}O_{5.8}C_{2.7}$	23.5%
Bulk	$ZrSi_{0.8}O_{3.0}C_{0.4}$	~6.5%	$TiSi_{1.3}O_{4.0}C_{0.4}$	~5.5%

Our objective was to study the evolution of the chemical composition, not the absolute values. Therefore, assuming the surface contamination level had not varied significantly between different samples, we have opted for XPS surface analysis instead of in-depth analysis to reduce time and financial costs. The XPS data concerning thin films deposited at different HMDSO amounts added to the gas mixtures is summarized in Table V-4.

Table V-4: XPS chemical composition and stoichiometric ratios corresponding to films deposited in ZTB/HMDSO/O_2 and TTIP/HMDSO/O_2 plasmas at different HMDSO fractions in plasma gas mixture (p_{total} = 2.0-2.5 mTorr, P_{MW} = 800 W, $V_{substrate}$ = floating).

HMDSO in plasma gas mixture (%)	**Atomic composition (%)**				**Atomic ratio**		
	M*	**Si**	**O**	**C**	**Si/M***	**O/M***	**C/M***
ZTB / HMDSO / O_2 plasma							
0	25.1	-	51.2	23.7	-	2.0	0.9
4.8	21.2	9.2	55.8	13.8	0.4	2.6	0.7
13.0	15.8	14.5	54.6	15.9	0.9	3.5	1.0
20.0	10.3	16.5	48.2	25.0	1.6	4.7	2.4
TTIP / HMDSO / O_2 plasma							
0	21.8	-	55.5	22.7	-	2.5	1.0
4.8	11.9	13.1	50.7	24.3	1.1	4.2	2.0
13.0	8.7	17.2	50.6	23.5	2.0	5.8	2.7
20.0	5.8	21.0	45.2	28.0	3.6	7.8	4.8

**M corresponds to Zr and Ti for ZTB and TTIP related data, respectively.*

ZTB

Figure V-3(a) graphically presents the evolution of the atomic content in thin films deposited in ZTB/HMDSO/O_2 plasma. Silicon at.% increased, while zirconium at.% decreased with addition of HMDSO to the gas mixture. At first, the fraction of oxygen atoms modestly increased, while afterwards it slowly decreased. The carbon atomic content decreased after initial introduction of HMDSO. With further HMDSO addition, carbon at.% increased steadily. Film stoichiometry changed significantly from $ZrSi_{0.4}O_{2.6}C_{0.7}$ to $ZrSi_{1.6}O_{4.7}C_{2.4}$ at 4.8% and 20% of HMDSO in the gas mixture, respectively.

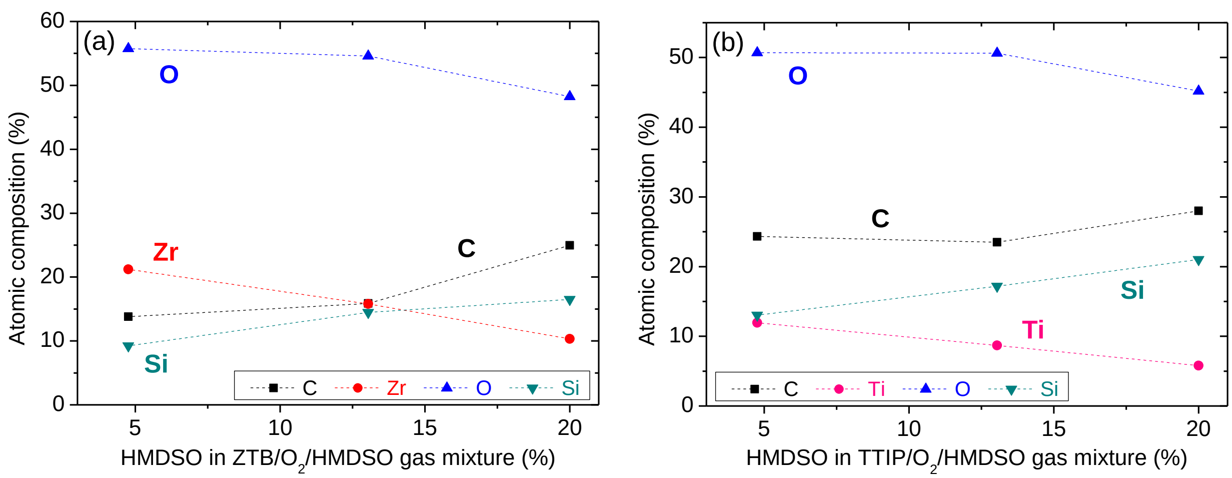

Figure V-3: Atomic composition of thin films deposited in (a) ZTB/HMDSO/O_2 and (b) TTIP/HMDSO/O_2 plasma as a function of gas mixture composition (p_{total} = 2.0-2.5 mTorr, P_{MW} = 800 W, $V_{substrate}$= floating).

TTIP

Figure V-3(b) shows the modifications of film chemical composition as a function of HMDSO addition to TTIP/O_2 plasma gas mixture. Silicon atomic fraction increased as HMDSO was added to the gas mixture, while titanium atomic proportion decreased. Carbon at.% in the films slowly increased, while oxygen at.% decreased. Relative to titanium atoms, the film became significantly richer in oxygen and carbon atoms. Film stoichiometric ratio evolved from $TiSi_{1.1}O_{4.2}C_{2.0}$ to $TiSi_{3.6}O_{7.8}C_{4.8}$ at 4.8% and 20% of HMDSO, respectively.

In comparison to $ZrSi_xO_yC_zH_w$ films, metal atomic fraction in the $TiSi_xO_yC_zH_w$ films is significantly lower, while Si/metal atomic ratio is higher. The observed difference and enhanced incorporation of Si atoms relative to Ti atoms can be explained by considering TTIP gas injection conditions (for more details see the "Introduction" of this chapter). It is possible that the percentage of TTIP in the gas mixture is effectively lower than the recorded value.

V.2.2 Chemical bonding

V.2.2.1 Identification of FTIR spectra

The objective of this subchapter is to investigate chemical bonding in "composite" thin films grown in O_2-rich plasma gas mixture of metalorganic (ZTB or TTIP) and organosilicon (HMDSO) precursors. To facilitate the identification of FTIR spectra of $ZrSi_xO_yC_zH_w$ and $TiSi_xO_yC_zH_w$ thin films, we first introduce the assignations of IR absorption peaks corresponding to thin films synthesized in organosilicon plasma. Figure V-4 presents a comparison of FTIR spectra corresponding to highly organic thin film deposited in 100% HMDSO, and SiO_2-like thin film obtained in 5% HMDSO/95% O_2 plasma gas mixture. The observed peak positions and associated assignations are reported in Table V-5.

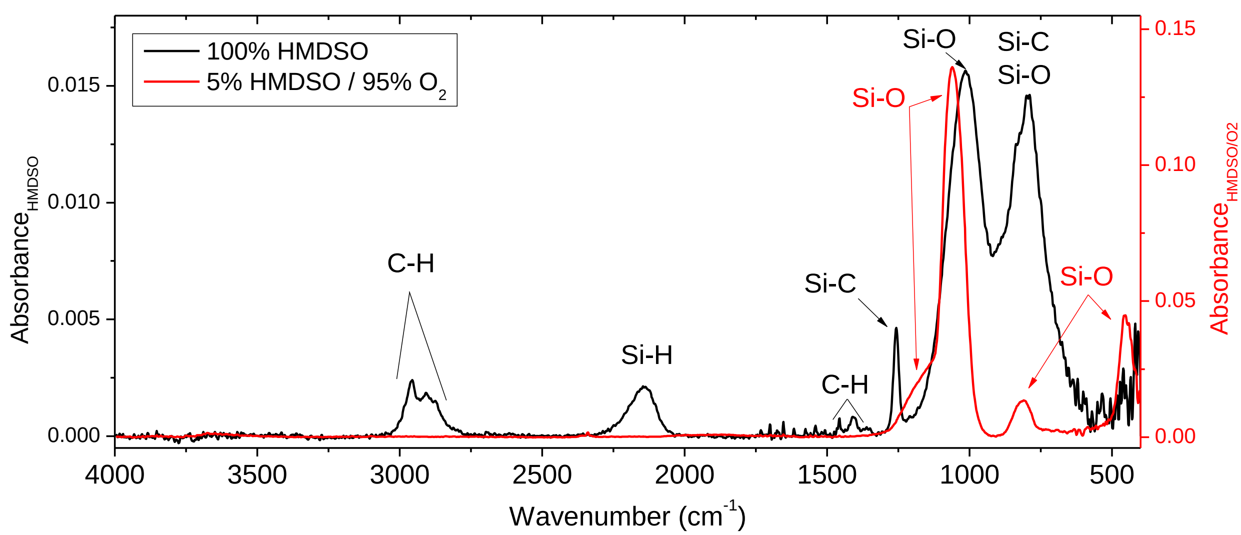

Figure V-4: FTIR spectra corresponding to thin films deposited in 100% HMDSO (p_{total} =1 mTorr) and in 5% HMDSO/95% O_2 (p_{total} = 2 mTorr) plasma (P_{MW} = 800 W, $V_{substrate}$= floating).

FTIR spectra of thin film grown in pure HMDSO plasma include four absorption bands (3000-2800 cm^{-1}, 2141 cm^{-1}, 1480-1330 cm^{-1}, 1258 cm^{-1}) which indicate the presence of hydrocarbon environment in the film. Peaks in 3000-2800 cm^{-1} band correspond to C-H stretching vibrations in CH_x groups [1], [3], [8], [10], [153]. The peak rising at 2141 cm^{-1} has been assigned to Si-H bond stretching [3], [214]. In the 1480-1330 cm^{-1} range, absorption peaks originate from C-H bending modes in CH_x groups [1], [3], [8]. The peak at 1355 cm^{-1} has been related to Si-CH_2-Si structure [214], [215]. At 1258 cm^{-1}, a peak attributed to symmetric bending vibration of Si-CH_x complex is observed [1], [3], [153], [214]. The peaks detected in the 1200-400 cm^{-1} range corroborate the presence of Si-O-Si bridge in the films. Si-O stretching and Si-O-Si bridge bending modes are observed at 1015 cm^{-1} and 795 cm^{-1}, respectively. The Si-O bending mode in Si-O-$(CH_3)_x$ possibly contributes to the 795 cm^{-1} peak [3].

In the spectra corresponding to the film deposited in O_2-rich HMDSO plasma, the bands representing hydrocarbon environments (3000-2800 cm^{-1}, 2141 cm^{-1}, 1480-1330 cm^{-1}, 1258 cm^{-1}) are absent. The peak at 1175 cm^{-1} and a shoulder at 1061 cm^{-1} are assigned to Si-O stretching vibration in the Si-O-Si structure. The peaks at 812 cm^{-1} and 455 cm^{-1} are attributed to Si-O-Si bridge bending mode [3], [216], [217].

Table V-5: Identification of IR absorption peaks corresponding to thin films deposited in 100% HMDSO (p_{total}=1 mTorr; text in black) and 5% HMDSO/95% O_2 (p_{total} = 2 mTorr; text in red) plasma (P_{MW} = 800 W, $V_{substrate}$= floating).

Wavenumber (cm^{-1})	**Assignation**	**References**
2957 2908 2875	C-H stretching in CH_x	[1], [3], [8], [10], [153]
2141	Si-H stretching	[3], [214]
1457 1409 1355	C-H bending in CH_x	[1], [3], [8]
1258	C-H bending and Si-C stretching in Si-CH_3	DFT calculations, [1], [3], [153], [214]
$1175^{shoulder}$ 1061	Si-O stretching in Si-O-Si	[1], [153]
1015	Si-O stretching in Si-O-Si	[8], [10], [217]
$837^{shoulder}$	Si-$(CH_3)_3$ bending	[3], [10], [153]
812	Si-O bending	[1], [216]
795	Si-O bending in Si-O-Si / Si-O-$(CH_3)_x$	[3]
455	Si-O bending in Si-O-Si	[216], [217]

The following text studies chemical bonding of "composite" metalorganic-organosilicon films. The performed identification of infrared absorption peaks in organosilicon and silicon oxide films is coupled with the analysis of FTIR spectra corresponding to metalorganic films carried out in Chapter III (Chapter III.3.2.1, p.82).

ZTB

Figure V-5 graphically presents the FTIR absorption spectrum corresponding to a thin film grown in ZTB/HMDSO/O_2 plasma (see Annex of this work for detailed image of the spectrum). The peaks observed in the spectrum have been assigned to the vibrations of the following bonds: Zr-O, Si-O, Si-C, Si-H, C-O, C=O, C=C, C-H, O-H. The summary of the peak positions and the corresponding assignations is presented in Table V-6.

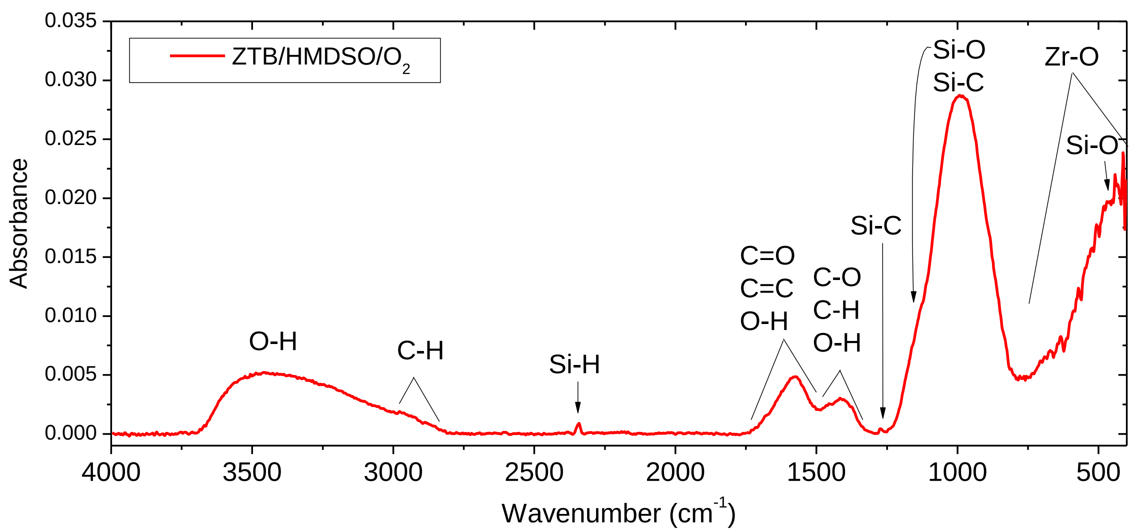

Figure V-5: FTIR spectrum of thin film deposited in 4% ZTB/13% HMDSO/83% O_2 plasma (p_{total} = 2.3 mTorr, P_{MW} = 800 W, $V_{substrate}$ = floating).

The large band spreading over 3720-2800 cm^{-1} was attributed to O-H bond stretching vibrations in H_2O absorbed by the film. This band overlaps with peaks that emerge at 2970 cm^{-1}, 2930 cm^{-1} and 2881 cm^{-1}, and correspond to stretching of the C-H bond in CH_x groups. At 2341 cm^{-1}, a narrow peak appears, assigned to an Si-H stretching mode.

In the complex 1750-1300 cm^{-1} band, four peaks have been identified. The large peak centred at 1575 cm^{-1} and a shoulder at 1700 cm^{-1} were primarily associated with C=O stretching vibrational mode in carbonate-like environments (visualized in Figure III-14, p.84). C=C bond vibrations may also contribute to the peaks in this IR region. The peaks centred at 1457 cm^{-1}, 1415 cm^{-1} and 1375 cm^{-1} were attributed to C-O bond stretching vibration in surroundings rich in oxygen atoms, and to C-H bending modes in CH_x. The bending of the O-H bond may contribute to the complex band that spreads over the 1750-1300 cm^{-1} range.

The IR absorption at 1269 cm^{-1} is characteristic to $Si(CH_x)_y$ structure. The peak corresponds to Si-C stretching and C-H bending vibrational modes.

The peak observed at 984 cm^{-1} and a shoulder at 1150 cm^{-1} were assigned to Si-O stretching vibration. Along with the Si-O vibration, the Si-C bending in $Si\text{-}(CH_x)_y$ structure was attributed to the peak at 984 cm^{-1}. In the 800-400 cm^{-1} range, numerous peaks originating from Zr-O bond vibrations overlap and create a wide band. Since the presence of silicon atoms in the films was confirmed by XPS (Table V-4, p.146), and the Si-O peak at ~1000 cm^{-1} was observed, it is reasonable to expect the appearance of the peak at ~ 450 cm^{-1} which corresponds to the Si-O bending mode.

TTIP

The IR absorption spectrum characteristic to thin films synthesized in TTIP/HMDSO/O_2 plasmas is shown in Figure V-6, while the corresponding numerical data and the peak assignations are reported in Table V-6. Peaks emerging in the spectrum have been assigned to Ti-O, Si-O, Si-C, Si-H, C-O, C=O, C=C, C-H, O-H bonds. The assignations are based on the literature on vibrational spectra of titanium oxide, silicon oxide and titania-silica "composite" films, DFT calculated spectra of HMDSO and TTIP molecules (Figure II-22, p.52, and Figure II-20, p.51) and FTIR analysis of $TiO_xC_yH_z$ (Chapter III.3.2.1, p.82) and $SiO_xC_yH_z$ (Chapter V.2.2.1, p. 148) films performed in this work.

The wide absorption band in 3750-2800 cm^{-1} range corresponds to O-H stretching vibration in absorbed H_2O. In this band, two pronounced peaks that originate from C-H stretching vibration in CH_X structure appear at 2966 cm^{-1}, 2939 cm^{-1}, and 2870 cm^{-1}. At 2339 cm^{-1} a peak assigned to Si-H stretching mode was detected.

The large band in 1750-1300 cm^{-1} range was primarily assigned to C=O and C-O stretching modes in environments similar to carbonate structures (visualized in Figure III-14, p.84). C=C stretching vibration might contribute to the peak found at 1564 cm^{-1} and the shoulder at 1690 cm^{-1}. The peaks identified at 1452 cm^{-1} and 1381 cm^{-1} were assigned to C-O stretching and C-H bending vibrations. At 1270 cm^{-1}, a distinct peak appears, which is ascribed to Si-C stretching and C-H bending in $Si(CH_x)_y$ environment.

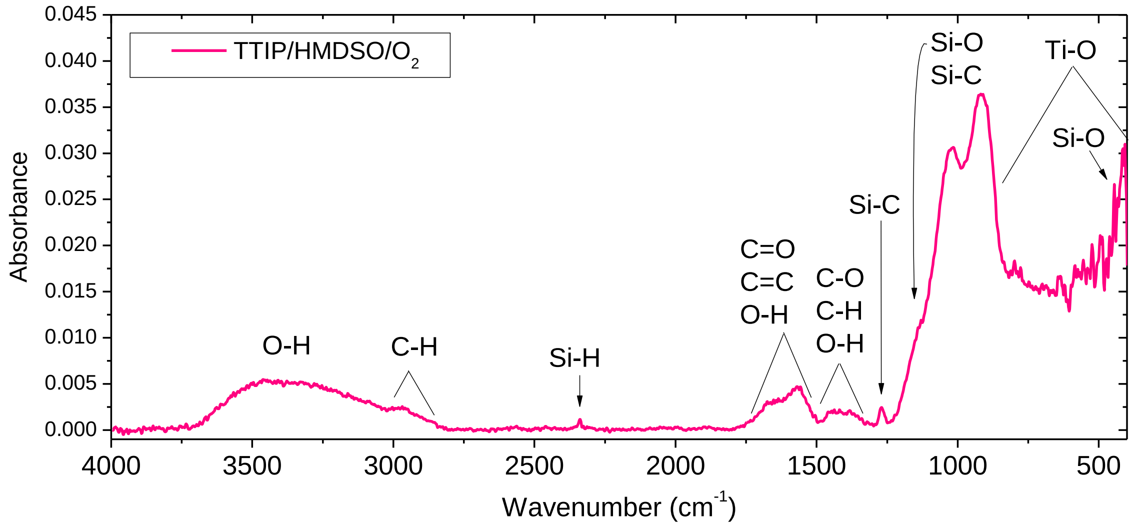

Figure V-6: FTIR spectrum of thin film deposited in 4% TTIP/13% HMDSO/83% O_2 plasma (p_{total} = 2.3 mTorr, P_{MW} = 800 W, $V_{substrate}$ = floating).

In the 1250-400 cm^{-1} range, peaks characteristic to Si-O, Si-C and Ti-O vibrational modes overlap and create a large band. The shoulder at 1152 cm^{-1} and peaks at 1026 cm^{-1}, 916 cm^{-1} and 450 cm^{-1} are attributed to Si-O stretching mode. Peaks emerging at 1026 cm^{-1} 916 cm^{-1} have also been assigned to Si-C bending vibration. Peaks corresponding to Ti-O bonds spread over 1000-400 cm^{-1} region.

Table V-6: Identification of IR absorption peaks corresponding to thin films deposited in ZTB/HMDSO/O_2 and TTIP/HMDSO/O_2 plasma (p_{total} = 2.1-2.5 mTorr, P_{MW} = 800 W, $V_{substrate}$ = floating).

ZTB / HMDSO / O_2		**TTIP / HMDSO / O_2**	
Peak position (cm^{-1})	**Assignation**	**Peak position (cm^{-1})**	**Assignation**
3720-2800	O-H stretching	3750-2800	O-H stretching
2970 2930 2881	C-H stretching in CH_x	2966 2939 2870	C-H stretching in CH_x
2341	Si-H stretching	2339	Si-H stretching
$1700^{shoulder}$	C=O stretching C=C stretching	$1690^{shoulder}$	C=O stretching C=C stretching
1575	C=O stretching C=C stretching O-H bending	1564	C=O stretching C=C stretching O-H bending
1457 1415 1375	C-O stretching O-H bending C-H bending	1452 1381	C-O stretching O-H bending C-H bending

ZTB / HMDSO / O_2		TTIP / HMDSO / O_2	
Peak position (cm^{-1})	**Assignation**	**Peak position (cm^{-1})**	**Assignation**
1269	Si-C stretching C-H bending in Si-$(CH_x)_y$	1270	Si-C stretching C-H bending in Si-$(CH_x)_y$
$1150^{shoulder}$	Si-O stretching in Si-O-Si	$1152^{shoulder}$	Si-O stretching in Si-O-Si
984	Si-O stretching Si-C bending in Si-$(CH_x)_y$	1026 916	Si-O stretching Si-C bending in Si-$(CH_x)_y$
800-400	Zr-O	1000-400	Ti-O
450	Si-O bending	450	Si-O bending

$ZrSi_xO_yC_zH_w$ and $TiSi_xO_yC_zH_w$ thin films exhibit a similar FTIR signature. The observed absorption peaks appear as a combination of peaks detected in spectra of organosilicon (Figure V-4) and metalorganic films (Chapter III.3.2.1, p.82). Several distinctions between the examined IR spectra are reviewed in the following text:

- The band spreading over 3750-2800 cm^{-1} range, attributed to O-H stretching in absorbed H_2O, was detected in films deposited in metalorganic/O_2 and metalorganic/HMDSO/O_2 plasmas. However, this band was not observed in films deposited in HMDSO and HMDSO/O_2 plasmas.
- 1750-1300 cm^{-1} band, primarily assigned to C-O and C=O bonding, is characteristic of metalorganic and "composite" metalorganic-organosilicon films. The band was also detected in the studies of thin films deposited from TEOS plasma [1], [3]. Yet, this band does not appear in the spectra of films synthesized in HMDSO plasma. An explanation of the observed difference might lie in the absence of the C-O bond in the HMDSO molecule, while ZTB, TTIP and TEOS molecules each contain four C-O bonds.
- The peak assigned to Si-H stretching is observed at 2141 cm^{-1} for organosilicon films. The centre of this peak is shifted by ~200 cm^{-1} towards higher wavenumbers (~2340 cm^{-1}) in the spectra of "composite" metalorganic-organosilicon films. It has been shown that the position of the Si-H peak is very sensitive to modifications in the electronegativity of neighbouring atomic groups [218]–[220]. Thus, the observed shift can principally be explained by the change in the environment of the Si atom. Compared films were deposited in 100% HMDSO

and O_2-rich metalorganic/HMDSO plasma. Therefore, the organosilicon film is expected to contain a higher fraction of carbon atoms, whereas the "composite" films should have a lower C at.% and higher O at.%. in comparison. The latter is evidenced by the intense Si-O and M-O (M: Ti or Zr) peaks observed in FTIR spectra and the presence of band corresponding to oxygen rich carbonate structures. To further corroborate our assumption, we have compared the XPS data corresponding to "composite" films (Figure V-2, p.145) with films deposited in 100% HMDSO in similar experimental conditions performed in Laplace Laboratory [3]. XPS has measured ~45 at.% of carbon and ~25 O at.% in organosilicon film, while ~6 C at.% and ~60 O at.% were detected in "composite" films. Accordingly, the Si atom environment is richer in O atoms in examined "composite" films compared to carbon rich surroundings in organosilicon films. The change in neighbouring atomic groups leads to the significant Si-H peak shift due to oxygen being more electronegative than carbon: χ_{oxygen}=3.5 vs χ_{carbon}=2.5.

V.2.2.2 Evolution of thin film chemical bonding with HMDSO addition to ZTB/O_2 and TTIP/O_2 plasma gas mixtures: comparative analysis

In the previous subchapter we have assigned the peaks observed in "composite" film FTIR spectra. In this part, the focus is on the evolution of absorption bands with HMDSO addition to metalorganic/O_2 plasma gas mixture. Figure V-7 presents 4000-400 cm^{-1} spectral range of IR absorbance by thin films grown at different quantities of HMDSO in the gas mixture. The studied IR range has been divided into three regions in the following discussion.

4000-2125 cm^{-1} region

Figure V-8 shows the evolution of film absorption peaks in the 4000-2125 cm^{-1} spectral range with the addition of HMDSO to ZTB/O_2 and TTIP/O_2 plasmas. The wide 3750-2800 cm^{-1} band, assigned to O-H stretching, is present in all the films and indicates the absorption of H_2O from the environment.

O-H band overlaps with peaks characteristic of C-H stretching in CH_x. Nonetheless, it can be observed that the C-H peaks become more pronounced with addition of HMDSO, implying an increase in C-H bonding present in the films.

At ~2340 cm^{-1}, a peak corresponding to Si-H stretching vibration appears with the introduction of HMDSO. Remarkably, the peak absorbance evolves in the same manner in both films synthesized in ZTB and TTIP plasma. With the increase of HMDSO quantity from 4.8% to 13%, the Si-H peak absorbance increases. As we further add HMDSO, at 20%, the peak disappears completely.

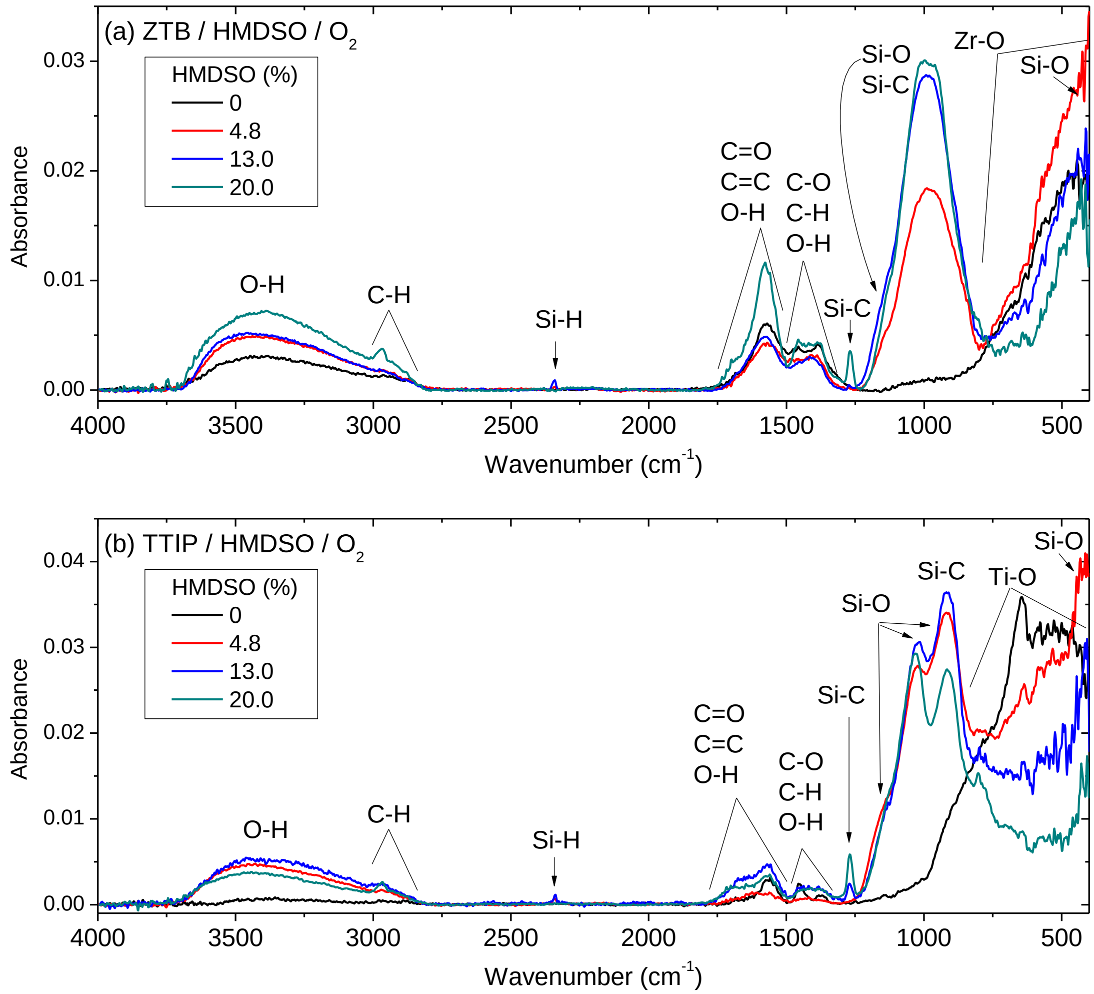

Figure V-7: Evolution of thin film FTIR spectra (4000-400 cm^{-1}) with HMDSO addition to (a) ZTB/HMDSO/O_2 and (b) TTIP/HMDSO/O_2 plasma (p_{total} = 2.00-2.50 mTorr, P_{MW} = 800 W, $V_{substrate}$ = floating). Absorbance: normalised by thin film thickness.

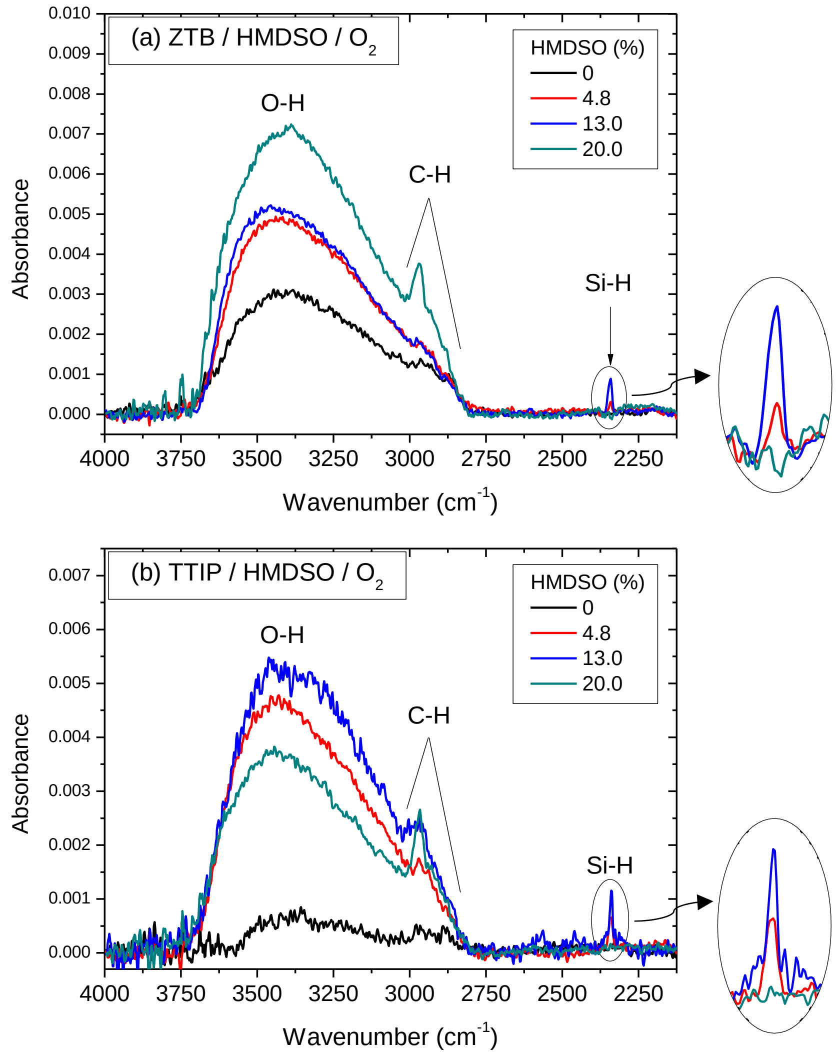

Figure V-8: Evolution of thin film FTIR spectra (4000-1800 cm^{-1}) with HMDSO addition to (a) ZTB/HMDSO/O_2 and (b) TTIP/HMDSO/O_2 plasma (p_{total} = 2.00-2.50 mTorr, P_{MW} = 800 W, $V_{substrate}$ = floating). Absorbance: normalised by thin film thickness.

1800-1230 cm^{-1} region

The modifications of IR spectra in the 1800-1230 cm^{-1} range, induced by the injection of HMDSO into the metalorganic/O_2 plasma gas mixture, are visualised in Figure V-9. Initially adding HMDSO to the gas mixtures leads to a rearrangement of the bonding structure evidenced in the 1800-1230 cm^{-1} band assigned primarily to C-O and C=O bonds in carbonate-like environment. The overall band absorbance decreased, and its shape was modified: the peaks identified for metalorganic films became less distinguishable.

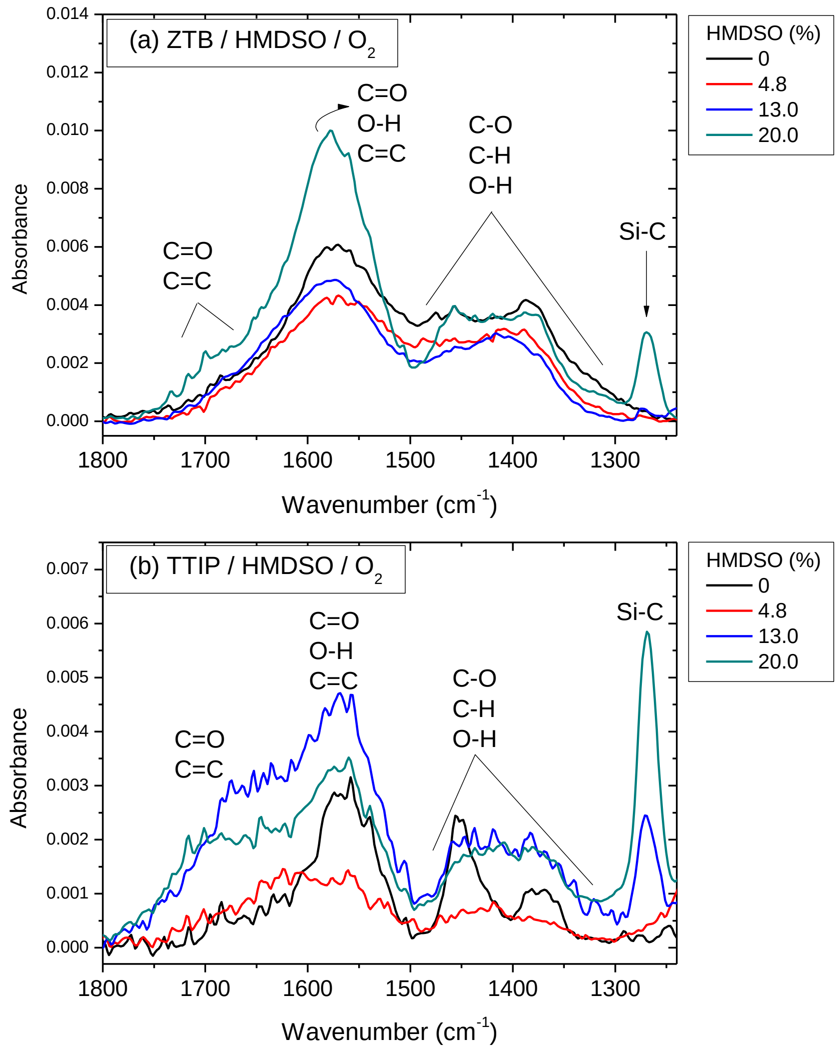

Figure V-9: Evolution of thin film FTIR spectra (1800-1230 cm^{-1}) with HMDSO addition to (a) ZTB/HMDSO/O_2 and (b) TTIP/HMDSO/O_2 plasma (p_{total} = 2.00-2.50 mTorr, P_{MW} = 800 W, $V_{substrate}$ = floating). Absorbance: normalised by thin film thickness.

For $ZrSi_xO_yC_wH_z$ films, the 1750-1300 cm^{-1} band remains fairly constant with HMDSO increasing from 4.8% to 13%. As we further added HMDSO, the shoulder at 1700 cm^{-1} became more pronounced and the absorbance of the peak at 1575 cm^{-1} increased significantly. In the spectra of $TiSi_xO_yC_wH_z$ films, the shoulder at 1690 cm^{-1} and the peak at 1564 cm^{-1} increased in absorbance as HMDSO fraction increased from 4.8% to 13%. With an additional injection of HMDSO, the absorbance decreased.

The absorbance of the 1500-1300 part of the band increased with HMDSO fraction in the gas mixtures. The change is observed at 13% and at 20% for films deposited in TTIP and ZTB plasma, respectively.

Considering that the films are grown in O_2-rich plasmas, and that the 1800-1230 cm^{-1} band is primarily assigned to bond vibrations in carbonate-like structures, the observed evolution implies an increase in concentration of C-O and C=O bonds with HMDSO increase. Moreover, since the peaks representing C-H stretching in CH_x become more pronounced, C-H bending vibration are expected to increasingly attribute to 1500-1300 cm^{-1} band with HMDSO addition.

In "composite" films, a 1270 cm^{-1} peak, assigned to Si-C bond, appeared at 13% of HMDSO and increased in absorbance at 20%. This development implies that the fraction of Si-C bonding in $Si(CH_x)_y$ environment increased with HMDSO.

1230-400 cm^{-1} region

Figure V-10 presents the 1230-400 cm^{-1} region of FTIR spectra corresponding to the examined thin films. With the introduction of HMDSO emerges an absorption band characteristic of Si-O and Si-C vibrations emerges: one large peak and a shoulder are observed in $ZrSi_xO_yC_wH_z$ and two peaks in $TiSi_xO_yC_wH_z$ films.

It appears that the Si-O and Si-C band increased in absorbance as HMDSO proportion increased from 4.8% in ZTB plasma. Concerning films deposited in TTIP plasma, it was difficult to draw conclusions about the evolution of the Si-O and Si-C peaks due to overlapping with Ti-O band.

In general, the absorbance of the M-O (M: Zr or Ti) band decreased with HMDSO addition. The initial increase can be observed in the lowest examined wavenumbers which is most probably the result of the Si-O peak presence that was observed at ~450 cm^{-1} in organosilicon spectra, along with Si-O and Si-C peaks around 1000 cm^{-1}. Since the Si-O peak overlaps with M-O band, it is not possible to distinguish its evolution from the observed spectra.

The review of the 1230-400 cm^{-1} spectral range confirmed the presence of Si-O and Si-C bonding in all "composite" films, as well as a decrease of M-O (M: Zr or Ti) bonding with HMDSO addition.

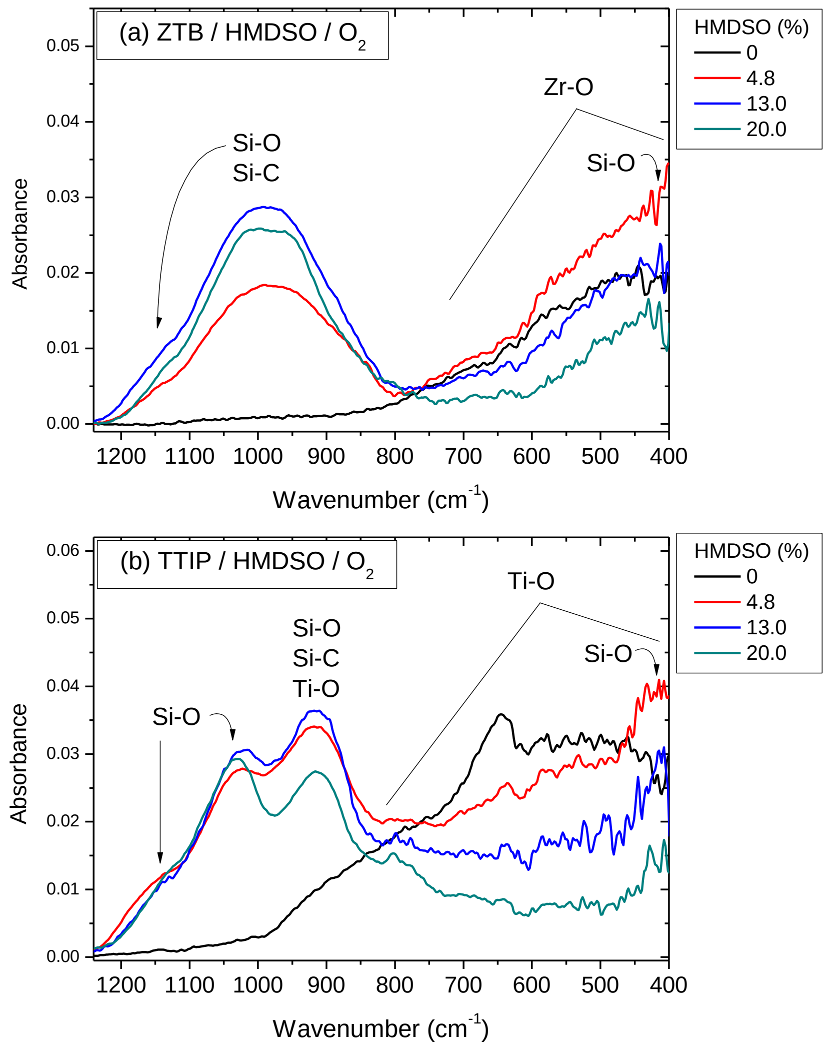

Figure V-10: Evolution of thin film FTIR spectra (1230-400 cm^{-1}) with HMDSO addition to (a) ZTB/HMDSO/O_2 and (b) TTIP/HMDSO/O_2 plasma (p_{total} = 2.00-2.50 mTorr, P_{MW} = 800 W, $V_{substrate}$ = floating). Absorbance: normalised by thin film thickness.

V.2.3 Thin film chemical composition and bonding: discussion

The preceding subchapters have presented the chemical analysis of thin films synthesized in ZTB/HMDSO/O_2 and TTIP/HMDSO/O_2 plasmas. The evolution of chemical composition of the film relative to the metal atom is presented in Figure V-11, whereas the conclusions based on the FTIR study are summarized in Table V-7.

With the introduction of HMDSO into the metalorganic/O_2 gas mixture, the films chemical composition and bonding structure changes. The Si atoms are incorporated into the film as evidenced by XPS analysis, as well as by the appearance of Si-O and Si-C peaks in the IR spectra.

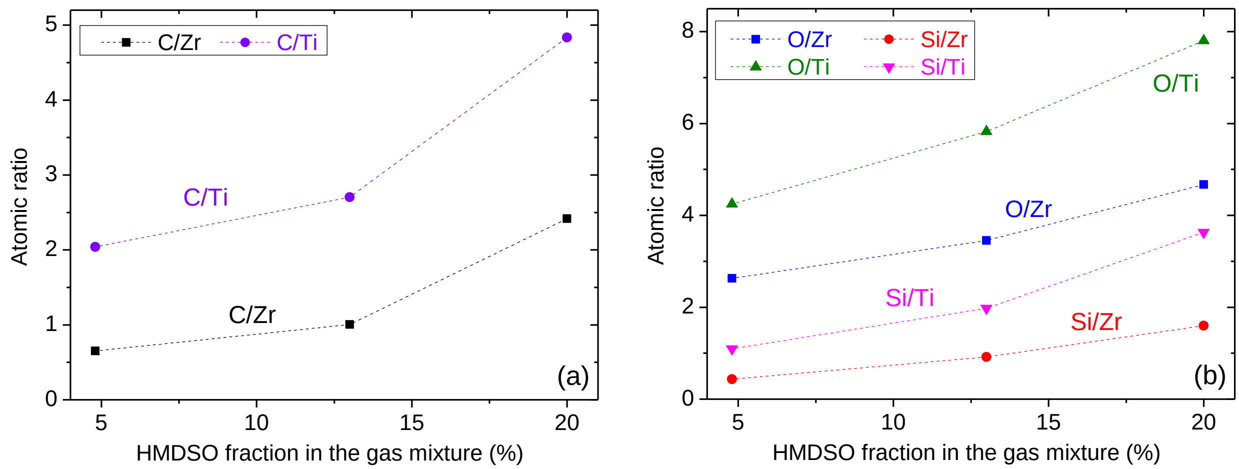

Figure V-11: Evolution of film atomic composition ratios (a) C/M, (b) Si/M and O/M, (M: Zr or Ti) as a function of HMDSO addition to the ZTB/HMDSO/O_2 and TTIP/HMDSO/O_2 gas mixtures (p_{total} = 2.0-2.5 mTorr, P_{MW} = 800 W, $V_{substrate}$ = floating).

As HMDSO proportion increased from 4.8% to 20%, the films became richer in Si, O and C atoms relative to the metal atom (Figure V-11).

- Concentration of M-O (M: Zr or Ti) bonds decreased due to the reduction of metal atomic percentage of the films as evidenced by XPS measurements (Table V-4, p.146).
- Si atoms are increasingly present in the deposits due to the addition of the source molecule (HMDSO) into the plasma gas mixture.
- Increase of carbon at. % with HMDSO addition was attributed to the presence of six carbon atoms in each HMDSO molecule. The carbon atoms that are increasingly incorporated into the films form C-O, C=O, Si-C and C-H bonds.
- In $TiSi_xO_yC_wH_z$ films, the concentration of C-O and C=O bonds in carbonate-like environments decreased to 20% of HMDSO after an initial increase. For $ZrSi_xO_yC_wH_z$ films, a constant increase was observed (Figure V-9, p.157). The difference in the corresponding stoichiometric ratios might provide an explanation: $ZrSi_{1.6}O_{4.7}C_{2.4}$ compared to $TiSi_{3.6}O_{7.8}C_{4.8}$ at 20% of HMDSO. Possibly, the carbon and silicon atomic content increased sufficiently in the films grown in TTIP/HMDSO/O_2 plasma to trigger a decrease in the formation of oxygen rich carbonate-like environment.
- Interesting to note is the disappearance of Si-H bond at 20% of HMDSO for both types of

"composite" films. The peak in question was detected in highly organic silicon oxide film (Figure V-4, p.148). Furthermore, with addition of HMDSO into the metalorganic/O_2 gas mixture, more hydrogen and silicon atoms are available for deposition. Thus, the observed behaviour of the Si-H peak was not expected. For Si-H bond to be formed, fragmentation of HMDSO molecule is necessary: the Si-O bond as well as the C-H bond need to be broken. The disappearance of the Si-H peak might be a result of changes in the chemistry of the plasma phase and/or surface reactions.

Table V-7: Summary of the observations made by FTIR analysis.

Gas mixture modification	Changes in chemical bonding
Introduction of HMDSO	• Zr-O ↘ | Ti-O ↘ • appearance of Si-O, Si-C, Si-H • C-O and C=O ↘ • O-H in absorbed H_2O present
Increase in HMDSO fraction from 4.8% to 20.0%	• Zr-O ↘ | Ti-O ↘ • Si-C ↗ • Si-H first ↗, disappears at 20% • C-H ↗ • O-H in absorbed H_2O present • $ZrSi_xO_yC_wH_z$ films: C-O and C=O ↗ • $TiSi_xO_yC_wH_z$ films: C-O and C=O ↗, at 20% ↘

V.3 Thin film morphology

V.3.1 Evolution of film morphological characteristics

This subchapter focuses on the morphological modifications of films induced by HMDSO addition to the ZTB/O_2 and TTIP/O_2 plasma gas mixtures. Since a mixture of organosilicon and metalorganic precursor was used, it was of interest to compare morphology of thin films deposited in O_2-rich HMDSO plasma with films synthesized in O_2-rich metalorganic plasmas. The corresponding SEM cross-sectional and surface images are shown in Figure V-12. As already presented and discussed in previous chapters, films obtained in 5% ZTB/95% O_2 and 5% TTIP/95% O_2 plasmas at 2 mTorr and floating potential exhibit columnar morphology. The SiO_2-like film, on the other hand, appears homogeneous in all directions. No defined microstructural formations can be distinguished. The surface of the film seems smooth on a nanometric level. To the best of our knowledge, the columnar morphology has not been observed in the numerous studies of organosilicon thin films deposited by low pressure ECR PECVD.

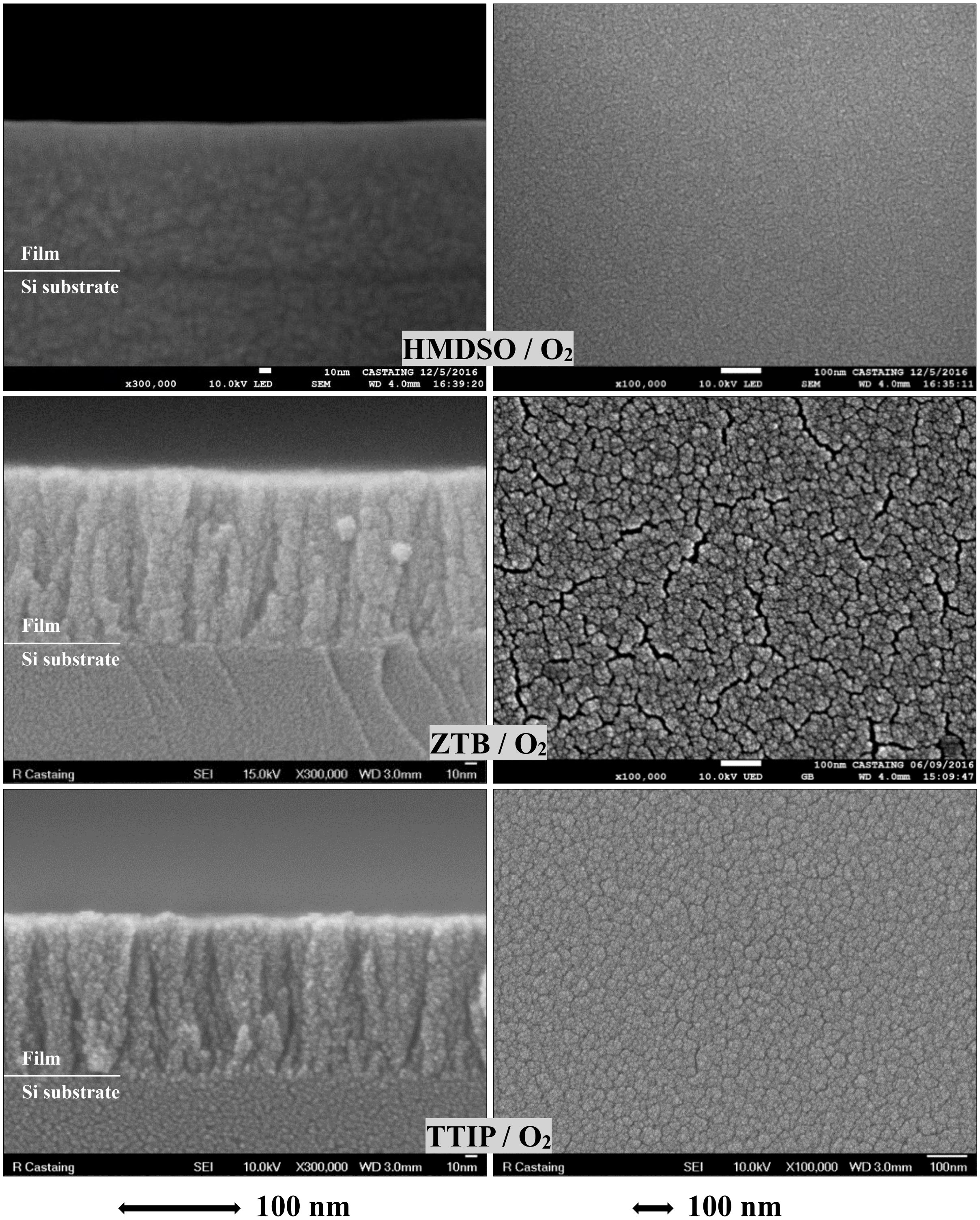

Figure V-12: SEM cross-sectional (left) and surface (right) images of silica-, zirconia- and titania-like thin films (gas mixture: 5% precursor/95% O_2, p_{total}=2 mTorr, P_{MW} = 800 W, $V_{substrate}$ = floating).

ZTB

Figure V-13 shows SEM cross-sectional micrographs of thin films deposited at different quantities of HMDSO in the ZTB/HMDSO/O_2 plasma gas mixture. Thin film obtained in ZTB/O_2 plasma has a columnar morphology. Columnar structures grew perpendicularly to the top surface of the substrate and they do not seem densely stacked. Each column consists of nanometric granular forms.

From what we could observe in the SEM images, the morphology of the film does not appear altered by the introduction of HMDSO into the gas mixture. With further increase, from 4.8% to 13% of HMDSO, the film microstructure was not significantly influenced. The films exhibit columnar morphology extending from the substrate to the top surface of the film.

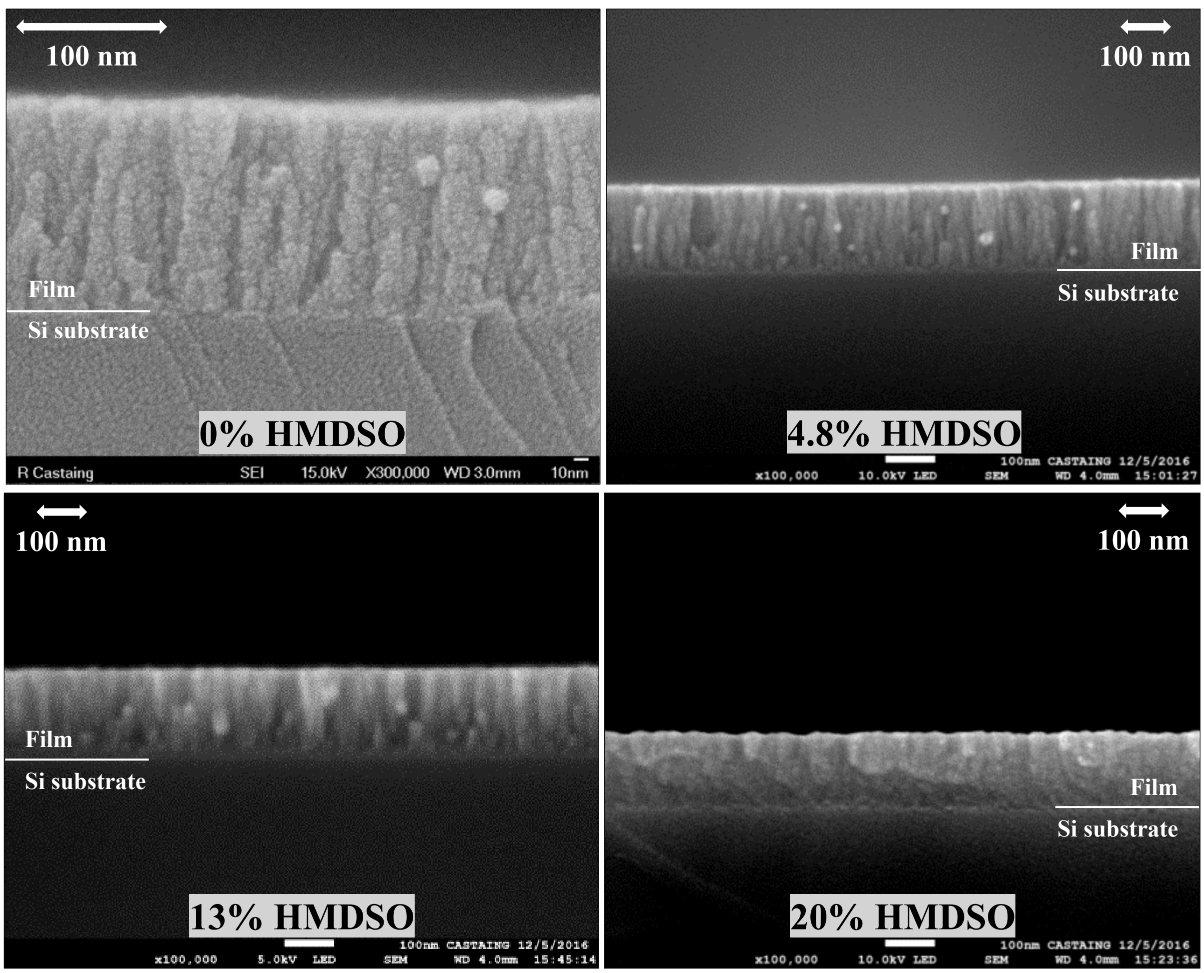

Figure V-13: SEM cross-sectional images of thin films deposited at different quantities of HMDSO in ZTB/HMDSO/O_2 plasma gas mixture (p_{total} = 2.0-2.5 mTorr, P_{MW} = 800 W, $V_{substrate}$ = floating).

At 20% of HMDSO in the gas mixture, the film growth mode was extensively modified leading to the disappearance of columnar growth. The bottom layer of the film seems uniform, whereas in the top layer, the onset of shapes that resemble the columnar structures is observed.

The film surface morphology at different gas mixture compositions can be seen in SEM images presented in Figure V-14. The surface of the film deposited in ZTB/O_2 plasma is composed of unevenly shaped mounds and narrow "cracking" patterns with maximal width of 15 nm.

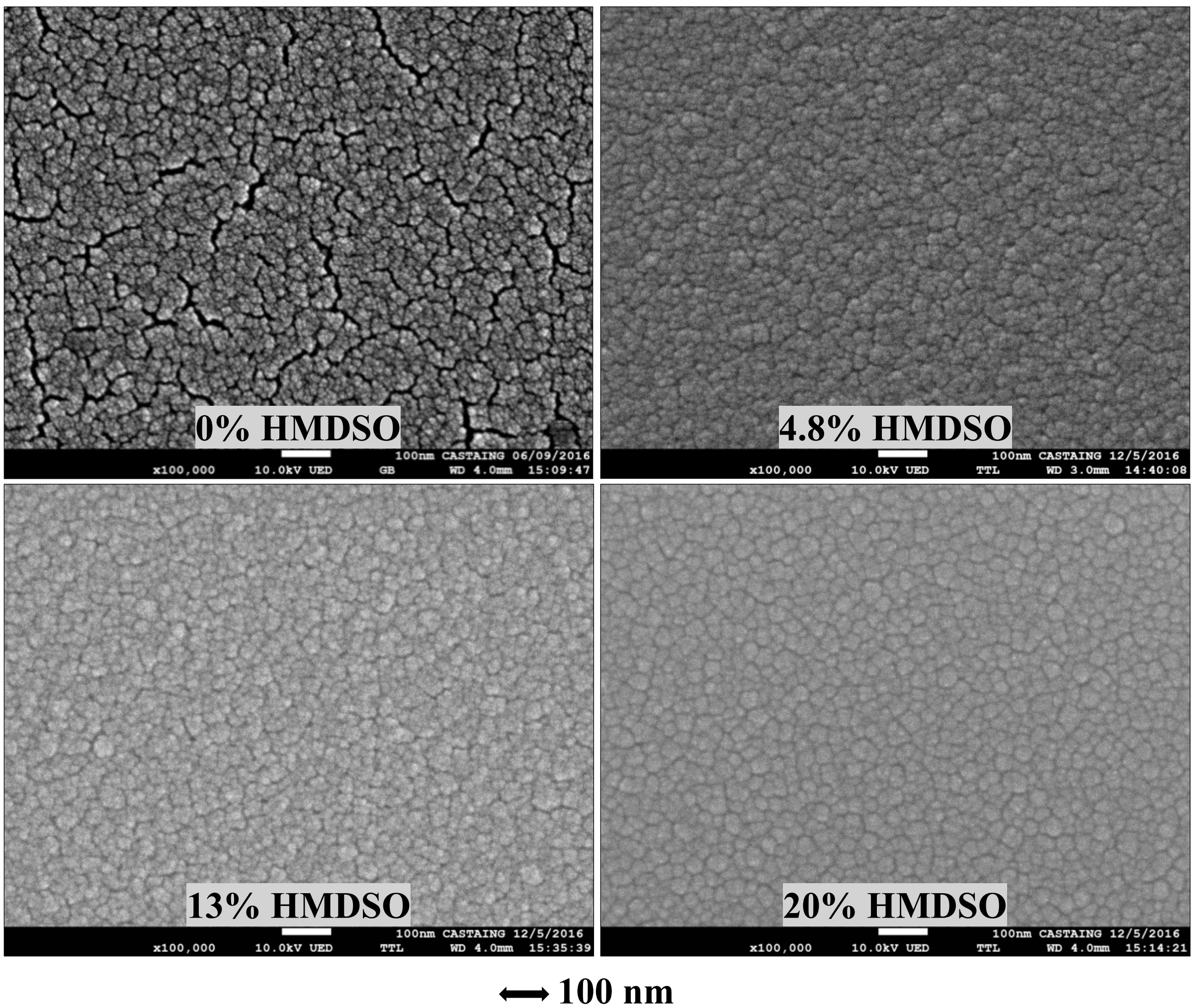

Figure V-14: SEM surface images of thin films deposited at different quantities of HMDSO in ZTB/HMDSO/O_2 plasma gas mixture (p_{total} = 2.0-2.5 mTorr, P_{MW} = 800 W, $V_{substrate}$= floating).

As HMDSO is added to the gas mixture, the evident voids disappear. At 4.8% and 13% of HMDSO, the film surface consists of irregular mounds with diameters mainly in 30-50 nm range.

With further increase to 20% of HMDSO, mounds with more defined edges and rounded shapes have developed. This observation agrees with the cross-sectional morphology of the film, where shapes reminding of columnar structures are observed in the upper layer.

TTIP

The evolution of thin film morphology as HMDSO was added to the TTIP/O_2 gas mixture has been examined by SEM imaging (Figure V-15). The film deposited in TTIP/O_2 plasma exhibits columnar microstructure. The columns grow in a direction perpendicular to the substrate surface and their widths increase with height. Intercolumnar voids can be distinguished in the SEM cross-sectional image. The film is composed of fine nanometric grains organized in columnar structures.

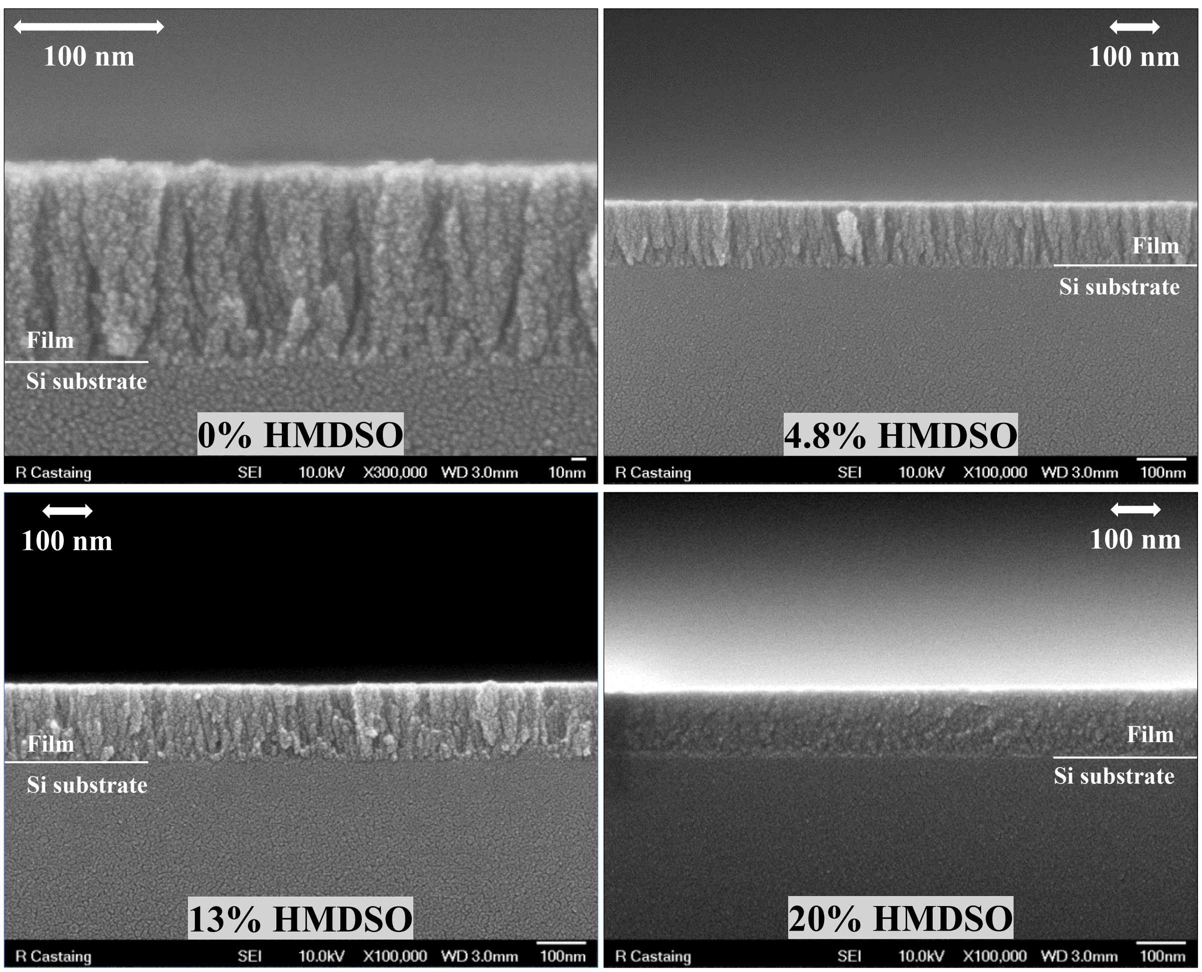

Figure V-15: SEM cross-sectional images of thin films deposited at different quantities of HMDSO in TTIP/HMDSO/O_2 plasma gas mixture (p_{total} = 2.0-2.5 mTorr, P_{MW} = 800 W, $V_{substrate}$ = floating).

When HMDSO is introduced to the gas mixture, thin film morphology remains columnar. It is difficult to distinguish differences in microstructural features between films deposited at 0% and at 4.8% of HMDSO by reviewing the obtained SEM images.

At 13% of HMDSO, the film morphology seems to change slightly, and the columns become less defined. The film is organized in column-like structures that grow from the substrate-film interface to the film top surface. With further increase of HMDSO quantity to 20%, film growth mode undergoes a drastic change. The microstructure appears completely homogeneous with no defined features. The film exhibits a granular nature.

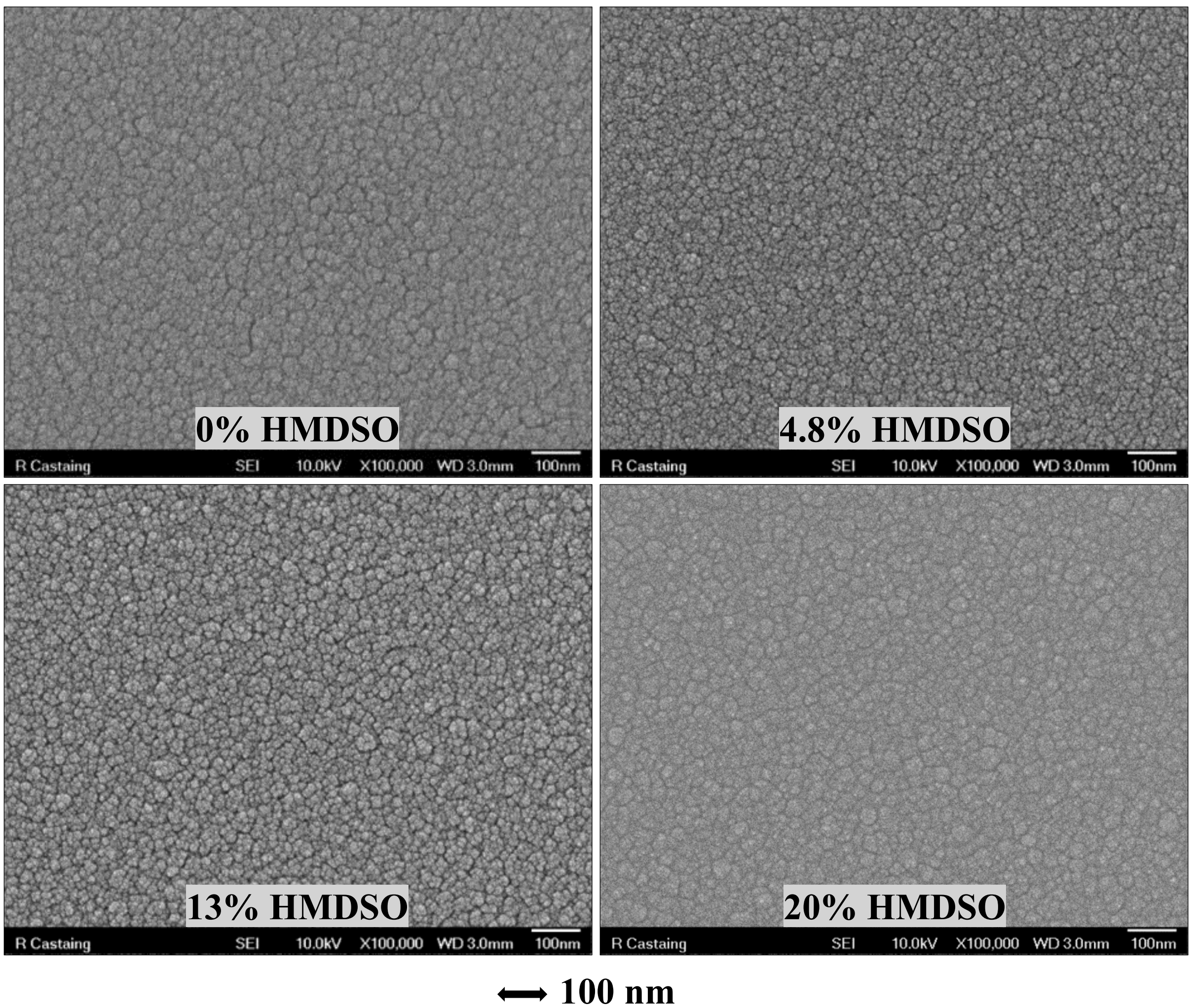

Figure V-16: SEM surface images of thin films deposited at different quantities of HMDSO in TTIP/HMDSO/O_2 plasma gas mixture (p_{total} = 2.0-2.5 mTorr, P_{MW} = 800 W, $V_{substrate}$ = floating).

Figure V-16 shows SEM surface images corresponding to thin films deposited in TTIP/O_2 and TTIP/HMDSO/O_2 plasmas. The addition of HMDSO into the TTIP/O_2 gas mixture does not seem to have a visible influence on the film surface morphology. In all film surfaces examined, fine grains are arranged in irregularly shaped mounds with diameters in the 20-50 nm range. None of the films exhibit formation of surface voids.

V.3.2 Thin film morphology as a function of HMDSO addition to ZTB/O_2 and TTIP/O_2 plasma gas mixture: comparative summary

The SEM imaging provided an insight into the modifications of morphological characteristics in the $ZrSi_xO_yC_wH_z$ and $TiSi_xO_yC_wH_z$ “composite” films, with the addition of HMDSO to the metalorganic/O_2 plasma gas mixture. The SiO_2-like film exhibits a compact and homogeneous microstructure, whereas oxygen-rich metalorganic films have columnar morphology (Figure V-12, p.162). Adding HMDSO to the ZTB and TTIP plasmas has strongly influenced the film microstructural features. At 20% of HMDSO, the columnar morphology of the films disappeared (Figure V-13, p.163 and Figure V-15, p. 165).

In the framework of Mr D. Li’s thesis [13], it has been shown that a small addition of HMDSO to TTIP/O_2 ICP low pressure plasma compromises the columnar morphology of films deposited at floating potential. The columnar morphology disappeared in the film with $TiSi_{0.9}O_{4.0}C_{1.6}$ surface stoichiometry. In our case, the columnar morphology was still present in the $TiSi_{2.0}O_{5.8}C_{2.7}$ film that was richer in Si, C and O atoms relative to ICP grown film. The column-like structures disappeared in the $TiSi_{3.6}O_{7.8}C_{4.8}$ film. This comparison implies that the chemical composition of the film does not play the sole crucial role in the modification of the film morphology.

In the films deposited in ZTB/HMDSO/O_2 plasma, the columnar morphology disappeared in $ZrSi_{1.6}O_{4.7}C_{2.4}$ film. For both types of deposits, columnar growth was observed even at relatively high silicon bulk atomic content (~20%; Figure V-2, p.145). The variations in the HMDSO gas mixture fraction have shown that it is possible to obtain columnar morphology in the films with a wide range of chemical compositions.

V.4 Insight into macroscopic physical properties of "composite" metal-silicon oxide thin films

The following text presents a very succinct inspection of the film refractive index and nanoporosity fraction. Data related to the optical constant is given in Table V-8. The refractive index *n* (at 632.8 nm) of silica-like thin film synthesized in 5% HMDSO/95% O_2 plasma was determined to be 1.48. This value is in agreement with values reported in the literature for silicon dioxide thin films [4], [221], [222]. In comparison, zirconia-like and titania-like films deposited in the same conditions exhibit higher *n* values. The combination of metalorganic and organosilicon precursors resulted in the "composite" films with refractive indices of medium values. Studies of $ZrSi_xO_y$ and $TiSi_xO_y$ films have shown that the refractive index decreases with a decrease in the metal (Zr or Ti) at.% and increase of Si at.% in the films [13], [103]. XPS analysis has shown a decrease of metal atomic fraction in the films, as well as an increase of the silicon at.% with the addition of HMDSO to the gas mixture (Table V-4, p.146).

Table V-8: Refractive index at 632.8 nm of thin films deposited in different plasma compositions (p = 2.00-2.30 mTorr, P_{MW} = 800 W, $V_{substrate}$ = floating).

Plasma gas mixture	Thin film refractive index
5% **HMDSO**/95% **O_2**	1.48
5% **ZTB**/95% **O_2**	1.78
5% **TTIP**/95% **O_2**	1.90
4% **ZTB**/13% **HMDSO**/83% **O_2**	1.66
4% **TTIP**/13% **HMDSO**/83% **O_2**	1.65

Film nanoporosity content was examined by ellipsometric porosimetry. In the films deposited in 5% ZTB/95% O_2 plasma at 2 mTorr, 3% of nanosized pores were detected. The nanoporosity level was undetectable in films grown in 5% TTIP/95% O_2 plasma (p_{total} = 2 mTorr) as well as in "composite" films deposited at 13% of HMDSO in the gas mixture.

V.5 Summary

In this chapter, we have explored the growth of thin films in oxygen-rich plasma gas mixture of metalorganic and organosilicon precursor. The “composite” $ZrSi_xO_yC_zH_w$ and $TiSi_xO_yC_zH_w$ with homogeneously distributed chemical composition have been successfully synthesized.

Characteristics of both types of “composite” films evolve in a similar manner as HMDSO is added to the metalorganic/O_2 gas mixture. The atomic content of silicon, oxygen and carbon in the films increases relative to the metal atomic fraction. The FTIR study confirmed the presence of M-O, Si-O, Si-C, Si-H, C-O, C=O and C-H bonding.

“Composite” thin films exhibit different morphological features depending on the amount of HMDSO added to the gas mixture. At very low HMDSO percentage, the film growth mode remains columnar. With further addition of HMDSO, the columnar structures disappear.

We have shown the possibility of depositing oxide thin films with a vast range of refractive index values, as well as varying morphological features.

Chapter VI

General conclusion and perspectives

A comparative study of thin films synthesized in plasmas generated from two metalorganic precursors, ZTB and TTIP, has been presented in this thesis. Chemical composition, physico-chemical and morphological characteristics as well as macroscopic properties of thin films have been evaluated for different process conditions:

- variation of chemical composition of the plasma gas mixture: increase of oxygen gas percentage from 0% to 95% (at constant total gas pressure of 1 mTorr);
- increase in total gas pressure of 5% metalorganic precursor + 95% O_2 plasma gas mixture.

Furthermore, we have synthesized "composite" $ZrSi_xO_yC_zH_w$ and $TiSi_xO_yC_zH_w$ thin films in oxygen-rich plasma gas mixture of metalorganic (ZTB or TTIP) and organosilicon precursor (HMDSO). Evolution of thin film characteristics has been studied as HMDSO was added to the gas mixture.

Research presented in this manuscript should serve as an advancement towards identifying mechanisms that govern thin film growth in low pressure metalorganic PECVD. A summary of research results and corresponding interpretations is given in the following *text* and *tables*.

Influence of oxygen gas percentage of plasma gas mixture

Film characteristics corresponding to ZTB and TTIP plasmas change in a similar way as the plasma gas mixture becomes rich in oxygen gas. Chemical composition of the films evolves from highly organic to almost inorganic. Accordingly, OES analysis indicates a decline in the concentration of hydrocarbon species. A decreasing amount of carbon atoms is deposited due to precursor dilution and etching achieved by an increasing number of oxygen atoms. Changes in the chemical composition of the films are evidenced in chemical bonding, with films becoming abundant in metal-oxygen bonds. Hydrocarbon environment is replaced by carbonate-like structures rich in oxygen atoms. The concentration of C-O and C=O bonds that form structures such as $Zr(CO_3)$/$Ti(CO_3)$ achieves highest value at ~80% of O_2. With further addition of oxygen gas, this value decreases due to carbon-deficient conditions. OES analysis had indicated analogous behaviour of the concentration of CO and CO_2 species in the plasma phase.

Film morphology films is strongly affected by the variation in plasma gas mixture. Uniform growth is transformed to columnar growth in oxygen-rich conditions. Columnar structures observed in titania-like films are significantly thinner in comparison to zirconia-like films. Monte Carlo simulations have confirmed our hypothesis that the difference in column width is a consequence of higher probability of surface relaxation of physisorbed Ti species in TTIP plasma, relative to Zr species in ZTB plasma.

Table VI-1: Evolution of thin film characteristics as O_2 fraction in plasma gas mixture increases: comparative summary of research findings.

<table>
<tr><th colspan="2">Oxygen gas in plasma gas mixture: 0% → 95%
(p_{total} = 1 mTorr)</th></tr>
<tr><th>ZTB / O_2</th><th>TTIP / O_2</th></tr>
<tr><td colspan="2">▪ growth rate: relatively stable at first; continuous decrease at >50% O_2</td></tr>
<tr><td>▪ $ZrO_{2.9}C_{4.8}$ → $ZrO_{1.9}C_{0.8}$</td><td>▪ $TiO_{2.9}C_{3.4}$ → $TiO_{2.5}C_{0.6}$</td></tr>
<tr><td colspan="2">▪ ↗ Zr-O/Ti-O; ↘ C-H
▪ ↘ C-C and C-O that form $ZrOC(CH_x)_y$ / $TiOC(CH_x)_y$
▪ C-O and C=O bonds that form carbonate-like environment ↗ at <80% O_2, ↘ at >80% O_2</td></tr>
<tr><td>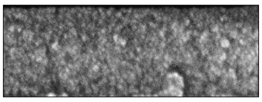 → 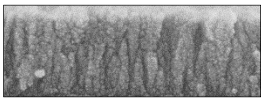
▪ R_a: 0.27 nm → 4.90 nm</td><td>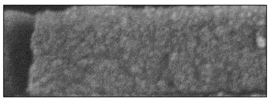 → 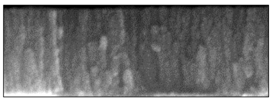
▪ R_a: 0.39 nm → 0.98 nm</td></tr>
<tr><td>▪ *n (at 632.8 nm)*: 1.59 → 1.84
▪ *density*: 2.1 g/cm^3 → 3.6 g/cm^3
▪ *open nanoporosity*: 8% → 2%</td><td>▪ *n (at 632.8 nm)*: 1.73 → 2.10
▪ *density*: 2.2 g/cm^3 → 2.9 g/cm^3
▪ *open nanoporosity*: 0 %</td></tr>
</table>

Influence of total gas pressure in oxygen-rich plasma

Majority of examined characteristics of zirconium oxide and titanium oxide films evolves in a similar manner as total gas pressure is increased. We have detected continuous increase of the growth rate, primarily explained by increased deposition of carbon and oxygen atoms, as corroborated by XPS investigation. In general, films become richer in carbon and oxygen atoms relative to the metal atom (Zr or Ti). Chemical composition change is further corroborated by an increase in concentration of C-O and C=O bonds that form carbonate-like environment in the films. We suspect that the paramount motive of the change in physico-chemical nature of the films lies in the plasma phase chemical composition. The evolution of nature and size of species that arrive to the substrate surface should have a significant influence on surface reactions, and the overall mechanism of thin film growth. Plasma phase might be significantly affected by:

- decreasing amount of injected power per particle, and
- decreasing mean free path of the particles.

Changes in these two parameters might lead to a lower effectiveness of precursor dissociation process and increased probability of chemical reactions in the plasma phase. It is possible that species in the plasma become larger and more organic as pressure increases. The analysis of the plasma phase by in-situ FTIR and MS should be performed to corroborate these hypotheses.

Unlike other examined characteristics, thin film morphology evolves differently in ZTB and in TTIP plasma. The increase in pressure induces a drastic change of the growth mode in ZTB plasma: from columnar to uniform in all directions, whereas the films grown in TTIP plasma exhibit columnar morphology over the whole pressure range. The distinction in morphological evolution between zirconia- and titania-like films might be the result of several characteristics such as different properties of central metal atoms or the differences in employed precursor injection systems. Investigating the plasma phase is crucial for understanding the observed behaviours.

Table VI-2: Influence of total gas pressure on thin film characteristics: comparative summary of research results.

Total gas pressure: 1 mTorr → 8 mTorr	
5% ZTB / 95% O_2	***5% TTIP / 95% O_2***
▪ continuous increase of the growth rate	
▪ $ZrO_{1.9}C_{0.8} \rightarrow ZrO_{2.4}C_{1.7}$	▪ $TiO_{2.5}C_{0.6} \rightarrow TiO_{2.7}C_{1.3}$
▪ ↗C-O and C=O that form carbonate-like structures	
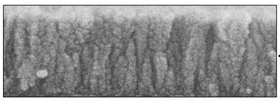 → 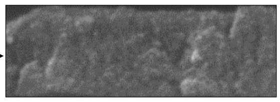	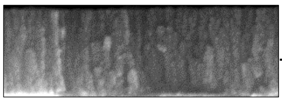 → 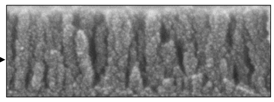
▪ *n (at 632.8 nm)*: 1.84 → 1.69 ▪ *density*: 3.6 g/cm^3 → 2.8 g/cm^3 ▪ *open nanoporosity*: 2% → 16%	▪ *n (at 632.8 nm)*: 2.10 → 1.79 ▪ *open nanoporosity*: 0% → 10%

Synthesis of "composite" thin films in metalorganic/HMDSO/O_2 plasma

In the last chapter of this thesis, we have explored the synthesis of thin films in oxygen-rich plasma gas mixture of metalorganic (ZTB or TTIP) and organosilicon (HMDSO) precursor. The "composite" $ZrSi_xO_yC_zH_w$ and $TiSi_xO_yC_zH_w$ thin films, with homogeneously distributed chemical compositions, have been successfully deposited. As HMDSO was added to the gas mixture, silicon, oxygen and carbon atoms were increasingly deposited relative to the metal atom. Identification of the FTIR spectra confirmed the presence of M-O, Si-O, Si-C, Si-H, C-O, C=O and C-H bonding.

Film morphology is affected by HMDSO addition to the plasma gas mixture. "Composite" films with columnar morphology are deposited at very low percentage of HMDSO. Film morphology becomes uniform with further addition of the organosilicon precursor.

Table VI-3: Characteristics of thin films deposited from metalorganic precursor+O_2+HMDSO plasma gas mixtures: comparative summary of research observations.

<table>
<tr><th colspan="2">HMDSO in plasma gas mixture: 4.8% → 20%
(p_{total} = 2.10 → 2.50 mTorr)</th></tr>
<tr><th>ZTB / O_2 / HMDSO</th><th>TTIP / O_2 / HMDSO</th></tr>
<tr><td colspan="2">▪ continuous increase of the growth rate</td></tr>
<tr><td>▪ $ZrSi_{0.4}O_{2.6}C_{0.7}$ → $ZrSi_{1.6}O_{4.7}C_{2.4}$</td><td>▪ $TiSi_{1.1}O_{4.2}C_{2.0}$ → $TiSi_{3.6}O_{7.8}C_{4.8}$</td></tr>
<tr><td colspan="2">▪ Zr-O/Ti-O ↘
▪ Si-C ↗; C-H ↗
▪ Si-H ↗, disappears at 20%
▪ C-O and C=O that form carbonate-like environment ↗</td></tr>
<tr><td>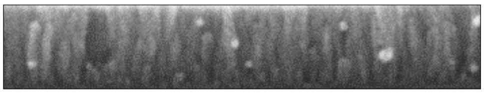
↓
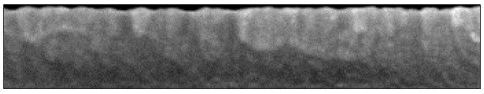</td><td>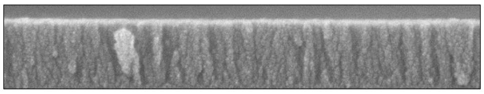
↓
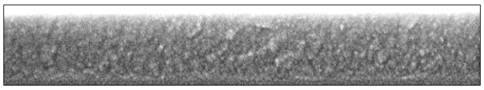</td></tr>
<tr><td>▪ *n (at 632.8 nm)*: 1.66 at 13% HMDSO</td><td>▪ *n (at 632.8 nm)*: 1.65 at 13% HMDSO</td></tr>
</table>

In the framework of this thesis, we have shown the possibility of synthesizing metal oxide and metal-silicon oxide thin films with a vast range of characteristics: uniform to columnar morphology; highly organic to almost inorganic; low to high refractive index. The comparative study of thin films grown in ZTB and TTIP plasmas indicated a predominantly similar comportment of the two metalorganic PECVD processes. Furthermore, our understanding of the difference between columnar growth mechanisms in ZTB and TTIP plasma has been significantly improved by coupling experimentally obtained results with theoretical simulations of thin film growth. Nevertheless, there are questions that remain unanswered and new ones arise. These are discussed in the following paragraph.

Perspectives

- Increase in total gas pressure had induced a particular evolution of thin film morphology. Before further studying gas pressure influence on thin film growth, it is important to repeat the study of TTIP plasma. The study should be performed by using the LVD injection system to confirm the observed differences in evolution of film morphology between ZTB and TTIP plasmas.
- Combining experimental PECVD and Monte Carlo simulations has proved to be successful in explaining certain morphological features of the films. It would be of interest to follow this pathway further by constructing hypotheses and specific experiments which could be modelled in Monte Carlo simulations, with the objective of deepening the

understanding of thin film growth mechanisms.

- Metalorganic precursors are frequently used in PECVD of metal oxide nanocoatings. Thus, it is of interest to further investigate general laws that govern thin film growth in this type of process by expanding the research to other metalorganic precursors such as Titanium (IV) tert-butoxide (TiTB) and Hafnium (IV) tert-butoxide (HfTB).

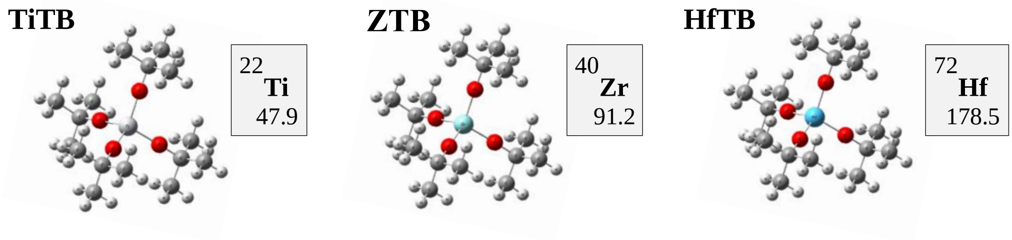

Figure VI-1: 3D molecular geometries of TiTB, ZTB and HfTB, and atomic mass and number corresponding to central atoms of each molecule (Ti, Zr and Hf, respectively).

- Species present in the plasma phase arrive at the surface and participate in different physical and chemical reactions leading to thin film growth. Therefore, to understand the PECVD process, it is crucial to have insight into the plasma phase. This includes examining the evolution of plasma chemical composition as a function of different process parameters.

  A new, sophisticated plasma analysis platform (Figure VI-2), currently under construction at LAPLACE, will allow a comprehensive study of the plasma phase. Main characteristics of the system will be the following:

  - Plasma sources: ECR and ICP;
  - In situ FTIR spectroscopy,
    - high detectivity (100 passes), and
    - wide range (from 4000 to 10 cm^{-1});
  - Mass spectroscopy; optical emission spectroscopy; Langmuir probe.

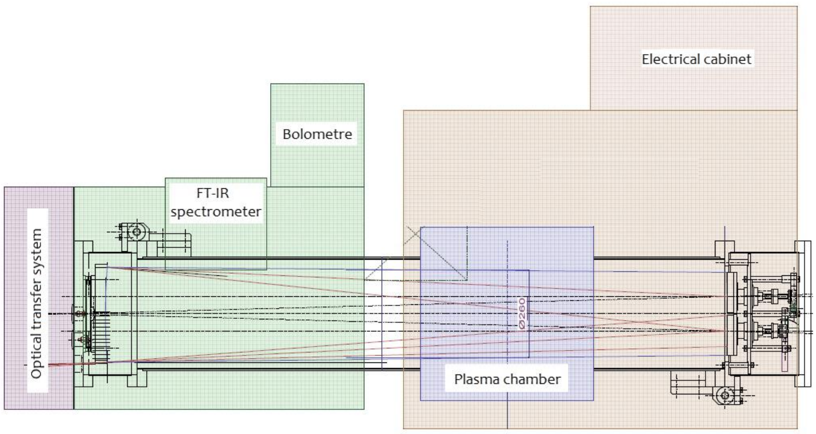

Figure VI-2: Schematic representation of the plasma analysis platform under construction at LAPLACE.

- Furthermore, in collaboration with Laboratory for Chemistry of Novel Materials at University of Mons, we have significantly advanced the preparation for plasma phase study. The method is based on the combination of in-situ FTIR, MS and DFT, with the objective of assisting the interpretation of experimental results by theoretical calculations. Supporting FTIR analysis with DFT appears to be a promising approach as already shown in the research of organic plasma [223], [224]. To assess the pertinence of this approach for metalorganic plasma, we have used FTIR and MS data collected in the framework of Mr R. Verhoef's thesis [12], and built a synthetic vibrational spectrum of the plasma phase (Figure VI-3).

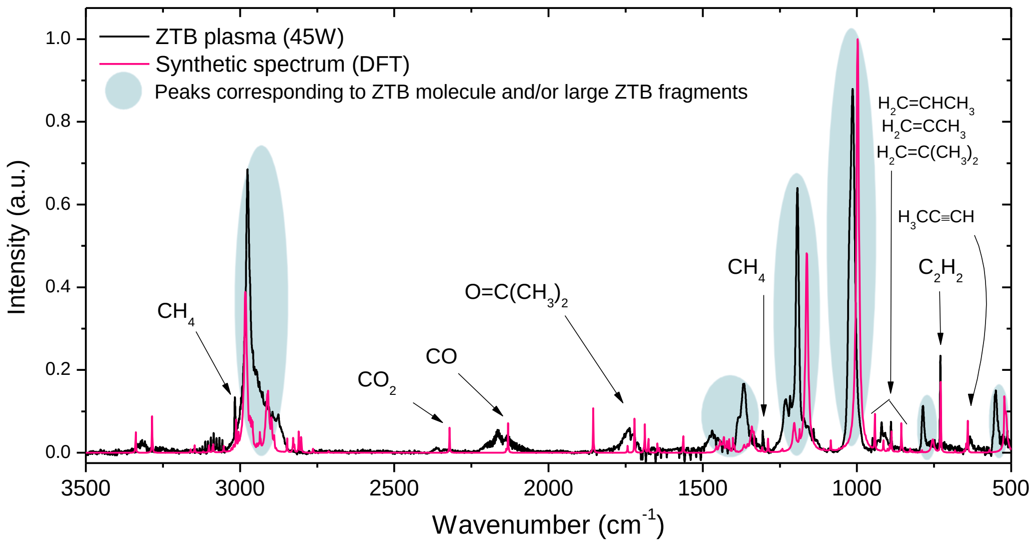

Figure VI-3: Synthetic IR spectrum compared to FTIR spectrum of ZTB plasma.

It has also been shown that coupling experimental data and DFT calculations allows proposing precursor dissociation pathways in the plasma phase and the ionisation source of MS spectrometer [224]. The method is based on the Gibbs free enthalpies of dissociation reactions. The operational principle involves calculating Gibbs free enthalpy difference between the reactants and the products. As preparation for envisioned comprehensive study of the precursor dissociation mechanism, we have calculated free enthalpy change in different dissociation reactions for ZTB, TTIP and HMDSO molecules (several examples are listed below; the form [X − Y] denotes species X lacking part Y (graphical representation shown in Figure VI-4)).

$$HMDSO \xrightarrow{3.87\ eV} CH_3 + [HMDSO - CH_3]$$

$$HMDSO^+ \xrightarrow{0.70\ eV} CH_3 + [HMDSO - CH_3]^+$$

$$HMDSO \xrightarrow{4.19\ eV} Si(CH_3)_3 + [HMDSO - Si(CH_3)_3]$$

$$[HMDSO - Si(CH_3)_3] \xrightarrow{0.48\ eV} CH_3 + [HMDSO - Si(CH_3)_3 - CH_3]$$

$$ZTB \xrightarrow{2.54\ eV} CH_3 + [ZTB - CH_3]$$

$$ZTB^+ \xrightarrow{4.23\ eV} {CH_3}^+ + [ZTB - CH_3]$$

$$ZTB^+ \xrightarrow{-0.63\ eV} CH_3 + [ZTB - CH_3]^+$$

$$ZTB^+ \xrightarrow{1.51\ eV} OC(CH_3)_3 + [ZTB - OC(CH_3)_3]^+$$

$$[ZTB - OC(CH_3)_3]^+ \xrightarrow{4.22\ eV} OC(CH_3)_3 + [ZTB - OC(CH_3)_3 - OC(CH_3)_3]^+$$

$$TTIP^+ \xrightarrow{-0.25\ eV} CH_3 + [TTIP - CH_3]^+$$

$$TTIP^+ \xrightarrow{1.36\ eV} OCH(CH_3)_2 + [TTIP - OCH(CH_3)_2]^+$$

$$[TTIP - OCH(CH_3)_2]^+ \xrightarrow{1.79\ eV} CH_3 + [TTIP - OCH(CH_3)_2 - CH_3]^+$$

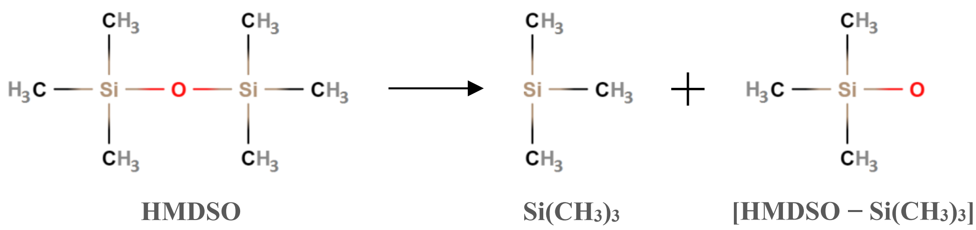

Figure VI-4: 2D graphical representation of the following dissociation reaction:
$HMDSO \rightarrow Si(CH_3)_3 + [HMDSO - Si(CH_3)_3]$.

Bibliography

[1] M. Latreche, “Contribution à l’étude des procédés de croissance de films minces obtenus par plasma RCER à partir de monomères organosiliciés,” Thesis, University of Toulouse III - Paul Sabatier, 1993.

[2] G. Dennler, “Dépôts PECVD de Composés de Silicium sur polymères: étude de la première phase des dépôts,” Thesis, University of Toulouse III - Paul Sabatier, 2002.

[3] A. Zenasni, “Couches a faibles permittivites diélectriques elaborees par plasma micro-onde d’organosilicies: Identification et étude des paramètres contrôlant la permittivité,” Thesis, University of Toulouse III - Paul Sabatier, 2003.

[4] I. Savin de Larclause, “Dépôt organosilicie par plasma froid basse pression et pression atmosphérique sur substrats microstructures,” Thesis, University of Toulouse III - Paul Sabatier, 2008.

[5] R. Delsol, P. Raynaud, Y. Segui, M. Latreche, L. Agres, and L. Mage, “Growth processes of dielectric thin films in a multipolar microwave plasma excited by distributed electron cyclotron resonance using tetraethylorthosilicate (TEOS) and oxygen precursors,” *Thin Solid Films*, vol. 289, no. 1–2, pp. 170–176, Nov. 1996.

[6] P. Raynaud, T. Amilis, and Y. Segui, “Infrared absorption analysis of organosilicon/oxygen plasmas in a microwave multipolar plasma excited by distributed electron cyclotron resonance,” *Appl. Surf. Sci.*, vol. 138–139, pp. 285–291, Jan. 1999.

[7] L. Agres, Y. Segui, R. Delsol, and P. Raynaud, “Oxygen barrier efficiency of hexamethyldisiloxane/oxygen plasma-deposited coating,” *J. Appl. Polym. Sci.*, vol. 61, no. 11, pp. 2015–2022, Sep. 1996.

[8] B. Despax and P. Raynaud, “Deposition of ‘Polysiloxane’ Thin Films Containing Silver Particles by an RF Asymmetrical Discharge,” *Plasma Process. Polym.*, vol. 4, no. 2, pp. 127–134, Feb. 2007.

[9] C. Saulou, B. Despax, P. Raynaud, S. Zanna, P. Marcus, and M. Mercier-Bonin, “Plasma deposition of organosilicon polymer thin films with embedded nanosilver for prevention of microbial adhesion,” *Appl. Surf. Sci.*, vol. 256, no. 3, pp. S35–S39, Nov. 2009.

[10] P. Raynaud, B. Despax, Y. Segui, and H. Caquineau, “FTIR Plasma Phase Analysis of Hexamethyldisiloxane Discharge in Microwave Multipolar Plasma at Different Electrical Powers,” *Plasma Process. Polym.*, vol. 2, no. 1, pp. 45–52, Jan. 2005.

[11] R. Cozzolino, “Etude de couches minces organométalliques déposées par procédé plasma basse pression à partir de Zirconium Tert Butoxide: application aux traitements antireflets,” Thesis, University of Toulouse III - Paul Sabatier, 2012.

[12] R. Verhoef, “Étude de la décomposition du Zirconium Tetra tert Butoxide en phase plasma et incidence sur les couches minces déposées,” Thesis, University of Toulouse III - Paul Sabatier, 2017.

[13] D. Li, “Synthèse par PECVD et caractérisation de couches minces de TiO2 et de TiSiO pour applications optiques,” Thesis, University of Nantes, 2013.

[14] M. Ohring, *The Materials Science of Thin Films*. 2013.

[15] F. Z. Bathaei, “Silicon device miniaturazation and its effect on processing techniques,” *Microelectronics J.*, vol. 20, no. 4, pp. 1–10, Jul. 1989.

[16] R. W. Keyes, “Physical limits of silicon transistors and circuits,” *Reports Prog. Phys.*, vol. 68, no. 12, pp. 2701–2746, 2005.

[17] J. Schmitz, “Low temperature thin films for next-generation microelectronics (invited),” *Surf. Coatings Technol.*, vol. 343, pp. 83–88, Jun. 2018.

[18] E. D. Nicholson, “Mechanical properties of thin films for aerospace applications,” in *Proceedings of SPIE*, 1994, vol. 2286, pp. 275–284.

[19] M. A. Ezazi, M. M. Quazi, E. Zalnezhad, and A. A. D. Sarhan, “Enhancing the tribo-mechanical properties of aerospace AL7075-T6 by magnetron-sputtered Ti/TiN, Cr/CrN and TiCr/TiCrN thin film ceramic coatings,” *Ceram. Int.*, vol. 40, no. 10, pp. 15603–15615, Dec. 2014.

[20] H. J. Griesser, *Thin film coatings for biomaterials and biomedical applications*. Woodhead Publishing, 2016.

[21] M. Mozafari, A. Ramedani, Y. N. Zhang, and D. K. Mills, “Thin films for tissue engineering applications,” in *Thin Film Coatings for Biomaterials and Biomedical Applications*, Elsevier, 2016, pp.

167–195.

[22] N. S. Murthy, V. B. Damodaran, S. H. Lee, A. S. Hwang, and H.-J. Sung, “Characterization of thin films for biomedical applications,” in *Thin Film Coatings for Biomaterials and Biomedical Applications*, Elsevier, 2016, pp. 81–115.

[23] J. A. Venables, G. D. T. Spiller, and M. Hanbucken, “Nucleation and growth of thin films,” *Reports Prog. Phys.*, vol. 47, no. 4, pp. 399–459, 1984.

[24] J. A. Nieminen and K. Kaski, “Criteria for different growth modes of thin films,” *Surf. Sci.*, vol. 185, no. 1–2, pp. L489–L496, Jun. 1987.

[25] G. H. Gilmer, H. Huang, and C. Roland, “Thin film deposition: fundamentals and modeling,” *Comput. Mater. Sci.*, p. 27, 1998.

[26] N. Kaiser, “Review of the fundamentals of thin-film growth,” *Appl. Opt.*, vol. 41, no. 16, p. 3053, 2002.

[27] A. von Keudell, “Surface processes during thin-film growth,” *Plasma Sources Sci. Technol.*, vol. 9, no. 4, pp. 455–467, Nov. 2000.

[28] D. Gebauer, M. Kellermeier, J. D. Gale, L. Bergström, and H. Cölfen, “Pre-nucleation clusters as solute precursors in crystallisation,” *Chem. Soc. Rev.*, vol. 43, no. 7, pp. 2348–2371, Mar. 2014.

[29] P. M. Martin, *Handbook of Deposition Technologies for Films and Coatings : Science, Applications and Technology.* Elsevier Science, 2009.

[30] K. Seshan, *Handbook of thin film deposition : techniques, processes, and technologies*. William Andrew, 2012.

[31] J. E. ten Elshof, “Chemical solution deposition techniques for epitaxial growth of complex oxides,” in *Epitaxial Growth of Complex Metal Oxides*, Elsevier, 2015, pp. 69–93.

[32] I. Langmuir, “Oscillations in Ionized Gases.,” *Proc. Natl. Acad. Sci. U. S. A.*, vol. 14, no. 8, pp. 627–37, Aug. 1928.

[33] U. S. Inan and M. Golkowski, *Principles of Plasma physics for Engineers and Scientists*. Cambridge University Press, 2011.

[34] D. W. Möller, “Fundamentals of Plasma Physics,” 2006.

[35] M. A. Lieberman and A. J. Lichtenberg, *Principles of Plasma Discharges and Materials Processing: Second Edition*. 2005.

[36] Y. P. Raizer, *Gas discharge physics*. Springer, 1997.

[37] H. Conrads and M. Schmidt, “Plasma generation and plasma sources,” *Plasma Sources Sci. Technol.*, vol. 9, no. 4, pp. 441–454, Nov. 2000.

[38] A. Soum-Glaude *et al.*, “Interaction ion/surface en PACVD basse frequence du TMS,” in *Plasma froids - Interactions plasma/surface : modeles, diagnostics et procedes*, MRCT/CNRS, Ed. 2009.

[39] G. Bertrand and R. Mévrel, “Zirconia coatings realized by microwave plasma-enhanced chemical vapordeposition,” *Thin Solid Films*, vol. 292, no. 1–2, pp. 241–246, 1997.

[40] B. Préauchat and S. Drawin, “Isothermal and cycling properties of zirconia-based thermal barrier coatings deposited by PECVD,” *Surf. Coatings Technol.*, vol. 146–147, pp. 94–101, 2001.

[41] G. K. Dalapati *et al.*, “Electrical Properties of and Conduction Mechanism in Ultrathin ZrO2 Films on Si1- yCy Heterolayers,” *Jpn. J. Appl. Phys.*, vol. 43, no. 6A, pp. 3498–3502, 2004.

[42] H. Suhr, “Applications and trends in plasma-enhanced organometallic chemical vapour deposition,” *Surf. Coatings Technol.*, vol. 49, no. 1–3, pp. 233–238, 1991.

[43] H.-L. Huang, Y.-Y. Chang, J.-C. Weng, Y.-C. Chen, C.-H. Lai, and T.-M. Shieh, “Anti-bacterial performance of Zirconia coatings on Titanium implants,” *Thin Solid Films*, vol. 528, pp. 151–156, Jan. 2013.

[44] M. R. Kalucrossed D Signerović, J. P. Schreckenbach, and H. L. Graf, “Zirconia coated titanium for implants and their interactions with osteoblast cells,” *Mater. Sci. Eng. C*, vol. 44, pp. 254–261, 2014.

[45] E. Zalnezhad, “Effect of structural evolution on mechanical properties of ZrO2 coated Ti-6Al-7Nb-biomedical application,” *Appl. Surf. Sci.*, vol. 370, pp. 32–39, 2016.

[46] B.-O. Cho, J. Wang, L. Sha, and J. P. Chang, "Tuning the electrical properties of zirconium oxide thin films," *Appl. Phys. Lett.*, vol. 80, no. 6, pp. 1052–1054, 2002.

[47] J. P. Chang and Y. S. Lin, "Dielectric property and conduction mechanism of ultrathin zirconium oxide films," *Appl. Phys. Lett.*, vol. 79, no. 22, pp. 3666–3668, 2001.

[48] L. Koltunski and R. A. B. Devine, "Infrared properties of room-temperature-deposited ZrO2," *Appl. Phys. Lett.*, vol. 79, no. 3, pp. 320–322, 2001.

[49] C. Mahata, M. K. Bera, P. K. Bose, and C. K. Maiti, "Paramagnetic defects and charge trapping behavior of ZrO2films deposited on germanium by plasma-enhanced CVD," *Semicond. Sci. Technol.*, vol. 24, no. 2, 2009.

[50] L. Liang, Y. Xu, D. Wu, and Y. Sun, "A simple sol-gel route to ZrO2films with high optical performances," *Mater. Chem. Phys.*, vol. 114, no. 1, pp. 252–256, 2009.

[51] N. . Zhang, Z. . Song, Q. Wan, Q. . Shen, and C. . Lin, "Interfacial and microstructural properties of zirconium oxide thin films prepared directly on silicon," *Appl. Surf. Sci.*, vol. 202, no. 1–2, pp. 126–130, Dec. 2002.

[52] S. Das, S. Jana, N. Das, S. S. Ghosh, and P. K. Biswas, "Study of spin coated multilayer zirconia and silica films for non-quarterwavelength optical design based antireflection effect at 1,054 nm," *J. Sol-Gel Sci. Technol.*, vol. 60, no. 2, pp. 116–124, 2011.

[53] Z. Elalamy, E. Drouard, T. M. Govern, L. Escoubas, J. J. Simon, and F. Flory, "Thermo-optical coefficients of sol-gel ZrO2thin films," *Opt. Commun.*, vol. 235, no. 4–6, pp. 365–372, 2004.

[54] S. Wang and J. Shen, "Fabrication of sol-gel derived ZrO2 thin film for HR coatings via rapid thermal annealing process," *J. Sol-Gel Sci. Technol.*, vol. 67, no. 2, pp. 339–343, 2013.

[55] I. J. Berlin, V. S. Anitha, P. V. Thomas, and K. Joy, "Influence of oxygen atmosphere on the photoluminescence properties of sol–gel derived ZrO2 thin films," *J. Sol-Gel Sci. Technol.*, vol. 64, no. 2, pp. 289–296, 2012.

[56] S. Bae, H. Choi, S. Choi, and Y. Oh, "Sol gel processing for epitaxial growth of ZrO2 thin films on Si(100) wafers," vol. 26, pp. 213–214, 2000.

[57] A. Naumenko, I. Gnatiuk, N. Smirnova, and A. Eremenko, "Characterization of sol-gel derived TiO2/ZrO2 films and powders by Raman spectroscopy," *Thin Solid Films*, vol. 520, no. 14, pp. 4541–4546, 2012.

[58] R. Álvarez *et al.*, "Morphological evolution of pulsed laser deposited ZrO2 thin films," *J. Appl. Phys.*, vol. 107, no. 5, p. 054311, Mar. 2010.

[59] K. Koski, J. Hölsä, and P. Juliet, "Properties of zirconium oxide thin films deposited by pulsed reactive magnetron sputtering," *Surf. Coatings Technol.*, vol. 120–121, pp. 303–312, Nov. 1999.

[60] T. Koch and P. Ziemann, "Effects of ion-beam-assisted deposition on the growth of zirconia films," *Thin Solid Films*, vol. 303, no. 1–2, pp. 122–127, Jul. 1997.

[61] G. Gottardi, N. Laidani, V. Micheli, R. Bartali, and M. Anderle, "Effects of oxygen concentration in the Ar/O2 plasma on the bulk structure and surface properties of RF reactively sputtered zirconia thin films," *Surf. Coatings Technol.*, vol. 202, no. 11, pp. 2332–2337, 2008.

[62] D. . Kuo, C. . Chien, and C. . Huang, "Zirconia and zirconia–silica thin films deposited by magnetron sputtering," *Thin Solid Films*, vol. 420–421, pp. 47–53, Dec. 2002.

[63] M. A. Cameron and S. M. George, "ZrO2 film growth by chemical vapor deposition using zirconium tetra-tert-butoxide," *Thin Solid Films*, vol. 348, no. 1–2, pp. 90–98, 1999.

[64] M. Balog, M. Schieber, M. Michman, and S. Patai, "The chemical vapour deposition and characterization of ZrO2 films from organometallic compounds," *Thin Solid Films*, vol. 47, no. 2, pp. 109–120, Dec. 1977.

[65] B. J. Gould, I. M. Povey, M. E. Pemble, and W. R. Flavell, "Chemical Vapour Deposition of ZrO, Thin Films monitored by," vol. 4, no. 12, pp. 1815–1819, 1994.

[66] J. . Holgado *et al.*, "Ar stabilisation of the cubic/tetragonal phases of ZrO2 in thin films prepared by ion beam induced chemical vapour deposition," *Thin Solid Films*, vol. 389, no. 1–2, pp. 34–42, Jun. 2001.

[67] D. J. Burleson, J. T. Roberts, W. L. Gladfelter, S. A. Campbell, and R. C. Smith, "A study of CVD growth kinetics and film microstructure of zirconium dioxide from zirconium tetra-tert-butoxide," *Chem. Mater.*, vol. 14, no. 3, pp. 1269–1276, 2002.

[68] D. Ni, Y. Lou, P. D. Christofides, L. Sha, S. Lao, and J. P. Chang, "Real-time carbon content control for PECVD ZrO2 thin-film growth," *IEEE Trans. Semicond. Manuf.*, vol. 17, no. 2, pp. 221–230, 2004.

[69] R. Cozzolino, Y. Segui, and P. Raynaud, "Characterization of ZrOxCyHz thin films deposited by MMP–DECR reactor using Zirconium Tert-Butoxide/O2 mixture," *Surf. Coatings Technol.*, vol. 205, Suppl, pp. S198--S203, Jul. 2011.

[70] B.-O. Cho, J. P. Chang, J.-H. Min, S. H. Moon, Y. W. Kim, and I. Levin, "Material characteristics of electrically tunable zirconium oxide thin films," *J. Appl. Phys.*, vol. 93, no. 1, pp. 745–749, Jan. 2003.

[71] P. Colpo, G. Ceccone, P. Sauvageot, M. Baker, and F. Rossi, "Characterization of zirconia coatings deposited by inductively coupled plasma assisted chemical vapor deposition," *J. Vac. Sci. Technol. a-Vacuum Surfaces Film.*, vol. 18, no. 4, pp. 1096–1101, 2000.

[72] H. J. Frenck, E. Oesterschulze, R. Beckmann, W. Kulisch, and R. Kassing, "Low temperature remote plasma-enhanced deposition of thin metal oxide films by decomposition of metal alkoxides," *Mater. Sci. Eng. A*, vol. 139, no. C, pp. 394–400, 1991.

[73] S. Mathur and T. Ruegamer, "Transparent and Scratch-Resistant C:ZrOx Coatings on Polymer and Glass by Plasma-Enhanced Chemical Vapor Deposition," *Int. J. Appl. Ceram. Technol.*, vol. 8, no. 5, pp. 1050–1058, Sep. 2011.

[74] S. Chu *et al.*, "Low-temperature synthesis of mesoporous TiO2 photocatalyst with self-cleaning strategy to remove organic templates," *Appl. Surf. Sci.*, vol. 258, no. 24, pp. 9664–9667, Oct. 2012.

[75] Y. Lu, L. Hao, Y. Hirakawa, and H. Sato, "Antibacterial Activity of TiO2/Ti Composite Photocatalyst Films Treated by Ultrasonic Cleaning," *Adv. Mater. Phys. Chem.*, vol. 02, no. 04, pp. 9–12, Jan. 2012.

[76] M. Zhou, S. Roualdès, J. Zhao, V. Autès, and A. Ayral, "Nanocrystalline TiO2 thin film prepared by low-temperature plasma-enhanced chemical vapor deposition for photocatalytic applications," *Thin Solid Films*, vol. 589, pp. 770–777, Aug. 2015.

[77] R. Nakano *et al.*, "Photocatalytic inactivation of influenza virus by titanium dioxide thin film," *Photochem. Photobiol. Sci.*, vol. 11, no. 8, p. 1293, Aug. 2012.

[78] M. Pelaez *et al.*, "A review on the visible light active titanium dioxide photocatalysts for environmental applications," *Appl. Catal. B Environ.*, vol. 125, pp. 331–349, Aug. 2012.

[79] J. Kowalski and H. Szymanowski, "Optical properties and morphology of PECVD deposited titanium dioxide films," *J. Achiev. Mater. Manuf. Eng.*, vol. 37, no. 2, pp. 298–303, 2009.

[80] A. Sobczyk-Guzenda *et al.*, "Characterization of thin TiO2 films prepared by plasma enhanced chemical vapour deposition for optical and photocatalytic applications," *Thin Solid Films*, vol. 517, no. 18, pp. 5409–5414, Jul. 2009.

[81] C. Martinet, V. Paillard, A. Gagnaire, and J. Joseph, "Deposition of SiO2 and TiO2 thin films by plasma enhanced chemical vapor deposition for antireflection coating," *J. Non. Cryst. Solids*, vol. 216, pp. 77–82, Aug. 1997.

[82] M. Mosaddeq-ur-Rahman, G. Yu, T. Soga, T. Jimbo, H. Ebisu, and M. Umeno, "Refractive index and degree of inhomogeneity of nanocrystalline TiO2 thin films: Effects of substrate and annealing temperature," *J. Appl. Phys.*, vol. 88, no. 8, p. 4634, Sep. 2000.

[83] S. Phadke, J. D. Sorge, S. Hachtmann, and D. P. Birnie, "Broad band optical characterization of sol–gel TiO2 thin film microstructure evolution with temperature," *Thin Solid Films*, vol. 518, no. 19, pp. 5467–5470, Jul. 2010.

[84] R. Sato, T. Kawai, and K. Kifune, "Optical properties of sol–gel processed TiO2 thin films up to the vacuum ultraviolet energy region," *J. Non. Cryst. Solids*, vol. 356, no. 25–27, pp. 1300–1304, Jun. 2010.

[85] T. Shimizu *et al.*, "Bioactivity of sol-gel-derived TiO2coating on polyetheretherketone: In vitro and in vivo studies," *Acta Biomater.*, vol. 35, pp. 305–317, 2016.

[86] Y. Leprince-Wang, K. Yu-Zhang, V. Nguyen Van, D. Souche, and J. Rivory, "Correlation between microstructure and the optical properties of TiO2 thin films prepared on different substrates," *Thin Solid*

Films, vol. 307, no. 1–2, pp. 38–42, Oct. 1997.

[87] D. Mergel, D. Buschendorf, S. Eggert, R. Grammes, and B. Samset, “Density and refractive index of TiO2 films prepared by reactive evaporation,” *Thin Solid Films*, vol. 371, no. 1–2, pp. 218–224, Aug. 2000.

[88] C. J. Tavares *et al.*, “PVD-Grown photocatalytic TiO2 thin films on PVDF substrates for sensors and actuators applications,” *Thin Solid Films*, vol. 517, no. 3, pp. 1161–1166, Dec. 2008.

[89] S. Vyas, R. Tiwary, K. Shubham, and P. Chakrabarti, “Study the target effect on the structural, surface and optical properties of TiO2 thin film fabricated by RF sputtering method,” *Superlattices Microstruct.*, vol. 80, pp. 215–221, Apr. 2015.

[90] C. S. Chua *et al.*, “Effect of Annealing Temperature on Microstructure and UV Light Photocatalytic Activity of TiO $_2$ Films Grown by Atmospheric Pressure CVD,” *Chem. Vap. Depos.*, vol. 20, no. 1-2–3, pp. 44–50, Mar. 2014.

[91] S. Mathur and P. Kuhn, “CVD of titanium oxide coatings: Comparative evaluation of thermal and plasma assisted processes,” 2006.

[92] C. Quiñonez, W. Vallejo, and G. Gordillo, “Structural, optical and electrochemical properties of TiO2 thin films grown by APCVD method,” *Appl. Surf. Sci.*, vol. 256, no. 13, pp. 4065–4071, Apr. 2010.

[93] S. Yamauchi, K. Ishibashi, and S. Hatakeyama, “Low Pressure Chemical Vapor Deposition of TiO2 Layer in Hydrogen-Ambient,” *J. Cryst. Process Technol.*, vol. 04, no. 04, pp. 185–192, 2014.

[94] N. C. da Cruz *et al.*, “Properties of titanium oxide films obtained by PECVD,” *Surf. Coatings Technol.*, vol. 126, no. 2–3, pp. 123–130, Apr. 2000.

[95] A. Granier *et al.*, “Influence of ion bombardment and annealing on the structural and optical properties of TiOx thin films deposited in inductively coupled TTIP/O2 plasma,” *Plasma Process. Polym.*, vol. 6, no. SUPPL. 1, pp. S741--S745, Jun. 2009.

[96] A. Borrás, J. Cotrino, and A. R. González-Elipe, “Type of Plasmas and Microstructures of TiO2 Thin Films Prepared by Plasma Enhanced Chemical Vapor Deposition,” *J. Electrochem. Soc.*, vol. 154, no. 12, pp. P152–P157, Dec. 2007.

[97] D. Li, M. Carette, A. Granier, J. P. Landesman, and A. Goullet, “Effect of ion bombardment on the structural and optical properties of TiO 2 thin films deposited from oxygen/titanium tetraisopropoxide inductively coupled plasma,” *Thin Solid Films*, vol. 589, pp. 783–791, Aug. 2015.

[98] T. Busani and R. A. B. Devine, “Dielectric and infrared properties of TiO $_2$ films containing anatase and rutile,” *Semicond. Sci. Technol.*, vol. 20, no. 8, pp. 870–875, Aug. 2005.

[99] M. Nakamura, S. Kato, T. Aoki, L. Sirghi, and Y. Hatanaka, “Formation mechanism for TiOxthin film obtained by remote plasma enhanced chemical vapor deposition in H2-O2mixture gas plasma,” *Thin Solid Films*, vol. 401, no. 1–2, pp. 138–144, Dec. 2001.

[100] H. Kato, T. Nango, T. Miyagawa, T. Katagiri, and Y. Ohki, “Characterization of hafnium and zirconium silicate films fabricated by plasma-enhanced chemical vapor deposition,” in *International Workshop on Gate Insulator, IWGI 2001.*, 2001, pp. 166–169.

[101] G. D. Wilk and R. M. Wallace, “Stable zirconium silicate gate dielectrics deposited directly on silicon,” *Appl. Phys. Lett.*, vol. 76, no. 1, pp. 112–114, 2000.

[102] M. Lemberger, A. Paskaleva, S. Zürcher, A. J. Bauer, L. Frey, and H. Ryssel, “Electrical characterization and reliability aspects of zirconium silicate films obtained from novel MOCVD precursors,” *Microelectron. Eng.*, vol. 72, no. 1–4, pp. 315–320, 2004.

[103] F. J. Ferrer, F. Frutos, J. García-López, A. R. González-Elipe, and F. Yubero, “Optical refractive index and static permittivity of mixed Zr-Si oxide thin films prepared by ion beam induced CVD,” *Thin Solid Films*, vol. 516, no. 2–4, pp. 481–485, 2007.

[104] W. J. Qi *et al.*, “Ultrathin zirconium silicate film with good thermal stability for alternative gate dielectric application,” *Appl. Phys. Lett.*, vol. 77, no. 11, pp. 1704–1706, 2000.

[105] S. L. Dhere, “Silica – zirconia alkali-resistant coatings by sol – gel route,” pp. 1647–1652.

[106] M. F. Morks and A. Kobayashi, “Development of ZrO2/SiO2bioinert ceramic coatings for biomedical application,” *J. Mech. Behav. Biomed. Mater.*, vol. 1, no. 2, pp. 165–171, 2008.

[107] C. Sun, H. Li, Q. Fu, H. Li, Y. Wang, and H. Wu, “ZrSiO4 Oxidation Protective Coating for SiC-Coated Carbon/Carbon Composites Prepared by Supersonic Plasma Spraying,” *J. Therm. Spray Technol.*, vol. 22, no. 4, pp. 525–530, 2013.

[108] H. Kato, T. Nango, T. Miyagawa, T. Katagiri, K. S. Seol, and Y. Ohki, “Plasma-enhanced chemical vapor deposition and characterization of high-permittivity hafnium and zirconium silicate films,” *J. Appl. Phys.*, vol. 92, no. 2, pp. 1106–1111, 2002.

[109] A. Kaiser, M. Lobert, and R. Telle, “Thermal stability of zircon (ZrSiO4),” *J. Eur. Ceram. Soc.*, vol. 28, no. 11, pp. 2199–2211, 2008.

[110] M. A. Russak, C. V Jahnes, and E. P. Katz, “Reactive magnetron sputtered zirconium oxide and zirconium silicon oxide thin films,” *J. Vac. Sci. Technol. A Vacuum, Surfaces, Film.*, vol. 7, no. 3, pp. 1248–1253, May 1989.

[111] G. D. Wilk, R. M. Wallace, and J. M. Anthony, “Hafnium and zirconium silicates for advanced gate dielectrics,” *J. Appl. Phys.*, vol. 87, no. 1, pp. 484–492, 2000.

[112] D. A. Neumayer and E. Cartier, “Materials characterization of ZrO2–SiO2 and HfO2–SiO2 binary oxides deposited by chemical solution deposition,” *J. Appl. Phys.*, vol. 90, no. 4, pp. 1801–1808, Aug. 2001.

[113] Y. J. Chung *et al.*, “Trimethylsilylcyclopentadienyl tris(dimethylamino)zirconium as a single-source metal precursor for the atomic layer deposition of ZrxSi1 -xO4,” *Thin Solid Films*, vol. 564, pp. 140–145, 2014.

[114] W.-K. Kim, S.-W. Kang, and S.-W. Rhee, “Atomic layer deposition of zirconium silicate films using zirconium tetra-tert-butoxide and silicon tetrachloride,” *J. Vac. Sci. Technol. A Vacuum, Surfaces, Film.*, vol. 21, no. 5, pp. L16--L18, Sep. 2003.

[115] M. Lemberger, “Zirconium silicate films obtained from novel MOCVD precursors,” *J. Non. Cryst. Solids*, vol. 322, no. 1–3, pp. 147–153, 2003.

[116] M. Filipescu *et al.*, “Properties of zirconium silicate thin films prepared by laser ablation,” *Mater. Sci. Semicond. Process.*, vol. 7, no. 4-6 SPEC. ISS., pp. 209–214, 2004.

[117] Z. J. Luo *et al.*, “Thermally Stable Ultra -thin Zr Silicate for CMOS Applications,” pp. 200–203.

[118] C. Jamois, R. B. Wehrspohn, L. C. Andreani, C. Hermann, O. Hess, and U. Gösele, “Silicon-based two-dimensional photonic crystal waveguides,” *Photonics Nanostructures - Fundam. Appl.*, vol. 1, no. 1, pp. 1–13, Dec. 2003.

[119] R. D. Roy, D. Sil, S. Jana, P. Kumar Biswas, and S. Kumar Bhadra, “Experimental Study of Perfectly Patterned Silica-Titania Optical Waveguide,” *Photonic Sensors*, vol. 2, no. 1, pp. 81–91, 2012.

[120] B. Louis, N. Krins, M. Faustini, and D. Grosso, “Understanding crystallization of anatase into binary SiO2/TiO2 sol-gel optical thin films: An in situ thermal ellipsometry analysis,” *J. Phys. Chem. C*, vol. 115, no. 7, pp. 3115–3122, Feb. 2011.

[121] P. Karasiński, C. Tyszkiewicz, R. Rogoziński, J. Jaglarz, and J.Mazur, “Optical rib waveguides based on sol-gel derived silica–titania films,” *Thin Solid Films*, vol. 519, no. 16, pp. 5544–5551, Jun. 2011.

[122] S. Larouche, H. Szymanowski, J. E. Klemberg-Sapieha, L. Martinu, and S. C. Gujrathi, “Microstructure of plasma-deposited SiO2/TiO2 optical films,” *J. Vac. Sci. Technol. A Vacuum, Surfaces, Film.*, vol. 22, no. 4, pp. 1200–1207, Jul. 2004.

[123] R. Laird and A. Belkind, “Cosputtered films of mixed TiO $_2$ /SiO $_2$,” *J. Vac. Sci. Technol. A Vacuum, Surfaces, Film.*, vol. 10, no. 4, pp. 1908–1912, Jul. 1992.

[124] X. Wang, H. Masumoto, Y. Someno, and T. Hirai, “Microstructure and optical properties of amorphous TiO2-SiO2 composite films synthesized by helicon plasma sputtering,” *Thin Solid Films*, vol. 338, no. 1–2, pp. 105–109, Jan. 1999.

[125] H. Demiryont, “Optical properties of SiO2 -TiO2 composite films,” *Appl. Opt.*, vol. 24, no. 16, pp. 2647–2650, Aug. 1985.

[126] S. Chao, W.-H. Wang, M.-Y. Hsu, and L.-C. Wang, “Characteristics of ion-beam-sputtered high-refractive-index TiO2-SiO2 mixed films,” *J. Opt. Soc. Am. A*, vol. 16, no. 6, p. 1477, Jun. 1999.

[127] X. Wang, G. Wu, B. Zhou, and J. Shen, “Thermal Annealing Effect on Optical Properties of Binary

TiO2-SiO2 Sol-Gel Coatings," *Materials (Basel).*, vol. 6, no. 1, pp. 76–84, Dec. 2012.

[128] L.-L. Yang, Y.-S. Lai, J. S. Chen, P. H. Tsai, C. L. Chen, and C. J. Chang, "Compositional Tailored Sol-Gel SiO2–TiO2 Thin Films: Crystallization, Chemical Bonding Configuration, and Optical Properties," *J. Mater. Res.*, vol. 20, no. 11, pp. 3141–3149, Nov. 2005.

[129] S. M. Lee *et al.*, "Application of rapid thermal process to solution-processed Ti-silicate films for enhancing permittivity without losing amorphous nature," *Curr. Appl. Phys.*, vol. 13, pp. S41–S44, Jul. 2013.

[130] J.-G. Yoon, H. K. Oh, and Y. J. Kwag, "Structural and Optical Properties of TiO2-SiO2 Composite Films Prepared by Aerosol-Assisted Chemical-Vapor Deposition," *J. Korean Phys. Soc.*, vol. 33, no. 6, pp. 699–704, 1998.

[131] X. Zhang, M. Zhou, and L. Lei, "TiO2 photocatalyst deposition by MOCVD on activated carbon," *Carbon N. Y.*, vol. 44, no. 2, pp. 325–333, Feb. 2006.

[132] F. Gracia, F. Yubero, J. P. Holgado, J. P. Espinos, A. R. Gonzalez-Elipe, and T. Girardeau, "SiO2/TiO2 thin films with variable refractive index prepared by ion beam induced and plasma enhanced chemical vapor deposition," *Thin Solid Films*, vol. 500, no. 1–2, pp. 19–26, Apr. 2006.

[133] S.-M. Lee, J.-H. Park, K.-S. Hong, W.-J. Cho, and D.-L. Kim, "The deposition behavior of SiO2–TiO2 thin film by metalorganic chemical vapor deposition method," *J. Vac. Sci. Technol. A Vacuum, Surfaces, Film.*, vol. 18, no. 5, p. 2384, Sep. 2000.

[134] J. W. Lim, S. J. Yun, and J. H. Kim, "Optical and electrical properties of TixSi(1-x)Oy films," *ETRI J.*, vol. 31, no. 6, pp. 675–679, 2009.

[135] R. Alvarez *et al.*, "On the microstructure of thin films grown by an isotropically directed deposition flux," *J. Appl. Phys.*, vol. 108, no. 6, p. 64316, Sep. 2010.

[136] R. Wilhelm, "ECR Plasma Sources," Springer, Boston, MA, 1993, pp. 161–179.

[137] Y. A. Lebedev, "Microwave discharges: Generation and diagnostics," *J. Phys. Conf. Ser.*, vol. 257, no. 1, 2010.

[138] J. Asmussen, T. A. Grotjohn, P. Mak, and M. A. Perrin, "The design and application of electron cyclotron resonance discharges," *IEEE Trans. Plasma Sci.*, vol. 25, no. 6, pp. 1196–1221, 1997.

[139] Y. W. Y. Weng and M. J. Kushner, "Electron Energy Distributions In Electron Cyclotron Resonance Plasmas for Materials Processing," *IEEE Conf. Rec. - Abstr. 1991 IEEE Int. Conf. Plasma Sci.*, vol. 72, no. July, pp. 33–42, 1991.

[140] T. Desmet, R. Morent, N. De Geyter, C. Leys, E. Schacht, and P. Dubruel, "Nonthermal plasma technology as a versatile strategy for polymeric biomaterials surface modification: A review," *Biomacromolecules*, vol. 10, no. 9, pp. 2351–2378, 2009.

[141] M. Nitschke, T. Götze, S. Gramm, and C. Werner, "Detachment of human endothelial cell sheets from thermo-responsive poly(NiPAAm-co-DEGMA) carriers," *Express Polym. Lett.*, vol. 1, no. 10, pp. 660–666, 2007.

[142] M. Pichot, A. Durandet, J. Pelletier, Y. Arnal, and L. Vallier, "Microwave multipolar plasmas excited by distributed electron cyclotron resonance: Concept and performance," *Rev. Sci. Instrum.*, vol. 59, no. 7, pp. 1072–1075, 1988.

[143] C. C. Huang, T. H. Chang, N. C. Chen, H. W. Chao, C. C. Chen, and S. F. Chou, "Generating electron cyclotron resonance plasma using distributed scheme," *Appl. Phys. Lett.*, vol. 101, no. 6, 2012.

[144] J. Pelletier, "Distributed ECR: Concept, Performances and Perspectives," Springer, Boston, MA, 1993, pp. 181–204.

[145] T. Lagarde, Y. Arnal, A. Lacoste, and J. Pelletier, "Determination of the EEDF by Langmuir probe diagnostics in a plasma excited at ECR above a multipolar magnetic field," *Plasma Sources Sci. Technol.*, vol. 10, no. 2, pp. 181–190, 2001.

[146] M. Diers, "Conception, étude et optimisation de nouvelles sources plasma à la résonance cyclotronique électronique: Application aux dépôts par voie chimique et par pulvérisation," Thesis, University of Grenoble, 2010.

[147] S. Béchu *et al.*, "Multi-dipolar microwave plasmas and their application to negative ion production,"

Phys. Plasmas, vol. 101601, no. 10, pp. 1–9, Oct. 2013.

[148] S. Béchu *et al.*, "Multi-dipolar plasmas for plasma-based ion implantation and plasma-based ion implantation and deposition," *Surf. Coatings Technol.*, vol. 186, no. 1–2, pp. 170–176, Aug. 2004.

[149] D. Bradley, "Metal alkoxides as precursors for electronic and ceramic materials," *Chem. Rev.*, pp. 1317–1322, 1989.

[150] C. T. Lynch, K. S. Mazdiyasni, J. S. Smith, and W. J. Crawford, "Infrared Spectra of Transition Metal Alkoxides.," *Anal. Chem.*, vol. 36, no. 12, pp. 2332–2337, Nov. 1964.

[151] P. D. Moran, G. A. Bowmaker, R. P. Cooney, K. S. Finnie, J. R. Bartlett, and J. L. Woolfrey, "Vibrational Spectra and Molecular Association of Titanium Tetraisopropoxide," 1998.

[152] H. Biederman, *Plasma Polymer Films*. Imperial College Press, 2004.

[153] R. A. Siliprandi, S. Zanini, E. Grimoldi, F. S. Fumagalli, R. Barni, and C. Riccardi, "Atmospheric Pressure Plasma Discharge for Polysiloxane Thin Films Deposition and Comparison with Low Pressure Process," *Plasma Chem. Plasma Process.*, vol. 31, no. 2, pp. 353–372, Apr. 2011.

[154] L. Zajíčková *et al.*, "Comparative study of films deposited from HMDSO/O2 in continuous wave and pulsed rf discharges," in *Plasma Processes and Polymers*, 2007, vol. 4, no. SUPPL.1, pp. S287–S293.

[155] M. Goujon, T. Belmonte, and G. Henrion, "OES and FTIR diagnostics of HMDSO/O2 gas mixtures for SiOx deposition assisted by RF plasma," *Surf. Coatings Technol.*, vol. 188–189, pp. 756–761, Nov. 2004.

[156] J. J. Ojeda and M. Dittrich, "Fourier Transform Infrared Spectroscopy for Molecular Analysis of Microbial Cells," 2012, pp. 187–211.

[157] B. J. Inkson, "Scanning electron microscopy (SEM) and transmission electron microscopy (TEM) for materials characterization," *Mater. Charact. Using Nondestruct. Eval. Methods*, pp. 17–43, Jan. 2016.

[158] D. P. Allison, N. P. Mortensen, C. J. Sullivan, and M. J. Doktycz, "Atomic force microscopy of biological samples," *Wiley Interdiscip. Rev. Nanomedicine Nanobiotechnology*, vol. 2, no. 6, pp. 618–634, Nov. 2010.

[159] K. Dorywalski, I. Maciejewski, and T. Krzyżyński, "Spectroscopic ellipsometry technique as a materials characterization tool for mechatronic systems—The case of composition and doping concentration monitoring in SBN crystals," *Mechatronics*, vol. 37, pp. 33–41, Aug. 2016.

[160] V. Rouessac, "Porosity analysis of thin films by coupled techniques." Institut Européen des Membranes, Montpellier, 2016.

[161] V. Rouessac, A. van der Lee, F. Bosc, J. Durand, and A. Ayral, "Three characterization techniques coupled with adsorption for studying the nanoporosity of supported films and membranes," *Microporous Mesoporous Mater.*, vol. 111, no. 1–3, pp. 417–428, Apr. 2008.

[162] "The International Union of Pure and Applied Chemistry (IUPAC)." https://iupac.org/.

[163] N. M. Harrison, "An Introduction to Density Functional Theory," *Technology*, vol. 2, no. 1, pp. 1–26, 1995.

[164] W. Koch and M. C. Holthausen, *A Chemist's Guide to Density Functional Theory*, vol. 3. 2001.

[165] J. W. Ochterski, "Vibrational Analysis in Gaussian," *White Pap.*, 1999.

[166] M. P. Andersson and P. Uvdal, "New scale factors for harmonic vibrational frequencies using the B3LYP density functional method with the triple-ζ basis Set 6-311+G(d,p)," *J. Phys. Chem. A*, vol. 109, no. 12, pp. 2937–2941, Mar. 2005.

[167] A. Kramida, Y. Ralchenko, J. Reader, and (2018) NIST ASD Team, "NIST Atomic Spectra Database (version 5.5.6), [Online]." National Institute of Standards and Technology, Gaithersburg, MD.

[168] F. Nicolazo, "Etude du procédé de dépôt de couches minces d'oxyde de silicium en plasma hélicon O2/TEOS," Université de Nantes, IMN, 1997.

[169] A. Granier, D. Chéreau, K. Henda, R. Safari, and P. Leprince, "Validity of actinometry to monitor oxygen atom concentration in microwave discharges created by surface wave in O2-N2 mixtures," *J. Appl. Phys.*, vol. 75, no. 1, pp. 104–114, Jan. 1994.

[170] R. W. B. (Reginald W. B. Pearse and A. G. (Alfred G. Gaydon, *The identification of molecular spectra*. Chapman and Hall, 1976.

[171] G. Herzberg, *Molecular spectra and molecular structure*. R.E. Krieger Pub. Co, 1989.

[172] B.-O. Cho, S. Lao, L. Sha, and J. P. Chang, "Spectroscopic study of plasma using zirconium tetra-tert-butoxide for the plasma enhanced chemical vapor deposition of zirconium oxide," *J. Vac. Sci. Technol. A Vacuum, Surfaces, Film.*, vol. 19, no. 6, p. 2751, 2001.

[173] S. Peter, F. Richter, R. Tabersky, and U. König, "Optical emission spectroscopy of a PCVD process used for the deposition of TiN on cemented carbides," *Thin Solid Films*, vol. 377–378, pp. 430–435, Dec. 2000.

[174] A. Granier *et al.*, "Investigation of plasma surface interactions during TiO2 deposition in an O2/TTIP low pressure ICP plasma," in *Proceedings of 20th International Symposium on Plasma Chemistry*, 2011.

[175] A. Granier, M. Vervloet, K. Aumaille, and C. Vallée, "Optical emission spectra of TEOS and HMDSO derived plasmas used for thin film deposition," *Plasma Sources Sci. Technol.*, vol. 12, no. 1, pp. 89–96, 2003.

[176] P. A. Agron, E. L. Fuller Jr, H. F. Holmes, and E. L. Fuller, "IR studies of water sorption on ZrO2 polymorphs," *J. Colloid Interface Sci.*, vol. 52, no. 3, pp. 553–561, 1975.

[177] K. S. Finnie, D. J. Cassidy, J. R. Bartlett, and J. L. Woolfrey, "IR spectroscopy of surface water and hydroxyl species on nanocrystalline TiO2 films," *Langmuir*, vol. 17, no. 3, pp. 816–820, 2001.

[178] H. Lin *et al.*, "In situ IR study of surface hydroxyl species of dehydrated TiO2: towards understanding pivotal surface processes of TiO2 photocatalytic oxidation of toluene," *Phys. Chem. Chem. Phys.*, vol. 14, no. 26, p. 9468, Jun. 2012.

[179] D. C. L. Vasconcelos, V. C. Costa, E. H. M. Nunes, A. C. S. Sabioni, M. Gasparon, and W. L. Vasconcelos, "Infrared Spectroscopy of Titania Sol-Gel Coatings on 316L Stainless Steel," *Mater. Sci. Appl.*, vol. 02, no. 10, pp. 1375–1382, Oct. 2011.

[180] B. O. Cho, S. X. Lao, and J. P. Chang, "Origin and effect of impurity incorporation in plasma-enhanced ZrO2deposition," *J. Appl. Phys.*, vol. 93, no. 11, pp. 9345–9351, 2003.

[181] G. Socrates, *Infrared and raman characteristic group frequencies : tables and charts.* John Wiley & Sons, 2007.

[182] S. Kouva, K. Honkala, L. Lefferts, and J. Kanervo, "Review: monoclinic zirconia, its surface sites and their interaction with carbon monoxide," *Catal. Sci. Technol.*, vol. 5, no. 7, pp. 3473–3490, Jun. 2015.

[183] Z.-Y. Ma, C. Yang, W. Wei, W.-H. Li, and Y.-H. Sun, "Surface properties and CO adsorption on zirconia polymorphs," *J. Mol. Catal. A Chem.*, vol. 227, no. 1–2, pp. 119–124, Mar. 2005.

[184] J. Kondo, H. Abe, Y. Sakata, K. Maruya, K. Domen, and T. Onishi, "Infrared studies of adsorbed species of H2, CO and CO2 over ZrO2," *J. Chem. Soc. Faraday Trans. 1 Phys. Chem. Condens. Phases*, vol. 84, no. 2, p. 511, 1988.

[185] W. Hertl, "Surface chemistry of zirconia polymorphs," *Langmuir*, vol. 5, no. 1, pp. 96–100, Jan. 1989.

[186] B. Bachiller-Baeza, I. Rodriguez-Ramos, and A. Guerrero-Ruiz, "Interaction of Carbon Dioxide with the Surface of Zirconia Polymorphs," *Langmuir*, vol. 14, no. 13, pp. 3556–3564, 1998.

[187] K. D. D. and and A. J. McQuillan*, "An Infrared Spectroscopic Study of Carbonate Adsorption to Zirconium Dioxide Sol−Gel Films from Aqueous Solutions," 1997.

[188] M. J. Alam and D. C. Cameron, "Preparation and characterization of {TiO} 2 thin films by sol-gel method," *J. sol-gel Sci. Technol.*, vol. 25, no. 2, pp. 137–145, 2002.

[189] N. T. McDEVITT and W. L. BAUN, "Infrared Absorption Spectroscopy in Zirconia Research," *J. Am. Ceram. Soc.*, vol. 47, no. 12, pp. 622–624, Dec. 1964.

[190] C. Pecharromán, M. Ocaña, and C. J. Serna, "Optical constants of tetragonal and cubic zirconias in the infrared," *J. Appl. Phys.*, vol. 80, no. 6, p. 3479, Jun. 1998.

[191] P. Piszczek, A. Grodzicki, M. Richert, A. Radtke, A. Wojtczak, and T. Glowiak, "Multicore Ti(IV) and Zr(IV) oxo carboxylates as precursors of thin films of TiO_2 and ZrO_2." .

[192] P. M. Kumar, S. Badrinarayanan, and M. Sastry, "Nanocrystalline TiO2 studied by optical, FTIR and X-

ray photoelectron spectroscopy: correlation to presence of surface states," *Thin Solid Films*, vol. 358, no. 1–2, pp. 122–130, Jan. 2000.

[193] M. Ivanda, S. Music̀, S. Popović, and M. Gotić, "XRD, Raman and FT-IR spectroscopic observations of nanosized TiO2 synthesized by the sol–gel method based on an esterification reaction," *J. Mol. Struct.*, vol. 480–481, pp. 645–649, May 1999.

[194] I. Oja, A. Mere, M. Krunks, C.-H. Solterbeck, and M. Es-Souni, "Properties of TiO2 Films Prepared by the Spray Pyrolysis Method," *Solid State Phenom.*, vol. 99–100, pp. 259–264, 2004.

[195] N. T. McDevitt and W. L. Baun, "Infrared absorption study of metal oxides in the low frequency region (700-240 cm−1)," *Spectrochim. Acta*, vol. 20, no. 5, pp. 799–808, May 1964.

[196] A. E. Saatci and O. Özdemir, "Electrical Characterization of Sol-Gel Derived TiO $_2$ Film on c-Si Substrate by Admittance Measurement," *Adv. Mater. Sci. Eng.*, vol. 2014, pp. 1–5, Aug. 2014.

[197] G.-W. Peng, S.-K. Chen, and H.-S. Liu, "Infrared Absorption Spectra and Their Correlation with the Ti-O Bond Length Variations for TiO $_2$ (Rutile), Na-Titanates, and Na-Titanosilicate (Natisite, Na $_2$ TiOSiO $_4$)," *Appl. Spectrosc.*, vol. 49, no. 11, pp. 1646–1651, Nov. 1995.

[198] V. G. Erkov, S. F. Devyatova, E. L. Molodstova, T. V. Malsteva, and U. A. Yanovskii, "Si–TiO2 interface evolution at prolonged annealing in low vacuum or N2O ambient," *Appl. Surf. Sci.*, vol. 166, no. 1–4, pp. 51–56, Oct. 2000.

[199] J.-Y. Zhang, I. W. Boyd, B. J. O'Sullivan, P. K. Hurley, P. V Kelly, and J.-P. Sénateur, "Nanocrystalline TiO2 films studied by optical, XRD and FTIR spectroscopy," *J. Non. Cryst. Solids*, vol. 303, no. 1, pp. 134–138, May 2002.

[200] M. Pelliccione, T. Karabacak, C. Gaire, G.-C. Wang, and T.-M. Lu, "Mound formation in surface growth under shadowing," *Phys. Rev. B*, vol. 74, no. 12, Sep. 2006.

[201] T. Karabacak, H. Guclu, and M. Yuksel, "Network behavior in thin film growth dynamics," *Phys. Rev. B*, vol. 79, no. 19, May 2009.

[202] R. Alvarez *et al.*, "Growth of SiO2 and TiO2 thin films deposited by reactive magnetron sputtering and PECVD by the incorporation of non-directional deposition fluxes," *Phys. status solidi*, vol. 210, no. 4, pp. 796–801, Apr. 2013.

[203] A. Borrás, A. Yanguas-Gil, A. Barranco, J. Cotrino, and A. R. González-Elipe, "Relationship between scaling behavior and porosity of plasma-deposited TiO 2 thin films," *Phys. Rev. B*, vol. 76, no. 23, Dec. 2007.

[204] A. Palmero, N. Tomozeiu, A. M. Vredenberg, W. M. Arnoldbik, and F. H. P. . Habraken, "On the deposition process of silicon suboxides by a RF magnetron reactive sputtering in Ar–O2 mixtures: theoretical and experimental approach," *Surf. Coatings Technol.*, vol. 177–178, pp. 215–221, Jan. 2004.

[205] R. Alvarez *et al.*, "Nanocolumnar growth of thin films deposited at oblique angles: Beyond the tangent rule," *J. Vac. Sci. Technol. B, Nanotechnol. Microelectron. Mater. Process. Meas. Phenom.*, vol. 32, no. 4, p. 041802, Jul. 2014.

[206] U. F. R. Sciences *et al.*, "Type of Plasmas and Microstructures of TiO[sub 2] Thin Films Prepared by Plasma Enhanced Chemical Vapor Deposition," *Thin Solid Films*, vol. 33, no. 1, p. P152, 2006.

[207] R. Alvarez *et al.*, "Modulating low energy ion plasma fluxes for the growth of nanoporous thin films," *Plasma Process. Polym.*, vol. 12, no. 8, pp. 719–724, 2015.

[208] A. Yanguas-Gil, J. Cotrino, A. Barranco, and A. R. González-Elipe, "Influence of the Angular Distribution Function of Incident Particles on the Microstructure and Anomalous Scaling Behavior of Thin Films," *Phys. Rev. Lett.*, vol. 96, no. 23, Jun. 2006.

[209] D. Smith and P. Baumeister, "Refractive index of some oxide and fluoride coating materials," *Appl. Opt.*, vol. 18, no. 1, p. 111, Jan. 1979.

[210] J. D. Traylor Kruschwitz and W. T. Pawlewicz, "Optical and durability properties of infrared transmitting thin films," *Appl. Opt.*, vol. 36, no. 10, p. 2157, Apr. 1997.

[211] J. R. DeVore, "Refractive Indices of Rutile and Sphalerite," *J. Opt. Soc. Am.*, vol. 41, no. 6, p. 416, Jun. 1951.

[212] J. Kischkat *et al.*, "Mid-infrared optical properties of thin films of aluminum oxide, titanium dioxide,

silicon dioxide, aluminum nitride, and silicon nitride," *Appl. Opt.*, vol. 51, no. 28, p. 6789, Oct. 2012.

[213] W. Groh and A. Zimmermann, "What is the lowest refractive index of an organic polymer?," *Macromolecules*, vol. 24, no. 25, pp. 6660–6663, Dec. 1991.

[214] C. Vautrin-Ul, C. Boisse-Laporte, N. Benissad, A. Chausse, P. Leprince, and R. Messina, "Plasma-polymerized coatings using HMDSO precursor for iron protection," *Prog. Org. Coatings*, vol. 38, no. 1, pp. 9–15, Feb. 2000.

[215] B. Despax and P. Raynaud, "Deposition of 'Polysiloxane' Thin Films Containing Silver Particles by an RF Asymmetrical Discharge," *Plasma Process. Polym.*, vol. 4, no. 2, pp. 127–134, Feb. 2007.

[216] T. N. Tran, T. Van Anh Pham, M. L. Phung Le, T. P. Thoa Nguyen, and V. M. Tran, "Synthesis of amorphous silica and sulfonic acid functionalized silica used as reinforced phase for polymer electrolyte membrane," *Adv. Nat. Sci. Nanosci. Nanotechnol.*, vol. 4, no. 4, p. 45007, Sep. 2013.

[217] T. García-Pérez, E. Rodríguez, E. Bittencourt, and Z. Jova, "Activation of HMDSO thin films with low pressure argon plasma and vacuum ultraviolet radiation," *Lat. Am. Appl. Res.*, vol. 42, no. 1, pp. 19–25, Jan. 2012.

[218] V. Verlaan *et al.*, "The effect of composition on the bond structure and refractive index of silicon nitride deposited by HWCVD and PECVD," *Thin Solid Films*, vol. 517, no. 12, pp. 3499–3502, 2009.

[219] M. H. Moore, T. Tanabe, and J. A. Nuth, "The SiH vibrational stretch as an indicator of the chemical state of interstellar grains," *Astrophys. J.*, vol. 373, 1991.

[220] E. San Andrés *et al.*, "Bonding configuration and density of defects of SiOxHy thin films deposited by the electron cyclotron resonance plasma method," *J. Appl. Phys.*, vol. 94, no. 12, p. 7462, 2003.

[221] W. A. Pliskin and R. P. Esch, "Refractive Index of SiO_2 Films Grown on Silicon," *J. Appl. Phys.*, vol. 36, no. 6, pp. 2011–2013, Jun. 1965.

[222] S. V. Mutilin and T. Khasanov, "The refractive index of homogeneous SiO2 thin films," *Opt. Spectrosc.*, vol. 105, no. 3, pp. 461–465, Sep. 2008.

[223] S. Ligot *et al.*, "Experimental and Theoretical Study of the Plasma Chemistry of Ethyl Lactate Plasma Polymerization Discharges," *Plasma Process. Polym.*, vol. 12, no. 5, pp. 405–415, May 2015.

[224] S. Ligot *et al.*, "Combining Mass Spectrometry Diagnostic and Density Functional Theory Calculations for a Better Understanding of the Plasma Polymerization of Ethyl Lactate," *J. Phys. Chem. B*, vol. 118, no. 15, pp. 4201–4211, Apr. 2014.

Annex

Table A-1: Synthetic IR spectrum of ZTB molecule calculated by DFT method in Gaussian09 software.

ZTB molecule	
Wavenumber (cm^{-1})	**Assignation**
2983.24-2981.4	C-H in CH_3 a-stretching in phase
2977.4-2972.70	C-H in CH_3 a-stretching out of phase
2917.06-2916.4	C-H in CH_3 s-stretching in phase
2908.87-2907.91	C-H in CH_3 s-stretching out of phase
1459.55-1456.41	C-H in CH_3 scissoring in phase
1441.07-1438.32	C-H in CH_3 scissoring out of phase
1430.33-1427.51	C-H in CH_3 scissoring out of phase
1416.71-1415.44	C-H in CH_3 scissoring out of phase
1367.59-1365.72	C-H in CH_3 wagging in phase
1341.97-1339.52	C-H in CH_3 wagging out of phase
1203.77-1201.68	C-H in CH_3 rocking
1162.76-1162.34	C-O stretching
1037.25	Zr-O s-stretching C-O s-stretching
997.93-997.29	Zr-O-C stretching
923.91-922.68	CH_3 rocking
874.91-872.42	CH_3 rocking
754.72-753.97	Zr-O stretching C-C s-stretching
517.83-516.97 499.71	C-C-C bending Zr-O stretching
460.31-459.0 455.2-451.49	Zr-O-C bending C-C-C bending
338.02-326.99	C-C-C bending

Table A-2: Synthetic IR spectrum of TTIP molecule calculated by DFT method in Gaussian09 software.

TTIP molecule	
Wavenumber (cm^{-1})	**Assignation**
2985.4-2983.8	C-H in CH_3 a-stretching in phase
2981.6-2980.0	C-H in CH_3 a-stretching out of phase
2979.7-2977.7	C-H in CH_3 a-stretching in phase
2972.2-2970.2	C-H in CH_3 a-stretching out of phase
2913.7-2912.3	C-H in CH_3 s-stretching in phase
2908.7-2907.2	C-H in CH_3 s-stretching out of phase
2869.9-2858.0	C-H in CH stretching
1450.7-1447.8	C-H in CH_3 scissoring in phase
1434.5-1433.3	C-H in CH_3 scissoring in phase
1430.3-1421.8	C-H in CH_3 scissoring out of phase
1359.6-1357.8	C-H in CH_3 wagging in phase
1343.1-1341.2	C-H in CH_3 wagging out of phase
1318.5-1311.5	C-H in CH bending
1155.7	Ti-O-C s-stretching
1141.1-1140.3	C-C-C bending
1108.7-1106.2	C-O stretching out of phase
1099.6-1097.3	C-C a-stretching
1015.2	Ti-O-C s-stretching in phase
996.9-990.8	Ti-O-C a-stretching
906.9-889.4	C-C-H bending
827.4-824.2	C-C-C s-stretching in phase
616.0-610.9	Ti-O a-stretching
569.0	Ti-O s-stretching
447.2-434.2 427.6 416.2-398.1	Ti-O-C bending C-C-C bending
325.4-322.0	C-C-C bending

Table A-3: Synthetic IR spectrum of HMDSO molecule calculated by DFT method in Gaussian09 software.

HMDSO molecule	
Wavenumber (cm^{-1})	**Assignation**
2976.4-2969.6	C-H in CH_3 a-stretching
2907.1-2903.8	C-H in CH_3 s-stretching
1418.7-1396.8	C-H in CH_3 scissoring
1250.8-1242.0	C-H in CH_3 wagging
1040.3	Si-O-Si a-stretching
873.0	Si-O-Si s-stretching Si-C-H bending
835.1-818.2	Si-C-H bending
743.9-736.9	Si-C-H bending
632.5	Si-O-Si s-stretching
588.8	Si-C s-stretching out of phase in $Si(CH_3)_3$
471.1	Si-O-Si s-stretching
311.1 307.7	Si-O-Si bending
241.3-238.7	C-Si-C bending CH_3 groups scissoring

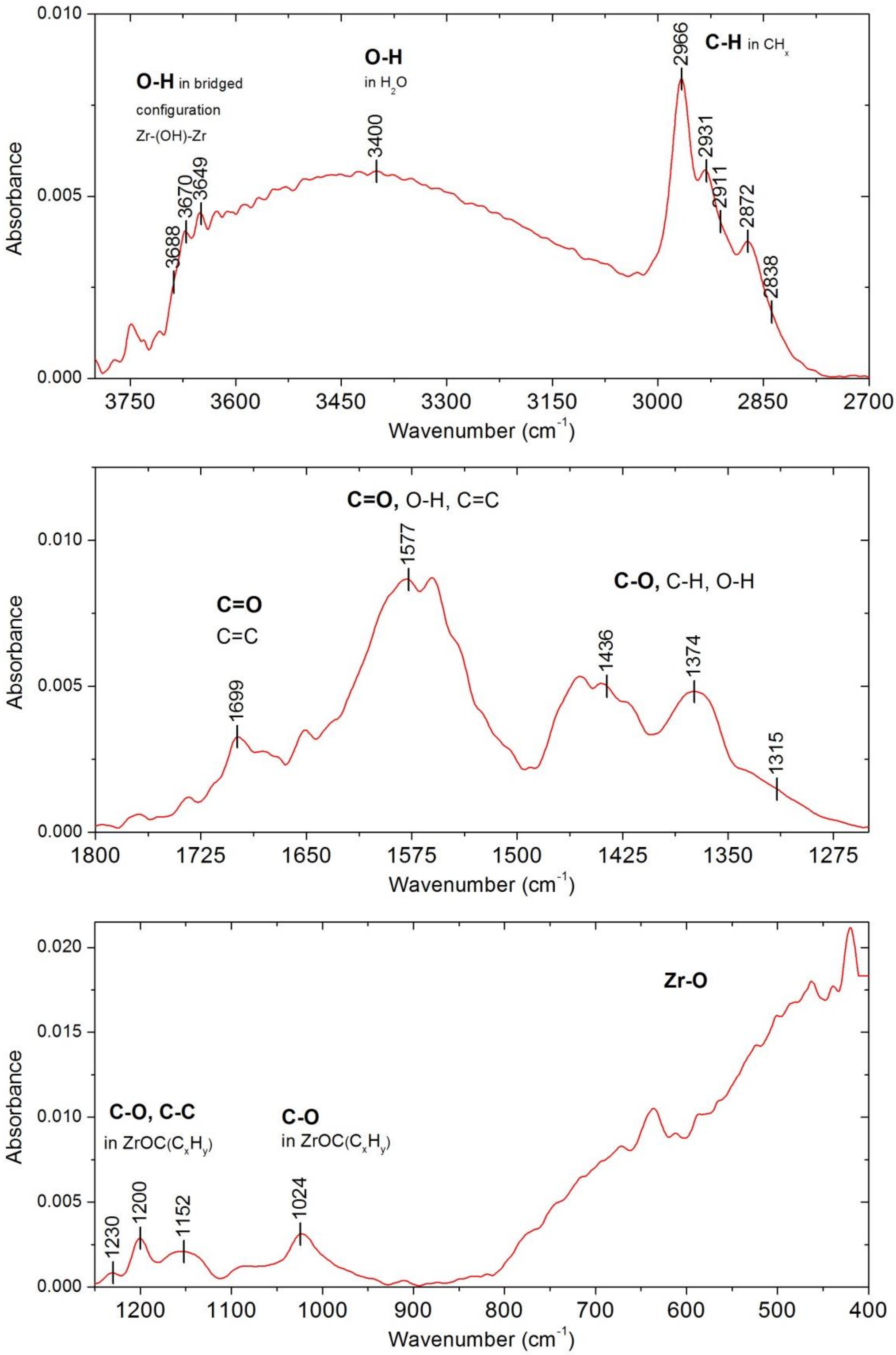

Figure A-1: FTIR spectrum of thin film deposited in 50% ZTB / 50% O_2 plasma (p_{total} = 1 mTorr, P_{MW} = 800 W, $V_{substrate}$= floating).

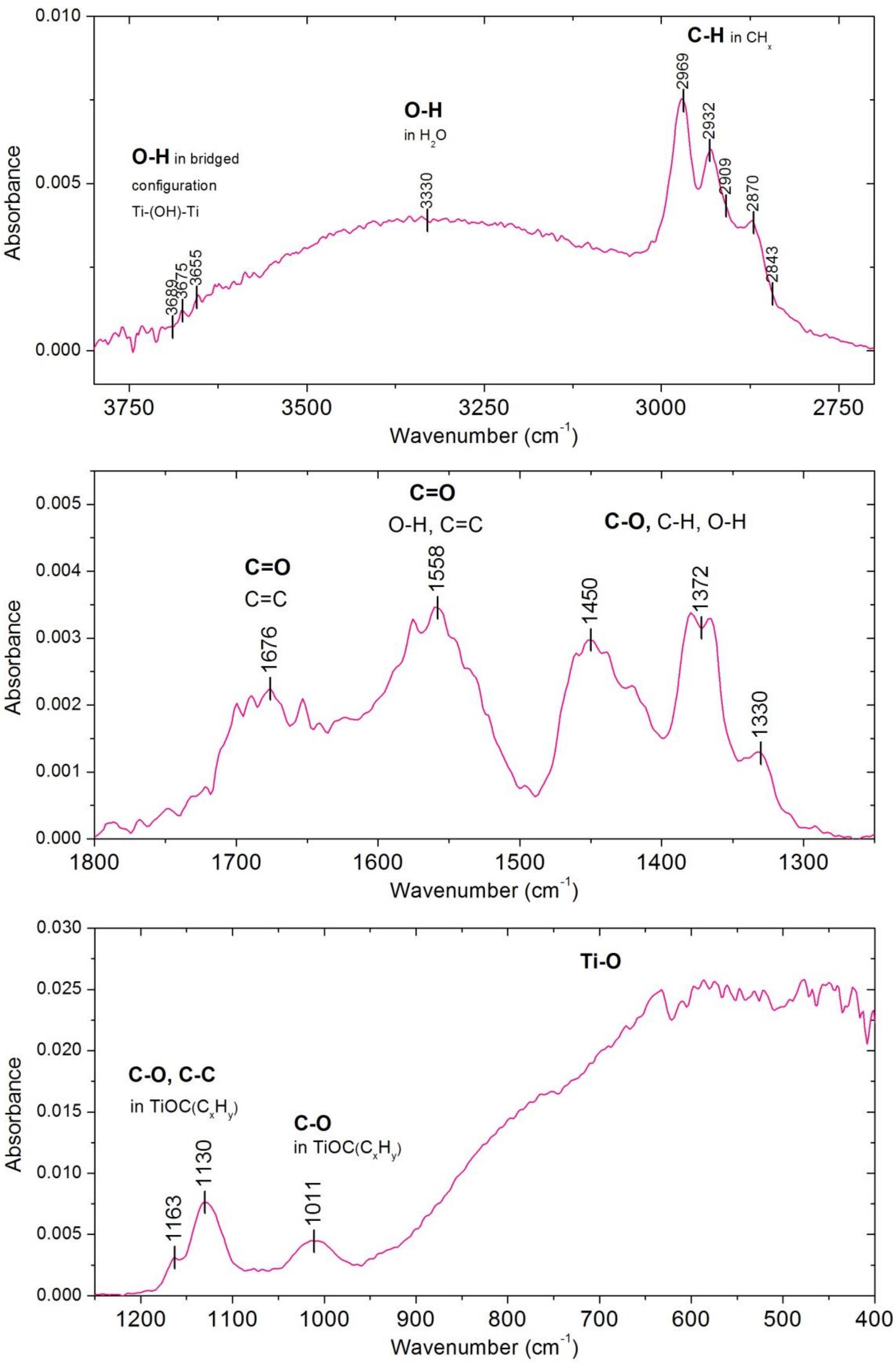

Figure A-2: FTIR spectrum of thin film deposited in 50% TTIP / 50% O_2 plasma (p_{total} = 1 mTorr, P_{MW} = 800 W, $V_{substrate}$= floating).

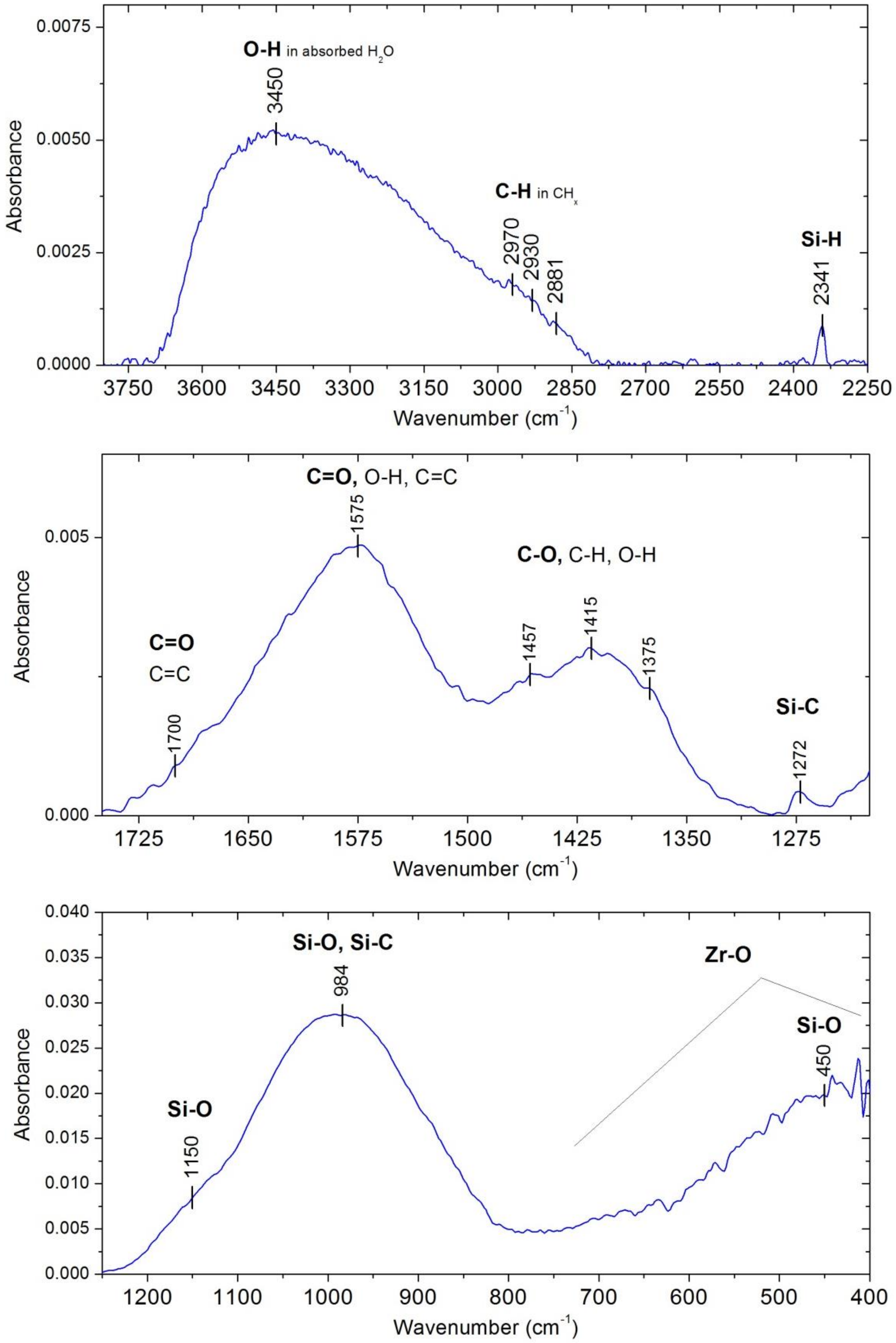

Figure A-3: FTIR spectrum of thin film deposited in 4% ZTB / 13% HMDSO / 83% O_2 plasma (p_{total} = 2.3 mTorr, P_{MW} = 800 W, $V_{substrate}$= floating).

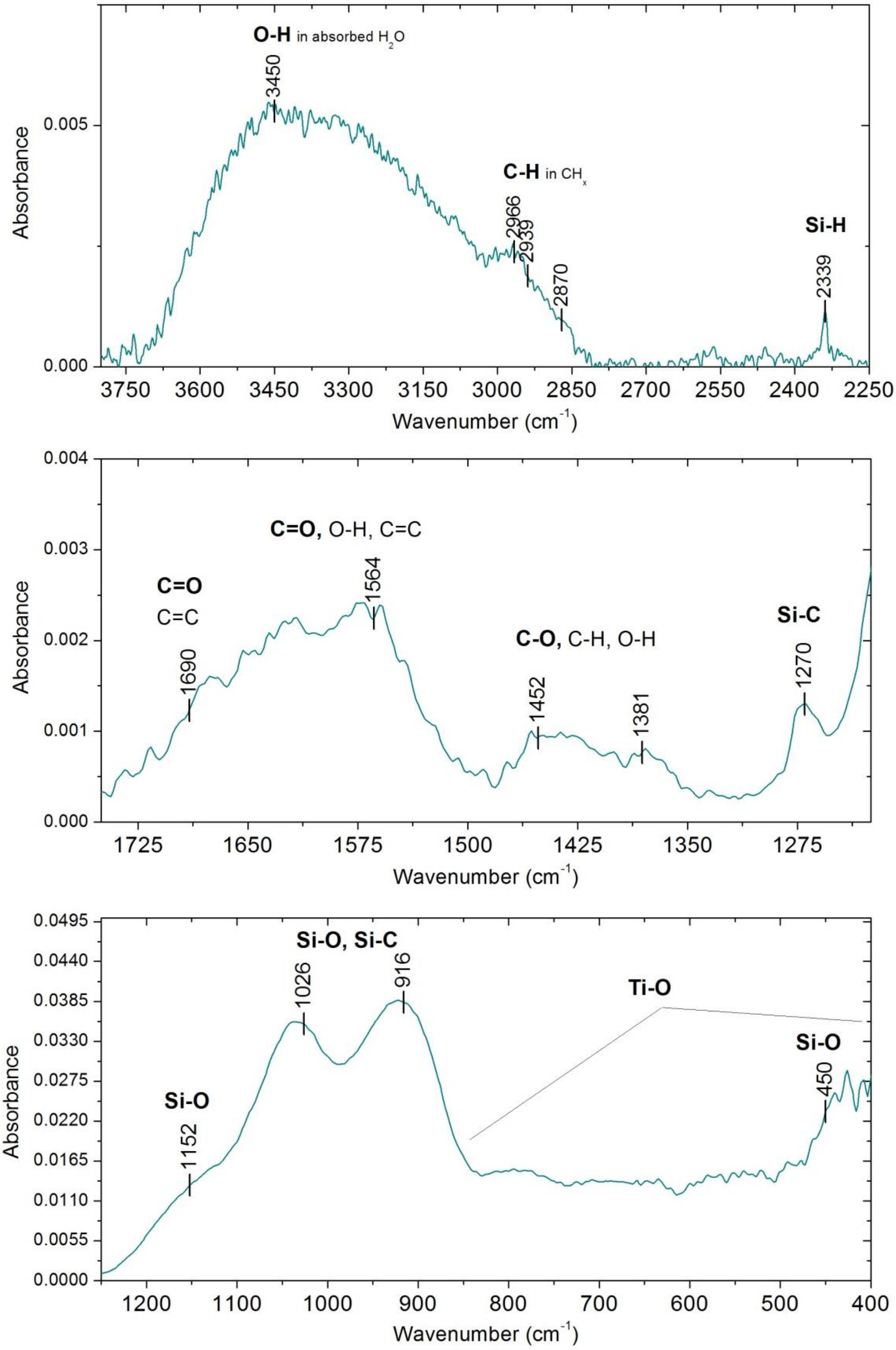

Figure A-4: FTIR spectrum of thin film deposited in 4% TTIP / 13% HMDSO / 83% O_2 plasma (p_{total} = 2.3 mTorr, P_{MW} = 800 W, $V_{substrate}$= floating).

Résumé

Dans ces travaux des couches minces d'oxyde métalliques et « composites » oxyde métalliques siliciés ont été obtenues par PECVD dans un réacteur plasma multi-dipolaire RCE à partir de mélanges gazeux composés d'oxygène et de de précurseurs organométalliques [le Zirconium (IV) tert-Butoxide (ZTB, $ZrO_4C_{16}H_{36}$) et le Titanium (IV) isopropoxide (TTIP, $TiO_4C_{12}H_{28}$)].
Dans la première partie de ce travail les travaux se sont focalisés sur l'étude des caractéristiques des couches minces en fonction du rapport O_2/précurseur. Dans les deux cas (oxyde de titane et oxyde de zirconium) nous avons montré que les propriétés analysées évoluent de manière similaire avec l'augmentation du rapport O_2/précurseur. La composition des films évolue d'une phase organique à une phase quasi inorganique avec l'addition d'O_2 dans le mélange. La croissance des couches passe d'un mode de croissance homogène à colonnaire (dans le plasma très fortement oxydé). D'un point de vue fondamental les colonnes obtenues expérimentalement en ZTB et TTIP ont été comparées à celles obtenues par simulation numérique (méthode de Monte Carlo) afin de comprendre les différences morphologiques observées (tailles de colonnes).
Ensuite, nous avons mis en évidence l'influence de la pression du mélange O_2 (95%)/précurseur (5%) sur la croissance de la couche: La composition chimique des films ne change pas significativement avec l'augmentation de la pression. Dans le cas du ZTB, la pression totale a une forte influence sur les caractéristiques structurales: en effet, pour des pressions >8 mTorr la croissance colonnaire disparaît. En revanche ce phénomène n'est pas observé dans le cas du TTIP.
Enfin, dans la troisième partie du travail nous avons démontré la possibilité de réaliser des dépôts de types $ZrSi_wO_xC_yH_z$ et $TiSi_wO_xC_yH_z$ en introduisant simultanément dans le réacteur plasma un précurseur organométallique (ZTB ou TTIP) et un précurseur organosilicié (HMDSO, $OSi_2C_6H_{18}$). L'augmentation du taux de HMDSO dans le mélange permet de passer d'un mode croissance colonnaire (faible teneur de HMDSO) à un mode de croissance Uniforme (plus forte teneur en HMDSO).
Ces travaux ont mis en évidence les diverses possibilités d'accéder à un grand panel de propriétés de couches en termes de densité, indices optiques et porosité.

Mots clés: PECVD basse pression, couches minces, oxyde métalliques, oxyde métalliques siliciés, ZTB, TTIP, HMDSO.

Abstract

In this thesis, metal oxide and metal oxide/silica « composite » thin films were obtained by PECVD in multi-dipolar ECR plasma reactor from gas mixtures composed of oxygen gas and metalorganic precursors [Zirconium (IV) tert-Butoxide (ZTB, $ZrO_4C_{16}H_{36}$) and Titanium (IV) isopropoxide (TTIP, $TiO_4C_{12}H_{28}$)].
In the first part of the thesis, the study focused on thin film characteristics as a function of O_2/precursor ratio. As O_2/precursor ratio increased, analysed properties evolve similarly in both zirconium and titanium oxide films. Composition of thin films progresses from organic to almost inorganic with addition of oxygen to plasma gas mixture. The growth mode evolves from homogeneous to columnar in highly oxidized plasma. From a fundamental point of view, columns obtained experimentally in ZTB and TTIP were compared with those obtained by theoretical simulation (Monte Carlo method) in order to understand the observed morphological differences (column width).
Further, we investigated the influence of total gas pressure of plasma gas mixture composed of O_2 (95%)/metalorganic precursor (5%) on thin film growth. Chemical composition of the films does not change drastically with the increase in pressure. In the case of ZTB, total gas pressure has a strong influence on the morphological characteristics: columnar growth disappears at pressures above 8 mTorr. This phenomenon was not observed in films deposited in TTIP plasma.
In the third part of this work, we have demonstrated the possibility of synthesising $ZrSi_wO_xC_yH_z$ and $TiSi_wO_xC_yH_z$ homogeneous thin films by simultaneously introducing a metalorganic precursor and an organosilicon precursor [Hexamethyldisiloxane (HMDSO, $OSi_2C_6H_{18}$)] into the reactor. Increase in the fraction of HMDSO in the plasma gas mixture induces a change in growth mode from columnar growth mode (low HMDSO content) to uniform growth mode (higher HMDSO content).
This work has highlighted the various possibilities of obtaining a large panel of thin film properties in terms of density, optical index and porosity.

Keywords: low pressure PECVD, thin films, metal oxide, metal oxide/silica, ZTB, TTIP, HMDSO.